Solar Chimney Power Plant

A Holistic Approach to the Improvement of the Flow within the Transition Section

Dissertation

zur

Erlangung des Grades
Doktor-Ingenieur (Dr.-Ing.)

der

Fakultät für Architektur und Bauingenieurwesen
an der
Bergischen Universität Wuppertal

von

Markus Günter Herbst (geb. Tschersich)

aus Mülheim an der Ruhr

April 2018

Die Dissertation kann wie folgt zitiert werden:

urn:nbn:de:hbz:468-20181211-122523-7
[http://nbn-resolving.de/urn/resolver.pl?urn=urn%3Anbn%3Ade%3Ahbz%3A468-20181211-122523-7]

Abstract

The process of optimization for engineering structures under fluid loads requires an adaptation of the structure itself. An isolated treatment of the physical processes involved is therefore not productive. A holistic approach is required which will be explained in the course of this work for a Solar Chimney Power Plant (SCPP). The outer shape of the Solar Chimney (SCH) looks like a Cooling Tower (CT), which is utilized in conventional power plants to emit superfluous heat from the process of energy production. Deduced from CTs, the SCH exhibits a high and slender structure with a hyperbolic shape in its lower part and variable in the upper part. The SCPP belongs to the renewable energies and impresses with its structural simplicity. Utilizing the buoyancy effect, green energy with no emission of CO_2 can be produced in form of electrical energy. This power plant is a good alternative to other technology like photovoltaic or Concentrated Solar Power Plant (CSPP) or even wind power.

Part I of this work summarizes the basics of the physical processes involved in the SCPP technology. Additionally, an introduction in the numerical analysis of fluid mechanic problems (Computational Fluid Dynamics (CFD)) is given. The three structural components, namely the Solar Collector (SC), the SCH and the turbines, as the major impact factor on the development of the flow field within the SCPP will be explained in detail at a later stage of this work for the process of a structural optimization.

In part II a mathematical 1D model is developed to investigate the influence of the heat storage effect of soil underneath the SC on the diurnal cycle of energy production. Due to simplifications in structure and fluid flow a spatial model had to be set up to rule out modelling errors. A first wind tunnel study at the University of Stellenbosch in South Africa on a scaled model of the SCPP provided essential results for further investigations. By the help of Particle Image Velocimetry (PIV) measurements the flow situation inside the SCPP has been illustrated for different v_{wind}/v_t ratios, expressing the ambient wind v_{wind} and the internal flow stream v_t, representing the buoyancy effect in a simplified manner. It has been shown that there is a strong influence of this velocity ratio on the flow field, especially inside the transition section. Due to the hitherto assumption of symmetry for the flow field a numerical model of the only prototype plant from Manzanares has been set up to compare real data with results obtained from numerical analysis. The same model has been used to show the influence of a redirecting variant inside the chimney base on the flow stream as it had been implemented in the Manzanares plant. Results underline the improving character due to the guidance effect of the installation why a Finite Element (FE) model has been built which includes both structural and fluid mechanic design aspects. Based on this model the influence of a diffuser chimney and the implementation of different variants of guidance inside the transition section will be clarified within the following course of this work.

Part III shows the investigation on the designed chimney model and for different influence factors gathered with pressure and Constant Temperature Anemometry (CTA) measurements at the wind tunnel in Bochum. The intended holistic approach has proven its applicability. A distinct improvement of the flow situation has been achieved with the implementation of redirecting variants and a diffuser for the upper part of the SCH which will lead to an increase in efficiency of the whole SCPP. Results show that the former assumption of symmetric inflow conditions shall be discarded with the aim of a more representative estimation of the real flow situation. The implementation of the new findings in future projects will help the SCPP technology to be competitive with other renewable technologies.

Zusammenfassung

Bei der Optimierung von strömungsmechanischen Prozessen an Ingenieurbauwerken ist ein wesentlicher Ansatzpunkt die Veränderung und Anpassung der Struktur an die vorliegenden Gegebenheiten. Hieraus ergibt sich, dass eine isolierte Betrachtung der physikalischen Prozesse des Strömungsmediums und die der Strukturparameter wenig zielführend ist. Ein ganzheitlicher Ansatz ist daher notwendig, wie er in dieser Arbeit anhand eines Aufwindkraftwerks aufgezeigt wird. Das Aufwindkraftwerk ähnelt von seiner Form her Kühltürmen, wie sie im konventionellen Kraftwerksbetrieb zum Zweck der Abkühlung des Prozesswassers genutzt werden. Hiervon abgeleitet ergibt sich die äußere Form eines schlanken, gleichzeitig aber sehr hohen Bauwerks mit hyperbolischem Höhenprofil im unteren Bereich und einer variablen Gestaltung in der oberen Hälfte. Als Teil der erneuerbaren Energien besticht das Aufwindkraftwerk dabei durch seine konstruktive Einfachheit und nutzt den thermischen Auftriebseffekt zur Erzeugung schadstofffreier und CO_2 neutraler elektrischer Energie und ist eine ernstzunehmende Alternative zu den Technologien wie Photovoltaik oder CSPP, aber auch zu weiteren Technologien wie der Windkraft.
Teil I dieser Arbeit fasst die Grundlagen der an der vorgestellten Aufwindkraftwerk Technologie beteiligten physikalischen Prozesse zusammen. Gleichzeitig erfolgt eine Einführung in die Grundlagen der numerischen Strömungsmechanik (CFD). Die Struktur als maßgeblicher Einflussfaktor auf die Entwicklung der Strömung innerhalb des Aufwindkraftwerks wird anhand einer detailierten Erläuterung der drei wesentlichen Bauteile Kollektordach, Aufwindturm und Turbinen vollzogen und an späterer Stelle in dieser Arbeit im Zuge einer statischen Optimierung noch ausführlicher besprochen.
In Teil II folgt die Entwicklung eines mathematischen Modells des Aufwindkraftwerks anhand dessen der Einfluss der Bodenspeicherfähigkeit auf den Tagesgang der Energieerzeugung untersucht wird. Das 1D Modell beruht dabei auf vereinfachten Annahmen der strömungsmechanischen Vorgänge, woraus sich die Notwendigkeit eines räumlichen Modells ergab. Erste Windkanalversuche an der University of Stellenbosch in Südafrika an einem Maßstabsmodell des Aufwindkraftwerks lieferten mit Hilfe der PIV Messtechnik wichtige Grundlagen zum Verständnis der Strömungssituation innerhalb des untersuchten Objekts. An diesem Modell wurde der Einfluss eines Geschwindigkeitsverhältnisses v_{wind}/v_t untersucht. Die Variable v_{wind} stellt dabei die äußere Strömung erzeugt durch Wind, v_t vereinfacht den thermischen Auftrieb dar. Dabei zeigte sich die große Abhängigkeit der Strömungssituation von diesem Geschwindigkeitsverhältnis, vornehmlich innerhalb des Umlenkungsbereichs zwischen Kollektordach und Aufwindturm im Bereich der Turbinen. Auf Grund der bis dato in vielen Veröffentlichungen getroffenen Annahme der Symmetrie der Strömung wurde ein numerisches Modell des bisher einzigen Prototypen von Manzanares aufbereitet, um die Möglichkeit des Vergleichs zwischen numerischen Ergebnissen und realen Messdaten zu nutzen. Gleichzeitig erfolgte eine Untersuchung des Einflusses einer Umlenkvariante innerhalb des Turmfußes, mit der eine Verbesserung der Strömungsführung erwartet wurde. Die Ergebnisse belegen den überaus positiven Effekt auf den Strömungsverlauf, weshalb ein FE Modell aufgebaut wurde, dass sowohl strukturmechanische, aber auch strömungsmech-

anische Designaspekte berücksichtigt. Das entwickelte Modell wird im weiteren Verlauf dieser Arbeit genutzt, um anhand eines statisch und strömungsmechanisch sinnvollen Modells die Frage nach dem Einfluss eines Diffusors im oberen Turmbereich zu klären und zudem eine Detailstudie verschiedener Einbau- und Umlenkvarianten im Turmfuß und deren Einfluss auf die Strömung durchzuführen.
Teil III stellt die experimentelle und numerische Untersuchung an dem vorab numerisch entwickelten und vor dem Gedanken der Optimierung entworfenen Turmmodell vor. Der Einfluss eines Turmdiffusors auf die Strömung, der Einbau verschiedener Umlenkvarianten und ein erzeugter Versperrungseffekt am Einlass des Kollektordachs werden mit Hilfe von Druckmessungen und der CTA Messtechnik aufgezeichnet. Der ganzheitliche Ansatz hat sich in den vorliegenden Untersuchungen als zielführend erwiesen. Eine deutliche Verbesserung der Strömungsführung und damit einhergehend eine Effizienzsteigerung des gesamten Aufwindkraftwerks kann mit Hilfe der Einbauten erreicht werden. Ergebnisse zum Einfluss aus Wind und Kollektorversperrung belegen ebenfalls, dass die bisherige Annahme der Symmetrie überholt ist und verworfen werden muss, mit dem Ziel einer realistischeren Einschätzung der Strömungssituation innerhalb des Aufwindkraftwerks. Die vorliegende Untersuchung hilft dabei, die hier gewonnenen Erkenntnisse bei zukünftigen Projekten rund um das Thema Aufwindkraftwerk umzusetzen und die Technologie damit konkurrenzfähig zu bisherigen erneuerbaren Energien zu machen.

Acknowledgements

First of all, I would like to thank my supervisor Prof. Dr.-Ing. Reinhard Harte for his support and motivation during my time at his chair for Statics and Dynamics of Structures at the University of Wuppertal. Doing my PhD has changed my way of thinking and made me to who I am now. Special thanks to Prof. Dr.-Ing. Dr.-Ing. Wilfried B. Krätzig, who unfortunately does not live to see, for the encouragement to do my research about the SCPP technology, the provided model just at the start of my own research and his friendly ear. It could not have been a better start. I am expressing my gratitude to Prof. Dr. Hanno Reuter from the University of Stellenbosch for his supervision during my stays at the University of Stellenbosch and to the team of the workshop for building my model and the support during my study. To M.Eng. Daniel Roux who made it possible to obtain results just in time during my stay in South Africa. To the chair for Water Management and Hydraulic Engineering of Univ.-Prof. Dr.-Ing. Andreas Schlenkhoff for using his high-speed camera and being head of the examination committee. I would particularly like to thank Prof. Dr.-Ing. Dr.-Ing. E.h. Dr. h.c.mult. Karl-Hans Laermann for his friendly ear and the huge interest in my work. I really enjoyed working together with you. To the BMBF and DLR, especially to Ms Ruppert-Elias, for the support during our collaborative work on the joint GERF research project. To CICIND for the financial support during my last year of research. To M.Sc. Daniel Witting for a fruitful and great collaboration during his own studies on his master thesis. To Lukas Arnold for his help and support with the set-up of my numerical analysis, his open ear and interest in my work. To the engineering company Niemann & Partner GbR and my former colleagues who placed the cornerstone which encouraged me to focus my research in the field of fluid mechanics. To my colleagues Prof. PhD Tarek Mekhail from the Aswan University in Egypt and M.Sc. Simon Tewolde from the University of Bochum for the perfect cooperation on the GERF project within the last five years. I would like to say thank you to my colleagues from the university and especially the chair I have been part of. To Prof. Dr.-Ing. Rüdiger Höffer for the utilization of his wind tunnel and being my second supervisor. To Prof. Dr.-Ing. Arndt Goldack for being part of the examination committee. To my colleagues Reinhard Elke and Uwe Wagner for the perfect cooperation, the construction of my wind tunnel models and their help during my studies.

To all my friends for their patience and understanding within the last few years. Thank you for listening and your friendship.

Der größte Dank gilt meinen Eltern Klaus und Monika, die mich während meines gesamten Lebens unterstützt haben. Ohne euch wäre ich nicht einen Meter weit gekommen.

Last but not least special thanks to my wife Sinja for her love and indulgence.

I thank God for saving my life and taking care of our beloved ones.

TO MY WIFE SINJA

Table of Contents

Glossary

Symbol	**Description**	**Unit**
Big Latin Letters		
A	Amplitude	K
	Area	m^2
	Variable	m
B	Soil heat flux	W/m^2
	Variable	m
C	Coefficient	-
	Model constants	-
D	Diameter	m
	Relative uncertainty	-
E	Emissive power	W/m^2
	Emissive power vector	W/m^2
	Latent heat flux	MN/m^2
	Modulus of elasticity	MN/m^2
	Radiation Energy	W/m^2
F	Fluid area	m^2
	Force	kN
	View or configuration factor	-
G	Dead load	kN
	Solar irradiation	kWh/m^2a
H	Height	m
	Losses	-
	Resistance	-
	Sensible heat flux	W/m^2
J	Energy	J
	Radiosity vector	W/m^2
K	Coefficient	-
L	Length	m
	Long-wave radiation	-
	Performance	W
N	Gained value	-
	Sample size	-
O	Model results	-
P	Generation of turbulence kinetic energy term	m^2/s^2
	Measured data	-
	Pitch	$^\circ$

Symbol	Description	Unit
	Precipitation	mm
	Pressure	Pa
Q	Radiation budget	-
	Soil heat flux	W/m^2
	Volume flow rate	m^3/s
R	Specific gas constant	J/kgK
RH	Relative humidity	%
S	Force	kN
	Modulus of mean-rate-of-strain tensor	-
	Momentum source	kN/m^3
	Short-wave radiation	-
T	Period of oscillating	sec
	Temperature	K
	Transmissivity	-
U	Velocity	m/s
U	Mean velocity vector	m/s
V	Velocity	m/s
W	Threshold value	-
	Velocity	m/s
	Wind load	kN
	Work	W
X	Distance	m
Y	Fluctuating dilatation	J/kg

Small Latin Letters

a	Coefficient	-
b	Coefficient	-
	Wien's displacement constant	-
c	(Pressure) coefficient	-
	Specific heat capacity	J/kgK
	Velocity of sound or velocity	m/s
d	Hydraulic diameter	m
	Thickness	m
e	Saturation vapour pressure	Pa
	Turbulence kinetic energy	J/kg
f	Compressive strength	N/mm^2
	Eigenfrequency or Frequency	Hz
	Friction factor	-
g	Constant of gravity	m^2/s
	Wexlers coefficients	-

Symbol	**Description**	**Unit**
h	Enthalpy	kJ/kg
	Heat transfer coefficient	W/m^2K
	Height or thickness	mm
i	Internal Energy	J
k	Coefficient	-
	Factor	-
	Roughness height	m
	Spread	m
	Thermal conductivity	W/mK
	Turbulence kinetic energy	J/kg
	Wave number	-
l	Latent heat	kJ/kg
	Length	m
m	Mass flow	kg/s
	Pressure potential exponent	-
	Thermal diffusion coefficient	m^2/sec
n	Area ratio	-
	In-plane force	kN
	Pressure loss exponent	-
	Sample size	-
p	Pressure	Pa
q	Energy flux	W/m^2
	Hit rate	%
	Radiation transfer	W/m^2
	Specific humidity	%
r	Radius	m
t	Temperature	°C
	Time	sec
u	Axial Component of Velocity	m/s
u	Velocity vector	m/s
v	Cross Component of Velocity	m/s
w	Vertical component of Velocity	m/s
x	Axial direction	-
y	Radial direction	-
z	Damping depth	m
	Tangential direction	m
	Vertical direction	m

Big Greek Letters

Γ	Diffusion coefficient	-

Symbol	Description	Unit
Δ	Difference	-
Φ	Dissipation function	N/m^2s

Small Greek Letters

α	Albedo	-
	Angle	$\circ$
	Thermal diffusivity	m^2/s
β	Constant	-
	Volume or thermal expansion coefficient	-
δ	Boundary layer height	m
	Differential	-
ϵ	Absorptivity	-
	Emissivity	-
	Rate of dissipation	J/kgs
	Second coefficient of viscosity	-
ζ	Resistance coefficient	-
η	Efficiency	-
θ	Blade twist angle	$\circ$
	Temperature	K
	Virtual potential temperature	K
λ	Friction coefficient	-
	Length-scale ratio	-
	Thermal conductivity	W/mK
	Wavelength	m
μ	Dynamic viscosity	kg/ms
	Friction coefficient	-
	Thermal conductivity	W/mK
ν	Efficiency factor	-
	Kinematic viscosity	m^2/sec
	Poisson's Ratio	-
	Resistance coefficient	-
ρ	Density	kg/m^3
σ	Stefan-Boltzmann constant	W/m^2K^4
τ	Stress	N/m^2
	Transmittance	-
ϕ	Relative humidity	%
ψ	Reduction factor	-
ω	Eigen angular frequency	Hz
	Circular frequency	Hz

Symbol	Description	Unit
	Specific dissipation	1/s

Math Operators

div	Divergence	
grad	Gradient	
loss	Losses	
∇	Nabla operator	

Subscripts

B	Ground	
D	Densimetric	
	Drag	
G	Dead Load	
	Gravity	
IR	Infrared	
L	Length	
M	Momentum	
P	Pressure	
Pra	Pitot static tube (Prandtl tube)	
R	Ratio	
T	Temperature	
a	Ambient	
air	Air	
atm	Atmosphere	
b	Position	
c	Component or Section	
cd	Concrete design	
$chimney$	Chimney	
cr	Critical	
d	Position	
	Water vapour	
eff	Effective	
f	Frequency	
	Friction	
fr	Friction	
g	Ground	
$glass$	Glass	
h	Heat	
	Hydraulic	
	Hydrodynamic	

Symbol	**Description**	**Unit**
i	i direction	
in	In	
	Initial	
$idealgas$	Ideal gas	
j	j direction	
k	k direction	
l	Length	
	Losses	
	Lower	
$laminar$	Laminar	
m	Mean or position	
max	Maximum	
$mean$	Mean	
$month$	Month	
n	Effective	
opt	Optimal	
out	Out	
p	Parameter	
PCU	Power conversion unit	
pe	Pressure external	
pi	Pressure internal	
r	Radial	
	Roof	
$roof$	Roof	
s	Section	
	Surface	
sc	Solar collector	
sca	Solar collector air	
$sigma$	Sigma or rms	
sky	Sky	
$soil$	Soil	
$spez$	Specific	
ss	Soil surface	
st	Section	
$support$	Support	
sys	System	
t	Tangential	
	Thermal	
	Tube	
ts	Total-to-static	

Symbol	Description	Unit
tt	Total-to-total	
$tube$	Tube	
$turbine$	Turbine	
$turbulent$	Turbulent	
u	Axial direction	
	Upper	
v	Radial direction	
var	Variant or variable	
$venturi$	Venturi	
w	Tangential direction	
	Water	
wf	Wind fence	
$wind$	Wind	
x	x direction	
y	y direction	
z	z direction	
0,1,2,...	Position	
01,02,03	Position	
11,22,12	Direction	
$20mm$	20 mm	
∞	Undisturbed condition	
ϵ	Marks the rate of dissipation	
λ	Length	
μ	Turbulent viscosity	
Φ	Dissipation	
$GltIA$	Glass to inner air	
$GltOA$	Glass to outer air	
$GltSo$	Glass to soil	
$IAtGl$	Inner air to glass	
$IAtSo$	Inner air to soil	
$OAtGl$	Outer air to glass	
$OAtSo$	Outer air to soil	
$SotGl$	Soil to glass	
$SotIA$	Soil to inner air	
$SotOA$	Soil to outer air	
$SotSo$	Soil to soil	

Superscripts

$*$	Mark	
$\dot{m}$	Specific mass	

Symbol	Description	Unit
$\overline{u}$	Mean or time-averaged	
$+$	Mark	
$'$	Derivation	
$''$	Second derivation	
$\widetilde{p}$	Density-weighted or Favre-averaged	

Key Figures

De	Dean number
Fr	Densimetric Froude number
Nu	Nusselt number
Pr	Prandtl number
Re	Reynolds number
Ri	Richardson number
Ri_f	Flux Richardson number

Acronyms

A | B | C | D | E | F | G | H | I | J | K | L | M | N | O | P | R | S | T | U | V | W

A

AC Alternate Current

ADM Actuator Disc Method

AMSL Above Mean Sea Level

ASW University of Aswan

B

BMBF Bundesministerium für Bildung und Forschung

BPG Best Practise Guideline

BUW Bergische Universität Wuppertal

C

CAD Computational Aided Design

CC Cylindrical Chimney

CCD Charged Coupled Device

CFD Computational Fluid Dynamics

CICIND Comité International des Cheminées Industrielles

CPU Central Processing Unit

CSPP Concentrated Solar Power Plant

CT Cooling Tower

CTA Constant Temperature Anemometry

D

DC Diffuser Chimney

DES Detached Eddy Simulation

DLR Deutsches Zentrum für Luft- und Raumfahrt

DNS Direct Numerical Simulation

DO Discrete Ordinate

E

EADM Extended Actuator Disc Method

ERCOFTAC European Research Community on Flow, Turbulence And Combustion

F

FDS Fire Dynamics Simulator

FE Finite Element

FSI Fluid-Structure-Interaction

FVM Finite Volume Method

FZJ Forschungszentrum Jülich GmbH

G

GERF German Egyptian Research Fond

GMT General Mean Time

GRP Glass-Reinforced Plastic

H

HVDC High Voltage Direct Current

I

ICH Industrial Chimney

IGV Inlet Guide Vane

IR Infrared

ITS-90 International Temperature Scale of 1990

J

JURECA Jülich Research on Exascale Cluster Architectures

K

KUP Krätzig und Partner - Ingenieurgesellschaft für Bautechnik mbH

L

LES Large Eddy Simulation

M

MVR Melt Flow Rate

N

NACA National Advisory Committee for Aeronautics

NIST National Institute of Standards and Technology

O

OGV Outlet Guide Vane

P

PC Polycarbonate

PCU Power Conversion Unit

PE Polyethylen

PIV Particle Image Velocimetry

PJM Pressure Jump Method

PPI Parts per Inch

PT Platinum Temperature Sensor

PV Photovoltaic

PVA Polyvinyl Acetal

PVC Polyvinylchlorid

R

RANS Reynolds Averaged Navier-Stokes

RC Reinforced Concrete

RH Relative Humidity

RMS Root Mean Square

RNG Re-Normalisation Group

RPM Revolutions per Minute

RUB Ruhr-Universität Bochum

S

S2S Surface to Surface Radiation Model

SC Solar Collector

SCH Solar Chimney

SCPP Solar Chimney Power Plant

SGS Subgrid Scale Modeling

SHM Structural Health Monitoring

SST Shear Stress Transport

STDF Science and Technology Development Fund

SUN Stellenbosch University

T

TKE Turbulence Kinetic Energy

U

UDF User Defined Function

ULS Ultimate Limit State

URANS Unsteady Reynolds Averaged Navier-Stokes

V

VBA Visual Basic for Applications

VBS Visual Basic Script

VGB Fachverband der Strom- und Wärmeerzeuger

VLES Very Large Eddy Simulation

VST Vicat Softening Point

W

WT Wind Tunnel

Chapter1

Motivation

1.1 Renewable Energies - Green Technology

Renewable energies have shown their ability to replace conventional energy sources like coal and nuclear energy. At the current state 24 % of the worldwide used energy has been produced by environmental friendly and greenhouse gas emission neutral energy sources. Technologies like the SCPP help to achieve the aim of producing green energy and have a market share of 26 % by 2020. Through its functional principle belongs the SCPP to the category of solar-thermal power plants like photovoltaic, parabolic trough power plants and the power tower technology, also known as CSPP. Main aims of *Green Technology* are:

- **Sustainability**
- **Cradle to Cradle**
- **Source Reduction**
- **Innovation**
- **Viability**

1.2 Solar Chimney Power Plant Technology

In the following section a small review of the SCPP technology and its main components will be presented.

The SCPP is a solar driven wind power plant driven by the buoyancy effect and a density difference between the air parcels connected by a tube, the SCH. The general concept consists of three parts the SCH, the SC and the wind turbine(s). First design concepts include a vertical axis turbine situated in the middle of the SCH base, cf. the prototype tower of Manzanares, Spain. Current concepts, except small scale power plants, usually include horizontal axis turbines situated around the circumference of the tower base. The quantity of turbines depend on the main dimensions of the SCH (height and diameter) and the SC (outer dimensions and height above ground) and therefore on the entire mass flow through the turbines. Figure 1.1 depicts the SCPP and its principle for the classical horizontal axis turbine concept on the left and the current concept for horizontal axis turbines on the right.

The heat storage capacity of the soil underneath the SC enables the system to run even at nocturnal hours and can be enhanced due to further preparations.

The SC of the SCPP is comparable to a huge greenhouse with open sides and a vertical opening in the center for the SCH. Different materials and set-ups have been tested. Single-glazing, double-

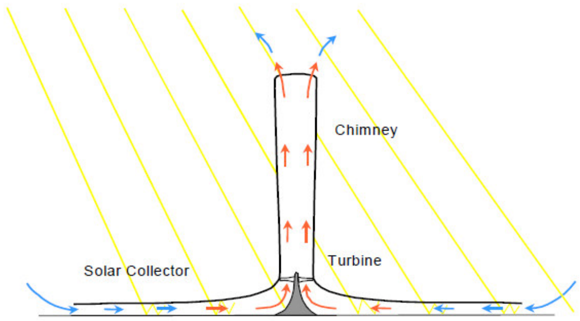

a) Classical Vertical Axis Turbine

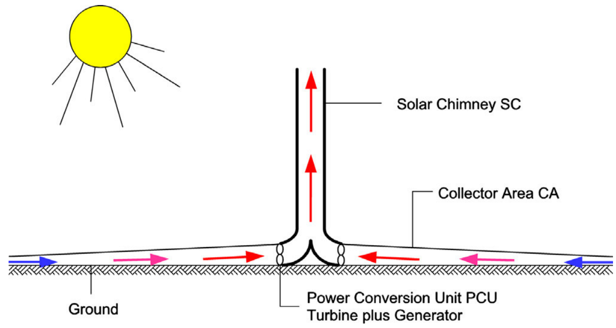

b) Horizontal Axis Turbines

Figure 1.1: Principle of the Solar Chimney [A.159] (left), [A.73] (right)

glazing, plastic or glass, normal white glass or special glass with filters have been part of several investigations, e.g. [A.38], [A.68], [A.125], [A.135]. Also glass for solar energy conversion systems and buildings consisting of a steal frame covered only by glass elements are discussed, cf. chapter 2.

The solar irradiation depending on the latitude, longitude and season penetrates the soil underneath the glass cover and is heated up instead. Depending on the albedo, natural or artificial, one of the main goals is to control the heat storage and release over the diurnal and yearly cycle. As nearly all "green energies" face this problem, that peak hours of energy consumption sometimes come together with shortages of production hours. Another possibility to alter the heat storage capacity is by using water bags or water ponds for storage, therefore see publications by [A.159], [A.20], [A.178] and [A.180]. Instead of bags a black painted ground or a ground covered with highly absorbing materials shows similar results, cf. publications by [A.144], [A.145] and [A.24].

Due to convection the stored heat energy warms up the air underneath the SC which results in cooperation with the inclination of the collector roof in a movement of the heated air towards the center to the SCH. Different concepts of single, double or even triple roof systems were investigated [A.136], [A.45], [A.69] to search for the optimum in harvesting the solar irradiation and generating an optimum of controllability of energy production, cf. chapter 3.

The air transports the thermal energy to the entrance of the turbine area where the air packages have to run through Inlet Guide Vanes (IGVs). They are necessary to canalize the arriving air packages to enter the turbines which are located radially around the SCH base. In early years of research on the field of SCPPs single or multiple vertical axis turbines were favoured, cf. [A.30], [A.39], [A.123].

After the thermal energy is transformed into electric energy the air packages are now highly turbulent and with a smaller velocity compared to the state in front of the turbines and now enter the SCH. This part of the SCPP was to this date rarely investigated. Only [T.13], [T.19] and [A.83] had a detailed look at the transition section between the SC and the SCH which is of main importance for the efficiency of a SCPP.

Most recent research deals with the profile shape of the SCH over height. The standard design with a non-tapered chimney and a tapered tower with constant or even with hyperbolic shape, as it can be found by CTs, are assessed under fluid mechanic and thermodynamic aspects, cf.

[A.140], [A.82], [A.168], [A.139] and [A.128].

At the chimney outlet the exiting air and the free atmosphere are forced to interact. Fluid dynamic phenomenons like the tip effect or inverse air streams known from CTs complete the investigation on the performance enhancement of the SCPP.

For a detailed overview of former experimental research on SCPPs a collection of all known SCPP models is given in appendix A. No guaranty of completeness it is nevertheless very astonishing that after these many years of research only one functional prototype, the one at Manazanares, Spain, exist. All other experimental power plants were in comparison small scale or not operative or missing one or another feature like the turbine.

1.3 Objectives of this Study

The main objectives of this dissertation are as follows. Firstly, a holistic approach to cover the fluid mechanic, thermodynamic and structural characteristics of a SCPP will be pursued. Therefore an improved model of the SCH will be set up. Secondly, the influence of changing flow situations on the flow field within the SCPP will be investigated. The major aim is the improvement of the flow situation, a reduction of flow losses and therefore an increase in efficiency. Following milestones will be resolved in the course of this dissertation:

- Implementation of the heat storage effect of soil underneath the SC in a mathematical 1D model. Its influence on the diurnal and annual cycle of energy production will be clarified.
- Investigation of the effect of wind on the plant performance. Due to ambient parameters the general assumption of symmetry for the inflow conditions cannot be maintained and its impact on the efficiency needs to be resolved.
- Influence of turbines on the flow field. An experimental investigation will show why it is important to take care for this effect.
- Influence of a diffuser on the SCH performance. The diffuser is designed under structural aspects to gain realistic results for the flow measurements. Measurements on a cone tower will be used as a reference.
- Implementation of redirecting variants inside the transition section. These variants will guide the air parcels from the horizontal to the vertical direction while decreasing possible flow losses. It will be tested if the reduced flow losses will lead to increased velocities inside the SCH and therefore and increased efficiency of the SCPP.
- Influence of blockage effects at the periphery of the SC. Due to natural or anthropogenic influencing factors the incoming flow can be hindered by entering the SC. The impact on the general flow field will be checked with the help of wind tunnel tests.
- Modelling of free and forced convection. Due to the buoyancy effect involved in the SCPP technology its effect on the flow parameter will be investigated numerically and experimentally.

Part I

Fundamentals

Chapter2

Structural Aspects of a Solar Chimney Power Plant

This chapter summarizes general structural aspects of the SCPP and its components. The structural system of the SC and SCH are shown and discussed briefly. Additional information about the ground underneath the SC and ways of improving the harvesting of energy are given. The transition section, which connects the SC with the SCH, where the flow experiences a diversion from the horizontal to vertical direction, will be presented here to give a first impression of the necessity of this work.

2.1 Solar Collector

The SC consists of a lightweight framework structure supporting the panels made of glass or special foils with well-defined material properties. The slope towards the center of the SC is defined by the outer diameter and limitations in maximal length of supporting elements. A positive slope corresponds to an inclination towards the center, whereas a negative slope corresponds to an inclination towards the outer rim of the SC. The tangential pitch P_t and radial pitch P_r of supports depends on weight of roof panels and height due to wind action namely on the outer surface. Strong winds should be taken into account for the static calculations, excitation and therefore dynamic load cases for the dynamic calculations, respectively. In figure 2.1 a greenhouse is depicted which shows the typical framework structure which has been used for the structural system of the SC. Details of measures and construction are dealt with in [S.8] as German and European standard.

Outer dimensions of typical greenhouses may vary but can be in the range of a few hundreds meters in length and width direction. For a SC the outer measures will exceed to 1 to 2 km. Research on greenhouses, their structural and functional characteristics and the design requirements can be found by [A.40], [A.41]. More figures and details on the SC for the SCPP at Wuhai Desert as one of the biggest prototypes in recent years can be found here [A.171]. The SC of the prototype at Manzanares is shown as a reference.

2.1.1 Structural System

The structural system of the SC can be described as a 3-dimensional frame structure. Due to cost and weight efficiency it is build lightweight. The radially around the SCH oriented pillars will be made of a lightweight material, too. Grid measures depend on the material properties and the

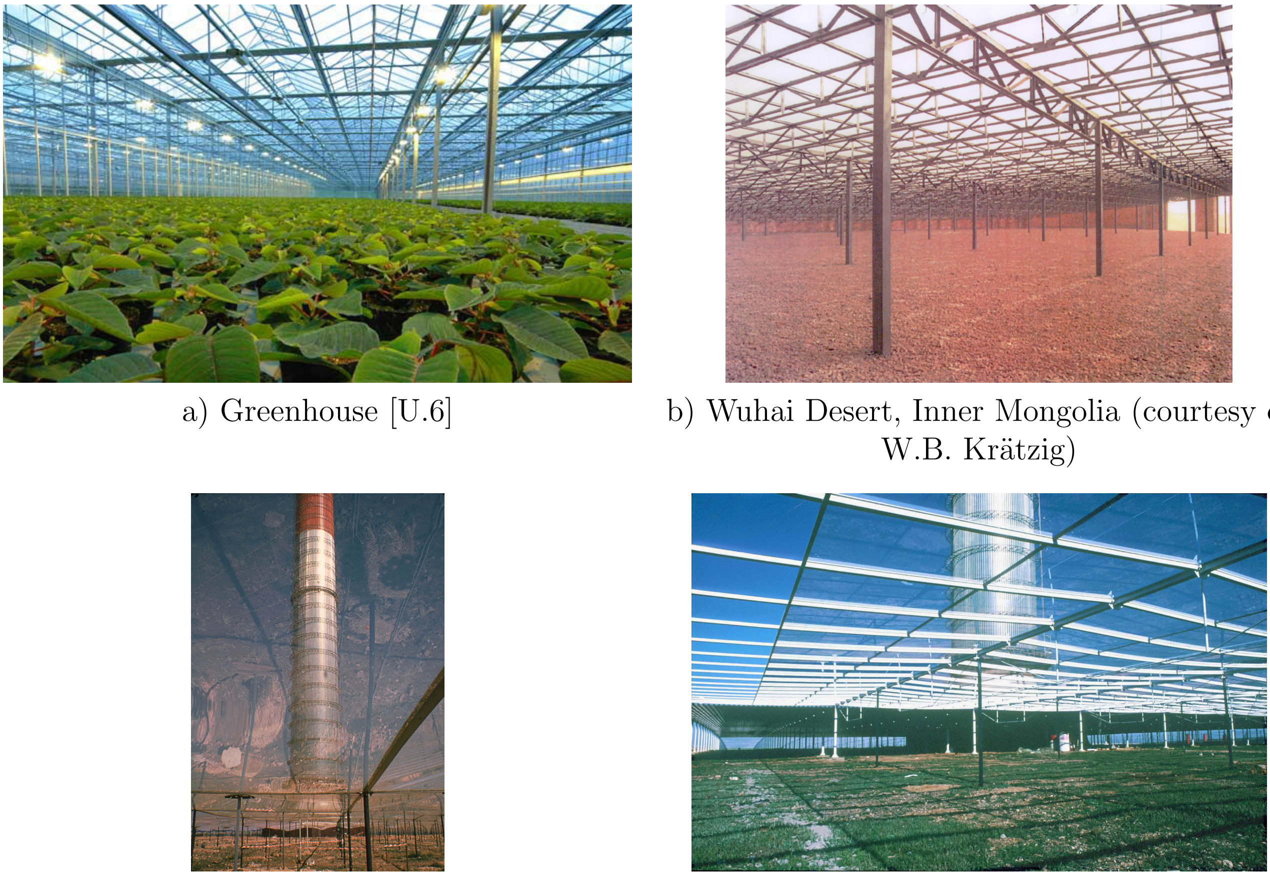

a) Greenhouse [U.6]

b) Wuhai Desert, Inner Mongolia (courtesy of W.B. Krätzig)

c) Manzanares - View Through the Polyester Collector Roof [U.11]

d) Manzanares - View Through the Glass Collector Roof [U.2]

Figure 2.1: Greenhouse Structure

static design. It is important to notice that a design with more pillars can perform better under structural aspects but will perform worse for the fluid dynamic process underneath the SC due to blockage of the flow.

On top of the framework structure, panels in quadratic shape made of glass or from a synthetic material, e.g. perspex, are fixed to the structure. Different concepts for the arrangement of the panels are conceivable, two of them are depicted in figure 2.2.

Joints between each panel and especially close to the SCH and the transition section should be flexible due to static and dynamic reasons. Due to joints it will be possible to remove particles, especially water or dust, through the SC to the ground which is of major importance due to the huge outer dimensions. Research was done by [A.107] and [A.80] who also investigated the impact of cleaning robotics on the SC structure. Also access roads on top of the SC should be taken into account before planning the SCPP.

For the outer shape many authors favoured a circular SC with double curved glass panels. This will be necessary if a SC with constant inclination angle is favoured, which is neither cost nor construction efficient. Therefore concepts with different SC shapes, cf. the prototype from [A.143] which is polygonal shaped, were investigated. Additionally, there is no proof that the SC needs to be circular at all. Also the perfect design depends on natural circumstances like ground

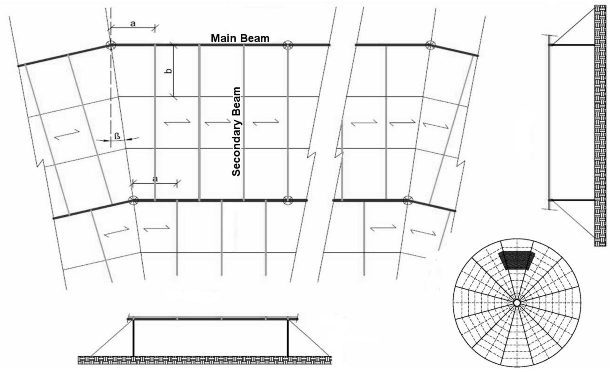

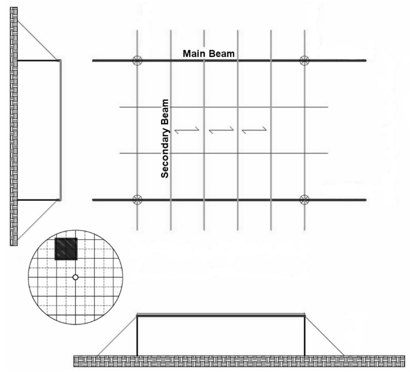

a) Circular Arrangement b) Rectangular Arrangement

Figure 2.2: Arrangement of the Glass Panels [A.107]

material and flatness of the terrain which can be influenced up to a certain point only.

2.1.2 Guide Vanes or Closing Walls at Outer Rim of the Solar Collector

Different applications of the SC, in particular the area close to the outer rim, for growing or drying food may make it necessary to use closing walls or guide vanes as flow protection. The wall at the outer rim could be build as a fence with a defined porosity, as a solid wall or as banked up earth respectively. Dimensions and distances to the SC have not been investigated yet. An investigation of the influence of closing walls on the flow stream underneath the SC and the performance of the whole power plant will be part of the experimental set-up of an improved SCPP model described in part III, section 11.3 of this work.

2.2 Ground - Properties and (Pre-)Treatment

The ground underneath the SC serves as a heat storage. Depending on the material properties the amount of stored heat varies in a wide range leading to different diurnal cycles of power production. Focus lies on the usability of the SCPP during night hours to be competitive with conventional energy sources. Therefore special treatment of the natural ground can become necessary.

Figure 2.3 shows different treatments of the natural vegetation underneath the SC and untreated conditions respectively.

Depending on the diurnal cycle of energy consumption and due to the natural vegetation that will grow unhindered underneath the SC, different treatments of the ground need to be taken into account. The aim is to decrease the natural albedo and increase the heat storage capacity. More on this can be found in chapter 4 and 6.

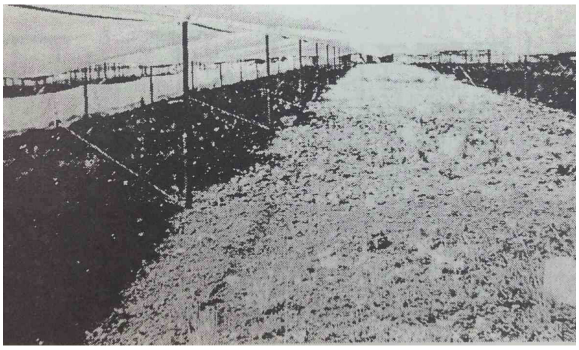

a) Test Stripe with Untreated Soil and Yellowing Grasses; on the Left and Right with Tarmac Treated Soil

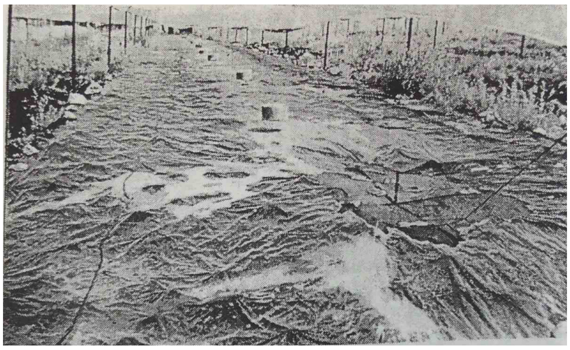

b) Low-Cost PE-Foil with Sand Depositions on Top

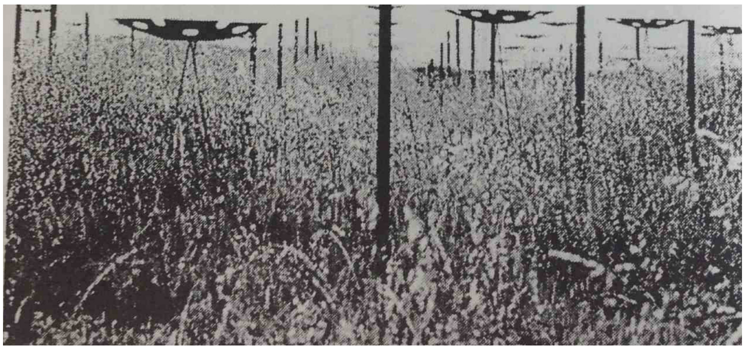

c) Plant Growth Till Height of Solar Collector

Figure 2.3: Ground Characteristics and Preparation [A.157]

2.3 Turbines and Housing

Special attention has to be paid to the turbines and housing of the turbines. The housing will be part of this work because it affects the flow situation behind the turbines and inside the transition section to a great extent. Their influence on the fluid mechanic, thermodynamic and on the structure itself will be discussed in the corresponding chapter. Figure 2.4 depicts some pictures and computational drawings of the turbine housing, a test rig for turbine testing and the completed turbines for two prototypes of a SCPP.

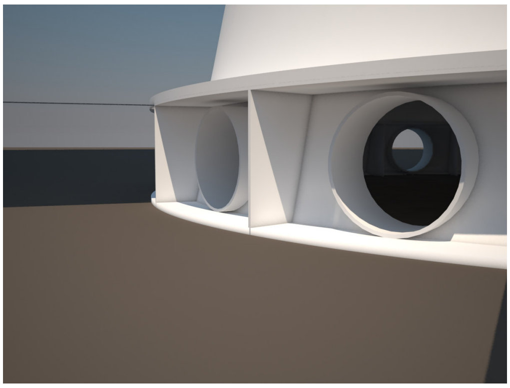

a) Turbine Housing (courtesy of KUP)

b) Multiple Turbine Rig

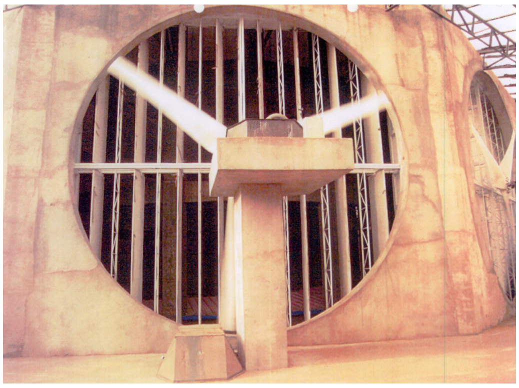

c) Turbine, Solar Chimney in Wuhan (courtesy of KUP)

d) Transition Section with Turbine Under Constrution, Manzanares

Figure 2.4: Turbine Rig and Housing [T.8], [U.11]

2.4 Transition Section

For the efficiency of a SCPP the transition section is of major importance. The flow needs to be redirected from a nearly horizontal level underneath the SC to a vertical direction inside the SCH. Therefore research has been performed on how to manage this redirection with minimal flow losses. The structural aspect and the cost of material have led to simple solutions. Figure 2.5 shows the upper part of the cone installation with the mounted turbine chosen at the Manzanares prototype which has been favoured by many researchers afterwards. Details and measures of the installation can be found by [A.157].

For the assumption of symmetric flow conditions this design solution fits perfectly. Throughout this work it will be shown that this assumption is not correct even for normal ambient conditions. Therefore new concepts need to be developed which combine the aspects of structural simplicity, aerodynamic behaviour and cost efficiency. In chapter 11 new designs for the installation will be tested at a wind tunnel model and in chapter 12 in a numerical simulation, respectively.

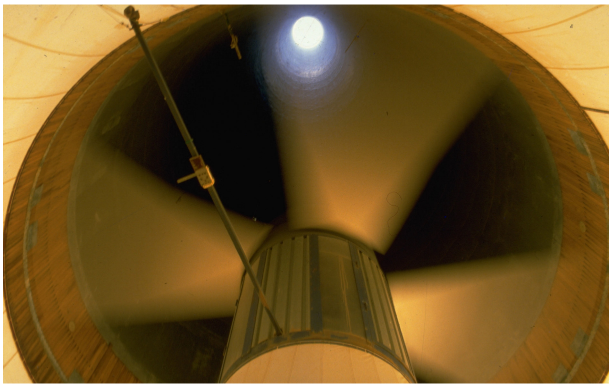

Figure 2.5: Transition Section at Manzanares [U.8]

2.5 Solar Chimney

The wide range of variants of a SCH with heights of up to 1,000 m and their structural design can be found in [A.72]. In early research papers heights of up to 1,500 m can be found which have been discarded in later research. A SCH of a medium height of 750 m seems at this point to be the most probable solution. Therefore figure 2.6 presents a design concept for a 750 m SCH.

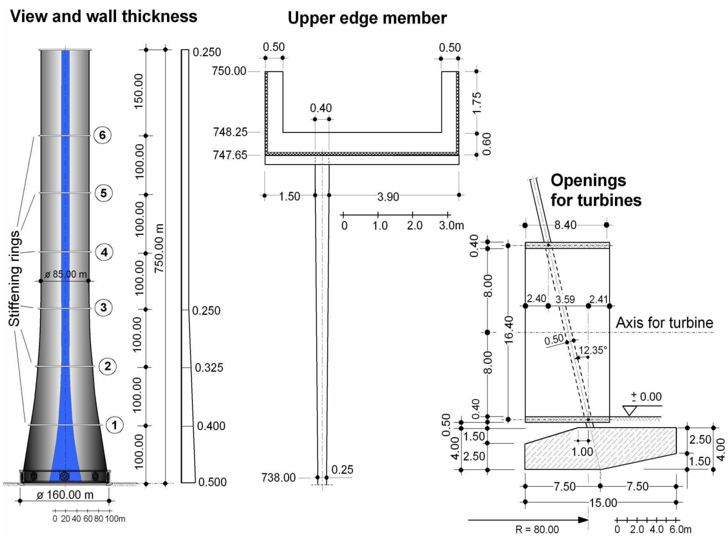

Figure 2.6: State of the Art Solar Chimney Design (750 m) [A.72]

The shown design corresponds to the computational drawing of the transition section already given in figure 2.4a). The SCH will be made of Reinforced Concrete (RC) in general C 50/60 with high compressive strength. Wall thickness varies from 1.0 m at the SCH base to 0.25 m at the top. Openings for turbines need to be designed in that way that they do not weaken the whole SCH structure. Therefore an increase of wall thickness in that region can be necessary. Stiffening rings and the upper edge member will also be made of RC.

2.5.1 Structural System

The structural system of a SCH is well known from CTs and Industrial Chimneys (ICHs). The measures of height and diameter and for the profile of wall thickness and general shape, either constant, converging or diverging, may vary from author to author. Also different concepts for the tower base and the turbine area can be found. They follow two major concepts, a shell or a column concept. Both got their assets and drawbacks. One indicator for a good concept is the eigenfrequency analysis following equation (2.1).

$$f = \frac{1}{T} = \frac{\omega}{2\pi} = k_f \frac{l}{r} \sqrt{\frac{E}{\rho_{spez}}} = k_f \frac{l}{r} c \tag{2.1}$$

where

T = Period of oscillating in s
f = Eigenfrequency in Hz
ω = Eigen angular frequency in Hz
k_f = Geometric frequency factor
l = Length in m
r = Radius in m
ρ_{spez} = Specific density in kg/m^3
E = Modulus of elasticity in MN/m^2
c = Velocity of sound in m/s

The analysis of different designs can be found by [T.10], [T.7] and [B.34].

2.5.2 Column or Shell Concept

In former research a SCPP was from the structural point of view very close to CTs with a column concept for the base of the SCH. Figure 2.7 shows the column area of one of the highest CTs in the world, the Niederaußem Power Plant in Germany during construction.

Figure 2.7: Column Area of the Cooling Tower Niederaußem, Germany During Construction (courtesy of KUP)

A special execution of the columns are the IGVs. Due to their dual function for SCPPs and especially for the SCH they have been designed in many different ways. With a single vertical axis turbine like the prototype of Manzanares this is a good design concept for the SCH base. Therefore figure 2.8 shows the IGV set-up and arrangement. The dual function can be seen very clearly.

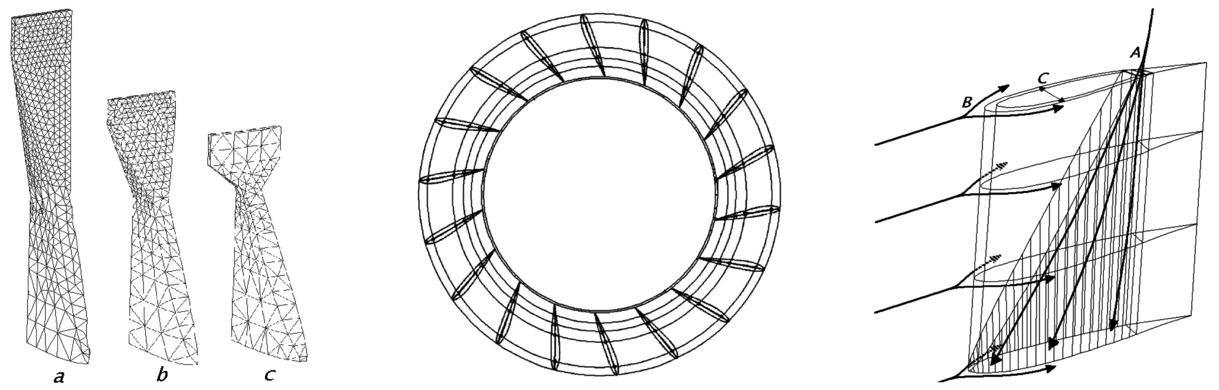

Figure 2.8: Inlet Guide Vane Set-Up, Arrangement and Dual Function [T.6] (a): 60 m, b): 30 m, c): 10 m) (left), (A: Structural Function, B: Aerodynamic Function, C: Maximum Section Width) (right)

The static design of the SCH above the column area can make it necessary to change the shape and outer measures of the IGVs respectively. An arrangement of the IGVs with a shift angle towards the center of the SCH result in a pre-swirl of the flow which leads to better efficiencies of the single turbine.

Current concepts favour a shell concept with turbines arranged in the circumference of the SCH base, which has been adopted for this work.

Therefore IGVs became in most cases redundant or they have been integrated in the shell concept. For more information about the pros and cons of IGVs compared to a shell concept without or included IGVs for the static design compare chapter 10. For the eigenfrequencies, the shell concept shows the best performance.

2.5.3 Spoke Wheels or Ring Stiffeners

In former research spoke wheels, cf. [A.12] and [A.173], have been used as stiffening devices of the SCH shell. Pre-stressed and made of steel ropes they have been positioned at different heights of the SCH. This concept is well known from spoke wheels and is a good choice to increase the stiffness of a tube like the SCH. Due to the huge heights and the blockage of the flow inside the SCH spoke wheels cause both structural and aerodynamic problems. Therefore for SCPPs this concept has been discarded and ring stiffeners have been favoured for all recent research. Made of RC they can be attached to the outer shell of a SCPP during construction directly. Under structural aspects they are a simple and efficient solution to change the dynamic behaviour of the SCH from a shell to a beam behaviour resulting in higher eigenfrequencies. The variation of outer measures and positions of the ring stiffeners over height has been part of many former research and will not be part of this study.

Chapter3

Basics of Fluid Mechanics

In this chapter the basics of Fluid Mechanics regarding a SCPP are summarized. A detailed explanation of the flow situation for the SC, the turbines, the transition section and the SCH will be given. Additional information about free jet flows will help the reader to understand the flow situation inside the transition section and shall give some forward look to the intentions of the experimental and numerical simulations presented in part II. Two approaches for a simple illustration of the process structure and the effect on the fluid flow by the turbines, namely the Actuator Disc Method (ADM) and Pressure Jump Method (PJM), are included. Both approaches are often used in CFD analysis to simulate the influence of a turbine or fan on the flow field. A brief discussion of the flow losses for all relevant parts complete this chapter.

3.1 Solar Collector Flow

The flow underneath the SC corresponds to a *Poiseuille flow* which is defined as a pressure induced flow usually in a circular pipe. Analogously it can be defined as a flow between two parallel plates with non-moving boundaries in contrast to drag induced flow generally known as *Couette flow*, cf. figure 3.1.

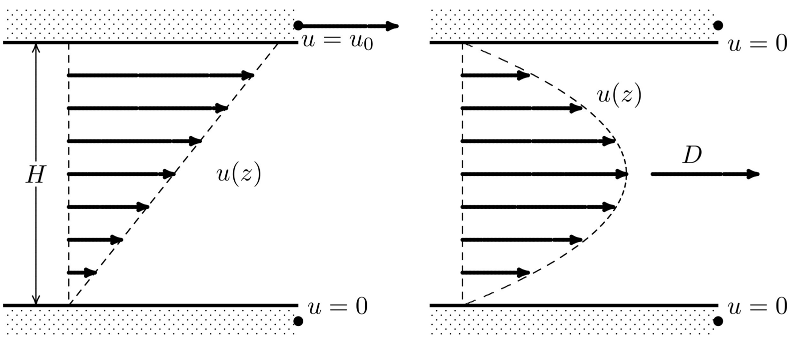

Figure 3.1: Couette Flow (left) and Poiseuille Flow (right) [B.12]

Following prerequisites have to be met:

(a) Stationary $\partial v/\partial t = 0$;

(b) Horizontal homogeneity $\partial v/\partial x$, $\partial v/\partial y = 0$;

(c) $w = 0$ given by continuity equation $\nabla \times v = 0$ from (b);

(d) $(1/\rho)\partial p/\partial x = \text{constant} = D$.

where

w = Vertical component of velocity in m/s

From Navier-Stokes equation (3.1)

$$\frac{\delta u_i}{\delta t} + u_k \frac{\delta u_i}{\delta x_k} = -\epsilon_{ijk} f_i u_k - \frac{\delta \Phi}{\delta x_i} - \frac{1}{\rho}\frac{\delta p}{\delta x_i} + \frac{\mu}{\rho}\left\{\frac{\delta^2 u_i}{\delta x_k^2} + \frac{1}{3}\frac{\delta}{\delta x_i}\left(\frac{\delta u_k}{\delta x_k}\right)\right\} \tag{3.1}$$

we get the following equation

$$D = \frac{1}{\rho}\frac{\delta p}{\delta x} = \nu \frac{\delta^2 u}{\delta z^2} \tag{3.2}$$

and with the boundary conditions from (3.3)

$$u(0) = u(H) = 0 \tag{3.3}$$

we get the *Poiseuille flow* equation (3.4)

$$u(z) = \frac{D}{2\nu} z(H - z) \tag{3.4}$$

A transformation of (3.4) in cylinder coordinates gives us the flow equation of straight ducts with a circular cross section known as the *Hagen-Poiseuille-Flow* or just *Tube Flow* equation.

It has to be mentioned that the assumption of parallel plates can be hold only approximately because the height of the SC will increase (pos. slope) or decrease (neg. slope) towards the centre. The inclination angle will be of a small value which allows us to use the Poiseuille flow equation.

The flow field underneath the SC is locally influenced by the ambient velocity profile. This depends on the wind velocity, the turbulence ratio and the ground roughness. Due to small entrance heights of approx. 2 m, the shape of the wind profile has only a small impact on the flow field. At the entrance the oncoming wind splits up in a part above and below the SC. The flow field on top of the SC plays a minor role for the flow field on the inside of a SCPP. A direct interaction can only take place in the case of (a) construction phase, (b) during maintenance or (c) a damage of the structural parts. Indirect interaction due to heat transfer between the ambient flow and the flow underneath the SC will have a decisive impact on the power production of the SCPP. More about the thermodynamics can be found in chapter 4.

For the flow field underneath the SC influence factors are the roughness of the supporting structure of the SC and the roughness of ground including preparations for a more efficient storage of heat during the day like water bags or equivalent components.

For the case of a fully developed flow assumption in the collector the roof shear stress is given by [A.149] shown in the following equation (3.5)

$$\tau_r = 0.02[(\rho^{0.8} v^{1.8} \mu^{0.2})/(H^{0.2})] \tag{3.5}$$

while the ground shear stress shown in (3.6) is

$$\tau_g = 0.014875 \rho v^2 (\epsilon_g/2H)^{0.254} [1.75(\mu/\rho v \epsilon_g)^{0.51} + 1] \tag{3.6}$$

The friction factor for smooth surfaces reveals to equation (3.7)

$$f = (1.82 \log 10Re - 1.64)^{-2} \tag{3.7}$$

and for rough surfaces to (3.8)

$$f = 0.3086[\log 10(6.9/Re + (\epsilon/(3.75d_h))^{1.11})]^{-2} \tag{3.8}$$

when $\epsilon/d_h > 10^{-4}$ and to (3.9)

$$f = 2.7778\log 10[(7.7/Re)^3 + (\epsilon/(3.75d_h))^{3.33}]^{-2} \tag{3.9}$$

for cases where $\epsilon/d_h \leq 10^{-4}$.

Research done by [A.147] and [A.145] shows that the flow is essentially fully developed shortly after the inlet to the collector. "The length of the initial stretch, i.e., the distance from the inlet section to the section in which the velocity differs from the velocity of the stabilized stream by only 1%, of a circular or rectangular pipe with a side ratio of between 0.7 and 1.5, can be determined in the case of laminar flow by *Shiller's formula*" [B.22], cf. equation (3.10)

$$\frac{L_{in}}{D_h} = 0.029Re \tag{3.10}$$

where

$$\begin{aligned} L_{in} &= \text{Length of the initial stretch in m} \\ D_h &= \text{Hydraulic diameter of the pipe in m} \end{aligned}$$

For turbulent flow inside an annular pipe with smooth walls the length of the initial stretch can be determined by the *Solodkin-Ginevskii* formula shown in equation (3.11)

$$\frac{L_{in}}{D_h} = b' lgRe + (a' - 4.3b') \tag{3.11}$$

where

$$\begin{aligned} a' &= f_1\left(\frac{D_{in}}{D_{out}}\right) \\ b' &= f_2\left(\frac{D_{in}}{D_{out}}\right) \\ D_{in} &= \text{Diameter of the inner pipe in m} \\ D_{out} &= \text{Diameter of the outer pipe in m} \end{aligned}$$

"The thickness of the boundary layer at a given distance from the initial section of a straight conduit can increase or decrease, depending upon whether the medium moves in a decelerating motion or an accelerating motion. A too sudden expansion can lead to the phenomenon of flow separation from the wall, accompanied by the formation of eddies" [B.22]. This phenomenon will be discussed in more detail in section 3.3.

3.1.1 Influence of Turbulence on Solar Collector Flow Field

The influence of turbulence on the flow field and its characteristics can be visualized best with a comparison between the velocity distributions inside a tube for laminar and turbulent flows which is depicted in figure 3.2.

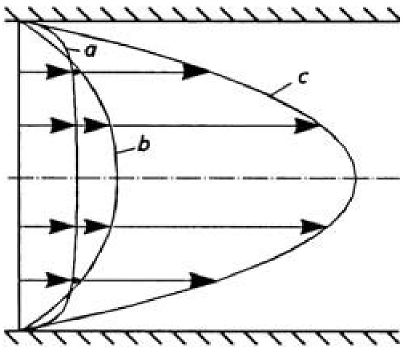

Figure 3.2: Velocity Distribution Inside a Tube [B.40] (a): turbulent, b): laminar, same volume flow rate like a), c): laminar, same pressure gradient like a))

For the laminar case the stabilized velocity profile is parabolic, for the turbulent case roughly logarithmic or exponential.

A good measure of turbulence is the Turbulence Kinetic Energy (TKE) or the *flux Richardson number* given in equation (3.12), which is a dimensionless quantity that defines the ratio of the buoyancy of the TKE equation and the negative of the shear term also from the TKE equation.

$$Ri_f = \frac{\frac{g}{\theta}\overline{w'\theta'}}{-\overline{w'u'}\frac{\delta\overline{u}}{\delta z}} \tag{3.12}$$

where

$\frac{g}{\theta}\overline{w'\theta'}$ = Buoyancy force

$\overline{w'u'}\frac{\delta\overline{u}}{\delta z}$ = Shear term

Equation (3.13) gives the turbulence energy

$$\underbrace{\frac{\delta\overline{e}}{\delta t}}_{\text{Local derivative}} + \underbrace{\frac{\delta}{\delta x_k}\left\{\overline{u}_k\overline{e} + \overline{u'_k e} - \nu\frac{\delta\overline{e}}{\delta x_k} + \frac{1}{\tilde{\rho}}\overline{u'_k p'}\right\}}_{\text{Divergence of energy fluxes}} = \underbrace{-\overline{u'_k u'_i}\frac{\delta\overline{u}_i}{\delta x_k} + \frac{g}{\tilde{\theta}}\overline{u'_3\theta'} - \nu\overline{\left(\frac{\delta u'_i}{\delta x_k}\right)^2}}_{\text{Production and dissipation of turbulence energy}} \tag{3.13}$$

where

$\frac{\delta\overline{e}}{\delta t}$ = Local derivative

$\overline{u}_k\overline{e}$ = Advection

$\overline{u'_k e}$ = Turbulent transport

$\nu\frac{\delta\overline{e}}{\delta x_k}$ = Molecular viscous transport

$$\frac{1}{\widetilde{\rho}}\overline{u_k' p'} = \text{Pressure diffusion}$$
$$\overline{u_k' u_i'}\frac{\delta \overline{u}_i}{\delta x_k} = \text{Production}$$
$$\frac{g}{\widetilde{\theta}}\overline{u_3' \theta'} = \text{Buoyancy flux}$$
$$\nu\overline{\left(\frac{\delta u_i'}{\delta x_k}\right)^2} = \text{Dissipation}$$

Equation 3.13 has been developed from equation 3.14 for the kinetic energy of the mean flow field

$$\frac{\delta}{\delta t}\frac{\overline{u}_i^2}{2} + \frac{\delta}{\delta x_k}\left\{\overline{u}_k \frac{\overline{u}_i^2}{2}\right\} + \frac{\delta}{\delta x_k}\left\{\overline{u}_i \overline{u_k' u_i'}\right\} = \frac{g}{\widetilde{\theta}}\overline{u}_i \overline{\theta}\delta_{i3} - \frac{1}{\widetilde{\rho}}\frac{\delta \overline{u}_i \overline{p}}{\delta x_i} + \nu \frac{\delta^2}{\delta x_k^2}\frac{\overline{u}_i^2}{2} - \nu\left(\frac{\delta \overline{u}_i}{\delta x_k}\right)^2 + \overline{u_k' u_i'}\frac{\delta \overline{u}_i}{\delta x_k} \quad (3.14)$$

that has been derived from the averaged Navier-Stokes equation [B.12]. For the application the determination of the flux terms can be difficult. Therefore a more user friendly approach will be used normally. Knowing the mean gradients of temperature and velocity of a turbulent flow, the *Richardson number* Ri will be used instead of the *flux Richardson number* Ri_f.

The impact of the supporting structure of the SC on the turbulence will not be discussed during that study and can only be estimated. Due to the huge scale and great amount of needed girders, pillars, etc. it will definitely influence the flow field underneath the SC.

3.1.2 Flow Field on Top of the Solar Collector Roof

The flow field on top of a SC corresponds to a flow, laminar or turbulent, at a flat plate. Starting at the front edge a laminar boundary layer develops. From a certain related length x_l, more specific, at $\mathrm{Re} = u_m x_l/\nu > 6 \times 10^4$ the boundary layer gets unstable. For Re lower than this point of indifference the flow is always laminar in contrast to higher Re where small disturbances of the flow field will change the flow from laminar to turbulent. Very high and low wave length disturbances will still be damped. Therefore the flow field contains laminar and turbulent parts. If Re reaches a critical value shown in equation (3.15)

$$Re_{cr} = u_m x_{cr}/\nu = 3 \times 10^5 \ \ to \ \ 5 \times 10^5 \quad (3.15)$$

the flow will become completely turbulent. The change of flow state depends to a great extent on the roughness of the plate and the starting conditions of the flow which trigger the critical Reynolds Number. Figure 3.3 shows the development of a flat plate boundary layer.

Heat and mass fluxes in turbulent flows are more intense than for laminar flows which will be important for the thermodynamic and fluid mechanic processes at the SC.

The *Nusselt number* Nu, explained in [A.18], can also be used as an indicator of laminar or turbulent flow.

Derived from measurements for the laminar flat plate flow following equations can be formed for the boundary layer height (3.16), the friction coefficient (3.17) and the drag coefficient (3.18)

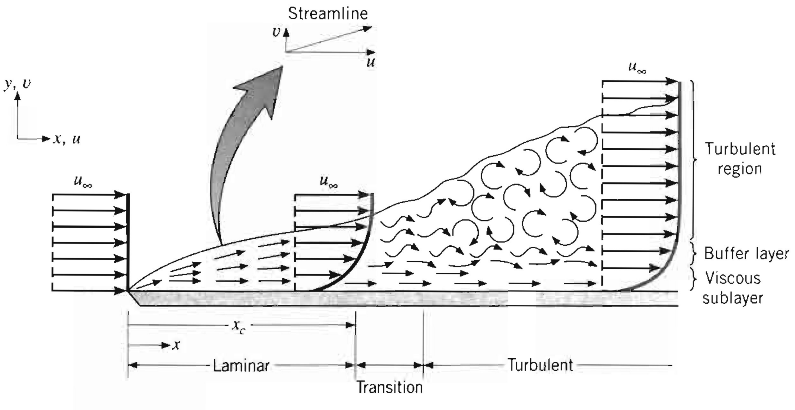

Figure 3.3: Velocity Boundary Layer Development on a Flat Plate [B.23]

[B.46].

$$\delta/x = 5.0/Re_x^{1/2} \tag{3.16}$$

$$c_f = 0.664/Re_x^{1/2} \tag{3.17}$$

$$C_D = 1.328/Re_L^{1/2} \tag{3.18}$$

For the turbulent flat plate flow equations (3.19), (3.20) and (3.21) can be used respectively.

$$\delta/x = 0.16/Re_x^{1/7} \tag{3.19}$$

$$c_f = 0.027/Re_x^{1/7} \tag{3.20}$$

$$C_D = 0.031/Re_L^{1/7} \tag{3.21}$$

Deposits of light elements, which can form ripples, cf. [A.80], especially in dry areas which cause shadowing effects, should be taken into account. The mechanism of sand and dust accumulation and removal on the SC can be seen in figure 3.4.

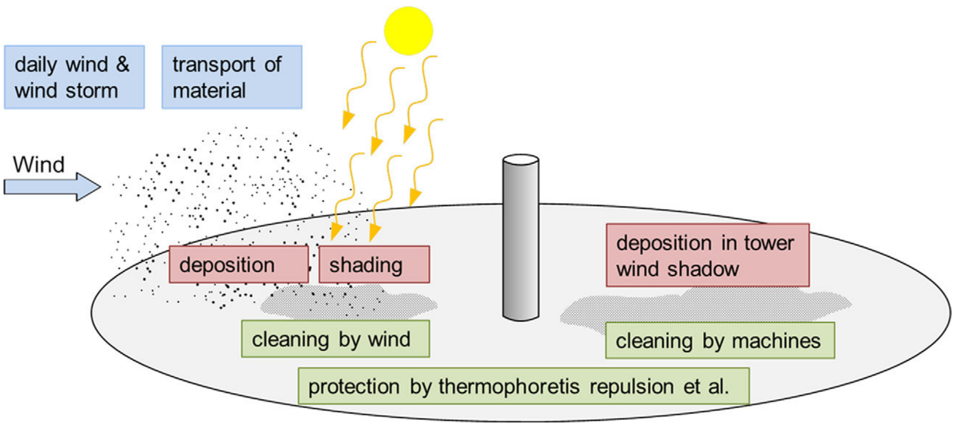

Figure 3.4: Mechanisms of Sand/Dust Accumulation/Removal on the Solar Collector [A.73]

For this work no shadowing or abrasion effects of the SC roof due to sand or dust have been taken into account. The material properties of all components presented within this study do not change over time.

3.1.3 Wind Fence at the Outer Rim of the Solar Collector

The effect of obstacles like solid or porous structures at the entrance of the SC will be discussed here briefly.

For the prototype at Manzanares the effect of wind fences at the entrance has been investigated and is depicted in figure 3.5.

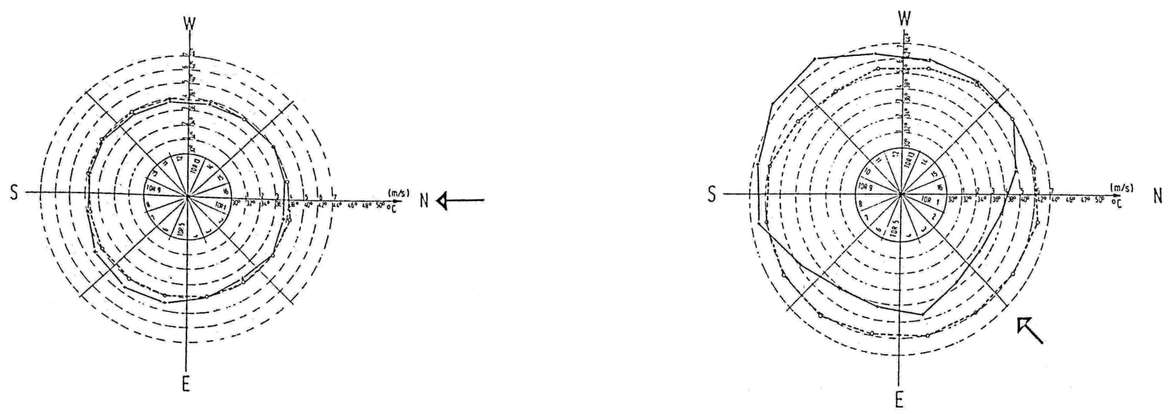

a) $v_a = 1.8\ m/s$ Wind Velocity b) $v_a = 8.0\ m/s$ Wind Velocity

Figure 3.5: Asymmetric Inflow Conditions (Velocity and Temperature) at the Inlets of the Solar Collector (Solid - Temperature, Dashed - Wind Velocity) [A.157]

Additional IGVs divide the circular shaped SC into eight parts. Between these IGVs a wind fence of 90 % porosity has been installed. The entrance height has been designed variable varying in the range of 20 cm $\div$ 30 cm. The velocity at this flow restriction lies in the range of $v_{wf} = 0.54$ to $0.43 \times v_a$. It can be found, that the velocity and temperature distribution is nearly symmetric for the case of the small ambient wind velocity. For the case of the higher wind velocity the temperature distribution shows a deviation to the lee side of the wind direction. This can be explained due to longer dwell time of the air packages at the lee side underneath the SC.

3.1.4 Flow Losses

"The fluid losses in the course of the motion of a fluid are due to the irreversible transformation of mechanical energy into heat. This energy transformation is due to the molecular and turbulent viscosity of the moving medium. There exist two different types of fluid losses:

- Frictional losses ΔH_{fr}
- Local losses due to separation, alteration of the configuration or at obstacles ΔH_l

The principle of superposition of losses is used not only with respect to a separate element of the conduit, but also in the hydraulic calculation of the entire system. This means that the losses found for separate elements of the system are summed arithmetically which gives the total resistance of the entire system ΔH_{sys}" [B.22].

In general, flow losses at the wind fence, the supporting structure and at additional installations on the ground can be found and are partly given in [A.157].

3.2 Turbine Properties

For the turbine(s) of a SCPP a few questions need to be clarified before starting the design process:

- Type of turbine - axial or radial
- Quantity of turbines
- Variable or constant speed turbine
- Degree of reaction
- Layout in terms of number of rotor and stator blade rows
- Main dimensions in terms of hub-to-tip ratio, number of blades, blade aspect ratio
- Range of blade adjustability

Due to the wide range of different designs the real flow field can change to a great extent. General properties of fluid mechanic and thermodynamic process are explained in the following subsections.

3.2.1 Axial-Flow vs. Wind Turbine

For SCPPs classical wind turbines will not be the first choice although some executions, cf. figure 2.4c), do not show any difference. Having a closer look at the flow field around the classical wind turbine, depicted in figure 3.6, someone can see, that both the control volume and vortex system behind this type of turbine obviously will not fit to the one of a SCPP.

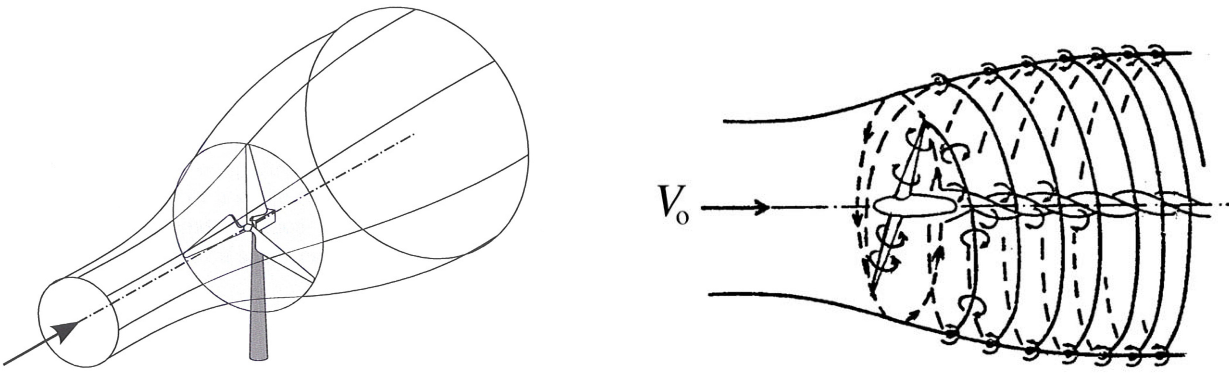

a) Control Volume [B.39]

b) Vortex System Behind a Wind Turbine [B.17]

Figure 3.6: Wind Turbine and Flow Field

The most important part missing is the housing around the turbine which will alter the flow field decisively and the usage of stator stages. Therefore axial flow turbines will be used for SCPPs.

Citing [A.13] there are three advantages of axial flow turbines used inside a SCPP over classical wind turbines:

+ They rotate faster than classical wind turbines developing the same power because they have a smaller diameter.
+ Noise is not a big problem because the turbine is enclosed and situated far from any impact area.
+ They do not have to be designed for extreme weather conditions in terms of wind strength, lightning and hail.
- Operate in extremely dry and hot conditions of up to 80 $°C$.

Before the flow enters the turbine stages it has to be directed via the IGVs into its direction. Taking into account fluid mechanic design criteria, unnecessary flow losses at the inlet can be avoided. Figure 3.7 shows some plans for possible inlet designs in shape of a bellmouth. This design will be pursued for the experimental and numerical simulations on the enhanced model of a SCPP which will be presented in chapter 11 and chapter 12, respectively.

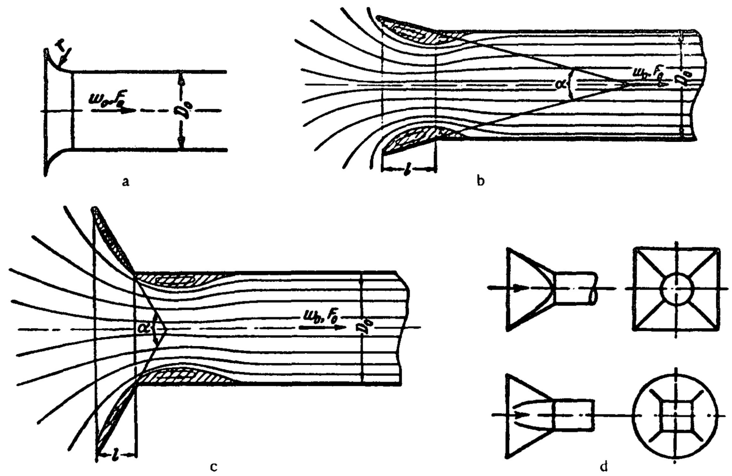

Figure 3.7: Plan of Smooth Inlet Stretches [B.22] (a) Bellmouth whose Section Forms Arc of a Circle, b) and c) Bellmouth Shaped Like Truncated Cones, d) Transition Pieces)

In a next step the flow at the turbine stage has to be investigated in detail. A detailed discussion of the characteristics of turbomachinery flow will go beyond the scope of this work and therefore only a brief discussion will be included in appendix G.

In general two-dimensional theory is used and for simplicity it is usually assumed, that the axial velocity remains constant. Figure 3.8 shows three turbine layouts with different installations.

Research done by [A.13] "implies that a fixed geometry turbine can be virtually perfectly matched to the plant by varying its speed appropriately during the day and during the seasons, with the lowest required turbine speed 38 % of the highest. The ratio of required lowest to highest speed is affected by the ratio of winter night time power to summer day time power, and that is primarily determined by the latitude of the plant location. (...) (Compared with this,) constant speed turbines will however demand adjustable blade rows. There are two other reasons for having adjustable blade rows:

- To control the turbine when the electrical load on the generator is interrupted.
- To shut off the flow through a turbine passage" [A.13].

Also the effect of pre-swirl caused by the IGVs or a stator stage on the turbine performance

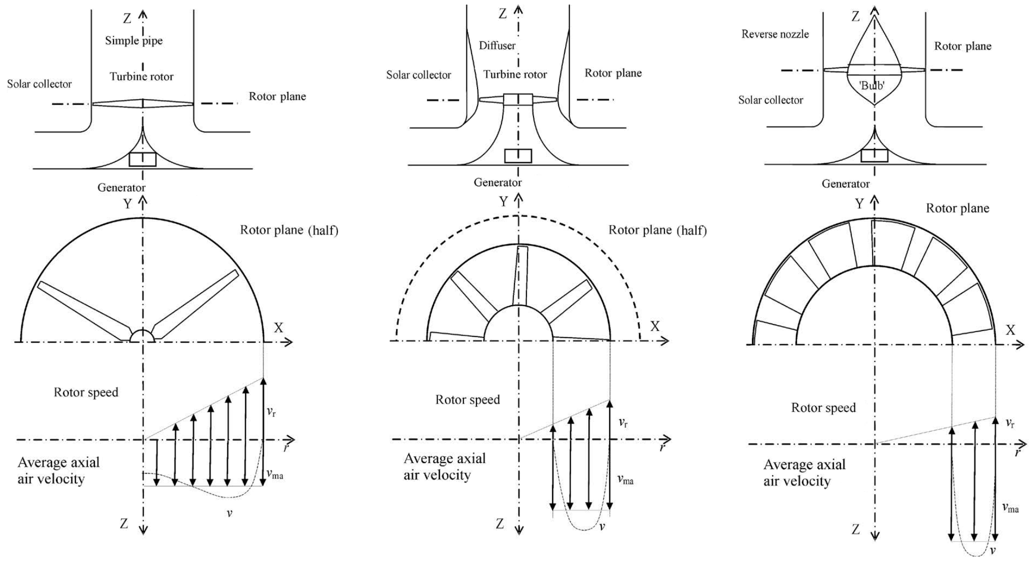

Figure 3.8: Basic Velocity Differences Between Simple Pipe Diffuser and Reverse Nozzle Type SC [A.100]

has been investigated by [A.10] and [T.1].

Last but not least the effect of an optimized outlet situation behind the turbine stage needs to be discussed. Therefore the installation of a diffuser with a divergence angle is depicted in figure 3.9.

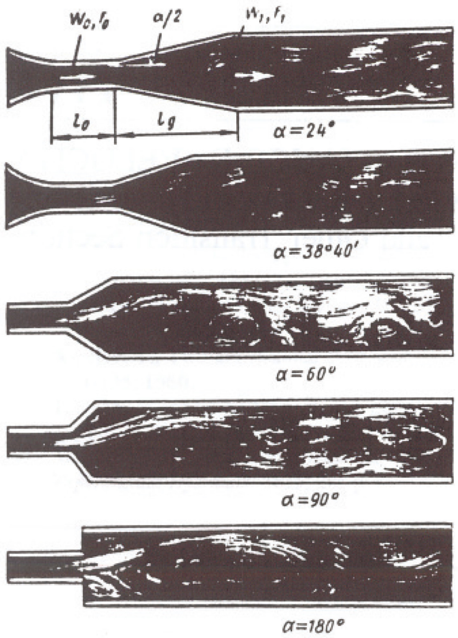

Figure 3.9: Flow Patterns in Diffusers with Different Divergence Angles [B.14]

"Axial turbines use radial-annular diffusers in which the increase of area is mainly due to the radial dimensions of the diffuser. The axial-radial diffuser is somewhat better from the aerodynamic point of view. Here, a radial bend follows a short annular diffuser. In this diffuser the radial turn is achieved at lower stream velocities, and the pressure losses are, accordingly, somewhat lower. At the same time the axial dimensions are much larger than those of a radial-annular diffuser" [B.22].

For distorted inflow conditions [T.22] has performed some numerical tests to check the performance of axial flow fans under this conditions.

3.2.2 Pressure Drop and Efficiency

The publication by [A.21] gives one of the fundamental research papers on wind energy and its usability. Although he focused on wind mills his statements for the maximum extractable energy have been used for axial flow turbines in many following research papers.

After his postulation the equation for the performance (3.22), finds its maximum in equation (3.23).

$$L = \frac{m}{2}(v_1^2 - v_2^2) \tag{3.22}$$

where

m $=$ Mass flow in kg/s
v_1 $=$ Entrance velocity in m/s
v_2 $=$ Exit velocity in m/s

$$L_{max} = \frac{16}{27}\frac{\rho}{2}v^3\frac{D^2\pi}{4} \tag{3.23}$$

where

D $=$ Diameter in m
v $=$ Wind Velocity in m/s

Due to losses by transforming from kinetic in mechanical energy and due to the fact that v_2/v_1 not always corresponds to the most favourable conditions, the effective power L_n is always smaller than L_{max}, cf. [A.21].

[A.9] developed a new equation (3.24) that gives the optimum ratio of turbine pressure drop to pressure potential.

$$(n - m)/(n + 1) \tag{3.24}$$

m $=$ Pressure potential exponent
n $=$ Pressure loss exponent

For $n = 2$ and a constant pressure potential, independent of flow rate ($m = 0$), the equation equals 2/3 and equation (3.23).

More on this can be found by [A.59], [A.10], [A.89], [A.152], [T.1], [A.62] and [A.86].

The efficiency of the Power Conversion Unit (PCU) components have been derived by [A.45]. For the inlet, mixing and horizontal-to-vertical components the efficiency can be calculated by using equation (3.25).

$$\eta_c = (\Delta p_{PCU} - \Delta p_c)/\Delta p_{PCU} \tag{3.25}$$

where

Δp_{PCU} = Pressure drop available across the whole PCU in Pa
Δp_c = Pressure drop over a specific component in Pa

For the axial turbines following assumptions have been used:

- The mass flow is equally shared by the various turbines
- Constant axial velocity through turbines
- Zero swirl at turbine inlet
- Free vortex design
- The *Soderberg loss model*, which is an analytical model commonly used in turbine design, is used to assess the aerodynamic losses in the turbine blade rows.

Table 3.1 lists the efficiencies of the various components of the PCU for peak power conditions for different diffuser area ratios.

Table 3.1: Plot of Efficiencies of the Various Components of the Power Conversion Unit (PCU) for Peak Power Conditions [A.45]

Component	**Variant** 1[1]	**Variant** 2[2]
-	%	%
Inlet	99.15	96.59
Mixing	98.58	96.64
Horizontal to Vertical	99.29	98.32
Turbine (tt)	90.07	89.79
Turbine (ts)	77.33	74.73
Drive Train	91.00	91.00
PCU (tt)	80.09	64.79

[1] Diffuser area ratio = $A_{turbine}/A_{chimney} = A_R = 1.0$.
[2] $A_R = 2.0$.

The drive train efficiency has been taken from former research to a constant value. From table 3.1 and figure 3.10 it can be seen that the efficiencies decrease with increasing diffuser area ratio.

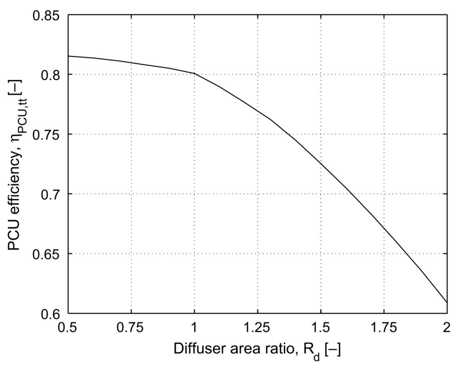

Figure 3.10: PCU Total-to-Total Efficiency vs. Diffuser Area Ratio for Multiple Horizontal Turbine Configuration [A.45]

Decreasing diffuser area ratio only leads to a slightly enhanced efficiency of a few percent.

3.2.3 Actuator Disc Method (ADM)

"The ADM represents the effect of an axial flow rotor by a step change in the tangential velocity through a parallel annulus, where the position of the step change coincides with the centre of the plane of rotation of the rotor. This particular method simulates the operation of an axial flow fan by calculating the effect of the individual fan blades on the flow through the machine, based on the lift and drag characteristics of the blade elements" [T.21]. The fan performance can only be predicted within the normal operating range of an axial flow fan which means that the flow over the fan blade needs to be predominantly in the axial and tangential directions.

"The Extended Actuator Disc Method (EADM) is therefore based on the model of Gur and Rosen (2005). It uses the same methods and equations used in the actuator disc method but compensates for the ADM's inability to simulate the operation of an axial flow fan accurately at low flow rates by extending the linear section of the airfoil lift coefficient vs. angle of attack curve" [T.21], also cf. [B.9].

3.2.4 Pressure Jump Method (PJM)

"The PJM utilises a static-to-static pressure increase that occurs at the location of the fan rotation plane. The value of the static pressure increase is based on the value of the volume flow rate passing through the fan rotation plane" [T.21].

Compared to the ADM only minimal amount of information is required for its implementation which is the main advantage of the PJM. Fan blade layout and profiles, which are required for the ADM, are often not available due to the reason of proprietary. Whereas the PJM is based on the fan static pressure vs. volume flow rate curve published by the fan manufacturer. Additional information about the test facility is required to compile the fan static pressure curve.

3.2.5 Flow Losses

The losses occurring in the PCU can be divided into three groups, namely a) aerodynamic, b) mechanical and c) electrical losses. Mechanical and electrical losses are summarized as drive train losses [A.45] and will not be discussed any further because this would exceed the course of this study. Whereas aerodynamic "(l)osses associated with the turbine blading are very important. An optimised turbine would have the minimum exit axial velocity component, but that could require an unrealistically large turbine, and there is little sense in having a combined turbine flow area that exceeds the chimney exit area. In order to minimise the amount of flow deflection required in the IGVs the turbine should run at the highest possible speed. For a given power demand, a higher turbine speed requires a smaller flow deflection reducing the losses, but a higher speed results in higher flow velocities relative to the rotor blades (increasing the losses) and also in more noise. Proper consideration of all these factors results in an optimised turbine" [A.13].

3.3 Transition Section

The transition section connects the SC and turbine area with the SCH and is therefore of major importance for the development of the flow field within the SCPP. The reader will see that there are many ways for design alternatives to the simplest case of a sharp bend redirecting the flow from nearly horizontal to vertical direction. Figure 3.11 shows an inlet stretch with various inlet shapes and the development of the *vena contracta* due to a change in the cross area.

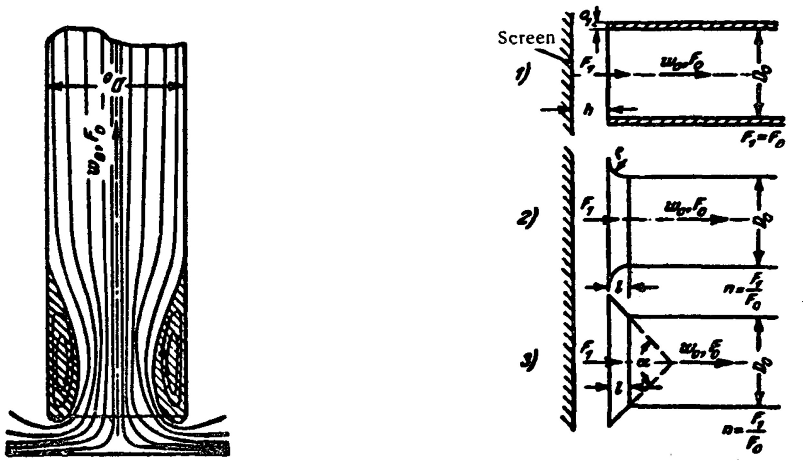

a) Vena Contracta b) Various Inlets with Screen

Figure 3.11: Vena Contracta and Various Inlets with Screen [B.22]

At the sharp corner the flow separation is clearly visible and leads to an area within the new cross section of recirculation. For the simple case of 2D symmetric flow the typical velocity field around the junction is depicted in figure 3.12.

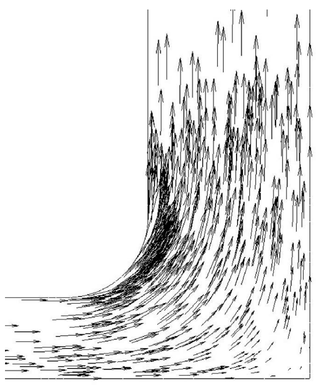

Figure 3.12: Typical Velocity Field Around the Junction of the Solar Collector and the Solar Chimney [A.102]

It is getting obvious that this solution does not show the optimal solution of diverting a flow. A better way for the design of the transition section is shown in figure 3.13 schematically.

The change of the profile of the SCH on the one hand and the integration of a cone in the middle of the transition section on the other hand will lead to an improved flow field where flow losses will be smaller than at the sharp bend solution. The numerical result of the velocity distribution

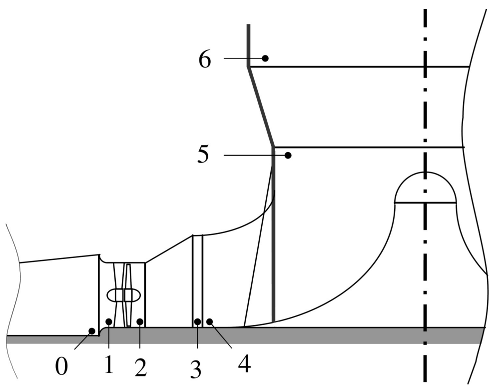

Figure 3.13: Schematic Drawing of the Solar Chimney Power Conversion Unit (PCU) Indicating the Various Stations in the Flow Passage [A.45] (0: Solar Collector Exit, 1: Turbine Inlet, 2: Turbine Exit, 3: Exit of Diffuser-Nozzle, 4: Exit of Mixing Section, 5: Exit of Vertical to Horizontal Transition Section, 6: Exit of Diffuser Section in the Solar Chimney)

inside the transition section is depicted in figure 3.14 for the symmetric flow case with smooth curvature.

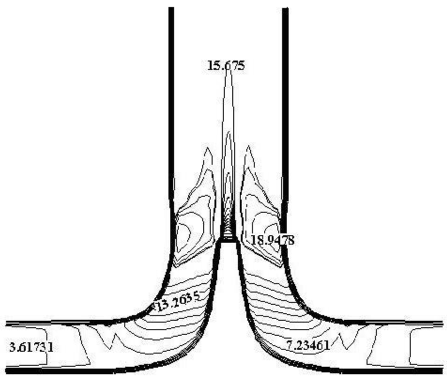

Figure 3.14: Velocity Distribution in m/s in the Solar Chimney and the Solar Collector [A.113]

The velocity contours show an increase in velocity due to the reduced width in the bend region. Results of isovelocity lines for different configurations of the SC and transition section are presented in [A.29] and [A.28]. It can be found that the velocity distribution changes to a great extent depending on both designs. For the flow field inside the SCH, at a certain distance to the transition section, the velocity distribution shows no difference for all investigated configurations.

More information on the transition section and its influence on the flow field can be found by [A.16], [A.99] and [A.98].

For the evaluation of different configurations for the transition section the flow losses, given by friction or resistance coefficient, need to be gathered and compared. This will be done by analysing the parts of the transition section like diffusers, curved segments which alter the stream direction and baffles. The most complete work on this can be found by [B.22] and [B.21] which will be used exclusively throughout this subsection if not stated otherwise.

3.3.1 Resistance Coefficient of Diffusers

"A diffuser is a gradually widening passage to make the transition from a narrow conduit to a wide one and the transformation of the kinetic energy of the stream into pressure energy, with minimum pressure losses. In such a divergent pipe the intensity of turbulence is greater than in a straight pipe, and the local friction resistances are also greater. The increase in the pipe section is accompanied by a drop in the mean stream velocity. Therefore, the total resistance coefficient of the diffuser, expressed in terms of the velocity in the initial section, is less for divergence angles below a certain value, than for the equivalent length of a constant-section pipe, whose area is equal to the initial section of the diffuser. An increase of the divergence angle beyond this limit leads to a considerable increase in the resistance coefficient, so that it finally becomes much larger than for the equivalent length of straight pipe. This angle can be calculated for the case of a straight diffuser of circular section by:

$$\alpha_{opt} = 0.43 \left(\frac{\lambda}{k_1} \times \frac{n_1 + 1}{n_2 - 1} \right)^{4/9} \tag{3.26}$$

where

λ = Friction coefficient of unit relative length of the stretch calculated
k_1 = Coefficient characterising the state of the boundary layer at the diffuser inlet
n_1 = Area ratio of the diffuser
n_2 = Area ratio of sudden enlargement of a multistage diffuser" [B.22].

For average values someone obtains $\alpha_{opt} \approx 6°$, for a diffuser of rectangular section, α_{opt} lies within the same range. For a plane diffuser this angle lies within the limits α_{opt} = 10 to 12°. Also see [B.21] for more variants of improving methods.

Figure 3.15 shows six different methods for improving the work of short diffusers.

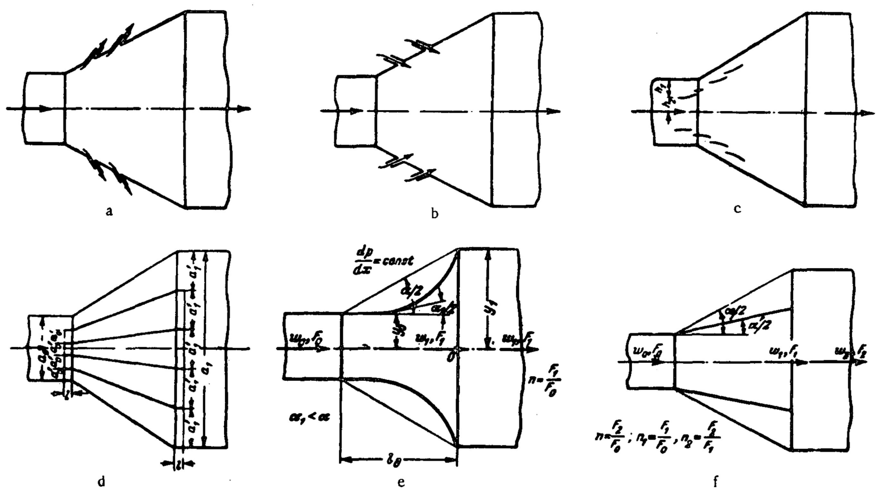

Figure 3.15: Different Methods for Improving the Work of Short Diffusers [B.22] (a): Suction of the Boundary Layer, b): Blowing Away of the Boundary Layer, c): Guide Vanes or Baffles, d): Dividing Walls, e): Curved Diffuser, f): Multistage (Stepped) Diffuser)

3.3.2 Resistance Coefficient of Curved Segments and Mixing of Flow Streams

The resistance coefficient of nonstandard converging wyes of normal shape as can be seen in figure 3.16 can be calculated using equation (3.27).

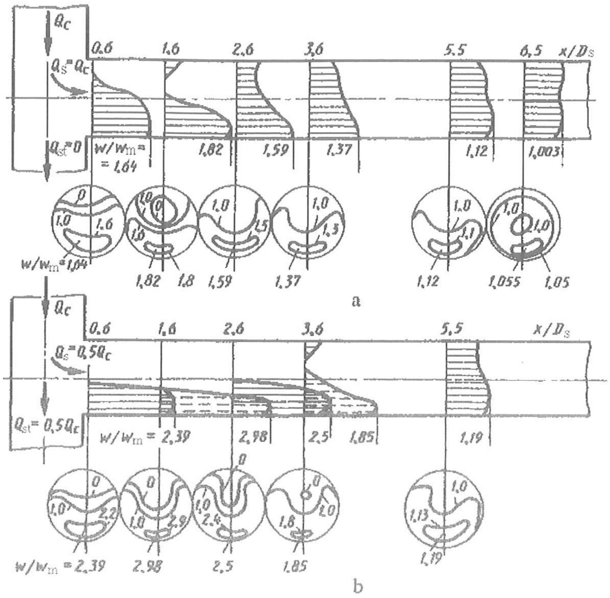

Figure 3.16: Profiles and Fields of Axial Velocity Components in a Side Branch of a Straight Equally Discharging Wye [B.21] (a): $Q_s = Q_c$; $Q_{st} = 0$, b): $Q_s = 0.5\ Q_c$; $Q_{st} = 0.5\ Q_c$)

$$\zeta_{c,s} = \frac{\delta p_s}{\rho w_c^2/2} = A\left[1 + \left(\frac{w_s}{w_c}\right)^2 - 2\frac{F_{st}}{F_c}\left(\frac{w_{st}}{w_c}\right)^2 - 2\frac{F_s}{F_c}\left(\frac{w_{st}}{w_c}\right)^2 \cos\alpha\right] + K_s \tag{3.27}$$

where

A, K_s, α = cf. [B.21], chapter 7
$w_{c;s;st}$ = Velocity in different sections in m/s
$F_{c;s;st}$ = Area of different sections in m

This case represents the flow situation inside the transition section of a SCPP where ambient wind causes an asymmetric flow field with flow through the turbines in both directions. For the case with nearly symmetric flow through all turbines equation (3.28) gives the resistance coefficient for the flow situation depicted in figure 3.17.

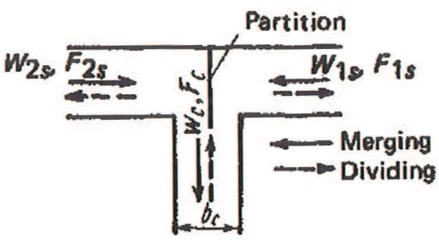

a) Symmetrical (Equilateral) Wye with a Sharp 90° Turn (Merging Without Partition)

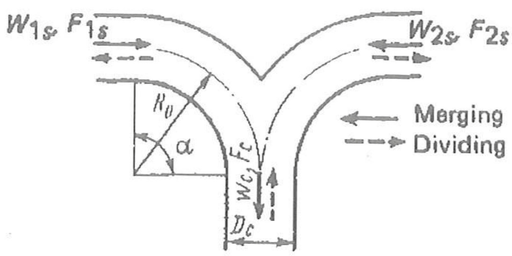

b) Symmetrical Wye with Smooth Turn Through 90°

Figure 3.17: Symmetrical Wye with Sharp and Smooth Turn [B.21]

$$\zeta_{1c,s} = \frac{\delta p_{1s}}{\rho w_c^2/2} = A\left\{1 + \left(\frac{F_c}{F_{1s}}\right)^2 + 3\left(\frac{F_c}{F_{1s}}\right)^2\left[\left(\frac{Q_{1s}}{Q_c}\right)^2 - \left(\frac{Q_{1s}}{Q_c}\right)\right]\right\} \tag{3.28}$$

where

$Q_{1s;c}$ = Flow rates for different branches in m^3/s

For the case of a smooth turn compare diagram 7.32 of [B.21]. Both figures include the merging of fluid streams, in this case of two. For the SCPP up to 16 streams need to be mixed partly behind the exits of the turbines and partly after the installation for the redirection where the flow enters the SCH.

The variation of the stream direction leads to a flow separation at the inner wall of the curved conduit. As a result of the separation, the main stream section is reduced, which propagates over a long distance downstream of the bend. This effect is shown in figure 3.18.

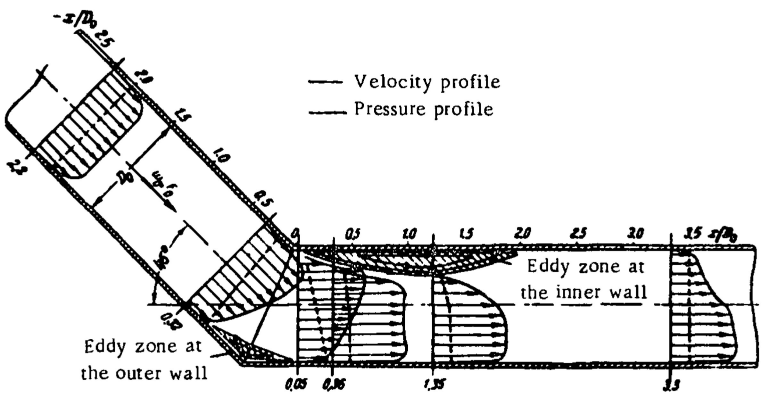

Figure 3.18: Variation of the Profiles of Velocities and Pressures in an Elbow and the Straight Stretch Following it [B.22]

"The appearance of a centrifugal force and the existence of a boundary layer at the walls explain the appearance of a transverse flow in a curved pipe. It also explains the formation of the so-called vortex pair which, superimposed on the main stream parallel to the channel axis, gives the streamlines a helical shape" [B.22], cf. figure 3.19.

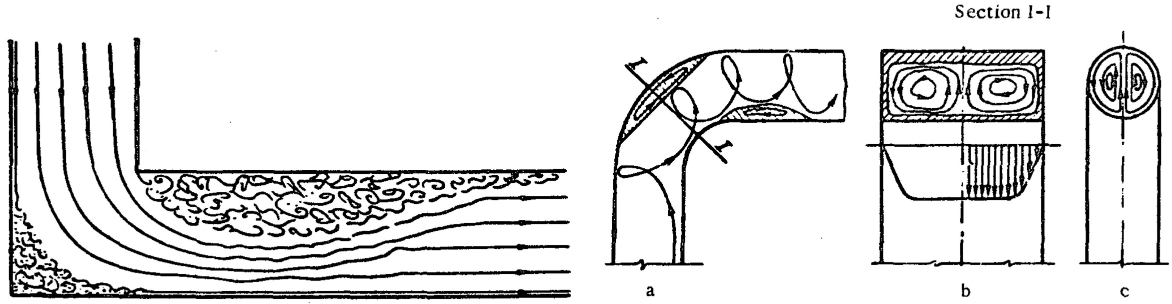

Figure 3.19: Stream Pattern in a 90° Elbow and Vortex Pair in an Elbow [B.22] (a): Longitudinal Section, b): Cross Section of Rectangular Conduit, c): Cross Section of Circular Pipe)

"With other conditions constant, the resistance of a curved pipe is highest when its inner wall makes a sharp corner at the bend; the stream separation from this wall is then most intense. It follows that the intensity of eddy formation and the resistance of a curved conduit increase with an increase in the angle of bend. The rounding of the corners (especially the inner wall) considerably attenuates the separation and reduces the resistance as a result. Since the most effective means for decreasing the resistance and equalizing the velocity distribution is the elimination of the eddy zone at the inner wall of the channel, the vanes located near the inner rounding will produce the largest effect. This makes it possible to remove some of the vanes located near the outer wall without altering the flow characteristics. In those cases when it is especially important to obtain a uniform velocity distribution immediately after the turn, the number of vanes is not reduced" [B.22], cf. figure 3.20.

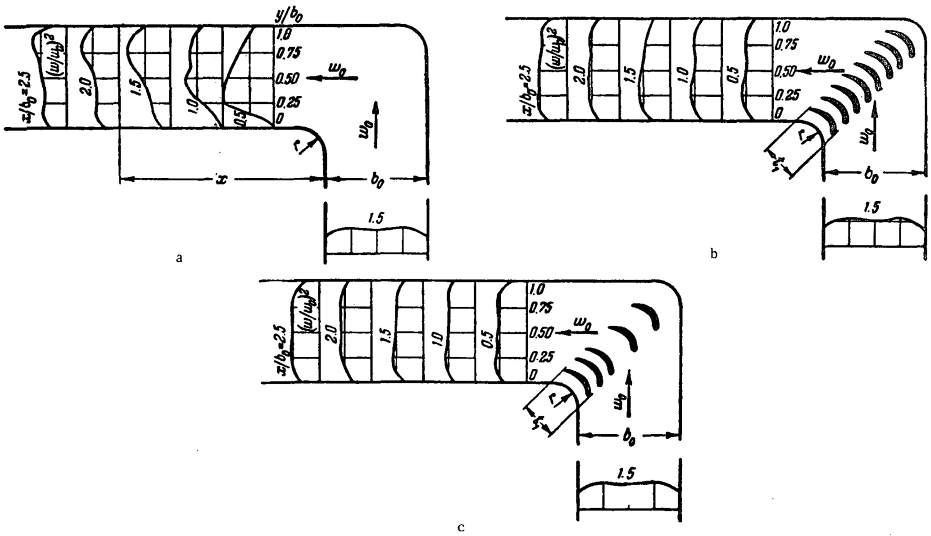

Figure 3.20: Distribution of Dimensionless Velocities in an Elbow [B.22] (a): Without Vanes, b): With a Normal Number of Vanes, c): With a Reduced Number of Vanes)

3.4 Solar Chimney Tube Flow

For the fundamentals of fluid mechanics for the flow field inside the SCH please compare section 3.1. In general the SCH corresponds to a circular tube and therefore the *Poiseuille flow* equation is valid. Its main difference to the SC is its vertical, instead of horizontal, extension.

The execution of the SCH with a cone, diverging or converging profile with straight or hyperbolic curvature will alter the flow variables and their distribution inside the SCH. The effect of a diverging shape profile on the eigenfrequencies and mode shapes will be investigated in chapter 10 and on the flow parameters in chapters 11 and 12, respectively.

3.4.1 Side Effects

The impact of the ambient flow field on the structure, grouped under the keyword Fluid-Structure-Interaction (FSI) and at the SCH outlet, well known as the *tip effect*, will not be part of this study. At least some publications will be mentioned, where the effects are discussed, [A.22], [A.31] and [T.4].

Another natural phenomenon is the effect of cold inflow at the top of the SCH known from CTs due to adverse thermal stratification. The reversed flow leads to a decrease in efficiency and therefore needs to be prevented. Figure 3.21 shows the periodic cold inflow into a CT.

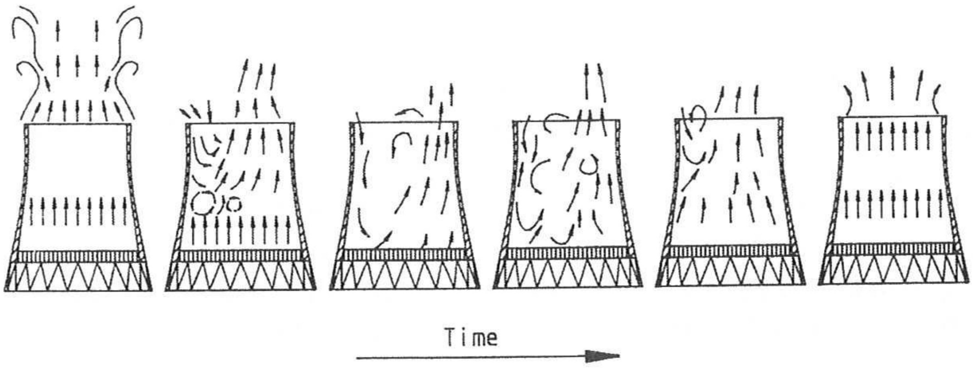

Figure 3.21: Periodic Cold Inflow Into Cooling Tower [B.26], [B.27]

According to [A.127], a CT and therefore the SCH, will experience cold inflow when $1/Fr_D > 2.8$, where the *densimetric Froude number* is represented by equation (3.30), cf. [T.20].

3.4.2 Flow Losses

The flow losses at the SCH will be divided into friction losses, including the resistance coefficients for flow barriers on the inside of the SCH and exit losses to the ambient.

Friction Loss

[A.137] presented some research on the friction pressure drop with different values of absolute roughness K_s for a 550 m of height and 82 m in diameter SCH. The results are shown in figure 3.22.

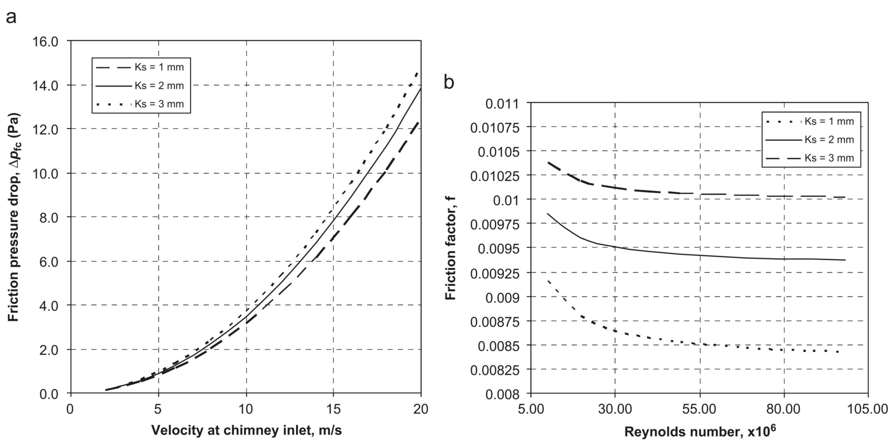

Figure 3.22: Pressure Drop in the Solar Chimney as a Function of Air Flow Velocity (a) and Friction Factor as a Function of Reynolds Number (b) [A.137]

It can be seen that the pressure drop due to friction is around $1 \div 2$ powers smaller than the pressure drop due to the pressure difference between the SCH base and the surrounding. The friction factor shown in figure 3.22 is calculated from [A.32].

More on the calculation of the friction factor and flow losses due to friction and the resistance coefficient can be found by [A.33], [A.27], [A.97] and [T.1].

Exit Loss

[A.137] states that the exit loss of a SCH is in the range of 3% of the pressure drop due to the difference at the SCH base and the surrounding and therefore can be neglected.

An approximation of the tower outlet loss coefficient during relatively quiet (no significant ambient winds) periods is given by [A.149] in equation (3.29)

$$K_{t0} = -0.28 Fr_D^{-1} + 0.04 Fr_D^{-1.5} \tag{3.29}$$

where

Fr_D = Densimetric Froude Number

which is determined by

$$Fr_D = (\dot{m}/A_6)^2 / [\rho_6(\rho_7 - \rho_6) g d_t] \tag{3.30}$$

where

d_t = Diameter of the solar chimney in m
A_6 = Area of the solar chimney outlet in m^2
ρ_6 = Density of fluid at the solar chimney outlet in kg/m^3
ρ_7 = Ambient fluid density in kg/m^3

3.5 Free Jet Flow

A prerequisite for the development of a free jet flow are mass forces and a gradient of density which act not parallel to each other, cf. [B.1]. Figure 3.23 shows the general structure of a free jet and the development behind a nozzle with laminar, transitional and turbulent flow state.

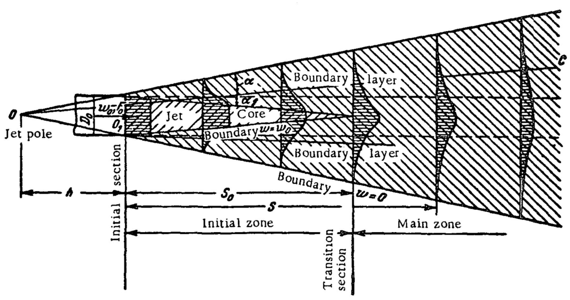

a) Pattern of a Free Jet

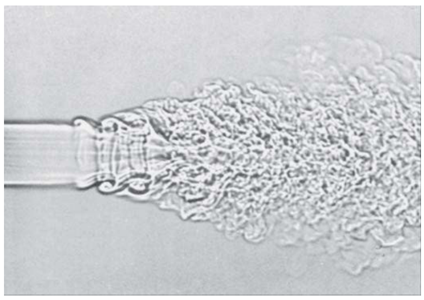

b) Subsonic Open Jet With Areas of Laminar, Transitional and Turbulent Flow

Figure 3.23: Free Jet Flow [B.22] (left), [B.11] (right)

[A.170] investigated the interaction between jets of same properties with its neighbours without ambient fluid movement. A model for the merging of an infinite line of equally spaced identical jets in a still ambient fluid is developed, which is shown in figure 3.24.

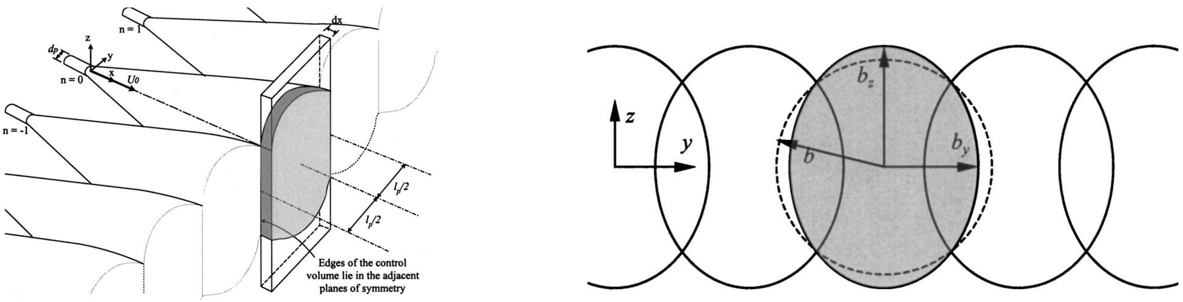

a) Line of Merging Jets with Control Volume b) Jet Deformation During Merging Process

Figure 3.24: Jet Interaction [A.170]

"A noticeable change (1%) in the gradient of the shape parameters occurs after x/l_p reaches 4.5 (...). This indicates the location where the interference of individual jets becomes strong enough to affect the bulk properties of the central jet. The flow reaches its two-dimensional limit when x/l_p $\approx$ 12. In the two-dimensional limit, the shape parameters take on their two-dimensional values (...). The merging region is therefore defined by 4.5 $<$ x/l_p $<$ 12 and this provides the basis for linear transformations of the spread (k) and the length-scale ratio (λ) values" [A.170].

More information on this can be found by [A.114], [A.78], [T.19], [A.164], [T.24] and [A.15].

3.5.1 Control and Synthetic Jets (Fluidic Actuator)

In this work the term control and synthetic jets will be used for small jets independent of the main flow stream that are used to enhance the mixing and turbulence of the flow field. In contrast to the definition of [B.32] where synthetic jets are made up of the surrounding fluid which is not the case for the current investigation.

3.5.2 Increase of Mixing and Turbulence

Figure 3.25 shows the interaction of a free jet with a perpendicular control jet.

Small amounts of forcing led to a substantially increased mixing and that the actuators need only slightly perturb the shear layer near the nozzle to cause a dramatic change in the overall flow development downstream, cf. [A.49].

Also see publications by [A.48] and [A.166] for more information.

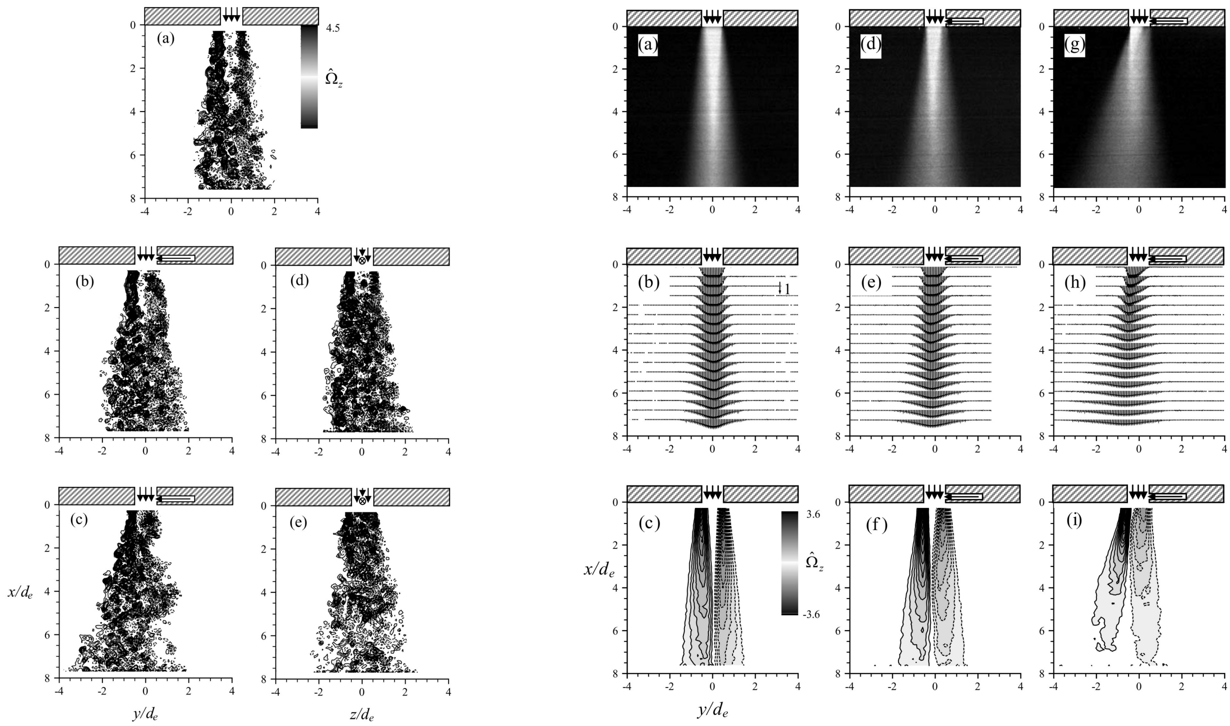

Figure 3.25: Instantaneous Vorticity Fields of the Baseline (left), Mean Images (a, d, g), Normalized Mean Velocity Vector Fields (b, e, h), and Mean Span Wise Vorticity (c, f, i) for the Baseline (right) [A.165] (a): free jet, (b to e (left) and d to i (right)) different momentum coefficients and directions

Chapter4

Basics of Thermodynamic

This chapter summarizes the thermodynamic aspects of a SCPP and its components. The processes of heat transfer due to convection, conduction and radiation will be explained at the corresponding parts of the SCPP. Also the thermodynamics of axial-flow turbines will be presented here.

4.1 Thermodynamic Aspects Between the Solar Collector and Soil Surface

In the case of direct and uninhibited solar irradiation on the earth's surface approximately 70 % of short wave length radiation reaches the soil surface and gets absorbed. 30 % are reflected by the atmosphere and therefore the planetary albedo is 30 %. So how does the solar irradiation heats up the atmosphere? This is done in two steps and on an indirect way. The solar irradiation heats up the soil surface in a first step which heats up the air layers on top due to the process of convection instead.

The increase of temperature of the atmosphere heated from the soil surface varies with altitude. For example three temperature rates, generally known as *temperature lapse rate*, are shown for different altitudes:

$dT/dt = 0.69\ Kh^{-1}$ for z = 100 m
$dT/dt = 1.40\ Kh^{-1}$ for z = 500 m
$dT/dt = 0.70\ Kh^{-1}$ for z = 1,000 m

For the air layer close to the soil surface (z = 0.0 m) the temperature rate lies by $1Kh^{-1}$. Measurements of the atmosphere show that this is only an approximation of the real situation.

In the case of the SCPP the solar irradiation reaches the SC first which also reflects and absorbs the arriving rays to a specific fraction depending on the material properties of the glass panels and the supporting frame structure. This will be specified within the next sections for the soil surface and the SC structure.

4.1.1 Glass and Supporting Structure

Throughout all publications available for the author the structure of the SC has been simplified to the glass panels neglecting the supporting structure completely. Therefore only investigations on different glass panels with varying material properties can be found.

The quality of glass, mainly the transparency, will influence the power output of a SCPP on a diurnal base depending on ambient air temperatures. It can be seen from results presented by [A.145], that even poor quality glass with a low transparency can lead to higher temperature differences between the SC and the air underneath resulting in a higher power output for winter mornings. In general high quality glass allows more of the solar irradiation to penetrate and strike the ground which leads to lower SC temperatures but to higher soil temperatures instead. For summer months the quality glass results in an increased power output throughout the day and slightly higher peak values.

More on the energy balance for the SC, soil and the SC air and the process of convection can be found by [A.145], [A.149], [A.147] and [A.146].

4.1.2 Soil Characteristics

The soil underneath the SC will be used as thermal storage. For the untreated case we assume homogeneous parameters, which is obviously not the case for real soil condition and needs to be taken into account if the deviation from the assumed parameters becomes too large. In the case of the SCPP the focus lies on the temperature development within the upper parts of the soil. A depth of one to two meters is affected by diurnal changes of ambient temperature. For areas underneath in general no change in temperature can be found. The heat flux caused by the change in temperature is shown in equation (4.1) and is called *soil heat flux.*

$$B = -\mu \frac{\partial T}{\partial z}, z < 0 \tag{4.1}$$

where

μ = Thermal conductivity of soil gained from measurements in W/mK

Due to convection the heated or cooled down soil causes a temperature gradient in the air parcels on top which leads to a turbulent heat flux. This *sensible heat flux* can be calculated using equation (4.2).

$$H = c_p \overline{\rho} \overline{w`\theta`} = -c_p \overline{\rho} K_h \frac{\partial \overline{\theta}}{\partial z} \tag{4.2}$$

where

c_p = Specific heat of air in kJ/kgK
K_h = Transfer coefficient (summarises the combined effects of processes such as atmospheric turbulence or vegetation activity)
ρ = Density of air in kg/m^3

In contrast we have the *latent heat flux* which does not cause a temperature gradient. The *latent heat flux* describes the evaporation of water from the generally wet soil which leads to the transport of steam to higher air layers. Equation (4.3) shows the latent heat flux.

$$E = l_v \overline{\rho} \overline{w`q`} = -l_v \overline{\rho} K_w \frac{\partial \overline{q}}{\partial z} \tag{4.3}$$

where

l_v = Latent heat of evaporation in kJ/kg
q = Specific humidity in %
K_w = Turbulent diffusion coefficient for steam in m^2/s

Figure 4.1 shows schematically the heat fluxes at the soil surface (air (top), soil (bottom)).

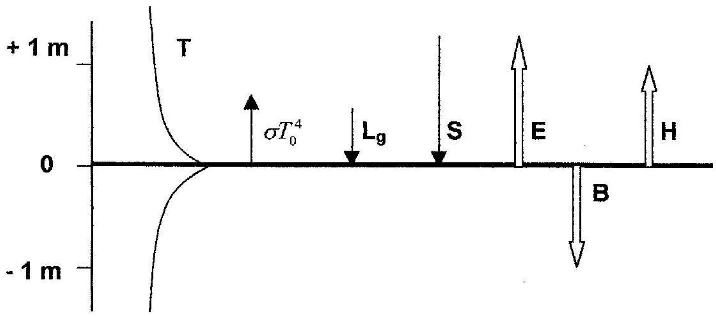

Figure 4.1: Heat Fluxes at the Soil Surface [B.12]

The soil surface only acts as a boundary layer between the two matters air and soil and therefore cannot serve as a heat storage. There has to be a balance of the energy fluxes at the boundary, which leads to equation (4.4).

$$S_0 + L_0 + B_0 + H_0 + E_0 = 0 \tag{4.4}$$

where

Index 0 = Energy fluxes taken from soil surface

For the short-wave radiation S_0 and long-wave radiation L_0 the term Q_0 for the radiation budget can be used. Having all energy fluxes the surface temperature T_0 can now be derived. Exemplarily the diurnal cycle of the former mentioned heat fluxes and the corresponding temperature are shown in figure 4.2 for barren and wet soil.

Close to the surface the potential temperature θ_0 equals the current ambient temperature T_0. The wanted surface temperature $\overline{\theta}_0$ can now be calculated using equation (4.5).

$$\sigma\overline{\theta}_0^4 = -(S_0 + L_{og} + B_0 + H_0 + E_0) \tag{4.5}$$

There is a strong dependency of the diurnal trend of $\overline{\theta}_0$ from the solar irradiation S_0. Also the turbulent heat fluxes H_0 and E_0 depend on changes of temperature and humidity of the air parcels close to the soil surface and therefore vary with time as it is the case for the heat flux B_0, too.

Two parameters which have a great influence on the thermal behaviour of different soil substances, namely the albedo α and the emissivity ϵ, can be found in [B.25] and will be used throughout this work at many points.

Lets move on from the top surface layer which acts, as we have seen so far, as a boundary between the two matters air and soil to the area of soil below the surface.

The change of heat within a volume per second can be written as:

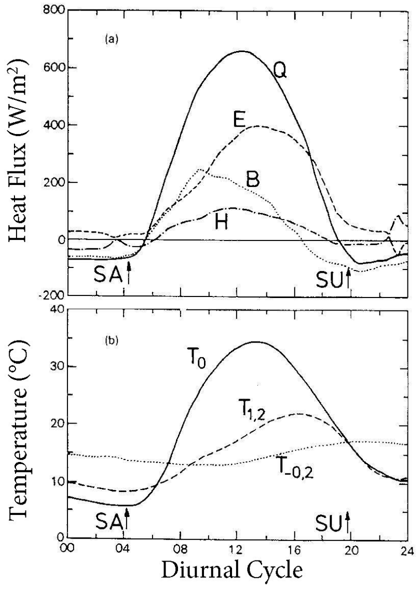

Figure 4.2: Diurnal Cycle of Heat Fluxes and Temperature at the Soil Surface for Barren and Wet Soil [B.12]

$$\rho_s c_s \frac{\partial T_s}{\partial t} = -\frac{\partial B}{\partial z_s} \tag{4.6}$$

where B is the divergence of the flux density.

So far we have got the influence of the solar irradiation on the temperature and the heat flux at the surface layer. Moving deeper into the soil structure there is still a diurnal trend of the temperature wave entering the deeper layers recognizable. The existing fluctuations of temperature can mathematically be split up into a mean value $\overline{T}_s(z_s)$ which depends only on z_s and the variation part. With a constant value for the mean temperature gradient at each depth the temperature at a specific depth can be calculated using equation (4.7).

$$\Delta T_s(z_s, t) = \Delta T_s(0, t_{max}) \times exp\left(-\sqrt{\frac{\omega}{2m_s}} z_s\right) cos(\omega)\left(t - \frac{z_s}{\sqrt{2m_s\omega}}\right) \tag{4.7}$$

where

m_s = Thermal diffusion coefficient in m^2/s
ω = Circular frequency in 1/s

From equation (4.7) someone can see that it includes an exponential damping depending on depth and a cyclic oscillation with a circular frequency ω.

For the soil heat flux we obtain equation (4.8).

$$B(z_s, t) = -\lambda_s \frac{\partial \overline{T}_s}{\partial z_s} + \Delta T_s(0, t_{max}) \lambda_s \sqrt{\frac{\omega}{m_s}} \times exp\left(-\sqrt{\frac{\omega}{2m_s}} z_s\right) cos\left[\omega\left(t - \frac{z_s}{\sqrt{2m_s\omega}}\right) + \frac{\pi}{4}\right] \tag{4.8}$$

where

λ = Thermal conductivity in W/mK

It also shows both the dependency on a constant part from the mean temperature gradient and a temporal part. Additionally, there is a phase shift of $\pi/4$, that leads to a diurnal wave that is ahead of the temperatures of 3 hours, for an annual wave this corresponds to 1 $^1/_2$ month.

Approximately the solution for the temperature gradient given in equation (4.7) and the soil heat flux given in equation (4.8) correspond to harmonic oscillation over time for idealized ambient conditions. The real trends for daily hours without solar irradiation better correspond to an attenuated exponential function. Figure 4.3 shows the diurnal cycle for soil temperature, soil heat flux and the profile of soil temperature, respectively.

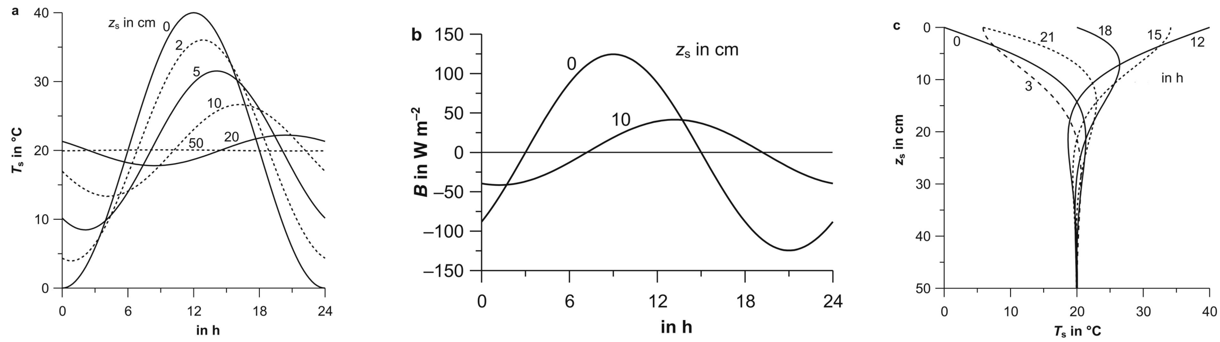

a) Diurnal Cycle of Soil Temperature

b) Diurnal Cycle of Soil Heat Flux

c) Profile of Soil Temperature

Figure 4.3: Diurnal Cycle of Soil Temperature, Soil Heat Flux and the Vertical Profile of Soil Temperature [B.25]

Last but not least is has to be mentioned that the assumption of a homogeneous soil structure not varying with depth and time used for the formulation of equations (4.7) and (4.8) cannot be hold for real life conditions. Also soil in general means a mixture of different matters and aggregate phase which needs to be investigated in first place. If these parameters are available all parts can be summed up to explain the real soil condition.

Additional numerical and experimental research on this field of interest was conducted by [A.43], [A.88], [A.57], [A.147], [A.146], [A.115], [A.177], [A.84], [A.26], [A.121] and [A.124]. General information on the principles of soil physics can be found by [B.29].

4.1.3 Heat Transfer at the Components of the Solar Collector

The heat fluxes at and within the SC are shown schematically in figure 4.4 for a single roof with the three components glass-air-soil.

All of the shown heat fluxes depend on the solar irradiation and the material properties of the SC, soil and air.

4.1.4 Temperature Boundary Layer

In chapter 3 and especially in section 3.1 the *Poiseuille flow* of the SC with its development of a boundary layer for the velocity was shown. Due to the influence of temperature and the heat

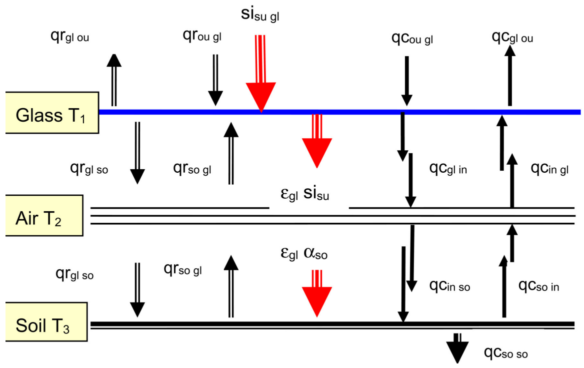

Figure 4.4: Schematic Heat Transfer of Simple Glass-Air-Soil Solar Collector [A.104]

transfer within the SC additionally a temperature boundary layer develops. For a description of the development the *Prandtl number* Pr, representing the ratio of diffusion of momentum to diffusion of heat in a fluid, is used for the case of forced convection. The Prandtl number can vary in a wide range from values Pr << 1 (liquid metals) to Pr >> 1 (heavy oils). The different developing temperature boundary layers are shown in figure 4.5 with ∂ the thickness of the velocity boundary layer and ∂_{th} the thickness of the temperature boundary layer.

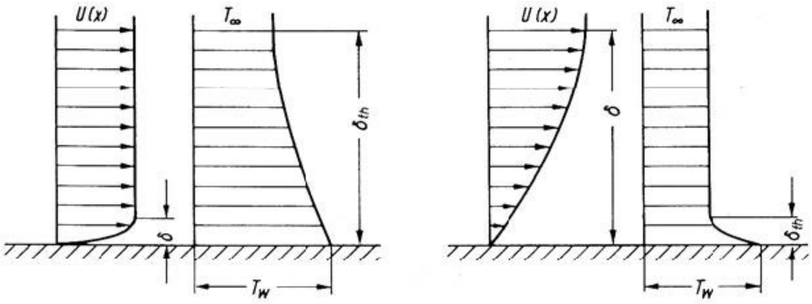

Figure 4.5: Comparison Between the Distribution of Velocity and Temperature of Boundary Layer Flows for Different Prandtl Numbers [B.40] (left: Pr << 1, right: Pr >> 1)

For Pr = 1 the thickness of the velocity and thermal boundary are equal.

4.2 Turbines

"We classify as turbomachines all those devices in which energy is transferred either to, or from, a continuously flowing fluid by the dynamic action of one or more moving blade rows. The word turbo or turbinis is of Latin origin and implies that which spins or whirls around. Essentially, a rotating blade row, a rotor or an impeller changes the stagnation enthalpy of the fluid moving through it by either doing positive or negative work, depending upon the effect required of the machine. These enthalpy changes are intimately linked with the pressure changes occurring simultaneously in the fluid" [B.9].

In the case of a SCPP axial-flow turbomachines, more specifically, axial-flow turbines are used. The thermodynamic properties will be explained briefly in the next subsection.

4.2.1 Thermodynamics of Axial-Flow Turbines

We need to distinguish between two-dimensional theory and three-dimensional flows within axial-flow turbines. For the two-dimensional theory it is assumed that the flow conditions at the mean radius fully represent the flow at all other radii. For small ratios of blade height to mean radius this is a reasonable approximation. Large ratios require a three-dimensional analysis which makes the calculations more complex. Fluid mechanic properties of axial turbines have been discussed in section 3.2. Here a short introduction into the thermodynamics of axial-flow turbines will be given.

Figure 4.6 shows the *Mollier diagram* of a turbine stage.

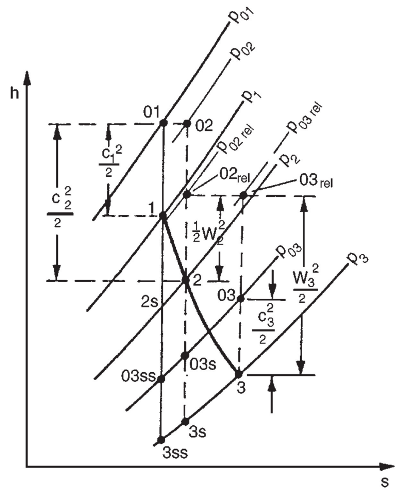

Figure 4.6: Mollier Diagram of a Turbine Stage [B.9]

Assuming adiabatic flow the work done on the rotor can be calculated by the stagnation enthalpy drop using equation (4.9).

$$\Delta W = \dot{W}/\dot{m} = h_{01} - h_{03} \tag{4.9}$$

where

$h_{01;03}$ = Stagnation enthalpy in kJ/kg at different stages
$\dot{m}$ = Specific mass in kg/s

For the case of a rotor and a nozzle row in front someone can see that the static pressure decreases from p_1 to p_2. The absolute static pressure reduces from p_2 to p_3 in the rotor row.

Detailed investigation on the thermodynamic cycle for a SCPP including the gas turbine cycle has been shown by [A.11].

4.2.2 Efficiency

A general expression for the efficiency, generally called performance, is given in (4.10) taken from [B.6], [B.9].

$$\text{Performance} = \frac{\text{Desired Output}}{\text{Required Output}} \tag{4.10}$$

which can be specified for a turbine to

$$\eta_0 = \frac{\text{Mechanical energy available at coupling of output shaft in unit time}}{\text{Maximum energy difference possible for the fluid in unit time}} \tag{4.11}$$

"There are several ways of expressing efficiency, the choice of definition depending largely upon whether the exit kinetic energy is usefully employed or is wasted" [B.9]. For the case of employed kinetic energy the turbine and stage adiabatic efficiency η, is the total-to-total efficiency and is defined as

$$\eta_{tt} = \Delta W_x / \Delta W_{x_{max}} = (h_{01} - h_{02})/(h_{01} - h_{02s}) \tag{4.12}$$

If the difference between the inlet and outlet kinetic energies is small, i.e. $\frac{1}{2}c_1^2 = \frac{1}{2}c_2^2$, then

$$\eta_{tt} = (h_1 - h_2)/(h_1 - h_{2s}) \tag{4.13}$$

When the exhaust kinetic energy is not usefully employed and entirely wasted, the relevant adiabatic efficiency is the total-to-static efficiency η_{ts}, cf. equation 4.12

$$\eta_{ts} = (h_{01} - h_{02})/(h_{01} - h_{02s} + \frac{1}{2}c_{2s}^2) = (h_{01} - h_{02})/(h_{01} - h_{2s}) \tag{4.14}$$

If the difference between inlet and outlet kinetic energies is small, equation (4.14) changes to

$$\eta_{ts} = (h_1 - h_2/(h_1 - h_{02s} + \frac{1}{2}c_1^2) \tag{4.15}$$

4.3 Transition Section

A particular importance lies on the SC to SCH transition section where the heated air needs to be diverted from a nearly horizontal to a vertical direction. Warm air coming from the SC entering the turbine area will experience a pressure drop and through the rotating blades a swirl effect resulting in not only axial but also radial and tangential velocity components behind the turbine. The swirl can be beneficial for the process of mixing afterwards but can also be removed by stator blades integrated into the turbine. The transition section has now two purposes. Firstly, all incoming highly three dimensional flow streams need to be mixed without huge losses and secondly, the formed stream tube needs to be redirected into the vertical direction. Figure 4.7 shows two configurations of the transition section where in a) the redirection of the flow streams from the horizontal to the vertical direction is performed before the merging process. In b) these two tasks are reverse.

Besides these general concepts for the layout of the transition section different concepts for installations implemented into the tower base have been investigated. They cover two main options, namely local and global redirection variants. A cone as it had been implemented into the prototype SCPP at Manzanares belongs to the global variants whereas figure 4.8 gathers some local redirection variants.

It is getting obvious that most of the variants are symmetric as it is the general case for the

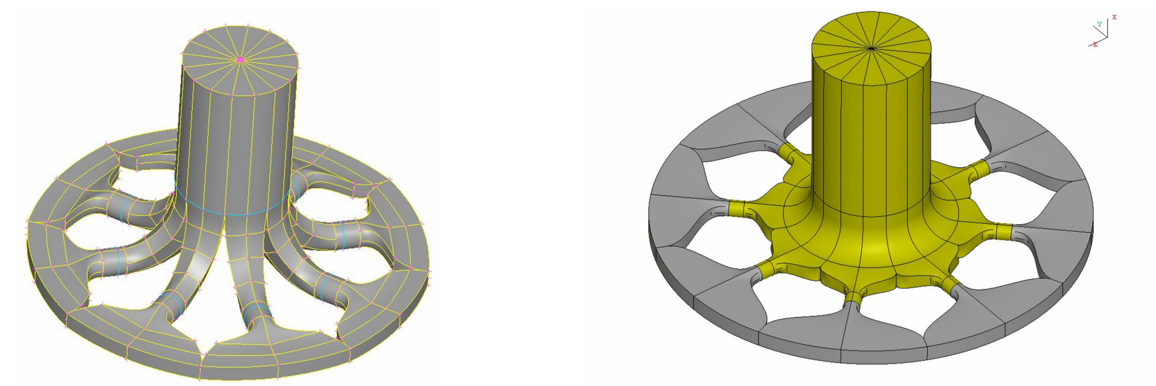

a) Configuration I b) Configuration II

Figure 4.7: Configurations of Transition Section [P.3]

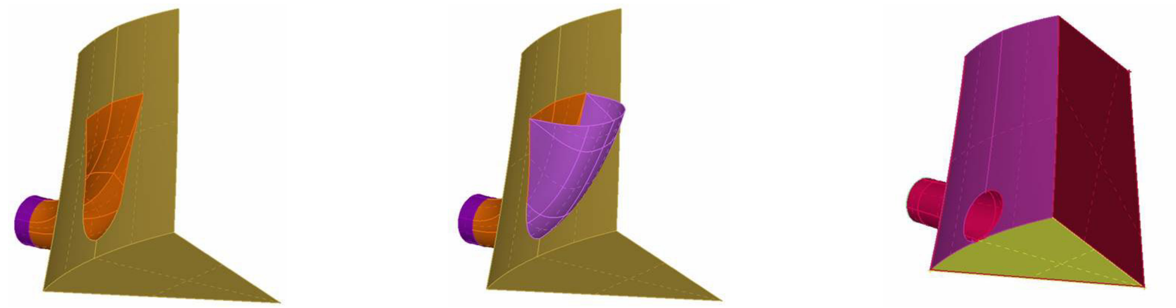

a) Diversion Without Internal Tent b) Diversion With Internal Tent c) Single Diffuser Behind Turbine

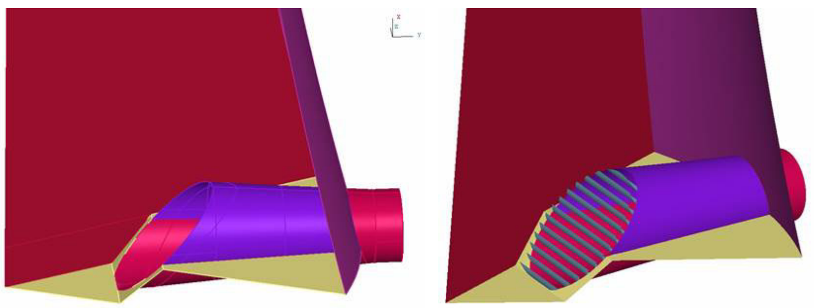

d) Diffuser with Extension e) Diffuser with Extension and 13 Baffles

Figure 4.8: Variants of Installation [P.3]

whole power plant. Also non-symmetric variants exist, one is shown in figure 11.6 of part III of this work. In this case only a quadrant of the SC has been built. The reason for this can be the reduction of cost on the one hand or the adaptation of the power plant to the conditions of the construction site on the other. Many former research has been done with the assumption of symmetry in structure and flow field. In the course of this work it will become clear that the generally stated assumption of symmetry cannot be uphold any longer. The assumption will only be true for perfect ambient conditions without the influence of wind, changing solar altitude and without any clouds. Even for the structure itself and the case of maintenance or break-down of one or more turbines this assumption does not describe the real situation perfectly.

The effect of different variants of installations on the flow field as well as the effect of wind and asymmetric inflow conditions, buoyancy and free and forced convection will be investigated in chapters 11 and 12 experimentally and numerically.

4.4 Solar Chimney Tube Flow

The flow inside the SCH, often referred to as internal or tube flow has been described in chapter 3 for the fluid mechanic properties and in parts in section 4.1 where it was assumed that the flow underneath the SC can be taken as a two dimensional tube flow. For the thermodynamic process within the SCH the development of the thermal boundary layer is of interest, which is shown schematically in figure 4.9 for the case of forced convection.

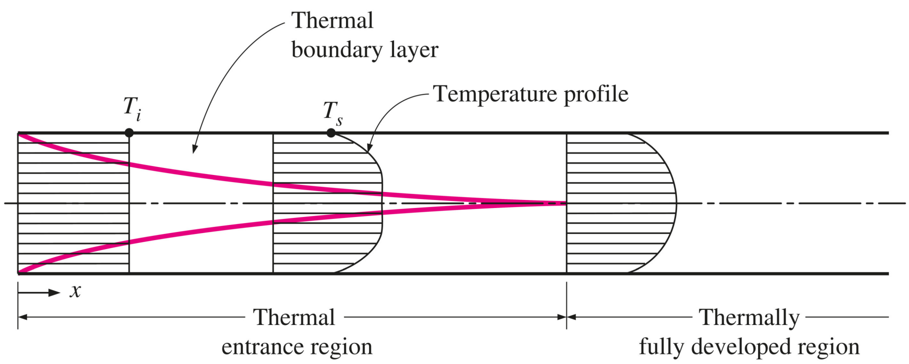

Figure 4.9: Development of the Thermal Boundary Layer in a Tube [B.5]

At same distance from the entrance a thermally fully developed region can be found. This thermal entry length can be calculated by using equation (4.16)

$$L_{t,laminar} \approx 0.05RePrD \tag{4.16}$$

for laminar flow and for the turbulent case shown in equation (4.17)

$$L_{t,turbulent} \approx 10D \approx L_{h,turbulent} \tag{4.17}$$

where

h = Hydrodynamic
t = Thermal
D = Tube diameter in m

This means, that in practice it is generally agreed, that the entrance effects are confined within a tube length of 10 diameters. The special case of equality of hydrodynamic and thermal entry length has been stated in subsection 4.1.4 for the case of Pr = 1.

For the efficiency of fluid flow and heat transfer, figure 4.10 depicts the variation of the friction factor and the convection heat transfer coefficient for flow in a tube.

It can be seen that both friction factor and heat transfer coefficient are highest at the inlet of the tube. The boundary layers (hydrodynamic and thermal) are both zero at this point. Both

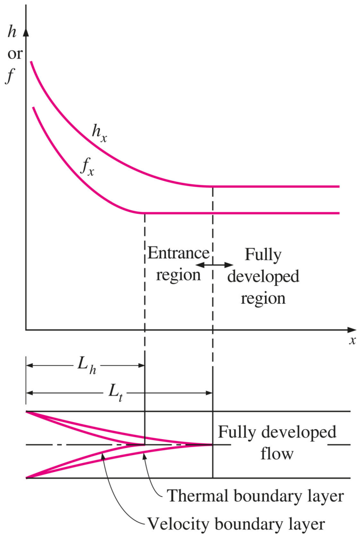

Figure 4.10: Variation of the Friction Factor and the Convection Heat Transfer Coefficient in a Tube (Pr > 1) [B.5]

variables decrease with increasing boundary layer height towards the fully developed region.

For the case of natural convection, the so called *chimney effect* develops within the SCH. The primary variable for expressing the occurring buoyancy force is temperature, which requires the knowledge of a property that represents the variation of the density of a fluid with temperature at constant pressure. This property is the *volume expansion coefficient* β shown in equation (4.18).

$$\beta = \frac{1}{\nu}\left(\frac{\delta \nu}{\delta T}\right)_P = -\frac{1}{\rho}\left(\frac{\delta \rho}{\delta T}\right)_P \tag{4.18}$$

For the case far away from the surface and a constant pressure P the equation simplifies to

$$\beta \approx -\frac{1}{\rho}\frac{\rho_\infty - \rho}{T_\infty - T} \tag{4.19}$$

or

$$\rho_\infty - \rho = \rho\beta(T_\infty - T) \tag{4.20}$$

where

ρ_∞ = Density at undisturbed condition in kg/m^3
T_∞ = Temperature at undisturbed condition in K

For the case of ideal gas, as it is assumed for all calculations, the *volume expansion coefficient* can be written as (4.21)

$$\beta_{ideal\ \ gas} = \frac{1}{T} \tag{4.21}$$

where

T = Absolute temperature in K

This means, that the buoyancy force is proportional to the density difference, which is proportional to the temperature difference at constant pressure. "Therefore, the larger the temperature difference between the fluid adjacent to a hot (or cold) surface and the fluid away from it, the larger the buoyancy force and the stronger the natural convection currents, and thus the higher the heat transfer rate" [B.5].

Results of numerical tests showing the isothermal and isovelocity lines for different Rayleigh numbers can be found by [A.111].

Analogous to the development of the velocity profile underneath the SC, shown in subsection 3.1.1, the same effect can be determined for the temperature profile. Under the influence of turbulence, the temperature profile becomes fuller which leads to a higher heat exchange at the surfaces. Therefore the friction losses increase as a consequence. For issues, where heat transfer plays a decisive role, turbulent flows are favoured and often exist in any case, cf. [B.1].

4.5 Ways of Heat Transfer

In this section all ways of heat transfer - convection, conduction and radiation - within a SCPP with their corresponding heat transfer coefficients shall be listed to show the thermal complexity contrary to the structural simplicity. The arrangement of the subsections follows the chronological order of an air parcel travelling through the whole system starting at the entrance of the SC and leaving at the SCH exit, in other words it will be adhere to the direction of the thermodynamic process.

Figure 4.11 shows the nomenclature for the different areas within a SCPP.

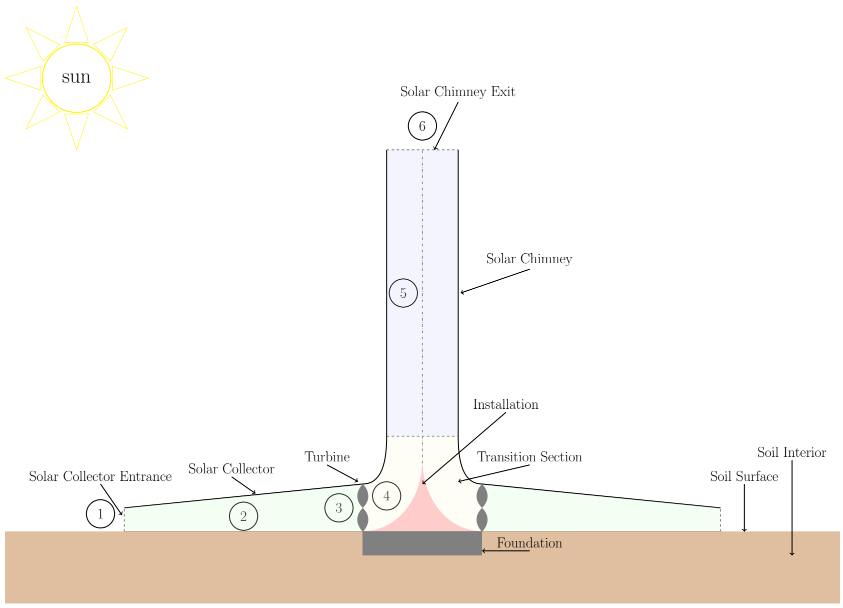

Figure 4.11: Solar Chimney Power Plant with Nomenclature (1: Ambient to Solar Collector, 2: Solar Collector, 3: Turbine Area, 4: Transition Section, 5: Solar Chimney, 6: Solar Chimney to Ambient)

For the information gathered in the following subsections and answering the question how to develop heat transfer coefficients, general sources are [B.10], [B.23], [B.24] and [B.1]. For heat transfer coefficients designed for a SCPP please compare the work from [T.20], [A.17], [A.19] and [A.18]. The unit of the heat transfer coefficients is W/m^2K and for the heat flux W/m^2 respectively.

4.5.1 Atmosphere ⇔ Solar Collector Roof

The actual net radiation transfer between a small horizontal surface and a large surrounding, in this case between the sky and the SC, can be calculated by using equation (4.22) and will be of the dimension W/m^2

$$q_{scsky} = \frac{Q}{A} = \epsilon\sigma(T_{sc}^4 - T_{sky}^4) \tag{4.22}$$

where

ϵ = Emissivity of opaque bodies
σ = Stefan-Boltzmann constant equal to 5.6697 x 10^{-8} W/m^2K^4

T_{sky} can be found in [B.10].

The heat transfer coefficient due to convection for the solar collector to the ambient air can be written as follows

$$h_{scsky} = \left[0.2106 + 0.0026 v \left(\frac{\rho T_m}{\mu g \Delta T}\right)^{1/3}\right] / \left[\frac{\mu T_m}{g \Delta T c_p k^2 \rho^2}\right]^{1/3} \tag{4.23}$$

where

T_m = Mean temperature between the solar collector and the ambient air in K
ΔT = Difference between the solar collector and the ambient air temperature in K
ρ = Density of air in kg/m^3
μ = Dynamic viscosity in m^2/s
c_p = Specific heat capacity in J/kgK
k = Thermal conductivity in W/mK

For the case, when the collector roof temperature only marginally exceeds the ambient temperature, equation (4.24) gets applicable.

$$h_{scsky} = 3.87 + 0.0022\left(\frac{v\rho c_p}{Pr^{2/3}}\right) \tag{4.24}$$

4.5.2 Atmosphere ⇔ Soil Surface

At the entrance of the SC, the only direct interaction between the sky and the soil surface can occur. [A.142] found, that "the profiles of the heat-transfer coefficient, temperature of the fluid and surface temperature at the ground strongly change in the entrance area. This behaviour is caused by interaction with the atmosphere (backflow). For small-velocity magnitudes (in the atmosphere) the heat-transfer coefficient is decreased at the ground and the temperature is increased at the ground. The reverse is valid for large-velocity magnitude". For the net radiation transfer and the heat transfer coefficient, equations (4.22), (4.23) and (4.24) are rewritten as

$$q_{sssky} = \frac{Q}{A} = \epsilon\sigma(T_{sc}^4 - T_{sky}^4) \tag{4.25}$$

$$h_{sssky} = \left[0.2106 + 0.0026v\left(\frac{\rho T_m}{\mu g \Delta T}\right)^{1/3}\right] / \left[\frac{\mu T_m}{g \Delta T c_p k^2 \rho^2}\right]^{1/3} \tag{4.26}$$

$$h_{sssky} = 3.87 + 0.0022\left(\frac{v \rho c_p}{Pr^{2/3}}\right) \tag{4.27}$$

4.5.3 Solar Collector Roof ⇔ Solar Collector Air

The heat transfer coefficient between the SC and the SC air can be written as follows

$$h_{scsca} = \frac{(f/8)(Re - 1,000)Pr}{1 + 12.7(f/8)^{1/2}(Pr^{2/3} - 1)}\left(\frac{k}{d_h}\right) \tag{4.28}$$

where

f = Friction factor
d_h = Hydraulic diameter in m

It can be distinguished between a heat transfer from the SC to the SC air or the other way around.

4.5.4 Solar Collector Roof ⇔ Soil Surface

The radiation heat transfer between two arbitrary surfaces can be found by using equation (4.29).

$$Q_1 = \frac{\sigma(T_2^4 - T_1^4)}{\dfrac{1-\epsilon_1}{\epsilon_1 A_1} + \dfrac{1}{A_1 F_{12}} + \dfrac{(1-\epsilon_2)}{\epsilon_2 A_2}} \tag{4.29}$$

From this it follows that the radiation heat transfer coefficient results in equation (4.30)

$$h_r = \frac{\sigma(T_2^2 + T_1^2)(T_2 + T_1)}{\dfrac{1-\epsilon_1}{\epsilon_1} + \dfrac{1}{F_{12}} + \dfrac{(1-\epsilon_2)A_1}{\epsilon_2 A_2}} \tag{4.30}$$

where

$A_{1;2}$ = Area of surface 1 and 2 respectively in m^2
F_{12} = View factor (configuration factor)
$T_{1;2}$ = Temperature of surface 1 and 2 respectively in K
$\epsilon_{1;2}$ = Emissivity factor of surface 1 and 2 respectively

For infinite plates equation (4.29) simplifies to

$$\frac{Q}{A} = \frac{\sigma(T_2^4 - T_1^4)}{\dfrac{1}{\epsilon_1} + \dfrac{1}{\epsilon_2} - 1} \tag{4.31}$$

4.5.5 Solar Collector Air ⇔ Soil Surface

For the convective heat transfer coefficient between the SC air and the soil surface both situations with the soil surface temperature being higher or lower than the SC air temperature as a function of the stream velocity need to be considered, cf. [A.19]. If the soil surface temperature $T_{ss} > T_{sca}$ equations (4.32) and (4.33) are applicable.

$$h_{sssca} = \left[0.2106 + 0.0026v\left(\frac{\rho T_m}{\mu g \Delta T}\right)^{1/3}\right] / \left[\frac{\mu T_m}{g \Delta T c_p k^2 \rho^2}\right]^{1/3} \tag{4.32}$$

$$h_{sssca} = 3.87 + 0.0022\left(\frac{v \rho c_p}{Pr^{2/3}}\right) \tag{4.33}$$

"In the unlikely case where the temperature of the air in the collector is greater than the ground surface temperature, the ground surface is approximated as a cooled horizontal surface, facing upwards. A cool, stable layer of air forms above the ground surface which, similar to the heated roof facing down, is "swept away" by the flowing collector air" [T.20]. Both equations stay valid for this situation.

4.5.6 Soil Surface ⇔ Soil Interior

The heat transfer from the soil surface to the soil interior as a process of conduction will be explained in more detail in chapter 6, where a mathematical one dimensional model of a SCPP will be presented. The model is based on measured data from [T.20] for the site of Sishen, South Africa. Data of the solar irradiation, ambient air temperature, wind speed and Relative Humidity (RH) have been implemented into the program code. Also the storage effect of the soil interior which is decisive for the power production through the night hours has been taken into account.

4.5.7 Further Ways of Heat Transfer

Further ways of heat transfer are listed here. They will not be explained in detail because of their minor role in the whole process of heat transfer within a SCPP or the information has already been provided in the previous subsections.

- Transition Section Air ⇔ Installation (Redirecting Variant) via convection
- Installation (Redirecting Variant) ⇔ Foundation via conduction
- Foundation ⇔ Soil Interior via conduction
- Atmosphere ⇔ Solar Chimney Wall via radiation
- Solar Chimney Wall ⇔ Air Inside the Solar Chimney via convection

Chapter5

Computational Fluid Dynamics (CFD)

In this chapter the general model and modelling parameters of CFD analysis are given. Both groups of parameters will have an impact on the gained results which need to be considered and quantified. Therefore sections 5.5, 5.6 and 5.7 give some indication of the review of all results. The Navier-Stokes equations in its general form for the conservation of continuity, momentum and energy are shown, and also for the case of Large Eddy Simulation (LES) and Reynolds Averaged Navier-Stokes (RANS). Results presented in part II and III rely on both modelling approaches.

5.1 Model Parameter

This section deals with the model parameters, in other words the global setting, of a CFD analysis. It includes the dimensionality, domain size and the boundary conditions. All of these parameters need to be chosen in the first place adapted for the existing problem.

Standing in contrast there are the modelling parameters, which define the solution techniques which will be explained within the next section.

5.1.1 2D- or 3D-Model

The dimensionality of a problem can vary from a 1D to a 3D case. Although many natural processes are three-dimensional they can be simplified due to symmetry conditions or well chosen boundary conditions and taken as 2D or 1D instead. This is also the case for investigations of the SCPP which represent a three-dimensional structure including a three-dimensional flow field. Starting with one-dimensional models which are used for analytical investigations of a fluid problem as it was done for the SCPP shown in chapter 6. More often 2D models have been used to investigate the flow structure because of their closer relationship to the real case. Ignoring ambient wind and the changing sun position as the main influence factors of the spatial variability, the flow field within a SCPP can be simplified to a 2D flow structure. Additionally, the center line of the SCH has led to a further simplification of a symmetric 2D flow field which helps saving computing time, which is one of the main reasons for reducing the dimensionality of a flow problem in numerical investigations.

Associated with the dimensionality, the boundary conditions need to be chosen carefully to represent the real flow situation in this simplified flow case. There are also dependencies of the available modelling parameters on the dimensionality which will be discussed in the next section.

5.1.2 Domain Properties

The domain represents the outer boundaries of the numerical flow case. Depending on the structural shape and the physical properties involved, different recommendations for the dimensions can be found. In the case of a SCPP a best practise guideline for similar flow situations, shown in subsection 5.6, gives good instructions for the size of the numerical model. These recommendations will ensure that the choice of the domain borders will not influence the results and will be kept in a moderate size regarding the necessary computing time. Not only the size, but also the shape of the surrounding domain can or may vary. Generally an ashlar-formed domain is used for the numerical investigation because of its simple construction. In contrast to this, [T.5] used a circular inlet boundary shape for the set-up of his numerical analysis. The input parameters like flow velocity and direction need to be adapted to this but will not affect the results.

Another field of research, where this domain adaption is done quite often, is the investigation of turbines as the ones used for the SCPP. Here the domain is often fit to the shape of the blades respectively which saves computing time and, of course, does not influence the outcome of the numerical investigations.

5.1.3 Boundary Conditions (Global and Local)

"Flows inside a CFD solution domain are driven by the boundary conditions. In a sense the process of solving a field problem (e.g. a fluid flow) is nothing more than the extrapolation of a set of data defined on a boundary contour or surface into the domain interior. It is, therefore, of paramount importance that we supply physically realistic, well-posed boundary conditions, otherwise severe difficulties are encountered in obtaining solutions. The single, most common cause of rapid divergence of CFD simulations is the inappropriate selection of boundary conditions" [B.44].

One has to differentiate between global and local boundaries, speaking of domain borders and boundaries between single parts or partitions within the numerical model respectively. No discussion of local boundaries will be done here but at the respective points instead.

For the global boundary conditions a brief discussion on their influence and necessity will be presented here. Only in rare cases a turbulent fluid flow is encased by solid walls as it can be found in an agitator. For the case of a SCPP we have both the inner and outer flow field, where the inner flow field is influenced by the ambient flow conditions to a great extent. Therefore the choice of the domain size is of major importance to determine the right boundary conditions. If the modelled fluid flow spreads across this domain, we call the border an *artificial border*. Incompressible flow situations always have an elliptical character in space, which shows that a certain point in space affects even points across these borders. It is not always clear where this influence has been attenuated completely. Therefore guidelines may give an appropriate proposal or different numerical models need to be developed to answer this question.

For the exact representation of the real world problem via numerical analysis the boundary conditions at these *artificial borders* should be known already before starting the analysis. As this is nearly impossible the domain size is chosen in that way that the unknown or vaguely known boundary conditions only influence the results to a small extent.

General approaches for the inflow, outflow and wall boundary conditions can be found by [B.15] and [B.44]. As a special case of a boundary situation, the *symmetry conditions* at a symmetry plane will be explained here.

Symmetry Conditions

The conditions at a symmetry boundary can be divided into two categories namely:

1) No flow across the boundary.
2) No scalar flux across the boundary.

At the symmetry boundary, normal velocities are set to zero and the values of all other properties just on the outside of the domain are equated to their values at the nearest node just inside the domain, cf. [B.44].

[B.15] states, that the application of symmetry boundary conditions in general is not allowed and does not lead to a realistic solution. It is possible, that the influence on the fluid flow parameters resulting from the symmetry boundary can lead to only small deviations within a small range close to the symmetry plane and therefore the approach of symmetry can be correct with slight changes in the results.

Symmetry conditions will help reducing computing time without affecting the numerical results to a great extent.

5.2 Modelling Parameter

This section includes the modelling parameters important for a CFD analysis, starting with the Navier-Stokes equations for the general case. Figure 5.1 shows schematically the three main model families Direct Numerical Simulation (DNS), LES and RANS with two sub-families, often called *hybrid models*, namely Detached Eddy Simulation (DES) and Unsteady Reynolds Averaged Navier-Stokes (URANS) as the most used ones.

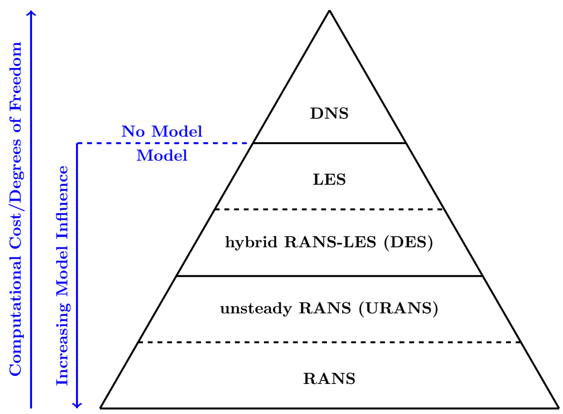

Figure 5.1: DNS, LES and RANS

The direct solution of the Navier-Stokes equations done by the DNS model will not be presented here, because it is no part of this work. Instead, LES and RANS will be explained in more detail as the most widely applied approximation in the CFD practice.

Figure 5.2 shows the hierarchy between these three levels of turbulence modelling based on the turbulent energy spectrum in function of wave number k, and the limits of the range of application of LES and RANS models.

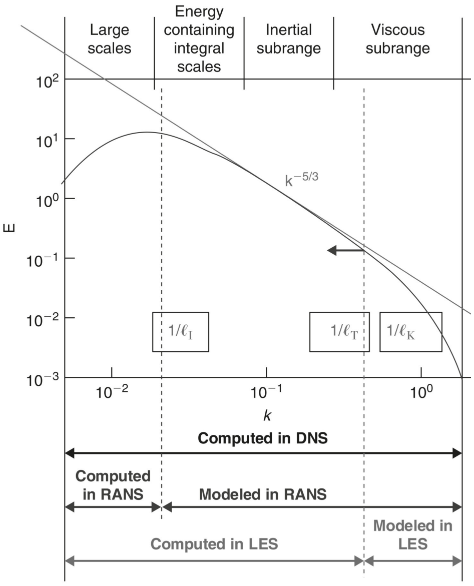

Figure 5.2: Energy Spectrum of Turbulence in Function of Wave Number k, with Indication of the Range of Application of the DNS, LES and RANS Models [B.20]

While with DNS the whole turbulence and energy spectrum is computed in time and space, turbulence models for LES and RANS increase in significance, which reduce computing cost but only approximate the complete solution of the Navier-Stokes equations. For LES the turbulent fluctuations are only computed above a certain length scale, while smaller turbulence is modelled by semi-empirical laws. RANS models ignore the turbulent fluctuations completely and aim at calculating only the turbulent averaged flow.

Figure 5.3 shows the difference in signal and turbulence spectrum for DNS, LES, hybrid models and RANS respectively.

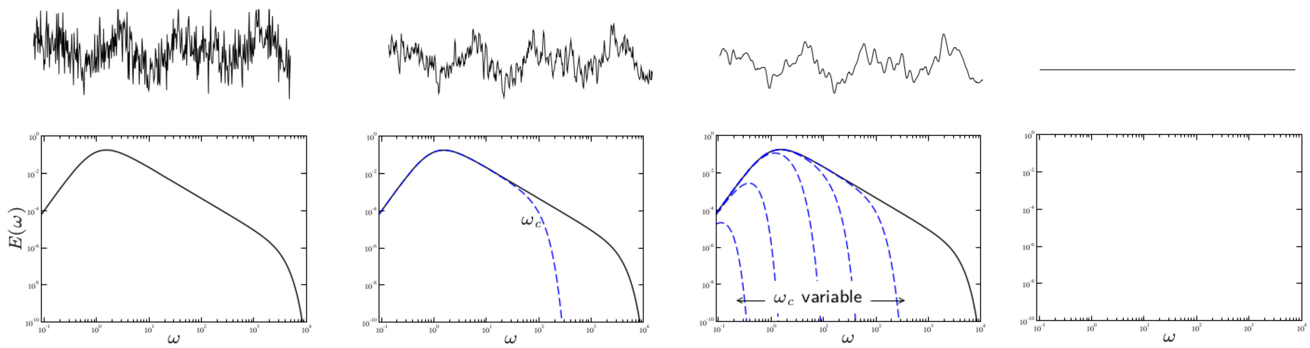

Figure 5.3: Signal and Spectrum of Turbulence for DNS, LES, Hybrid and RANS (from left to right) [T.23]

The signal plots depict the decreasing fluctuations with increasing turbulence modelling (from left to right) in the signal and the change in the turbulence spectrum as a consequence thereof.

The impact of the turbulence model on the results of a natural combustion process is shown by the example presented in figure 5.4.

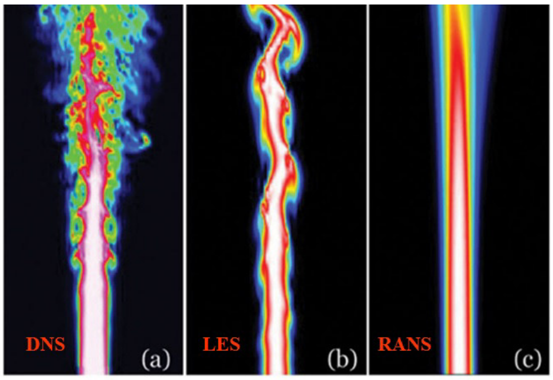

Figure 5.4: Numerical Result Using DNS, LES and RANS for a Natural Combustion Process [U.9]

The turbulence of the free jet seen in the DNS result diminishes with LES and RANS until a really smooth jet stream with the RANS model shows only small fluctuations and no steep changes in the plume.

5.2.1 Navier-Stokes Equations

The Navier-Stokes equations are given in equations (5.1), (5.2) and (5.3) in general form for the u, v and w component.

$$\rho\frac{\Delta u}{\Delta t} = -\frac{\delta p}{\delta x} + \frac{\delta}{\delta x}\left[2\mu\frac{\delta u}{\delta x} + \lambda\ div\ \mathbf{u}\right] + \frac{\delta}{\delta y}\left[\mu\left(\frac{\delta u}{\delta y} + \frac{\delta v}{\delta x}\right)\right] + \frac{\delta}{\delta z}\left[\mu\left(\frac{\delta u}{\delta z} + \frac{\delta w}{\delta x}\right)\right] + S_{Mx} \tag{5.1}$$

$$\rho\frac{\Delta v}{\Delta t} = -\frac{\delta p}{\delta y} + \frac{\delta}{\delta x}\left[\mu\left(\frac{\delta u}{\delta y} + \frac{\delta v}{\delta x}\right)\right] + \frac{\delta}{\delta y}\left[2\mu\frac{\delta v}{\delta y} + \lambda\ div\ \mathbf{u}\right] + \frac{\delta}{\delta z}\left[\mu\left(\frac{\delta v}{\delta z} + \frac{\delta w}{\delta y}\right)\right] + S_{My} \tag{5.2}$$

$$\rho\frac{\Delta w}{\Delta t} = -\frac{\delta p}{\delta z} + \frac{\delta}{\delta x}\left[\mu\left(\frac{\delta u}{\delta z} + \frac{\delta w}{\delta x}\right)\right] + \frac{\delta}{\delta y}\left[\mu\left(\frac{\delta v}{\delta z} + \frac{\delta w}{\delta y}\right)\right] + \frac{\delta}{\delta z}\left[2\mu\frac{\delta w}{\delta z} + \lambda\ div\ \mathbf{u}\right] + S_{Mz} \tag{5.3}$$

For the development of the Finite Volume Method (FVM), the Navier-Stokes equations can be rewritten in the most useful form:

$$\rho\frac{\Delta u}{\Delta t} = -\frac{\delta p}{\delta x} + div(\mu\ grad\ u) + S_{Mx} \tag{5.4}$$

$$\rho\frac{\Delta v}{\Delta t} = -\frac{\delta p}{\delta y} + div(\mu\ grad\ v) + S_{My} \tag{5.5}$$

$$\rho\frac{\Delta w}{\Delta t} = -\frac{\delta p}{\delta z} + div(\mu\ grad\ w) + S_{Mz} \tag{5.6}$$

The conservative or divergence form of the system of equations, which governs the time-dependent three-dimensional fluid flow and heat transfer of a compressible Newtonian fluid the following equations give the continuity equation in (5.7), the momentum equations for the directions x, y and z in (5.8), (5.9) and (5.10), and the energy equation in (5.11), where S_M is the momentum source and Φ the dissipation function.

$$\frac{\delta \rho}{\delta t} + div(\rho \mathbf{u}) = 0 \tag{5.7}$$

$$\frac{\delta(\rho u)}{\delta t} + div(\rho u \mathbf{u}) = -\frac{\delta p}{\delta x} + div(\mu \ grad \ u) + S_{Mx} \tag{5.8}$$

$$\frac{\delta(\rho v)}{\delta t} + div(\rho v \mathbf{u}) = -\frac{\delta p}{\delta y} + div(\mu \ grad \ v) + S_{My} \tag{5.9}$$

$$\frac{\delta(\rho w)}{\delta t} + div(\rho w \mathbf{u}) = -\frac{\delta p}{\delta z} + div(\mu \ grad \ w) + S_{Mz} \tag{5.10}$$

$$\frac{\delta(\rho i)}{\delta t} + div(\rho i \mathbf{u}) = -p \ div \ \mathbf{u} + div(k \ grad \ T) + \Phi + S_i \tag{5.11}$$

Both pressure p and internal energy i are functions of density and temperature which is stated in equations (5.12) and (5.13), generally known as the equations of state.

$$p = p(\rho, T) \tag{5.12}$$

$$i = i(\rho, T) \tag{5.13}$$

In this work we will solve the Navier-Stokes equations for the 2D- or 3D-flow case with air as medium taken as incompressible for all calculations. All information are taken from [B.44] and [B.15].

5.2.2 Large Eddy Simulation (LES)

The characteristic of turbulence, that it consists of large and small eddies, is used for the LES assumption. While large eddies interact with and extract energy from the mean flow, smaller eddies are nearly isotropic and have a universal behaviour. The behaviour of large eddies meanwhile is dictated by the geometry of the problem and is highly anisotropic. Therefore the LES approach distinguishes between both parts of the turbulence where the boundary between small and large is variable as can be seen at the Very Large Eddy Simulation (VLES) approach in contrast to the usually used LES approach. The Navier-Stokes equations are changed in that way that for the LES approach larger eddies still need to be computed for each problem with a time-dependent simulation. Smaller eddies, due to their universal behaviour will be captured by turbulence models instead.

"Instead of time-averaging, LES uses a spatial filtering operation to separate the larger and smaller eddies. The method starts with the selection of a filtering function and a certain cutoff width with the aim of resolving in an unsteady flow computation all those eddies with a length scale greater than the cutoff width. In the next step the spatial filtering operation is performed on the time-dependent flow equations. During spatial filtering information relating to the smaller, filtered-out turbulent eddies is destroyed. This, and interaction effects between the larger, resolved eddies and the smaller unresolved ones, gives rise to sub-grid-scale stresses or Subgrid Scale Modeling (SGS) stresses. Their effect on the resolved flow must be described by means of an SGS model. If the finite volume method is used, the time-dependent, space-filtered flow equations are solved on a grid of control volumes along with the SGS model of the unresolved stresses. This yields the mean flow and all turbulent eddies at scales larger than the cutoff width" [B.44].

The filtered unsteady Navier-Stokes equations for the LES momentum equations for u, v and w are given in equations (5.14), (5.15) and (5.16), and the LES continuity equation in (5.17) respectively.

$$\frac{\delta(\rho\overline{u})}{\delta t} + div(\rho\bar{u}\bar{\mathbf{u}}) = -\frac{\delta\overline{p}}{\delta x} + \mu\ div(grad(\overline{u})) - (div(\rho\overline{u\mathbf{u}}) - div(\rho\bar{u}\bar{\mathbf{u}})) \tag{5.14}$$

$$\frac{\delta(\rho\overline{v})}{\delta t} + div(\rho\bar{v}\bar{\mathbf{u}}) = -\frac{\delta\overline{p}}{\delta y} + \mu\ div(grad(\overline{v})) - (div(\rho\overline{v\mathbf{u}}) - div(\rho\bar{v}\bar{\mathbf{u}})) \tag{5.15}$$

$$\frac{\delta(\rho\overline{w})}{\delta t} + div(\rho\bar{w}\bar{\mathbf{u}}) = -\frac{\delta\overline{p}}{\delta z} + \mu\ div(grad(\overline{w})) - (div(\rho\overline{w\mathbf{u}}) - div(\rho\bar{w}\bar{\mathbf{u}})) \tag{5.16}$$

$$\frac{\delta\rho}{\delta t} + div(\rho\bar{\mathbf{u}}) = 0 \tag{5.17}$$

The overbar in this and all following equations in this section indicates a filtered flow variable. Figure 5.5 shows the application of a box filter on the signal u with two different sizes.

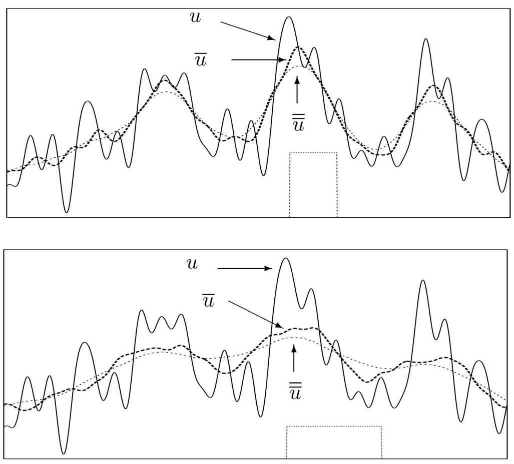

Figure 5.5: Filtered Velocity Signals for LES [B.15]

Most common filtering techniques are the *Gaussian filter* and the *spectral cutoff*. More on the filtering functions can be found by [B.15], [B.44] and [B.35].

In general the LES approach necessitates that the flow problem will be solved for the three-dimensional case. An exception can be found by, e.g. currents in shallow water, where the flow structure behaves two-dimensional due to the geometry of the channel. Thus a two-dimensional LES calculation can be used which will provide wrong results for most fluid problems, cf. [B.15]. The main difference lies in the characteristics of the vortexes which behave more stable for the 2D-case than it will be observed for the real 3D-flow field.

5.2.3 Reynolds-Averaged Navier-Stokes (RANS)

Using the RANS approach, the focus lies on the mean flow and the effects of turbulence on the mean flow parameters. The Navier-Stokes equations will be needed in a time averaged form shown in equations (5.18), (5.19), (5.20), (5.21) and (5.22), which stand for the momentum equations for u, v and w, the continuity equation and a scalar transport equation, respectively.

$$\frac{\delta(\rho\tilde{U})}{\delta t} + div(\bar{\rho}\tilde{U}\tilde{\mathbf{U}}) = -\frac{\delta\overline{P}}{\delta x} + div(\mu\ grad\ \tilde{U}) + \left[-\frac{\delta(\overline{\bar{\rho}u'^2})}{\delta x} - \frac{\delta(\overline{\bar{\rho}u'v'})}{\delta y} - \frac{\delta(\overline{\bar{\rho}u'w'})}{\delta z}\right] + S_{Mx} \quad (5.18)$$

$$\frac{\delta(\rho\tilde{V})}{\delta t} + div(\bar{\rho}\tilde{V}\tilde{\mathbf{U}}) = -\frac{\delta\overline{P}}{\delta y} + div(\mu\ grad\ \tilde{V}) + \left[-\frac{\delta(\overline{\bar{\rho}u'v'})}{\delta x} - \frac{\delta(\overline{\bar{\rho}v'^2})}{\delta y} - \frac{\delta(\overline{\bar{\rho}v'w'})}{\delta z}\right] + S_{My} \quad (5.19)$$

$$\frac{\delta(\rho\tilde{W})}{\delta t} + div(\bar{\rho}\tilde{W}\tilde{\mathbf{U}}) = -\frac{\delta\overline{P}}{\delta z} + div(\mu\ grad\ \tilde{W}) + \left[-\frac{\delta(\overline{\bar{\rho}u'w'})}{\delta x} - \frac{\delta(\overline{\bar{\rho}v'w'})}{\delta y} - \frac{\delta(\overline{\bar{\rho}w'^2})}{\delta z}\right] + S_{Mz} \quad (5.20)$$

$$\frac{\delta\bar{\rho}}{\delta t} + div(\bar{\rho}\tilde{\mathbf{U}}) = 0 \quad (5.21)$$

$$\frac{\delta(\bar{\rho}\tilde{\Phi})}{\delta t} + div(\bar{\rho}\tilde{\Phi}\tilde{\mathbf{U}}) = div(\Gamma_{\Phi}\ grad\ \tilde{\Phi}) + \left[-\frac{\delta(\overline{\bar{\rho}u'\phi'})}{\delta x} - \frac{\delta(\overline{\bar{\rho}v'\phi'})}{\delta y} - \frac{\delta(\overline{\bar{\rho}w'\phi'})}{\delta z}\right] + S_{\Phi} \quad (5.22)$$

Extra terms appear in the time-averaged flow equations due to the interactions between various turbulent fluctuations. These extra terms are modelled with classical turbulence models, which will be explained for the most common ones in the next subsection. Due to the low computing cost the RANS approach has been the mainstay of CFD over the last decades while LES is gaining more and more influence with decreasing hardware cost.

The overbar in all equations indicates a time-averaged variable and the tilde indicates a density-weighted or Favre-averaged variable.

5.2.4 Turbulence Modelling (k-ϵ, k-ω)

One of the most common turbulence models are the k-ϵ and the k-ω models. Both belong to the group of two equation models, which means, that they consist of two extra transport equations to represent the turbulent properties of the flow. Therefore it is possible to describe history effects like convection and diffusion of turbulent energy.

For the k-ϵ model, k represents the turbulent kinetic energy, meaning the energy in the turbulence and ϵ represents the rate of dissipation of turbulent kinetic energy, therefore the scale of the turbulence.

We can distinguish between three different formulations of the k-ϵ model, namely the standard, realisable and the Re-Normalisation Group (RNG) model. Only the standard formulation of the k-ϵ model will be presented here.

(5.23) shows the turbulent kinetic energy equation for k and (5.24) the equation for the rate of dissipation of turbulent kinetic energy ϵ and (5.25) the model constants.

$$\frac{\partial}{\partial t}(\rho k) + \frac{\partial}{\partial x_j}(\rho k u_i) = \frac{\partial}{\partial x_j}\left[\left(\mu + \frac{\mu_t}{\sigma_k}\right)\frac{\partial k}{\partial x_j}\right] + P_k + P_b - \rho\epsilon - Y_M + S_k \tag{5.23}$$

$$\frac{\partial}{\partial t}(\rho \epsilon) + \frac{\partial}{\partial x_i}(\rho \epsilon u_i) = \frac{\partial}{\partial x_j}\left[\left(\mu + \frac{\mu_t}{\sigma_\epsilon}\right)\frac{\partial \epsilon}{\partial x_j}\right] + C_{1\epsilon}\frac{\epsilon}{k}(P_k + C_{3\epsilon}P_b) - C_{2\epsilon}\rho\frac{\epsilon^2}{k} + S_\epsilon \tag{5.24}$$

$$C_{1\epsilon} = 1.44,\ C_{2\epsilon} = 1.92,\ C_\mu = 0.09,\ \sigma_k = 1.0,\ \sigma_\epsilon = 1.3 \tag{5.25}$$

The term P_b represents the buoyancy effect which is important for the modelling of a SCPP flow field. The variable $C_{3\epsilon}$ depends on literature and is meant to be used only with the P_b term.

For the k-ω model also two extra equations need to be solved. Herein k stands for the kinetic turbulent energy similar to the k-ϵ turbulence model and ω represents the specific dissipation. The three most common k-ω models are the *Wilcox's*, the *Wilcox's modified* and the *Shear Stress Transport (SST)* k-ω models. The equations for the *Wilcox's* formulation will be presented here. Equation (5.26) shows the turbulent kinetic energy for k, equation (5.27) the specific dissipation rate ω and equation (5.28) the closure coefficients and auxiliary relations.

$$\frac{\delta k}{\delta t} + U_j\frac{\delta k}{\delta x_j} = \tau_{ij}\frac{\delta U_i}{\delta x_j} - \beta^* k\omega + \frac{\delta}{\delta x_j}\left[(\nu + \sigma^*\nu_T)\frac{\delta k}{\delta x_j}\right] \tag{5.26}$$

$$\frac{\delta \omega}{\delta t} + U_j\frac{\delta \omega}{\delta x_j} = \alpha\frac{\omega}{k}\tau_{ij}\frac{\delta U_i}{\delta x_j} - \beta\omega^2 + \frac{\delta}{\delta x_j}\left[(\nu + \sigma\nu_T)\frac{\delta \omega}{\delta x_j}\right] \tag{5.27}$$

$$\alpha = \frac{5}{9},\ \beta = \frac{3}{40},\ \beta^* = \frac{9}{100},\ \sigma = \frac{1}{2},\ \sigma^* = \frac{1}{2},\ \epsilon = \beta^*\omega k \tag{5.28}$$

More information on the different turbulence models can be found by [U.3] and [B.44].

5.2.5 Radiation Model (S2S)

Within this work the effect of radiation has been modelled in ANSYS Fluent using the Surface to Surface Radiation Model (S2S). "The surface-to-surface radiation model can be used to account for the radiation exchange in an enclosure of gray-diffuse surfaces. The energy exchange between two surfaces depends in part on their size, separation distance, and orientation. These parameters are accounted for by a geometric function called a "view factor". The main assumption of the S2S model is that any absorption, emission, or scattering of radiation can be ignored; therefore, only "surface-to-surface" radiation need be considered for analysis" [S.1].

For the S2S, the energy flux leaving a surface is composed of reflected and directly emitted energy. The reflected energy flux is dependent on the incident energy flux from the surroundings, which then can be expressed in terms of the energy flux leaving all other surfaces. Equation (5.29) shows the energy leaving from a surface k

$$q_{out,k} = \epsilon_k \sigma T_k^4 + \rho_k q_{in,k} \tag{5.29}$$

where

$q_{out,k}$ = Energy flux leaving the surface in W/m^2
ϵ_k = Emissivity
σ = Stefan-Boltzmann constant equal to 5.6697 x 10^{-8} W/m^2K^4
$q_{in,k}$ = Energy flux incident on the surface from the surroundings in W/m^2

"The amount of incident energy upon a surface from another surface is a direct function of the surface-to-surface "view factor", F_{jk}. The view factor F_{jk} is the fraction of energy leaving surface j that is incident on surface k. The surfaces used in the calculation of a view factor can be mesh faces or clusters of faces. The incident energy flux $q_{in,k}$ can be expressed in terms of the energy flux leaving all other surfaces as" [S.1]

$$A_k q_{in,k} = \sum_{j=1}^{N} A_j q_{out,j} F_{jk} \tag{5.30}$$

where

A_k = Area of surface k in m^2
F_{jk} = View factor between surface k and surface j

With some rearrangements and simplifications equation (5.30) can be written as

$$J_k = E_k + \rho_k \sum_{j=1}^{N} F_{kj} J_j \tag{5.31}$$

where

J_k = Energy that is given off (or radiosity) of surface k
E_k = Emissive power of surface k

or as matrix form

$$KJ = E \tag{5.32}$$

where

K = N $\times$ N matrix

J = Radiosity Vector
E = Emissive power vector

Therefore equation (5.32) is called *radiosity matrix equation.*

Another commonly used model is the Discrete Ordinate (DO) radiation model.

More information on the available radiation models can be found by [B.44], [S.4] and [S.1].

5.2.6 Shell Conduction Model

"By default, ANSYS Fluent treats walls as having zero-thickness and presenting no thermal resistance to heat transfer across them. If a thickness is specified for a wall (thereby making it a thin wall) then the appropriate thermal resistance across the wall thickness is imposed, although conduction is considered in the wall in the normal direction only. There are applications, however, where conduction in the planar directions of the wall is also important. For these applications, you have two options: you can either mesh the thickness, or you can use the shell conduction approach. Shell conduction can be used to model one or more layers of wall cells without the need to mesh the wall thickness in a preprocessor. When the shell conduction approach is utilized, you have the ability to easily switch on and off conjugate heat transfer on any wall" [S.4]. The second approach has been used for the calculations on a model of the Manzanares SCPP presented in chapter 9. Additionally, its effect on the gained results is compared to the solution without the usage of the shell conduction model.

5.3 Computational Grid Parameter

In numerical analysis the grid plays a decisive role for achieving reliable results and a realistic representation of the real world problem. Therefore it is of major importance to build a grid that suits not only quality expectations, therefore see subsection 5.3.2, but also fits to the investigated fluid problem, consisting of the obstacle and the fluid stream. Closely tied to the grid quality is the selection of a structured or an unstructured grid, which will be discussed in subsection 5.3.1. Last but not least, a brief discussion of the connection between two or more grids which is accompanied by the partitioning of the domain, will be given in 5.3.3.

For complex flow structures and coupling of grids, pre-meshing of cross-sections can help to meet the necessary requirements for a high-resolution and a body-fitted mesh, cf. [A.81].

5.3.1 Structured or Unstructured Grids

In general we can distinguish between structured or unstructured grids. As grid quality has a direct impact on the overall accuracy of a CFD simulation, the choice of a mesh topology is often a matter of personal choice. Grid generation tools help to find the grid matching to the current flow problem but it is still inevitable to know about the pros and cons of each mesh type.

"It has to be emphasized that structured grids will, compared to unstructured grids, often be more efficient from CFD point of view, in terms of accuracy, Central Processing Unit (CPU) time and memory requirement" [B.20]. Although this is widely known, unstructured grids have become the most common approach in solving CFD problems. This is due to the impossibility of generating an automatically structured grid for any arbitrary geometry without any grid adaptation. This grid adaptation allows a local refinement in a certain region of the domain, without affecting the grid point distribution on the outside of that region. This gives one major advantage of unstructured over structured grids.

For the case of a SCPP both methods have been used in previous publications. In many cases either structured or unstructured meshes have been generated, or the flow domain has been divided into different parts to allow a grid generation for each part separately from the other. Results for this will be presented in subsection 5.3.3.

Figures 5.6 and 5.7 show a 2D and a 3D structured and unstructured grid respectively.

The 2D grid is of special type, also called quadtree or non-conformal grid, with hanging nodes at the boundaries and in the recirculation zone. For the 3D structured case a Cartesian grid with non-uniform cell sizes has been used.

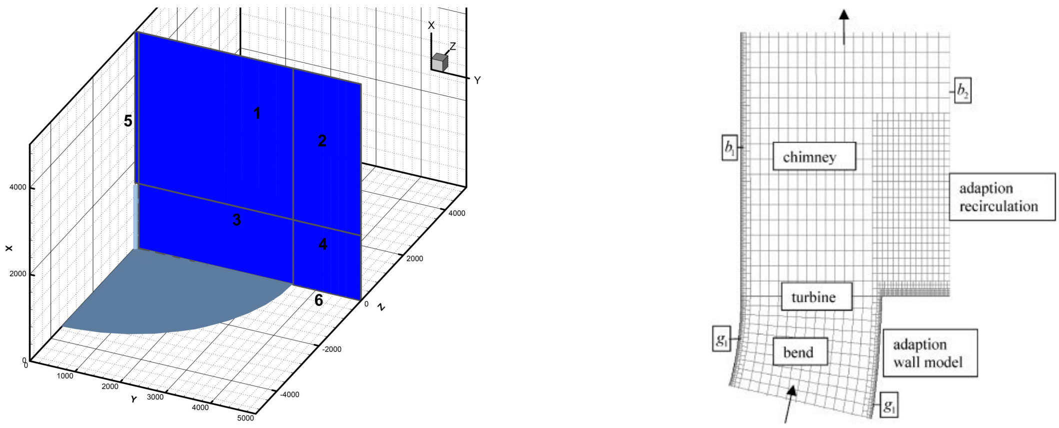

Figure 5.6: Domain and Grid Generation [T.11] (left), [A.142] (right)

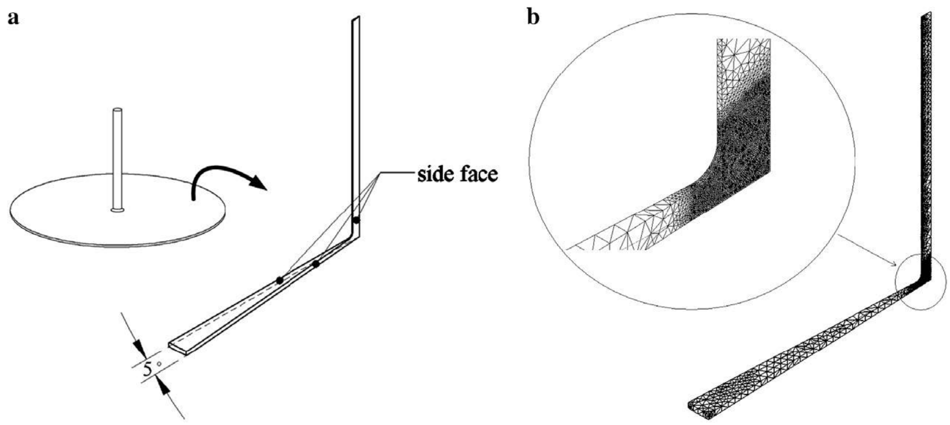

Figure 5.7: Computational Domain with (a) 5 Degree Axis-Symmetric Section and (b) Numerical Grid [A.103]

An extensive compilation of structured and unstructured grid types can be found by [B.20]. Results presented in this work exhibit structured grids if possible.

5.3.2 Grid Quality

In [S.3] the mesh metric and therefore the quality of the generated mesh can be evaluated by the following variables: Aspect Ratio, Jacobian Ratio, Warping Factor, Parallel Deviation, Maximum Corner Angle, Skewness and Orthogonal Quality. With values for Min, Max, Average and Standard Deviation the user can quickly see if the generated grid meets the requirements. For results presented in this work these quality measures have been used if possible.

5.3.3 Partitioning of Domain/Model

If it is not possible to use a structured mesh for the whole domain, someone can use the partitioning function available in all major CFD software packages. Special matching conditions have to be met at the boundaries between the grids and have been used for some results presented within part II.

Figure 5.8 shows the application of the partitioning function for two different concepts of a SCPP.

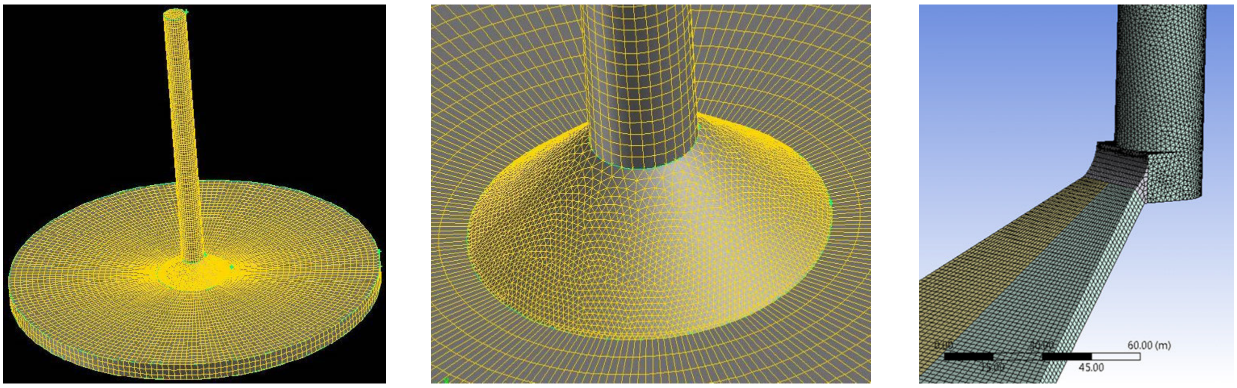

a) Grid Model of a Solar Chimney Power Plant | b) Grid Model of the Transition Section | c) Different Concept for the Solar Collector

Figure 5.8: Numerical Model of a Solar Chimney Power Plant [A.85] (left, middle), [A.101] (right)

It can be seen, that the left model in figure 5.8 exhibits a structured grid for the area of the SC and the SCH and an unstructured grid for the transition section. Meanwhile the SCPP depicted on the right exhibits a structured grid only for the SC.

5.4 Solving Parameter

The pressure-based solver based on the pressure-velocity coupled method with the *SIMPLE* and *SIMPLEC* algorithms have been used for all numerical simulations within this work. For the spatial discretization the gradient has been calculated by the *Least Squares Cell Based* method. For all other parameters like momentum, energy, turbulent kinetic energy, and so on, *Second Order Upwind*, for pressure *Second Order* discretization has been chosen, respectively.

For the *under-relaxation factors* the basic setting has been left unchanged.

5.5 Verification and Validation

The procedure of *"Verification"* and *"Validation"* is deeply rooted in mathematical and numerical models of physical processes in nature. While verification will deal with the accuracy and correctness of complex logical structures, e.g. computer codes, validation deals with the question, how formal constructs of nature, e.g. mathematical models, can be tested by physical observation.

"Briefly, verification is the assessment of the accuracy of the solution to a computational model by comparison with known solutions. Validation is the assessment of the accuracy of a computational simulation by comparison with experimental data" [A.138].

Or in other words: "Verification is solving the equations right. Validation is solving the right equations" [B.38].

Figure 5.9 shows the different phases of modelling of a physical process and the role of verification and validation.

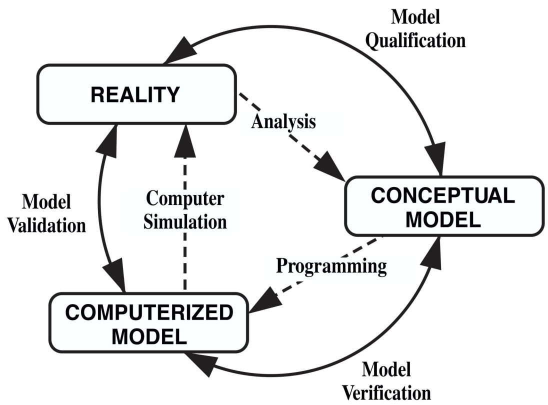

Figure 5.9: Phases of Modelling and Simulation and the Role of Verification and Validation [A.138]

For further information please see publications by [A.154] and [S.15].

5.6 Best Practise Guideline

One important question that arises when using CFD for the simulation of flow problems is the reliability and the confidence we can attach to the results. Therefore European Research Community on Flow, Turbulence And Combustion (ERCOFTAC) has developed a Best Practise Guideline (BPG), which shall give advices to achieve high-quality CFD results. The guideline covers topics like the error analysis, the turbulence modelling and the validation and sensitivity tests of CFD models with examples and suggestions. BPGs also give advice of the domain size for a reliable CFD analysis. Figure 5.10 shows the boundaries for one-directional and multi-directional simulations for the investigation of flow fields around buildings.

More on this can be found by [B.4] and [U.4].

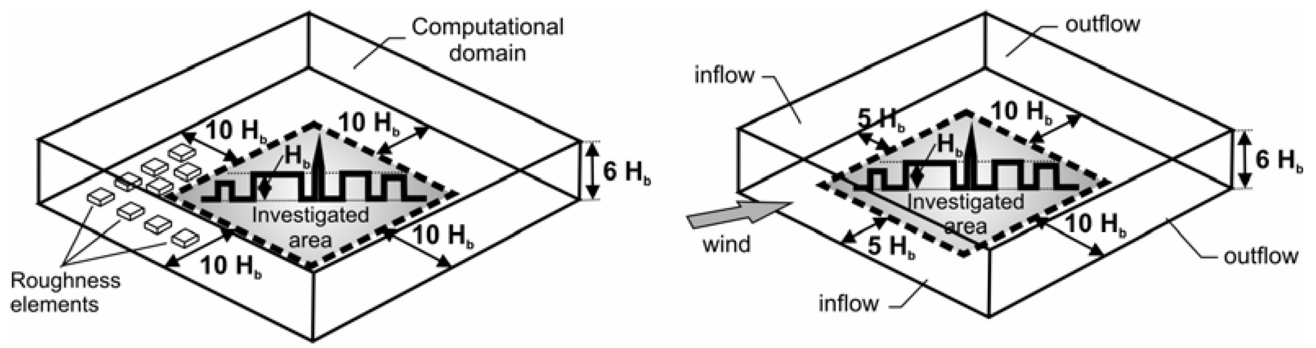

Figure 5.10: Boundaries in Multi-Directional and one Directional Simulation [B.13]

5.7 Errors and Uncertainties

The error and uncertainty analysis is one of the main fields of numerical and experimental analysis to gain reliable results. Figure 5.11 shows a list of possible errors and uncertainties, cf. [U.3] and [B.44].

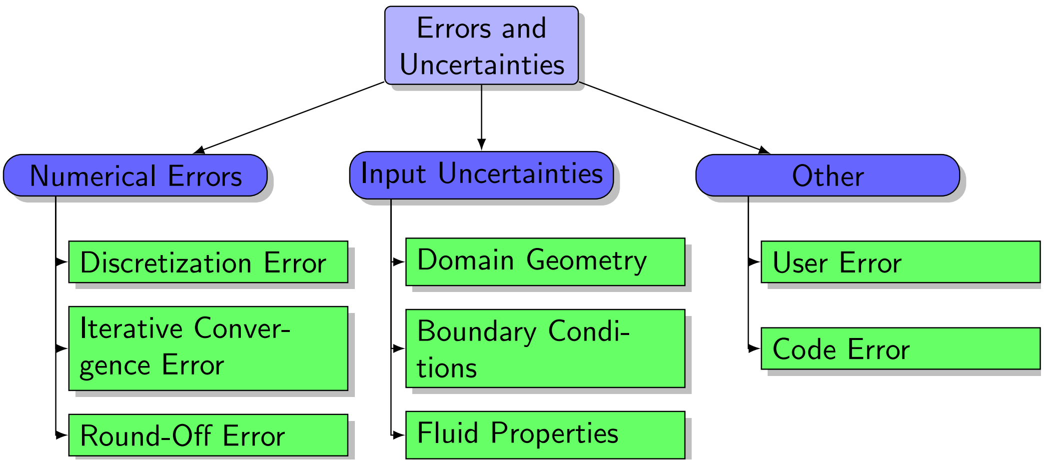

Figure 5.11: Errors and Uncertainties

In general you find two ways user defined their results as converged. Firstly, you bring the accuracy of all, or of some of your residuals down to machine accuracy, [B.4], [B.13]. Secondly, you bring it down to a point where no more movement in accuracy takes place. The combination would be the perfect solution, but as we will see, cannot be achieved in every performed test, due to different reasons.

Manual [S.2] gives three indicators, that convergence has been reached:

1) The residuals have decreased to a sufficient degree. The solution has converged when the Convergence Criterion for each variable has been reached.
2) The solution no longer changes with more iterations. Sometimes the residuals may not fall below the convergence criterion. However, monitoring the representative flow variables through iterations may show that the residuals have stagnated and do not change with further iterations.
3) The overall mass, momentum, energy, and scalar balances are obtained. The net imbalance should be less than 0.2 of the net flux through the domain when the solution has converged.

Another way measuring the uncertainty of model results is called *Hit Rate* and is defined as shown in the following equation

$$q = \frac{N}{n} = \frac{1}{n}\sum_{i=1}^{n} N_i \tag{5.33}$$

where

$$N_i = \begin{cases} 1 \text{ for } \left|\frac{P_i - O_i}{O_i}\right| \leq D \; or \; |P_i - O_i| \leq W \\ 0 \; else \end{cases}$$

The *Hit Rate* defines a percentage of model results O_i within an allowed range D from measured data P_i where D accounts for the relative uncertainty of the comparison data. "Only those differences are counted that are above a threshold value W which describes the repeatability of the measured data. For comparison with wind tunnel data a hit rate of q > 66 % is demanded, while comparisons with model results or analytic solutions demand a hit rate of q > 95 %" [A.161].

For more information on the application of the *Hit Rate* please compare publications by [A.46], [P.4] and [A.47].

Part II

Pre-Investigation (Analytical - Experimental - Numerical)

Chapter6

Mathematical 1D-Model of a Solar Chimney Power Plant at Fullscale

In this chapter a mathematical 1D-model of a SCPP will be presented. The model has been developed under Microsoft Excel using Visual Basic for Applications (VBA) to give a fast, stable, easy to handle and common tool, which can be executed on every standard computer. The influence of relative humidity, quantity of elements, soil heat flux and the minimal soil temperature on the total energy output have been tested.

6.1 Intention

The intention for designing a 1D-Model of a SCPP is motivated by its complexity in the fluid mechanic and thermodynamic process which needs to be taken into account by modelling such kind of power plant numerically or experimentally. The template for the following work can be found by [A.104] who provided all necessary information to the author. Changes have been done by the author with the permission of the originator.

The program code written under Microsoft Excel and making use of the Excel-Solver gives a fast, stable, easy to handle and common tool which delivers reliable results for different configurations of a SCPP.

Following assumptions have been made for the 1D-Model:

- The thermo-fluiddynamics are modelled within one-dimensional flow tube theory.
- The collector bottom is horizontal with equal ambient air pressure everywhere.
- The solar radiation heat power transfers are modelled one-dimensionally, transverse to the flow.
- Air is assumed as an ideal gas.
- The entire model is approximated as stationary.

Due to the simplified manner night hours are modelled within the program code as hours of the day with a solar irradiation of 1 W/m^2. This gives an error of less than 1 %.

As the start temperature of the soil the variable $T0_{month,i}$ has to be inserted manually. Measurements of the real soil temperatures at a site will give more accurate results for the effective output of the SCPP.

The data for the solar irradiation in W/m^2 and the ambient air temperature in $°C$ have been taken from [A.147] and have been adopted to the program code. These meteorological conditions apply to Sishen, South Africa.

6.2 Excel Solver

The Solver bundled with Microsoft Excel is a powerful analysis tool used for optimization and can be used for business and engineering models. In conjunction with VBA it can be used for solving multiple models which use different input parameters and constraints even more powerful. The pre-installed solver tool is easy too handle and very fast in process time.

Careful handling is a prerequisite by changing the operating system because of a changed behaviour of this black box tool of the Microsoft Office product family.

The aim is to get a steady-state solution for the mass flows of air, temperature for air and soil and the heat fluxes which can be met for all calculations.

This has been achieved by taking care of the convergence via two separate convergence criteria which have been implemented into the program code. The first loop takes care of the temperatures within the SC and has been determined as 0.001. For the second loop over the soil heat flow a value of 0.01 has been chosen as convergence.

6.3 Input Parameter

Tables 6.1 and 6.2 show the input parameters and their corresponding values for the calculations within this chapter.

Table 6.1: Input Parameters - Part 1 of 2

Parameter	Symbol	Unit
Ambient Parameters		
Solar Irradiation	G	kWh/m^2a
Temperature	T_0	°C
Relative Humidity	RH	%
Solar Collector Parameters		
Friction Coefficient of Solar Roof (Glass + Frame Structure)	μ_{roof}	–
Friction Coefficient of Supporting Columns	$\mu_{support}$	–
Turbine and Transition Section Parameters		
Resistance Coefficient at Tube Contraction	ν	–
Efficiency Factor of Turbines	$\nu_{turbine}$	–
Glass Parameters		
Emittance	ϵ_{glass}	–
Light-Transmittance	τ_{glass}	–
Thickness	h_{glass}	mm
Friction Coefficient	μ_{glass}	–

Table 6.2: Input Parameters - Part 2 of 2

Parameter	**Symbol**	**Unit**
	Heat Transfer Coefficients	
Outer Air to Glass	OAtGl	W/m^2
Glass to Outer Air	GltOA	W/m^2
Glass to Soil	GltSo	W/m^2
Soil to Glass	SotGl	W/m^2
Outer Air to Soil	OAtSo	W/m^2
Soil to Outer Air	SotOA	W/m^2
Glass to Inner Air	GltIA	W/m^2
Inner Air to Glass	IAtGl	W/m^2
Inner Air to Soil	IAtSo	W/m^2
Soil to Inner Air	SotIA	W/m^2
Soil to Soil	SotSo	W/m^2
	Solar Chimney Parameters	
Resistance Coefficient	$\nu_{chimney}$	–
	Soil Parameters	
Emittance	ϵ_{soil}	–
Thermal Conductivity	λ_{soil}	W/mK
Mass Density	ρ	kg/m^3
Thickness of Upper Layer	$h_{soil,u}$	m
Thickness of Lower Layer	$h_{soil,l}$	m

6.4 Verification and Validation

The procedure of verification and validation, which has been discussed in general in section 5.5, has been conducted for the program code and the results. Physical and numerical results from other publication, e.g. [A.160] and [T.20], have been taken as a reference.

6.4.1 Influence of Partitions of Solar Collector and Solar Chimney

Although the presented mathematical model does not belong to the group of numerical models we still have to check the modelling parameters foremost the quantity of partitions, which corresponds to the grid size in CFD, of the SC and SCH. It is clear that both can be modelled using only one part or cell. This will affect the calculated temperatures, mass flows and heat fluxes to a great extent. Therefore the required quantity of partitions was calculated when the steady-state had been reached and has been taken as constant throughout all following calculations. The influence on the annual energy output can be found in section 6.6 and the corresponding subsections.

6.4.2 Base Load of a Solar Chimney Power Plant

The SCPP is triggered in first place by the density difference between the inlet at the rim of the SC and the outlet at the top of the SCH. The corresponding velocities and mass flows can be calculated by using *Bernoulli's Principle*. Equation (6.1) shows the *Bernoulli Equation* in its energy form.

$$\frac{p_1}{\rho} + \frac{1}{2}v_1^2 + gz_1 + W = \frac{p_2}{\rho} + \frac{1}{2}v_2^2 + gz_2 - loss = const \tag{6.1}$$

where

$p_{1;2}$ = Pressure in Pa at point 1 and 2 respectively
$v_{1;2}$ = Velocity in m/s at point 1 and 2 respectively
$z_{1;2}$ = Height in m at point 1 and 2 respectively
W = Work done by the turbines in m^2/s^2

The additional energy flux produced by earth's surface will be explained within the next paragraphs. On global average 50 % of the solar irradiation are available at the surface. Therefore the Stefan-Boltzmann law states that every body with a temperature above absolute zero emits energy which is shown in table 6.3 for a body with different temperature and has been calculated by using equation (6.2).

Table 6.3: Radiation Energy of a Body Depending on Its Temperature [B.30]

T [°C]	-20	-10	0	10	20	30
E [W/m^2]	233	272	316	365	419	479

$$E = \sigma T^4 \tag{6.2}$$

The maximum of radiation energy within the spectral range can be calculated by using *Wien's displacement law* given in equation (6.3).

$$\lambda_{max} \times T = b = const \tag{6.3}$$

where

λ_{max} = Wavelength where the spectral radiance becomes maximal
T = Absolute temperature in K
b = Constant of proportionality called Wien's displacement constant

For an effective temperature of the sun of 5,750 K the solar radiant spectrum shown in figure 6.1 peaks at around 0.5 μm. Therefore the average temperature of earth lies at 288 K which results in a peak for the second curve, showing the radiant energy emission, at 10 μm.

This changes of course between different places on earth due to different soil materials, daily temperatures, etc.

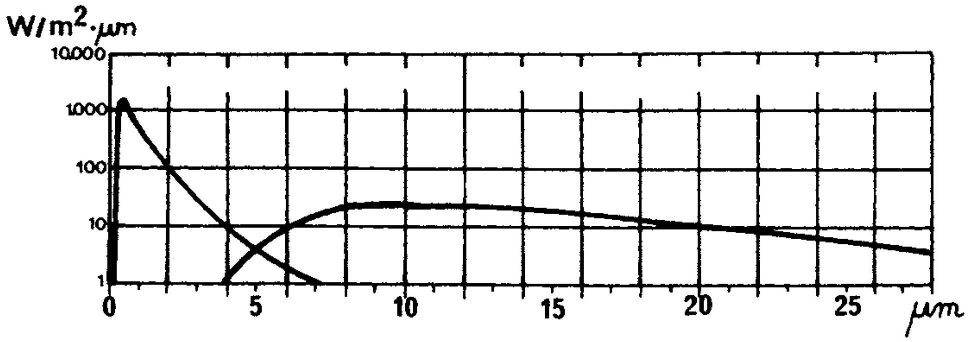

Figure 6.1: Spectral Irradiation and Emission [B.30]

By comparing the calculated radiant energy from equation (6.2) and the effective radiant energy E_{eff} you will notice a discrepancy. Less radiant energy will leave earth's surface as expected after the statement of Stefan-Boltzmann. This originates from the fact of heating up of the atmosphere due to the absorption of long wave length irradiation by the surface and a downward terrestrial radiation. This is commonly known as the *Greenhouse Effect*. Therefore the effective radiant energy can be written as:

$$E_{eff} = E - E_{atm} = \sigma T^4 \times E_{atm} \tag{6.4}$$

where

E_{atm} = Downward terrestrial radiation in W/m^2

Figure 6.2 shows the average yearly heat emission and radiation balance of earth.

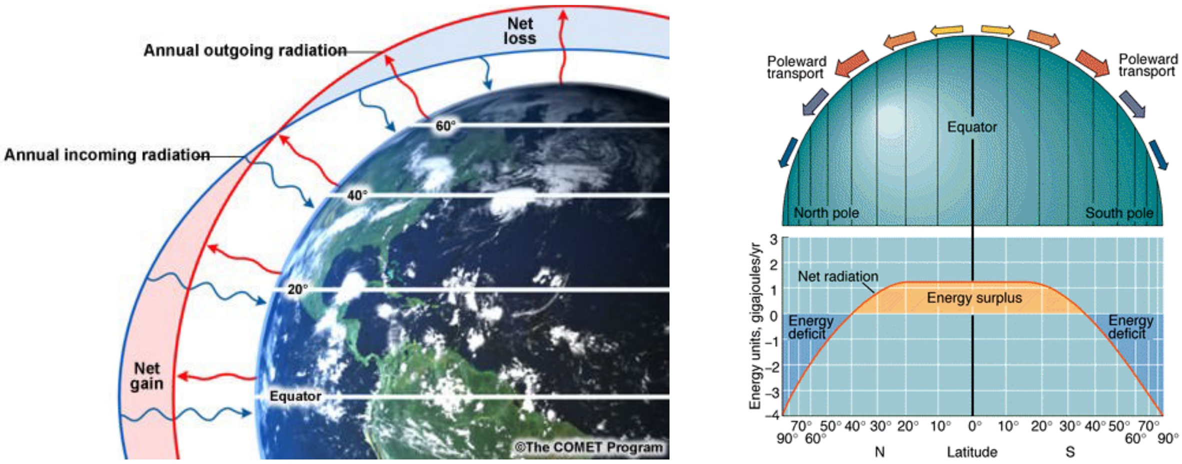

Figure 6.2: Average Yearly Heat Emission and Radiation Balance of Earth [U.7]

Someone can recognize the energy deficit at the poles and the surplus at the equator. The global energy budget is in balance because absorption and emission of the system earth-atmosphere are equal. Due to the transport of heat by air and water currents the meridional exchange between the different regions on earth constant average temperatures can be found within the climate zones.

For the program code used and developed in this chapter this detail will be implemented by monthly average values of the heat fluxes of earth's surface for the chosen site of construction.

Also see [A.52] and [A.150] for more information on this important aspect which not only influences the choice of construction site for a SCPP but the energy output as well.

6.5 Physical Influence Parameters on Energy Output

In this section the influence of air as the fluid material and its properties, ambient wind, the altitude of the construction site, the albedo of the soil material and the temperature inside the SCPP on the energy output will be discussed in detail. Their corresponding formulas and additional figures or tables will be listed here.

6.5.1 Relative Humidity (RH)

The influence of the RH on the density of air will be discussed here which leads to equation (6.5).

$$\rho = \frac{p}{R_f \times T} = \frac{p}{R_{air} \times T} \times \left[1 - \varphi \times \frac{p_d}{p} \times (1 - R_{air}/R_d)\right] \tag{6.5}$$

where

R_{air} = Specific gas constant for dry air in $J/(kg \times K)$, $R_{air} = 287.058\ J/(kg \times K)$
R_d = Specific gas constant for water vapour in $J/(kg \times K)$, $R_d = 461.523\ J/(kg \times K)$
φ = Relative humidity in %
p = Ambient pressure in Pa
p_d = Saturation vapour pressure in Pa (adapted from *Magnus Formula*)

For dry air φ equals zero. The approximation of the saturation vapour pressure above a plane of water can be calculated by using equation (6.6) derived from the *Magnus Formula*.

$$p_d = 611.2 \times \exp\left(\frac{17.62 \times t}{243.12 + t}\right) \tag{6.6}$$

where

t = Temperature in °C in the range of -50°C to +100°C

Another basic formulation of the saturation vapour pressure over water developed by *Wexler* and published in 1976, cf. [A.5] and [A.71], is given in equation (6.7) with its saturation vapour pressure coefficients in table 6.4.

$$ln e_s = \sum_{i=0}^{6} g_i T^{i-2} + g_7 ln T \tag{6.7}$$

where

e_s = Saturation vapour pressure in Pa over water in the range of 0°C to +100°C
T = Temperature in K

This formulation is used for the extension of the program code presented in this chapter. "It is worth noting that the errors discussed in this paper (resulting from the different formula-

Table 6.4: Saturation Vapour Pressure Coefficients

g_i	**Wexlers Coefficients**	**ITS-90** *Scale*[1]
g_0	-2.9912729×10^3	-2.8365744×10^3
g_1	-6.0170128×10^3	-6.028076559×10^3
g_2	1.887643854×10^1	1.954263612×10^1
g_3	$-2.8354721 \times 10^{-2}$	$-2.737830188 \times 10^{-2}$
g_4	1.7838301×10^{-5}	1.6261698×10^{-5}
g_5	$-8.4150417 \times 10^{-10}$	$7.0229056 \times 10^{-10}$
g_6	$4.4412543 \times 10^{-13}$	$-1.8680009 \times 10^{-13}$
g_7	2.858487	2.7150305

[1] International Temperature Scale of 1990 (ITS-90).

tions and approximations) are much less than observational errors in humidity values due to the hygrometers" [A.5].

[A.157] mentions that the vapour pressure of the ambient air has been found as one of the major operational parameter for SCPPs. Besides the small impact on the efficiency of the SCH there is a bigger impact on the SC efficiency. Therefore figure 6.3 gives the monthly average of the diurnal cycle of relative humidity measured at the site of Manzanares for three different month.

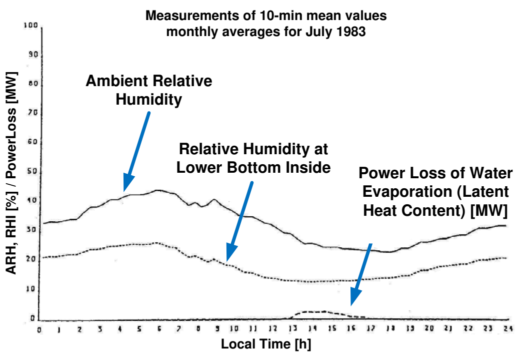

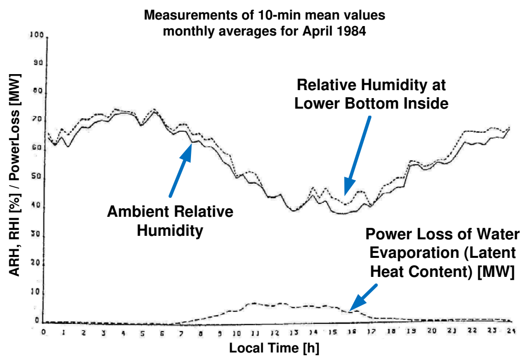

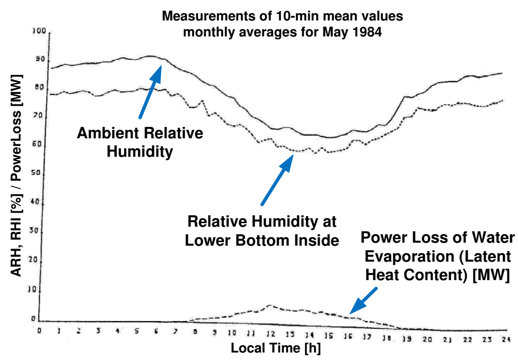

Month/Year	Mai 83	Jun 83	Jul 83	Aug 83	Sep 83	Okt 83	Nov 83	Dez 83
RH min [%]	33.6	-	22.5	30.7	-	23.2	67.9	70.6
RH max [%]	82.4	-	43.8	73.3	-	60.6	97.9	98.8
RH [%]	60.8	-	32.3	48.5	-	41.6	86.1	92.4
P [mm H2O]	1.0	22.5	1.0	8.0	12.0	-	-	-

Month/Year	Jan 84	Feb 84	Mrz 84	Apr 84	Mai 84	Jun 84	Jul 84	Aug 84	Sep 84
RH min [%]	81.9	31.9	-	37.5	64.1	43.4	32.1	29.2	47.5
Rh max [%]	100.0	73.5	-	74.9	92.2	77.0	60.4	67.9	75.4
RH [%]	96.4	55.0	-	56.1	79.4	57.5	44.7	47.1	61.3
P [mm H2O]	40.0	35.7	44.1	84.3	125.4	3.8	2.0	1.7	0.0

Figure 6.3: Monthly Average of Diurnal Cycle of Relative Humidity and Precipitation [A.157]

It can be seen that there is a strong correlation between the relative humidity on the inside and outside of the SCPP system. Also a dependency on the total amount of water inside the ambient air can be found which changes the ratio of relative humidity on the inside and outside.

Additionally, the influence of the temperature gradient underneath the SC on the density of air has been implemented into the program code by using ITS-90 in combination with the relative humidity.

6.5.2 Wind Pressure at Outer Rim of Solar Collector

The effect and influence of ambient wind at the outer rim of the SC plays a decisive role which has not been implemented into the program code due to reasons of simplicity. Nevertheless will this effect be discussed in chapter 7 based on the experimental set-up and results of a wind tunnel model of a SCPP.

6.5.3 Fresh Water Production

Some authors have developed a concept of fresh water production using the humidity of air which runs the turbines of the SCPP. The psychrometry as a field of engineering deals with the determination of physical and thermodynamic properties of gas-vapour mixtures. It can be used to find the dew point temperature of air inside the SCPP system. [B.45] gives the dew point depending on temperature and relative humidity.

If it would be possible to control the precipitation of condensation water within the SCPP, fresh water could be collected at the SCH base to supply people living close to the power plant. If the water would be of bad quality or the effort of transportation would outweigh the benefit it still could be used for cleaning the SC. More on this can be found by [T.20] who discusses the case of fresh water production for the site of Sishen, South Africa.

6.5.4 Altitude

The density change of air with altitude can be calculated by using the *barometric formula* given in (6.8):

$$\rho_z = \rho_0 \frac{T_0}{273.15 + T} \frac{p_z}{p_0} \tag{6.8}$$

where

ρ_z = Density of Air at Height z above Mean Sea Level in kg/m^3
ρ_0 = Density of Air at Height z=0 in kg/m^3, $\rho_0 = 1.225\ kg/m^3$
T_0 = Temperature at Height z=0 in K, T_0=288.15 K
T = Temperature at Height z in $^\circ C$
p_z = Pressure of Air at Height z in mbar
p_0 = Pressure of Air at Height z=0 in mbar, p_0=1013.3 mbar

For the case of Sishen, the altitude is around 1,300 m Above Mean Sea Level (AMSL). More information can be found by [B.2] and [B.18].

6.5.5 Soil Parameters (Soil Heat Flux, Temperature)

The main focus within this chapter lies on the implementation of a more detailed representation of the soil heat flux throughout the annual cycle. Therefore an adjustment of the trends of the soil heat flux for each hour and each month is necessary. Due to the partitioning of the SC, explained in subsection 6.4.1, an adjustment for each element has been performed.

The current approach is oriented at the mean values of yearly heat fluxes from the soil surface in W/m^2, which can be found, e.g. [B.30]. In general they can attain values of 150 bis 200 W/m^2 for high latitudes and increase to 250 bis 300 W/m^2 for tropical regions. So far results have been obtained by using this mean values as a basis whereby peak values have been discarded to receive realistic values.

Figure 6.4 shows the typical variation of soil temperature with depth at different times of a day in summer.

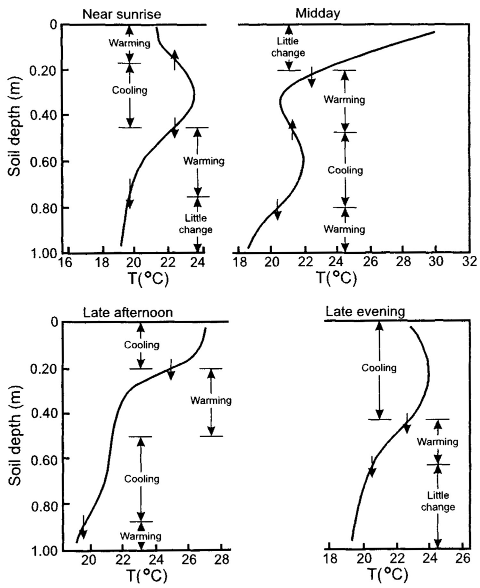

Figure 6.4: Typical Variation of Temperature with Depth at Different Times of Day in Summer [B.19]

It can be seen that only the region close to the surface underlies a strong fluctuation throughout the day. With increasing depth this effect diminishes and the temperature stays nearly constant. The time history of measured and calculated data of stored heat power compared with the global radiation for the case of Manzanares are presented in figure 6.5.

A small shift in the maximal values can be found but the general course looks nearly the same. Peak values of the stored heat power, of course, are a few times smaller than the global radiation. Additionally the thermal energy balance of the ground store for a 5 MW power plant is depicted in figure 6.6.

It shows the extraction of energy from the ground during cold month and the transfer of energy

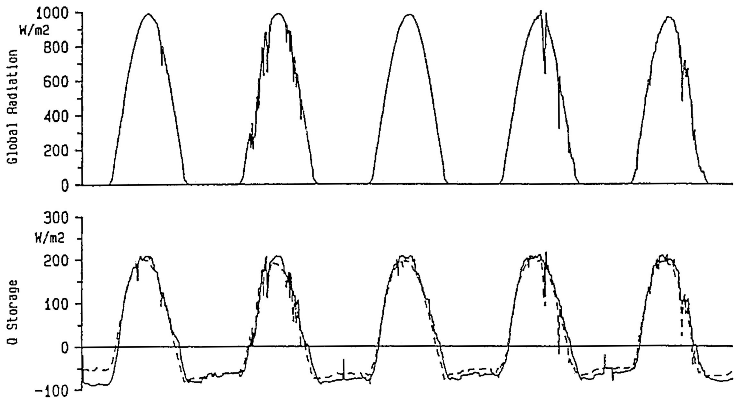

Figure 6.5: Measured Data of Stored Heat Power (Solid - Measured, Dashed - Calculated) [A.160]

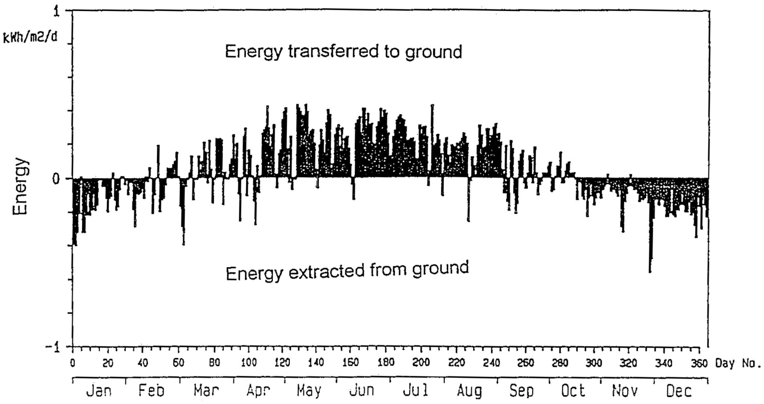

Figure 6.6: Thermal Energy Balance of the Ground Store for a 5 MW Plant [A.160]

to the ground during warm month. The whole energy system is in balance as it has been shown in figure 6.2.

Equation (6.9) gives the *Fourier's equation of heat conduction.*

$$Q_B(z,t) = k' \times \frac{\partial T(z,t)}{\partial z} \tag{6.9}$$

where

$Q_B(z,t)$	= Soil heat flux in W/m^2
T(z,t)	= Temperature in K
z	= Depth (z positive in the direction of the force of gravity) in m
k'	= Thermal conductivity in W/mK
$\partial T(z,t)/\partial z$	= Vertical temperature gradient in K/m

Assumptions for the *Fourier's equation of heat conduction* are:

- Steady state heat conduction
- One directional heat flow
- Bounding surfaces are isothermal in character that is constant and uniform temperatures are maintained at the two faces
- Isotropic and homogeneous material and thermal conductivity k' is constant
- Constant temperature gradient and linear temperature profile

- No internal heat generation.

For the case of transient conditions equation (6.10) is needed to describe the continuity of the heat flux.

$$-\rho c_w \frac{\partial T(z,t)}{\partial t} = \frac{\partial Q_B(z,t)}{\partial z} \tag{6.10}$$

where

ρ = Density in kg/m^3
c_w = Specific heat capacity in J/kgK
t = Time in s

From this (6.9) can be written as

$$\frac{\partial T(z,t)}{\partial t} = \alpha \frac{\partial^2 T(z,t)}{\partial z^2} \tag{6.11}$$

where

$\alpha = \frac{k'}{\rho c_w}$ = Thermal diffusivity in m^2/s

Furthermore it makes sense to develop an equation for a periodically changing temperature at the surface as it is the case on earth under natural conditions. Equation (6.12) gives the heat conduction equation for a periodic temperature profile at the surface.

$$\Delta Q_B(z,t) = \underbrace{-A_0\sqrt{\omega \rho c_w \alpha} \times \underbrace{\exp\left[\frac{-z}{z_D}\right]}_{\text{Damping}}}_{\text{Change in Amplitude}} \times \sin\left[\omega_P(t-t_m) + \underbrace{\frac{\pi}{4} - \frac{z}{z_D}}_{\text{Phase Shift}}\right] \tag{6.12}$$

where

$\Delta Q_B(z,t)$ = Variance of the heat flux in W/m^2
A_0 = Amplitude of temperature at the surface in K
ω_P = Angular frequency of the daily and yearly cycle in $1/s$
z_D = Damping depth in m
t_m = Point in time when T_m is reached in s

The adapted equation (6.13) has been implemented into the program code to calculate the heat conduction for measured values.

$$\begin{aligned} Q_B(z,t) = -\sqrt{\omega \rho c_w \alpha} \times \exp\left[\frac{z}{z_D}\right] \Bigg[(T_0(t) - T_m) \times \sin\left[\frac{\pi}{4} + \frac{z}{z_D}\right] + A_0 \times \cos\left[\omega_P(t-t_m)\right] \\ \times \sin\left[\frac{\pi}{4} - \frac{z}{z_D}\right]\Bigg] \end{aligned} \tag{6.13}$$

where

$Q_B(z,t)$ = Heat flux depending on depth and time in W/m^2

T_m = Mean temperature in K

$T_0(t)$ = Temperature of the surface depending on time in K

The heat flux can be divided into a high frequency daily and low-frequency annual course. Both values will be added together for each time step which results in a total heat flux.

More on this can be found by [T.2] and [B.33].

6.5.6 Albedo

The albedo explained in subsection 4.1.2 alters the soil temperature profiles as can be seen in figure 6.7.

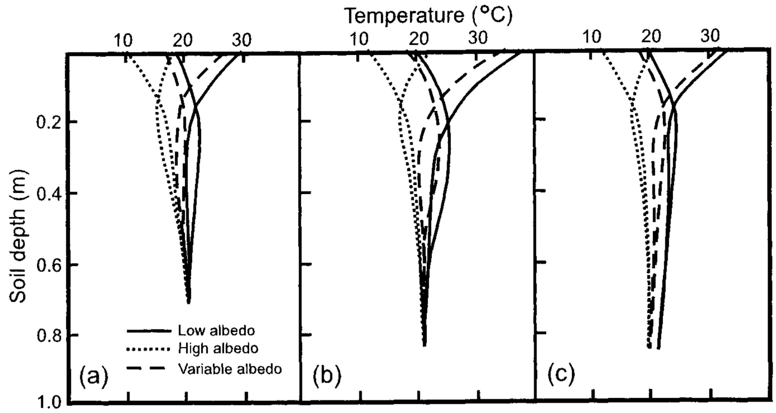

Figure 6.7: Soil Temperature Profiles at Midday and at Midnight Under Different Albedo Conditions [B.19] (a) 2nd, b) 6th, c) 10th day of simulated evaporation)

In general, higher soil temperatures for depth close to the surface can be found throughout all graphs for the three albedo conditions. With decreasing albedo the maximum soil temperatures increases. The time course of soil temperature at three depth for a small period are depicted in figure 6.8 for three values of surface reflectivity.

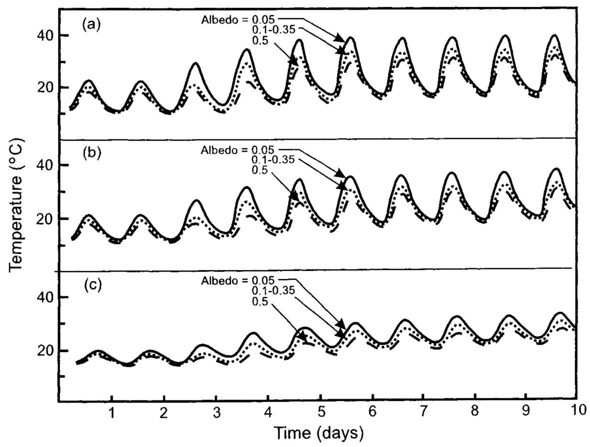

Figure 6.8: Time Course of Soil Temperature at Three Depths for Different Surface Reflectivity [B.19] (a) at surface, b) in seedbed, c) below seedbed)

For the shown period a general increase in temperature can be found and the daily gradient between the highest and lowest temperature increases, too.

6.5.7 Minimal Temperature of Soil Underneath the Solar Collector

The effect of a limiting value for the soil temperature has been investigated, covering a small but realistic range of 10 to 12 $°C$. This is mainly due to the lack of additional data for the construction site of Sishen.

6.6 Results

In this section the results of the program code for four different variants of a SCPP under different conditions will be presented. The annual energy output will be compared because the course of energy production for each month, which is the benefit of this programmed code, can only be found within a few publications. This makes it difficult to compare a calculated monthly value with the result from another source.

The results have been verified and validated with data from other computational and experimental results and have shown a good match. Also the maximum and minimum of the reached temperatures underneath the SC have been checked for each variant to control the reliability of the program code. Table 6.5 shows the parameters for the four used variants. The height of the SCH, the diameter of the SC and the glass cover have been varied.

Table 6.5: Parameters of the Four Variants

Variant	Height of Solar Chimney	Diameter of Solar Collector	Glass Cover
-	m	m	-
A	500	2,000	single glazed
B	750	3,500	single glazed
C	500	2,000	double glazed
D	750	3,500	double glazed

6.6.1 Influence of Relative Humidity

The influence of the RH on the annual energy output is presented. Therefore table 6.6 gives the results for the four variants taking into account the RH and the case without considering RH.

A comparison with data from [T.3] shows that the effect of the RH on the annual energy output is implemented correctly. The obtained deviation given for each variant in the last column of the table shows that the effect on the annual energy output is diminishing small and lies in the range of ≤ 1.6 %. For the presented variants it has an decreasing effect on the energy output. One cannot rule out the possibility that there are constellations where it will have an positive effect on the energy output.

Table 6.6: Influence of Relative Humidity on Annual Energy Output

Variant	Without RH	With RH	Deviation
-	GWh	GWh	%
A	49.659	49.328	-0.7
B	193.975	191.616	-1.2
C	79.493	79.176	-0.4
D	347.953	342.317	-1.6

6.6.2 Solar Collector Partitions

The influence of elements or partitions of the SC have been investigated to clarify if there is any change in the annual energy output. In its simplest way the SC could be represented with only one element which has not been investigated here. The basic version consists of nine equally sized elements and has been increased to 18 and 19. Table 6.7 shows the results and the respective deviation.

Table 6.7: Influence of Solar Collector Partitions on Annual Energy Output

Variant	9-Elements	18-Elements	19-Elements	Dev. 18-Elements	Dev. 19-Elements
-	GWh	GWh	GWh	%	%
A	49.328	49.204	49.333	-0.3	-0.1
B	191.616	189.997	191.393	-0.9	-0.1
C	79.176	80.878	80.726	$+2.1$	$+1.9$
D	342.317	346.171	348.428	$+1.1$	$+1.8$

The absolute change in annual energy output is for all investigated cases ≤ 2.1 %. It can be stated that at a particular element size, meaning the reduction of the element quantity below a certain level, a convergence of the results cannot be achieved. Therefore, as generally known from CFD analysis, an upper boundary for the element size has to be met to gain reliable results. In this case for all following calculations a minimal quantity of nine elements has been used.

6.6.3 Solar Chimney Partitions

The influence of elements of the SCH on the annual energy output has been investigated. Therefore four configurations have been tested with changing quantity of elements for the SC and SCH respectively. Table 6.8 collects the results where, e.g. 18/9, stands for 18 Elements for the Solar Collector/9 Elements for the Solar Chimney.

Table 6.8: Influence of Solar Chimney Partitions on Annual Energy Output

Variant	18/9-Elements	18/18-Elements	Dev.	19/9-Elements	19/18-Elements	Dev.
-	GWh	GWh	%	GWh	GWh	%
A	49.204	49.205	±0.0	49.333	49.333	±0.0
B	189.997	189.969	±0.0	191.393	191.365	±0.0
C	80.878	80.865	±0.0	80.726	80.713	±0.0
D	346.171	346.126	±0.0	348.428	348.382	±0.0

The results support the conclusion that there is no influence of the quantity of SCH elements on the annual energy output even for less than the minimum of nine elements. This is due to the fact that the SCH has been taken as an adiabatic wall and only the friction loss has been implemented into the program code which does not change with the quantity of elements.

6.6.4 Soil Heat Flux

The soil heat flux has been implemented into the program code as described in subsection 6.5.5. The case of constant heat flux is used as reference. Table 6.9 shows the results for (i) a constant heat flux, (ii) a variable daily heat flux, (iii) a combined variable heat flux for day and year, both cases without a base load and last but not least (iv) the combination of a variable heat flux for day, year and a changed base load.

Table 6.9: Influence of Soil Heat Flux on Annual Energy Output

Variant	Constant Heat Flux	Variable Heat Flux (day)	Deviation	Variable Heat Flux (day+year)	Deviation	Variable Heat Flux (d+y+b)	Difference
-	GWh	GWh	%	GWh	%	GWh	%
A	49.328	24.506	-50.3	25.059	-49.2	49.778	+0.9
B	191.616	94.141	-50.9	92.542	-51.7	193.234	+0.8
C	79.176	45.165	-43.0	47.316	-40.2	85.318	+7.8
D	342.317	201.441	-41.2	209.275	-38.9	376.350	+9.9

b = Base load.
d = Day.
y = Year.

The results show, that the change in annual energy output for the different cases is smaller than expected. The first two cases show the huge impact of the base load on the gained results. If the variability of the heat flux is modelled for the day or day + year therefore plays a minor role. Concluding, that results without taking into account the base load underestimate the annual energy output by not less than 50 %. The total base load has not been changed for the first two simulations A and B. For C and D a smaller value for the base load has been implemented which leads to a deviation in results. Looking at the daily and monthly courses of the calculated energy output, which will not be presented in this work, it has been found that the calculation of the soil heat flux for each day and year respectively has the big advantage of gaining reliable results for each hour and not only for the total amount per year. Also a shift of the maximum energy that can be harvested for each month can be found. The maximum is shifted from June to September, which shows a more realistic representation of the real soil behaviour, cf. [T.2].

The additional computational effort for the implemented calculation of the soil heat flux for each hour is worth the benefit you are getting from the results especially when the course of energy production is taken for the design of a grid delivering the energy to the connected households. This effort can be even more reduced by using Visual Basic Script (VBS) to start the VBA routine in batch mode.

6.6.5 Minimal Soil Temperature

The lowest soil temperature that can be reached throughout the year is called minimal soil temperature. For the case of Sishen in South Africa this parameter has been varied for only two temperatures, namely 10 and 12 $°C$. The results are presented in table 6.10.

Table 6.10: Influence of Minimal Soil Temperature on Annual Energy Output

Variant	$10°C$	$12°C$	Deviation
-	GWh	GWh	%
A	24.506	25.536	+4.0
B	94.141	98.218	+4.3
C	45.165	46.726	+3.5
D	201.441	208.374	+3.4

A reduction to a minimal soil temperature of $8°C$ is not necessary because the average temperatures at the given site are always higher throughout the whole course of the year. As expected an influence on the annual energy output due to the changed minimal soil temperature has been found. The difference lies in the range of 4 % and therefore cannot be neglected. If measured data are available the possible temperature values should be determined and different runs with changed temperature values should be performed to gain a realistic range for the annual energy output.

6.7 Conclusion

The presented results show that the developed program code is a good approach of the real power plant. Reliable and realistic results can be obtained and have been cross-checked with other results from computational and experimental studies. The current model is fast and only less computational effort is needed. Additionally, the commonly known and used tool VBA of Microsoft Excel does not need any knowledge about CFD software and therefore is easy to handle. The batch mode VBS provides the possibility of saving computational cost and gives the opportunity of queuing different runs at once.

The gained results will be used to develop a more sophisticated approach of a SCPP taking into account 2D and 3D effects, ambient wind conditions, a detailed reproduction of the transition section, to name only a few parameters, and will be presented within the next chapters.

Chapter7

Wind Tunnel Studies at Stellenbosch, South Africa

This chapter summarizes the work on a wind tunnel model of a SCPP at the wind tunnel facility at Stellenbosch University, South Africa. PIV and pressure measurements have been performed and the PIV results are presented here. The set-up of the model and measuring equipment and also the procedure for camera calibration will be explained in detail. Two mass flows, one produced by the wind tunnel representing the ambient wind field and a second one inside the SCH have been modelled. Both are in a range of 5 to 20 m/s while the results are given for different ratios and three different measuring planes respectively. Preliminary tests have been performed to get best results for the PIV measurements and reduce flashing up of the laser light on the taken flow field pictures.

7.1 Range of Simulations

Two different models have been tested at the wind tunnel facility in Stellenbosch. Due to flashing up effects of the laser light on the taken flow field pictures during the preliminary tests, Model I has been used for the calibration procedure of Model II only. Therefore no results for Model I will be presented in the course of this work. All details to the two designed models and the wind tunnel at Stellenbosch are gathered in appendix B. Table 7.1 shows the configurations for the tests of Model II.

Table 7.1: Configurations Model II

Laser Position	**Velocity WT** v_{wind}	**Velocity Tube** v_t	**Cameras**	**Repetition Measurement**
-	m/s	m/s	-	-
Horizontal (0 mm)	5, 10, 20	5, 10, 15	2	yes
Horizontal (12 mm)	5, 10, 20	5, 10, 15	2	yes
Vertical	5, 10, 20	5, 10, 15	1	yes

Three different layers, three different velocities v_{wind}, representing the wind speed, and three velocities v_t, which have been derived from a measured mass flow inside the chimney, have been combined and results will be presented within the next sections. A velocity v_t inside the tower of 5 m/s correspond to a mass flow of $\dot{m}_{venturi} = 0.021$ kg/s under normal ambient conditions, $v_t = 10$ m/s to $\dot{m}_{venturi} = 0.042$ kg/s and $v_t = 15$ m/s to $\dot{m}_{venturi} = 0.063$ kg/s respectively. The horizontal level of 0 mm corresponds exactly to the middle of the turbine openings whereas the horizontal level of 12 mm is moved upwards. Hereby a better interpretation of the three-dimensionality of the flow structure was targeted.

7.1.1 2D Particle Image Velocimetry (PIV)

For the measurement of the velocities and the spatial distribution within the three measuring planes a 2D PIV system with a dual power laser from Dantec Dynamics has been used. A traversing mechanism for the laser was used to adjust the position of the laser plane.

More information about the laser, the seeding generator and the flow sense cameras are listed in section B.5 of the appendix. General information about the basics of PIV measurements and former research which has faced similar problems than the current one can be found at [P.1], [P.2], [B.36], [A.108] and [A.175].

Two seeding positions for the two seeding generators were tested to find the best distribution of the droplets at the measuring plane. One position at the inlet of the wind tunnel facility and one close to the collector inlet. Both positions are depicted in figure 7.1.

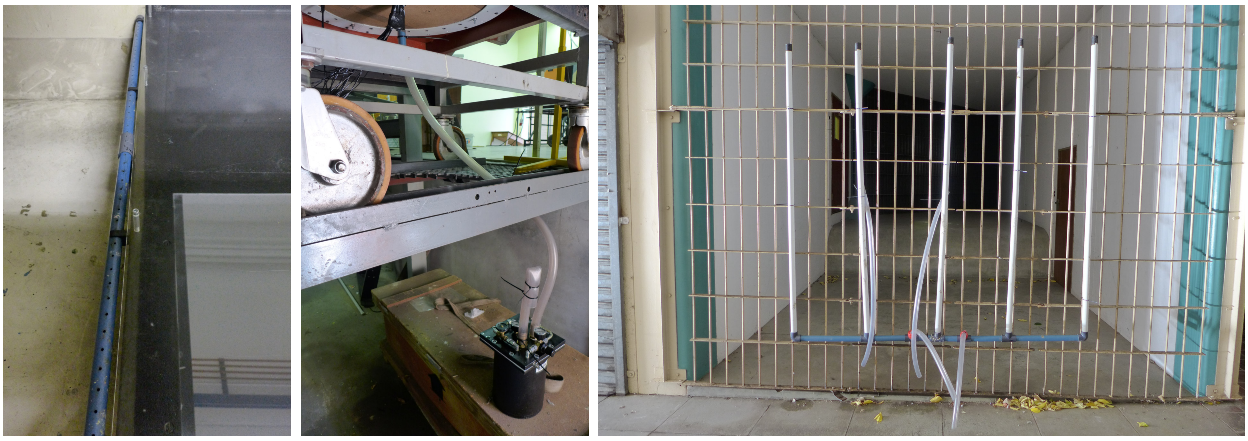

Figure 7.1: Seeding Positions (Collector Inlet (left), Inlet of the Wind Tunnel Facility (right))

As seeding material conventional gear lubricant oil was used which leads to an average droplet size of 2 μm. It was found that by placing the seeding right in front of the collector inlet due to the kind of divider, therefore a normal pipe was prepared with small holes in a certain grid, the distribution was very poor at the measuring plane. The results from the PIV measurements showed that the process of mixing was not finished at all and streamlines coming from every hole could be detected. Therefore a position right at the inlet of the wind tunnel was chosen as seeding position.

7.1.2 Volume/Mass Flow Measurements

To ensure a constant mass flow through the chimney a *venturi flow meter* has been built relying on the international codes [S.5], [S.6] and [S.7] for the measurement of fluid flow by means of pressure differential devices inserted in circular cross-sections conduits. In section B.3.1 of the appendix the *venturi flow meter* used at Stellenbosch is shown.

7.2 Calibration

The calibration data of the pressure transducers used for the pitot static tube and all pressure points are collected in section B.4 of the appendix. Temperature and RH have been measured in an adjoined room of the university. Pictures of the location of the pitot static tube and the arrangement of the PIV system can be taken from sections B.3.3 and B.3.4 respectively.

7.3 Analysis of PIV Data

For the analysis of the PIV data DynamicStudio(R) V3.41.48 from Dantec Dynamics has been used. The raw data files have been filtered using peak, moving and range validation filters to sort out false and unrealistic values. In figure 7.2 the analysis tree which has been applied to all measurements is depicted.

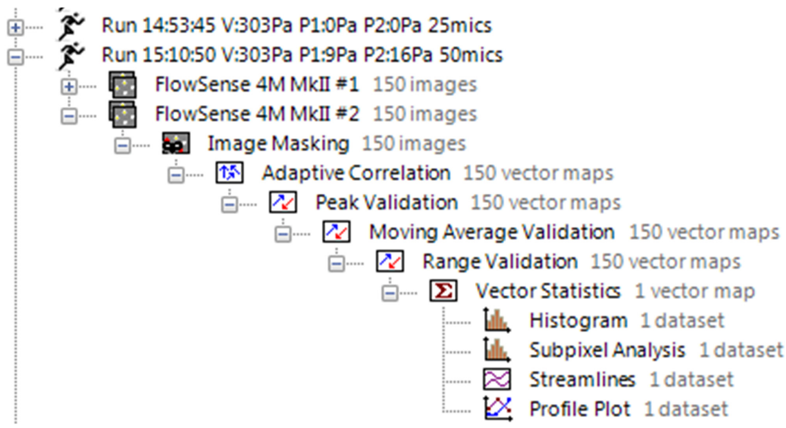

Figure 7.2: Analysis Tree

7.3.1 Validation

The manual of Dantec Dynamics states that reliable and independent data can be obtained if at least 20 values for each configuration have been saved and used for the analysis. Fortunately we had 150 images for each of the three runs. Therefore a comparison between each run and a combined one has been conducted. Figure 7.3 shows exemplarily the opposed results for 150 and 450 images respectively for one configuration.

As can be seen there are only marginal differences between these two results. Also the histograms are given which show the quality of the gained results for each pixel or data point within

150 Images	**450 Images**

Velocity Vectors

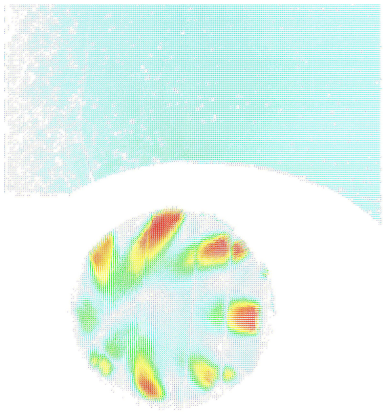

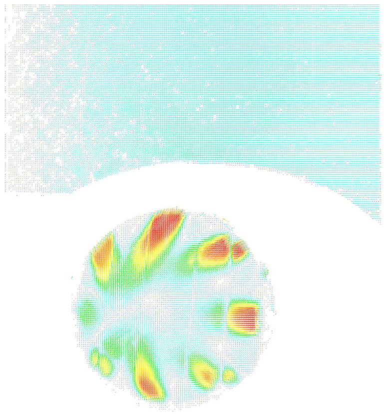

Histogram

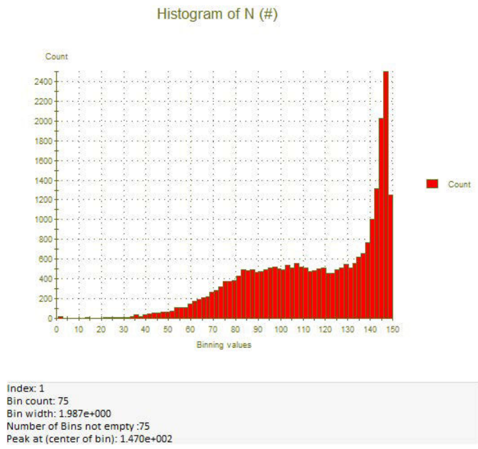

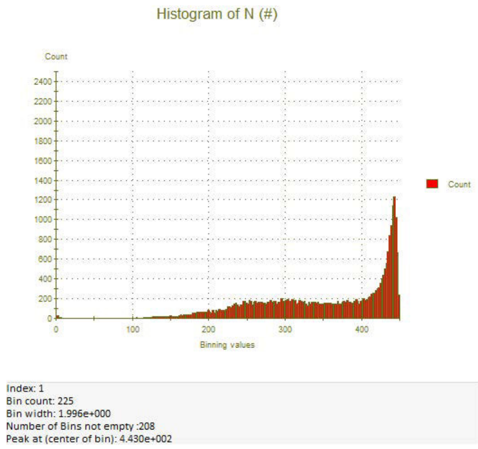

Figure 7.3: Influence of Number of Samples

each image. The range of the measurements is 2,048 x 2,048 pixels. For most of them nearly all images could be used for the final graphic of the velocity vectors. Even here the global appearance looks similar for both data series. The results also show that a mask had to be put on the area close to the tower because of flashing up of the perspex during the measurements. Also it would have been helpful to have results around the circumference of the tower, the focus lies on the flow field on the inside of the tower and therefore did not influence the following measurements.

7.3.2 Results

For the interpretation of the results, which will be presented within this subsection, it is of major importance to deliver a small explanation beforehand. Maximum values of all images are dependent on the used filters, which has been explained before. Therefore it has been proven beforehand that the repetition measurements show similar results and that the histogram states that the found maximum values are reliable. The more measuring data can be found for one pixel and only less need to be discarded the more reliable is the calculated value.

The velocity vector distributions for all combinations of free stream and tube velocities v_{wind}/v_t for the upstream velocity field matches the readings from the pitot static tube and are listed in figure B.13 of the appendix. Close to the tower circumference an effect on the velocity distribution can be found. For a free stream velocity of $v_{wind} = 5$ and 10 m/s nearly all vectors show a constant reading for all images. For the highest free stream velocity of $v_{wind} = 20$ m/s an effect of the tower on the upstream velocity distribution due to an impoundment of the air parcels independently of the tube velocity exists.

Furthermore a discussion of the results for the three investigated planes will take place. The results for all repetition measurements are listed here or in the appendix to illustrate that deviations between the three results can occur which can lead to false interpretation. Therefore repetition measurements are more than necessary to prove the reliability of the gained results.

Figure 7.4 shows the velocity vectors for the case of $v_t = 15$ m/s and zero free stream velocity v_{wind}.

Measurement	**First Repetition**	**Second Repetition**
m/s	m/s	m/s

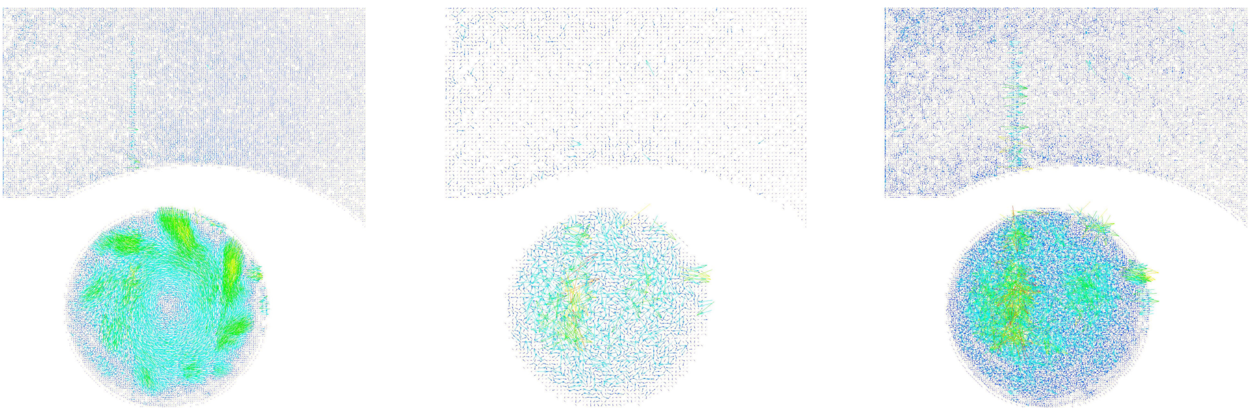

v_t **= 15 m/s,** v_{wind} **= 0 m/s**

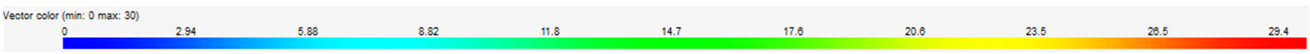

Figure 7.4: Results Horizontal Level 0 mm (Flow From Right to Left) - Part 1 of 2

It is obvious that although the boundary conditions have been the same for all three measurements the results do not reflect this fact. This is traced back to the occurrence of a small current within the wind tunnel due to its direct connection to the ambient. As a consequence results without any free stream velocity v_{wind} will not be presented for the other configurations and measuring planes.

Figure 7.5 shows the results for different ratios of the velocity streams for the horizontal level of 0 mm.

Except one image ($v_t = 15$ m/s, $v_{wind} = 10$ m/s) all repetition measurements fit to the original measurement. This could be affiliated to a wrong set-up of v_{wind} or a different filter and will be neglected for all further interpretation. All images show the entering air flow through the turbine holes into the chimney interior. With increasing tube velocity the impact length into the

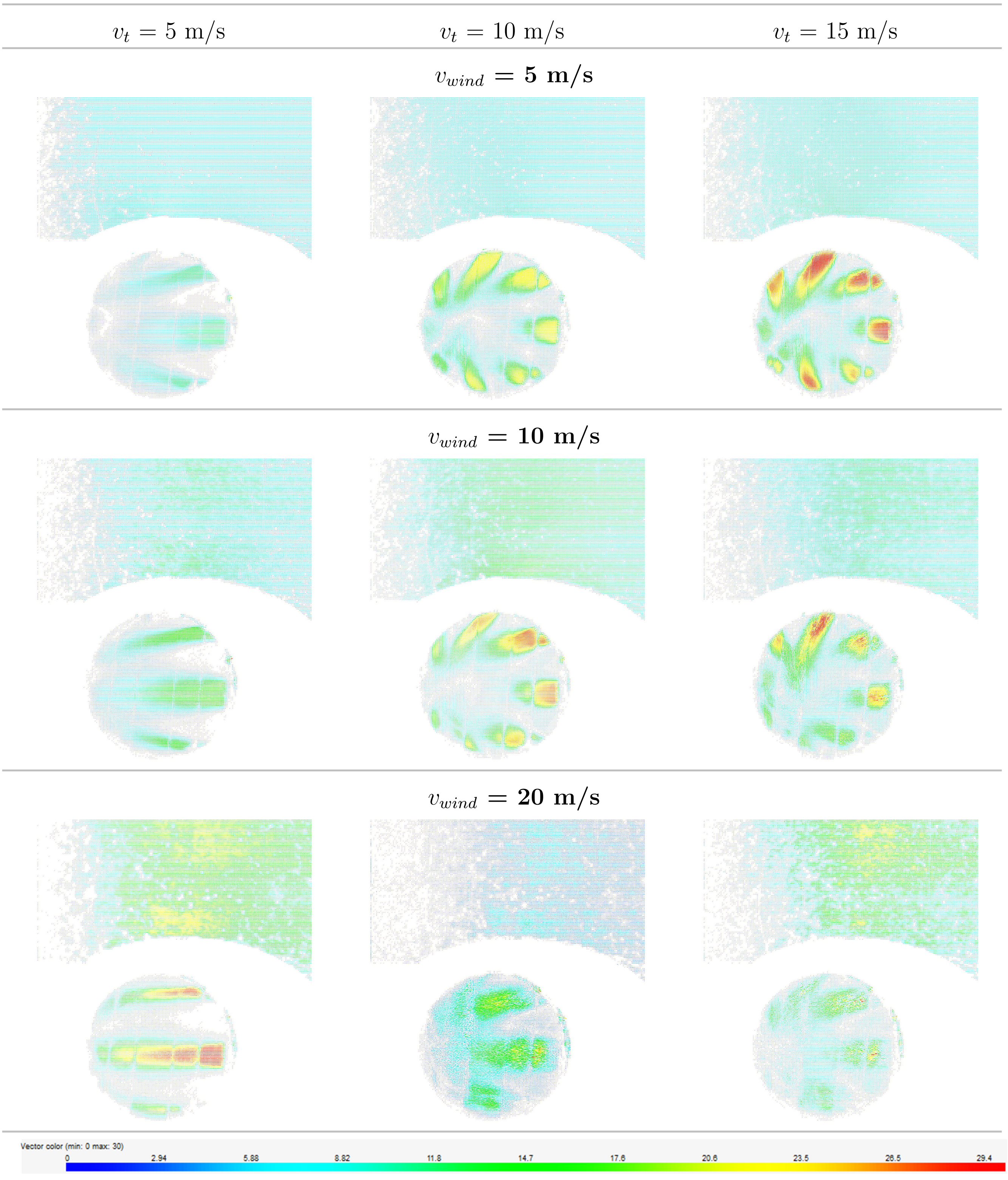

Figure 7.5: Results Horizontal Level 0 mm (Flow From Right to Left) - Part 2 of 2

chimney decreases and the maximum velocity increases. This is due to the faster diversion inside the chimney. The width of each single flow stream also decreases due to the suction through the chimney. For a small free stream velocity all eight opening jets can be found. At v_{wind} = 20 m/s only three jets on the windward side entering the chimney are visible on the images. This matches the ambient flow field of a circular cylinder with suction on the lee-side. This supports the conclusion that the flow field inside the turbine openings is far away from being symmetrically. Even for a small impact from the ambient flow field a diversion of the flows through the turbine openings in the direction of the wind direction can be found.

For a better understanding of the spatial distribution of the velocity field even into the vertical direction figures 7.6 and 7.7 illustrate the results for the horizontal level of 12 mm.

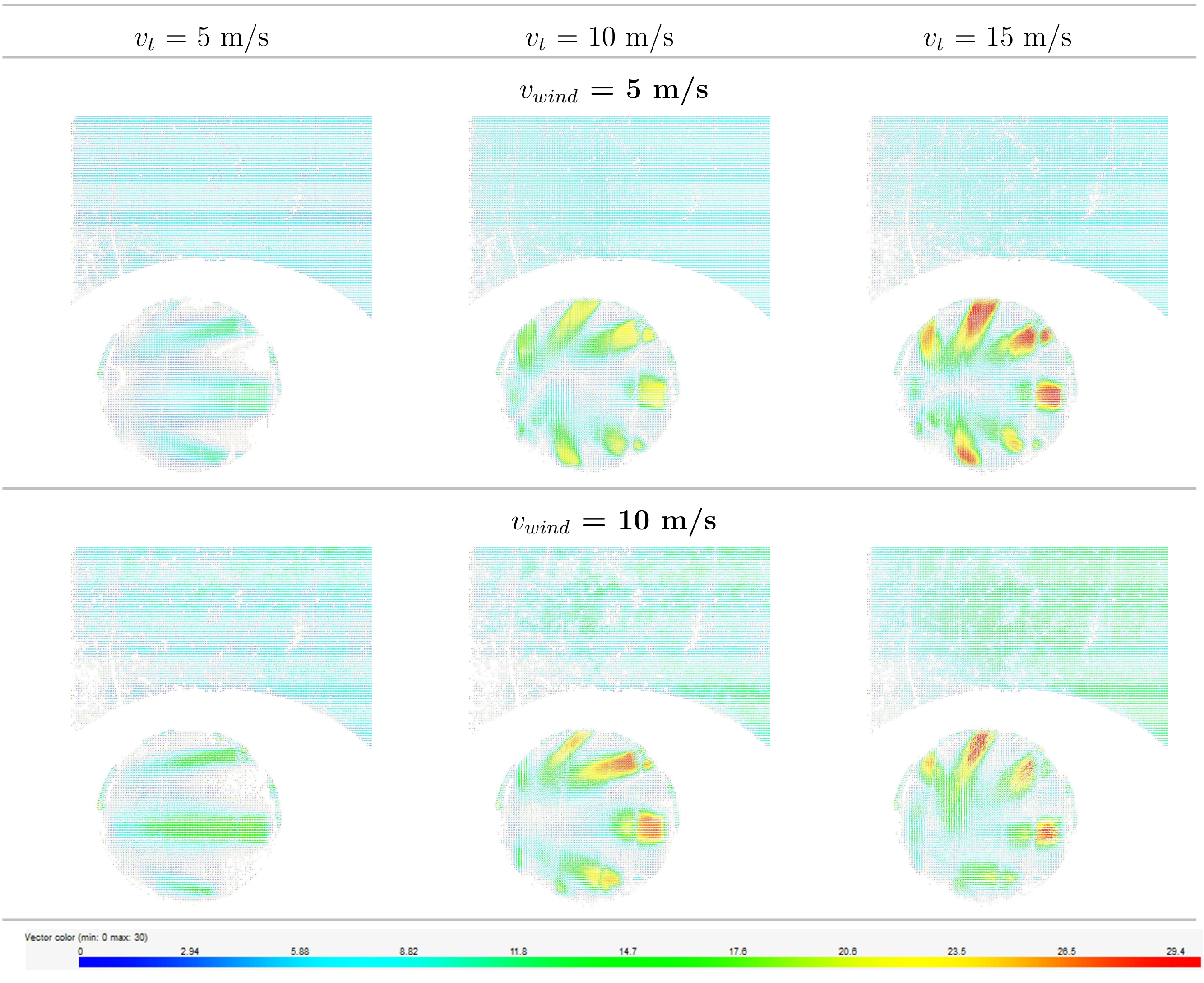

Figure 7.6: Results Horizontal Level 12 mm (Flow From Right to Left) - Part 1 of 2

There are only marginal changes between both horizontal levels for small internal and external flow speeds. Due to the diversion of the flow streams entering the tower into the vertical direction, changes in the entering length and the maximum velocity can be found for higher velocities.

The velocity distributions for the vertical plane are depicted in figures 7.8 and 7.9.

Inside the chimney the diversion from the horizontal into the vertical direction can be seen close to the lee side of the tower wall. With increasing tube velocity the flow stream gets diverted faster after entering the chimney through the turbine openings. Also the width of the stream widens with both increasing tube and free stream velocity. The diversion into the vertical direction can also

$v_t = 5$ m/s	$v_t = 10$ m/s	$v_t = 15$ m/s

v_{wind} **= 20 m/s**

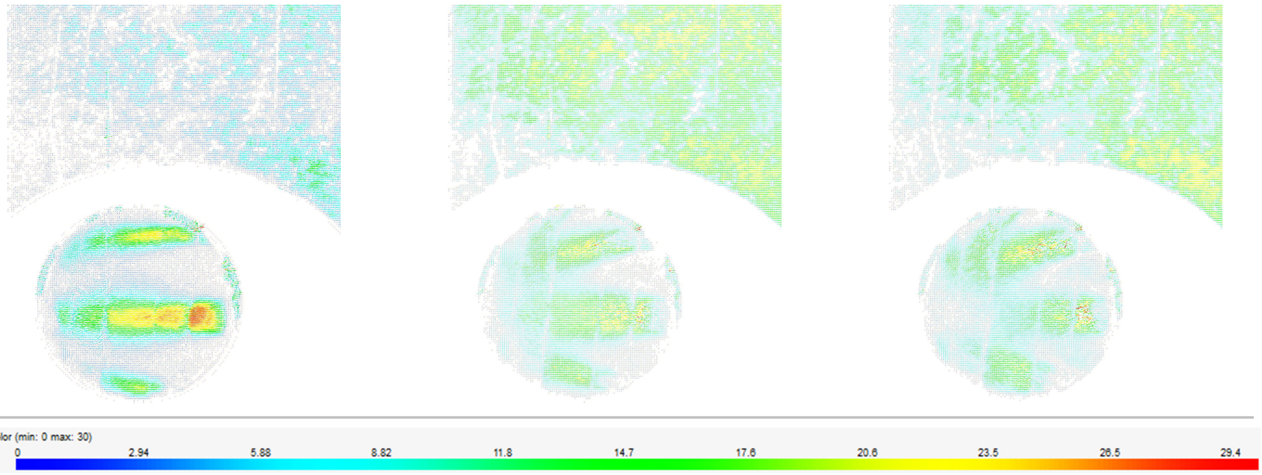

Figure 7.7: Results Horizontal Level 12 mm (Flow From Right to Left) - Part 2 of 2

$v_t = 5$ m/s	$v_t = 10$ m/s	$v_t = 15$ m/s

v_{wind} **= 5 m/s**

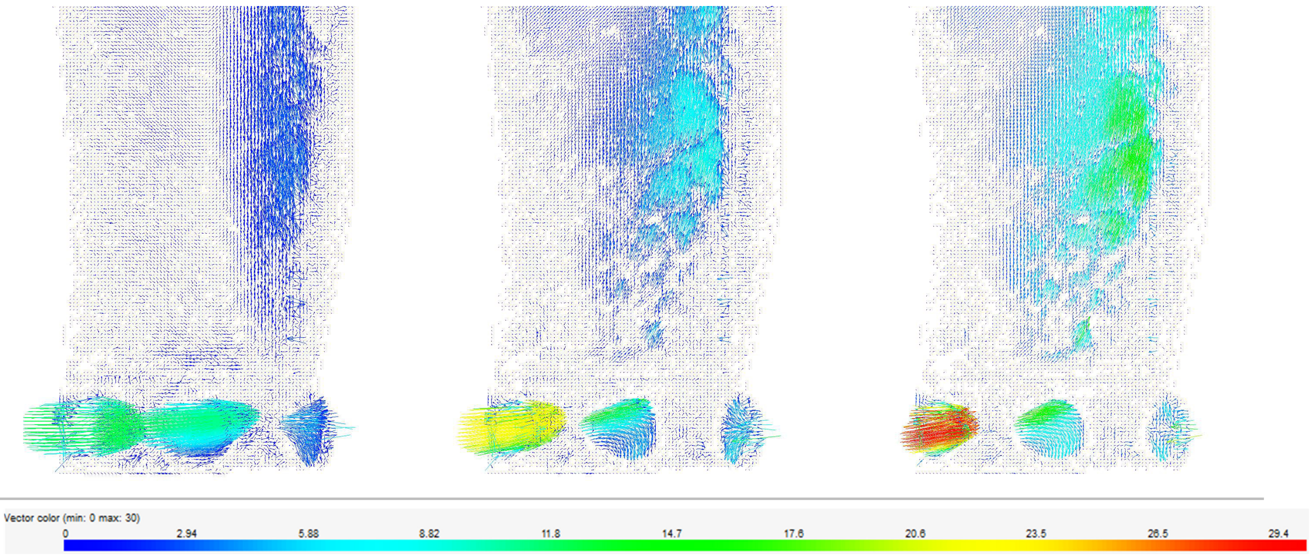

Figure 7.8: Results Vertical Centre (Flow From Left to Right) - Part 1 of 2

be seen by looking at the velocity vectors directly at the openings. Both the maximum velocity and the diversion angle increase for the case of increasing free stream or/and tube velocity.

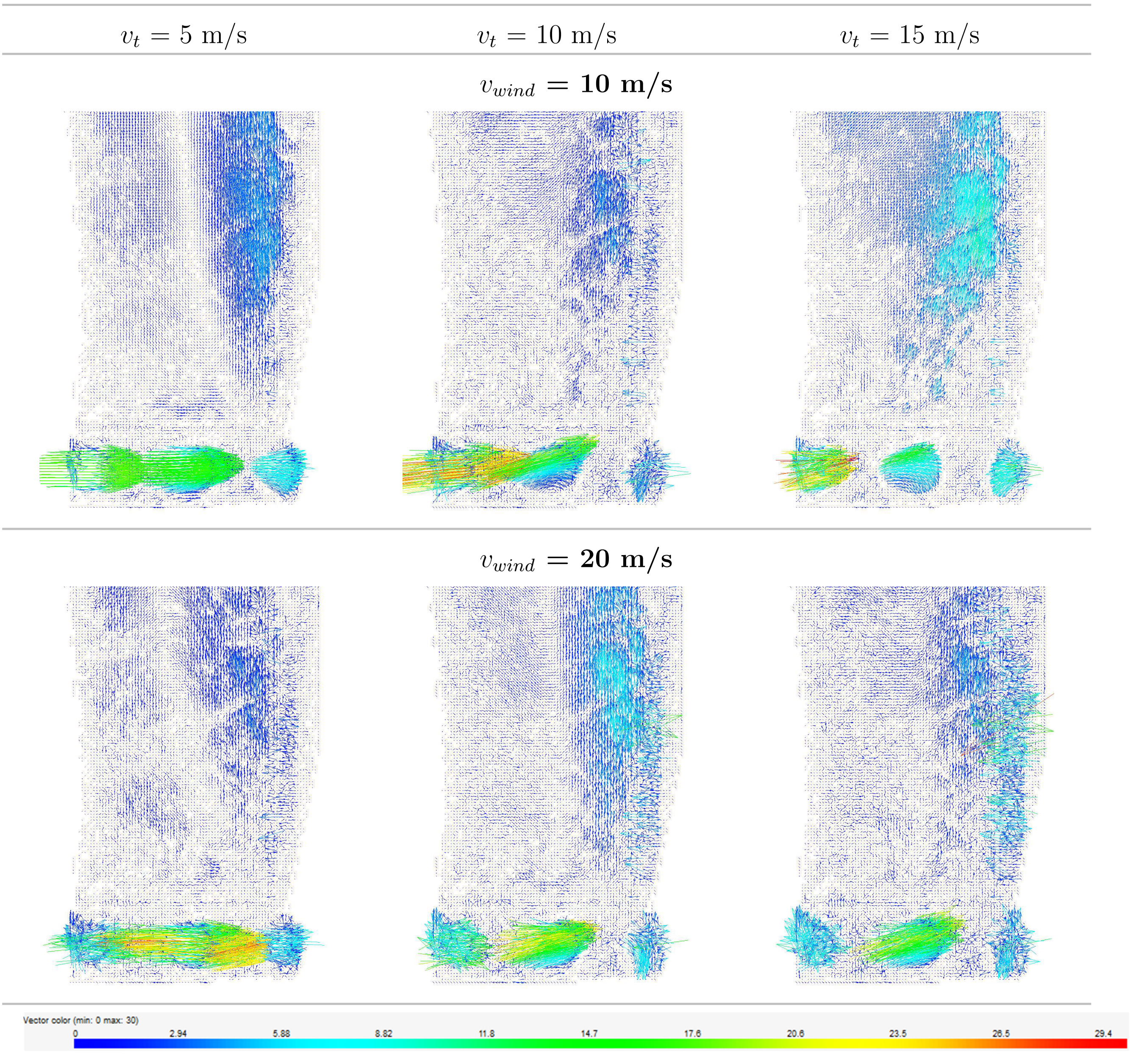

Figure 7.9: Results Vertical Centre (Flow From Left to Right) - Part 2 of 2

7.4 Conclusion

The influence of ambient wind and a second flow within the SCH model on the distribution inside the transition section has been investigated. It has been found that there is a dependency of the velocity distribution on v_{wind} or the ratio v_{wind}/v_t. The influence of the windward turbine openings on the flow field increases with increasing v_{wind} or v_{wind}/v_t respectively. In contrast to former research and the general assumption that the flow field within the transition section is symmetric, the tests have shown the complete opposite. Only for the case of zero ambient wind the distribution follows this assumption. Therefore it is of major importance to investigate the influence and effect of this finding on the flow field within the whole SCPP and especially within the lower part of the SCH which will be effected most. Also the effect of an installation for redirecting the flow on the general flow behaviour shall be looked into in more detail. Both will be done on the basis of a numerical analysis of the prototype SCPP of Manzanares in chapter 9 and with the aid of an improved model, which will be presented in part III.

Chapter8

CFD Analysis of the Wind Tunnel Model from Stellenbosch

This chapter deals with the numerical analysis of the wind tunnel model presented in the former chapter 7. Two models have been set-up, one with the commercial ANSYS Fluent software and one with the open source Fire Dynamics Simulator (FDS) tool. The latter one was taken as a reference due to some advantages over ANSYS Fluent but was disregarded later. A mesh study, a comparison between the turbulence models k-ϵ and k-ω and the influence of boundary conditions on the gained results were performed.

8.1 Model Set-Up, Main Parameters and Results

The dimensions of the computational model fit exactly the experimental dimensions of the wind tunnel model presented in the previous chapter. Two CFD models have been set up, one with the commercial ANSYS Fluent software and one with the open source FDS tool. For both models a mesh study has been performed and general flow parameters have been checked for convergence. While FDS uses LES for modelling the flow, in ANSYS Fluent the k-ϵ and k-ω turbulence models were chosen. Due to the different approaches of meshing used in ANSYS Fluent and FDS the influence of structured or unstructured meshes on the total amount of cells and the results have been compared.

8.1.1 ANSYS Fluent

The calculation parameters for the ANSYS Fluent computation are listed in table 8.1.

The simulation time of 3 seconds reaches the stationary range of the flow on the inside of the SCPP model. This has been checked by the time course of the mass flow leaving the tower outlet.

Figure 8.1 shows a contour plot and the unstructured grid of the ANSYS Fluent model.

A mesh study for four different maximum element sizes has been performed and the quantity of nodes and elements is given in table 8.2.

In table 8.3 the gained results for the mass flow, velocity and pressure for two planes and y^+ values are listed. Plane 1 corresponds to the horizontal level of 0 mm and plane 2 to 12 mm respectively, as it has been introduced within the previous chapter.

Someone can see that the change in mass flow at the tower outlet, the velocity and pressure

Table 8.1: Calculation Parameters ANSYS Fluent

Parameter	**Current Study**
Precision	Double Precision
General	Transient + Gravity
Models	k-ϵ (Standard or Realizable, Standard Wall Functions) + Energy
Boundary Conditions	Velocity Inlet, Pressure Outlets (Tower, Domain), Walls
Solution Methods	Simple, Least Square Cell Based, Second-Order
Report Plots	Mass Flow Stream on Tower Outlet
Convergence Criteria	$1e^{-6}$ (Energy) and $1e^{-3}$ (other Residuals)
Time Step Size	0.01÷0.001
Simulation Time	3 sec

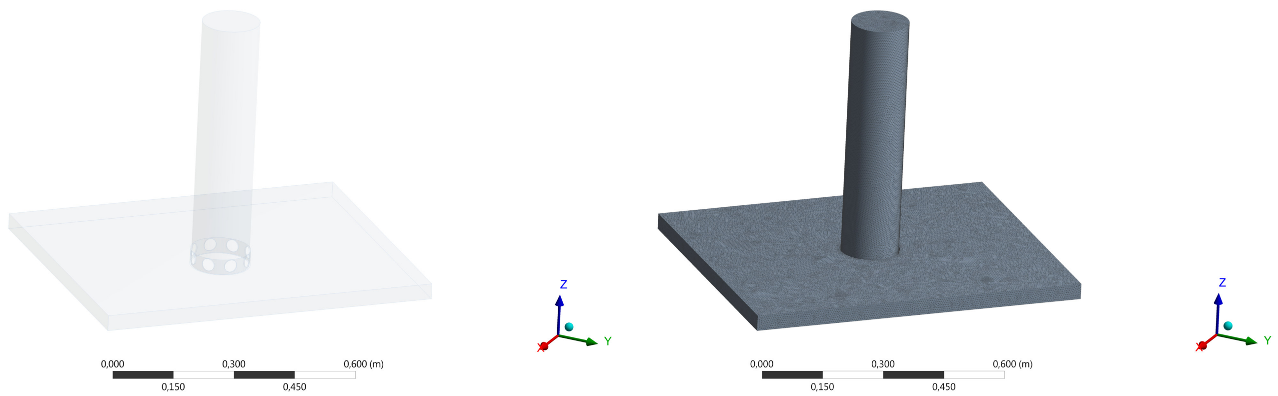

a) Contour Plot b) Grid with a Cell Size of 5 mm

Figure 8.1: Numerical Model (ANSYS Fluent)

Table 8.2: Mesh Study (Tetrahedra Elements)

No	**Nodes**	**Elements**	**max. Element Size**
-	-	-	m
1	38,591	197,852	0.020
2	44,799	227,418	0.015
3	75,213	384,901	0.010
4	333,875	1,783,406	0.005

■ Final Grid for all Following Model Tests.

at both planes are marginal, indicating that the results are converged. The y^+ values fit perfectly in the expected range of $30 \leq y^+ \leq 300$ for nearly all cell sizes. Except for a cell size of 0.010 and 0.005 m the y^+ value falls in some cases below the lower boundary. Due to the small size

Table 8.3: Results of Mesh Study

Parameter	1	2	3	4	Unit
Mass Flow Tower	-0.021	-0.021	-0.021	-0.021	kg/s
max. Velocity (plane 1)	9.696	9.486	9.795	9.798	m/s
max. Velocity (plane 2)	9.422	9.423	9.465	9.503	m/s
max. Velocity (domain)	9.844	9.642	10.094	10.406	m/s
max. Pressure (plane 1)	17.964	17.968	17.870	17.972	Pa
max. Pressure (plane 2)	13.186	13.415	12.236	11.579	Pa
max. Pressure (domain)	17.964	17.968	17.870	17.972	Pa
max. y^+ (domain)	105.3	78.5	59.1	42.0	-

of the turbine walls y^+ lies below 30 for some cells throughout all configurations which makes it necessary to put a special focus on the flow at this area. It also becomes obvious that there are numerical effects when the element size falls below 10 mm. Therefore configuration 3 with an overall element size of 10 mm has been used for all following calculations.

In general one of the two turbulence models, namely k-ϵ and k-ω, are used for this kind of flow structure presented here. A comparison between both models show that there is an influence on the results in the range of ≤ 5 %. This confirms the findings of other authors and therefore lies in an acceptable range. Results are presented in table 8.4.

Table 8.4: k-ϵ vs k-ω ($v_{wind} = 5$ m/s and $\dot{m}_{venturi} = 0.021$ kg/s)

Parameter	k-ϵ	k-ω	Unit
max. Velocity (plane 1)	9.977	9.646	m/s
max. Velocity (plane 2)	9.252	9.273	m/s
max. Velocity (domain)	9.977	9.646	m/s
max. Pressure (plane 1)	18.480	17.706	Pa
max. Pressure (plane 2)	13.311	12.845	Pa
max. Pressure (domain)	18.540	17.706	Pa
max. y^+ (domain)	104.3	95.3	-

The minimum value of y^+ is still below the lower boundary for some cells but a detailed look has shown that the influence on the flow parameter is only marginally and therefore can be neglected.

It also has been tested if the numerical modelling of the domain sides, left and right, as solid walls or as pressure outlets has any impact on the gained results. Results are presented in table 8.5.

The variation lies in the range of ≤ 2 % while the influence of the general flow field close to the domain sides has not been investigated in detail because of neglecting effects on the flow situation

Table 8.5: Influence of Boundary Condition

Parameter	**Wall**	**Pressure Outlet**	**Unit**
max. Velocity (plane 1)	9.696	9.606	m/s
max. Velocity (plane 2)	9.422	9.306	m/s
max. Velocity (domain)	9.844	10.018	m/s
max. Pressure (plane 1)	17.964	18.108	m/s
max. Pressure (plane 2)	13.186	13.583	m/s
max. Pressure (domain)	17.964	18.108	m/s
max. y^+ (domain)	105.3	155.0	-

in and around the tower.

Figures 8.2 and 8.3 show the contour and vector plots for the three different planes, three wind v_{wind} and one tube velocity v_t, which is given here as the mass flow $\dot{m}_{venturi}$ inside the tower. Results for $\dot{m}_{venturi} = 0.042$ kg/s and 0.063 kg/s can be found in appendix C.

A maximum calculated velocity is given for each configuration and plane respectively.

The results confirm the results of the PIV measurements and emphasize the special flow character of each velocity ratio v_{wind}/v_t. For small tube velocities only three flow streams entering the chimney from the windward side can be detected. The length of these streams go through the whole chimney leaving at the lee side with only less air entering at the sides of the tower. A diversion of the flow from the horizontal into the vertical direction can be detected lately at the inner lee side of the tower. With increasing tube flow the horizontal extension of the streams entering the tower decrease and the flow diversion occurs much faster. For medium to high tube velocities air also enters the tower through the lee side openings which leads to eight detectable jets on both planes. The influence can also be seen on the plots for the vertical plane while there is still a shift of the diverted jet to the lee side of the tower.

8.1.2 Fire Dynamics Simulator (FDS)

The calculation parameters for the FDS analysis are listed in table 8.6.

The model domain made up of rectilinear volumes, which is a prerequisite of all FDS calculations, is depicted in figure 8.4.

All circular structures, in this case the tower and the turbine openings, are modelled as polygons, where the number of nooks depend on the cell size. The advantage of a fast grid generation comes along with the impossibility of reproducing circular structures within the model. Even for very small cell sizes the polygonal character endures.

The results for the FDS simulations will be presented here. All in all three models with different cell size have been built. The domain can be divided in all three directions by just setting the wanted quantity of cells which has lead to the following meshes shown in table 8.7.

Horizontal Level 0 mm

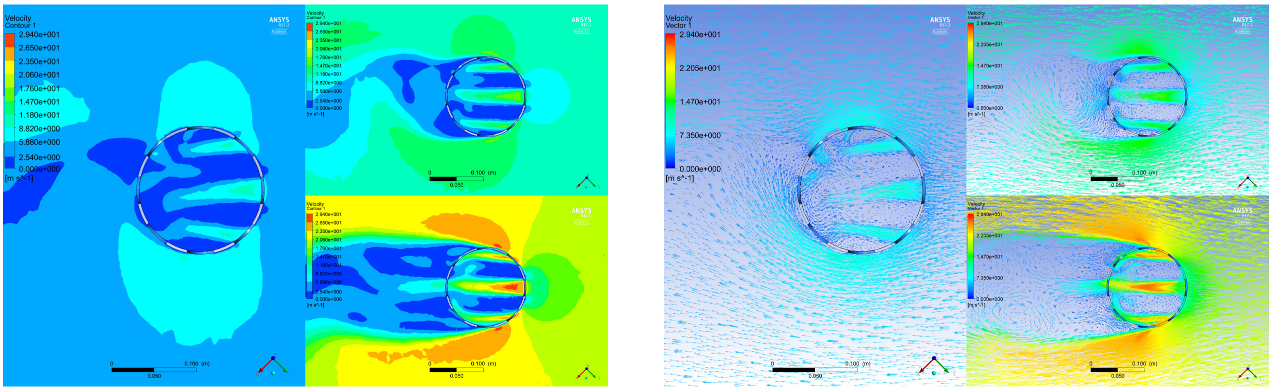

$v_{max,5}$= 10.25 m/s (left); $v_{max,10}$= 17.20 m/s (right top); $v_{max,20}$= 31.51 m/s (right bottom)

Horizontal Level 12 mm

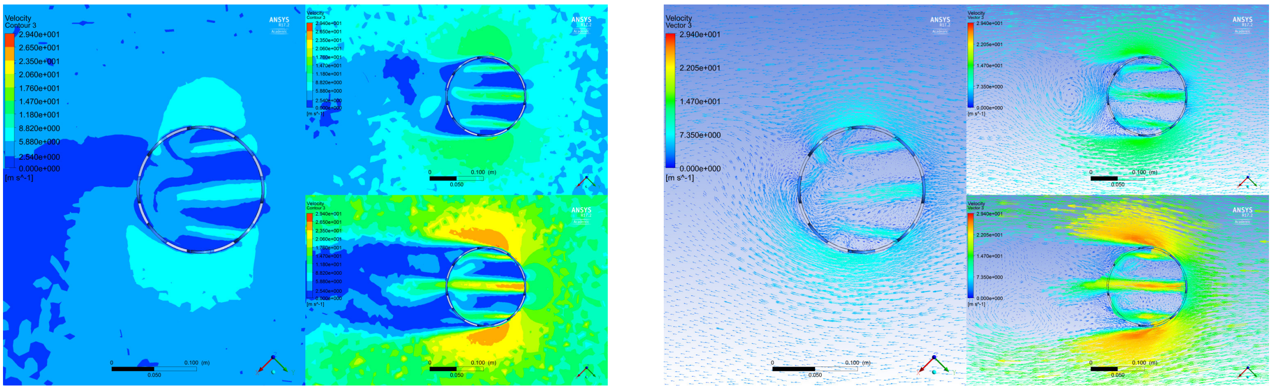

$v_{max,5}$= 9.44 m/s (left); $v_{max,10}$= 15.94 m/s (right top); $v_{max,20}$= 27.57 m/s (right bottom)

Figure 8.2: Results for v_{wind} = 5, 10, 20 m/s and $\dot{m}_{venturi}$ = 0.021 kg/s (Flow From Right to Left) - Part 1 of 2

Vertical Centre

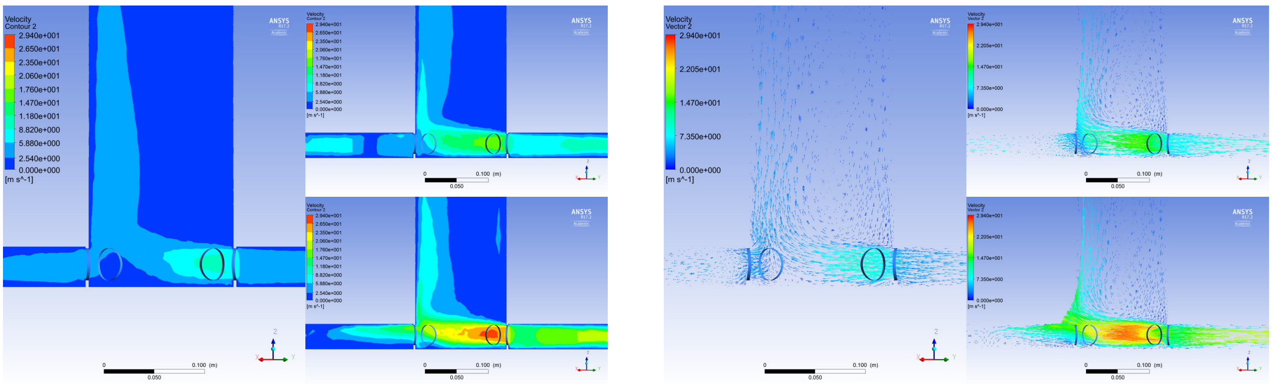

$v_{max,5}$= 9.39 m/s (left); $v_{max,10}$= 15.95 m/s (right top); $v_{max,20}$= 27.28 m/s (right bottom)

Figure 8.3: Results for v_{wind} = 5, 10, 20 m/s and $\dot{m}_{venturi}$ = 0.021 kg/s (Flow From Right to Left) - Part 2 of 2

Table 8.6: Calculation Parameters FDS

Parameter	**Current Study**
General	Transient + Gravity
Models	LES
Boundary Conditions	WIND, OPEN, Outflow (tower), INERT
Report Plots	Mass Flow Stream on tower outlet
Convergence Criteria	Standard
Time Step Size	variable
Simulation Size	5 sec

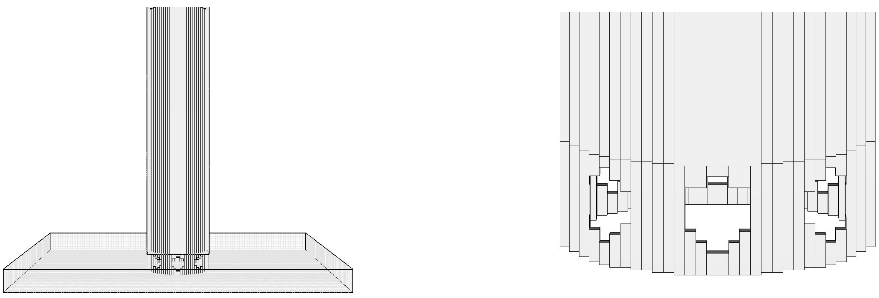

a) Side View b) Turbine Openings

Figure 8.4: Numerical Model (FDS) for a Cell Size of 10 mm

Table 8.7: Mesh Study FDS

Cell Size	**Segmentation Solar Collector**	**Segmentation Solar Chimney**	**Quantity of Cells**
mm	x × y × z	x × y × z	-
10	75 × 45 × 5	15 × 15 × 63	31,050
5	150 × 90 × 10	30 × 30 × 125	247,500
1	750 × 450 × 50	150 × 150 × 625	30,937,500

It is obvious that the quantity of cells increases eightfold with a decreasing cell size by a factor of two. For the finest model the supercomputer Jülich Research on Exascale Cluster Architectures (JURECA) had to be used because the local computers did not have enough computing power.

Figure 8.5 presents the results of ANSYS Fluent and FDS exemplarily.

Depicted are the velocity contour plots for both software packages at the same time step of 10 seconds and 10 mm cell size for the FDS model. Although the mass flow at the tower outlet

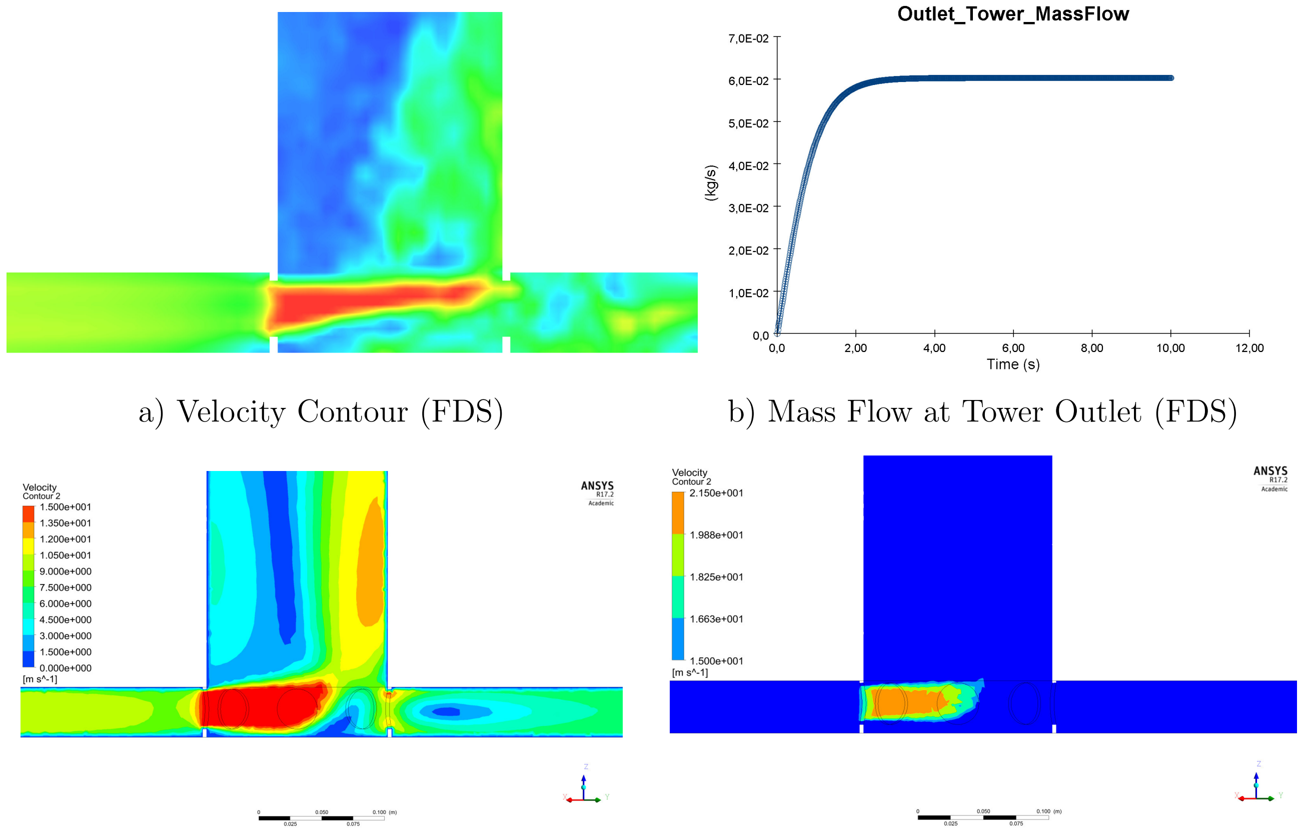

a) Velocity Contour (FDS)   b) Mass Flow at Tower Outlet (FDS)

c) Velocity Contour (ANSYS Fluent)   d) Deviation Between Both Results

Figure 8.5: ANSYS Fluent vs. FDS ($v_{wind} = 10m/s$, $\dot{m}_{venturi}$ = 0.063 kg/s, t = 10 s)

calculated by FDS is given. It can be found that the mass flow has converged after three seconds. Both contour plots have the same key to emphasize the difference in the results. Last but not least a plot showing the deviation in the velocities is given. There someone can see that the maximum velocity within the jet coming from the turbine opening calculated by FDS is way too small compared to the ANSYS Fluent result. The difference lies in the range of 7.5 m/s.

For a cell size of 5 mm and 1 mm the maximum detected velocity increases and therefore gets closer to the results of the ANSYS Fluent calculation. The enormous computational effort coming along with such a fine model outweighs the advantage of the simple grid generation which lead to the decision to skip the FDS simulation. There is also the possibility to design a grid with different cell sizes for different regions of the domain, in this case smaller cells in the area close to the tower base would become necessary, which has not been investigated here. With more computational power FDS might be a good alternative to conventional software packages for such kind of flow structures.

8.2 Conclusion

The results of the numerical simulation show a good coincidence with the experimental findings presented within the previous chapter. It has been proven that both utilized software packages can be used for the reproduction of such kind of flow structure. Nevertheless, a mesh study and a comparison between the gained results need to be performed, that numerical errors can be ruled out. The influence of two turbulence models, namely k-ϵ and k-ω, has been examined here. Due to only small deviations within the results, all following analyses will be performed using the k-ϵ turbulence model as it has been found in many other publications. Although the flow within the transition section and the SCH, respectively, is highly turbulent, a stationary state can be found which will be used for the following investigations, experimentally and numerically.

Chapter9

Stationary 3D-CFD Model of the Prototype in Manzanares, Spain

The prototype at Manzanares, Spain with one single vertical axis turbine and an installation for redirecting the flow into the vertical direction has been the basis for many publications by the present date. In this chapter the influence of the radiation and shell conduction model on the results of temperature and velocity profiles shall be investigated. Therefore the S2S model, implemented in ANSYS Fluent, and the 1D shell conduction model have been utilized. The solar load has been calculated with the Solar Ray Tracing model. Main goal of this analysis is to find the best configuration for the following studies on an improved SCPP model presented in part III of this work.

9.1 Set-Up of the Numerical Model

All parameters for the prototype have been taken from [A.67], [A.66], [A.157] and [A.160]. For the sake of comparison, a few other publications on this topic will be cited here, namely [A.3], [A.85], [A.142], [A.63], [A.177], [A.174], [A.100], [A.122], [A.92], [A.1] and [A.77]. The authors from [A.54] also implemented the influence of the turbine on the flow structure. Publications dealing with natural and forced convection, where buoyancy is the driving force of the SCPP, are [A.35] and [A.34]. Instead of the S2S model the authors of [A.55] used the DO model also available under ANSYS Fluent.

The main model dimensions for the established numerical model are given in table 9.1.

Flow and temperature boundary conditions are listed in table 9.2 for all components defined within ANSYS Fluent.

Many publications lack of information about the input parameters which are essential for the understanding and interpretation of the presented results. Therefore table 9.3 collects all input parameters for the SC, SCH, ground and transition section, respectively.

Ambient conditions for Manzanares, Spain are implemented into the program code to get comparable results, which are shown in table D.1 of the appendix.

For all calculations the pressure-based solver with the SIMPLEC scheme and for the gradient, the least squares cell based algorithm were chosen. For all other parameters the second order (upwind) discretization has been used. The k-ϵ model with realizable function and the standard wall functions with full buoyancy effects were enabled. The solar irradiance has been modelled

Table 9.1: Main Dimensions of the Numerical Model

	Reference Values	**Unit**
Solar Tower		
Tower Height	194.6	m
Tower Diameter	5.0	m
Material	steel	-
Solar Collector		
Collector Height	1.7 ÷ 2.0	m
Collector Diameter	244.0	m
Collector Thickness	0.006	m
Material	glass (semi-transparent)	-
Turbine (not modelled)		
Turbine Diameter	10.0	m
Height Above Ground	9.0	m
Orientation	vertical axis	-
Ground		
Depth	20	m
Material	blackened limestone	-

Table 9.2: Boundary Conditions

Component	**Flow Boundary Condition**	**Temperature Boundary Condition**
Inlet	Pressure Inlet	298 K
Outlet	Pressure Outlet	296 K
Collector	Wall (no slip)	shell conduction
Ground	Wall (no slip)	1D shell conduction
Transition	Wall (no slip)	adiabatic
Chimney	Wall (no slip)	adiabatic

using the solar load model implemented in ANSYS Fluent. The computation for the steady state condition uses air as an ideal-gas.

Table 9.3: Input Parameters

Parameter	Variable	Range	Unit
Solar Collector			
absorptivity (Visible)	ϵ_v	$0.1 \div 0.9$	-
absorptivity (IR)	ϵ_{IR}	$0.05 \div 0.6$	-
density	ρ	2500	kg/m^3
emissivity (ext+in)	ϵ	$0.9 \div 1.0$	-
heat transfer coefficient	h	$6 \div 8$	W/m^2K
roughness height	k_s	0.001	m
specific heat	C_p	481	J/kgK
thermal conductivity	k	0.9	W/mK
transmissivity (Visible)	T_e	$0.71 \div 0.85$	-
transmissivity (IR)	T_v	$0.05 \div 0.75$	-
Ground			
absorptivity (Visible)	ϵ_v	$0.8 \div 0.9$	-
absorptivity (IR)	ϵ_{IR}	0.8	-
density	ρ	2000	kg/m^3
emissivity (ext+in)	ϵ	$0.9 \div 1.0$	-
heat transfer coefficient	h	$5 \div 8$	W/m^2K
roughness height	k_s	0.05	m
specific heat	C_p	750	J/kgK
temperature (z = -20.0 m)	T_{soil}	$293 \div 298$	K
thermal conductivity	k	1.8	W/mK
Transition Section			
absorptivity	ϵ	0.8	-
roughness height	k_s	0.009	m
Solar Tower			
absorptivity	ϵ	0.8	-
density	ρ	8030	kg/m^3
roughness height	k_s	0.009	m
specific heat	C_p	502.48	J/kgK
thermal conductivity	k	16.27	W/mK

9.2 Model With Cone in the Transition Section

Two models have been tested, one with and the other without a cone in the transition section. Its main dimensions are collected in table 9.4 and it has been implemented in the middle of the transition section.

Table 9.4: Main Dimensions of the Cone Structure

	Value	**Unit**
Height	8.5	m
Diameter	22.0	m
Top Diameter	2.5	m
General Shape	nearly circular	-
Material	steel	-

All details have been taken from the Manzanares prototype. Figure 9.1 depicts the whole model and the zoomed-in view on the transition section with the implemented cone structure.

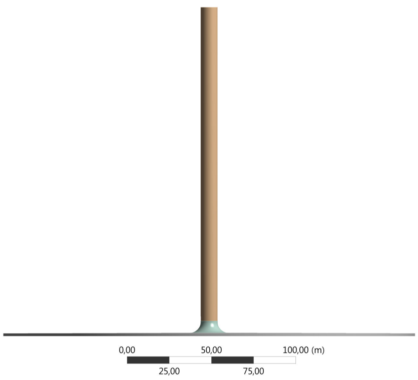

a) Side View of Whole Model

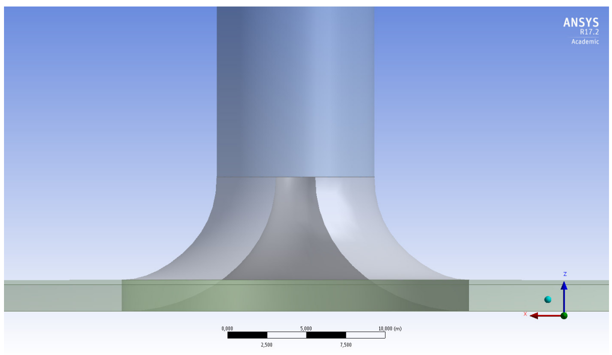

b) Side View of the Transition Section

Figure 9.1: Model View

9.3 Grid Independence Test

The model has been divided into three parts, namely the SC, SCH and transition section and are connected via contact zones as defined under ANSYS. For the SC and SCH a structured mesh using quads and for the transition section an unstructured mesh with tetrahedra elements have been developed. The maximum area size is 0.2 m and 0.4 m for all tetrahedra elements. Table 9.5 shows the tested grids.

Table 9.5: Tested Grids

No.	Nodes	Cells
1	2,572,824	4,084,775
2	3,015,705	4,388,903
3	4,988,351	6,320,836
4	4,992,724	6,325,741
5	4,993,040	6,327,623
6	5,033,504	5,963,246

■ Final Grid for Model Without Cone.
■ Final Grid for Model With Cone.

The standard configuration uses the S2S and 1D shell conduction model without the cone structure. All in all four configurations have been tested which will be abbreviated throughout the course of this work as shown in table 9.6.

Table 9.6: Abbreviation

Configuration	Abbreviation
Reference (Radiation, Shell Conduction, No Cone)	A
Without Cone and Without Radiation Model	B
Without Cone and Without Shell Conduction Model	C
Model With Cone	D

Table 9.7 shows the results for the velocity and temperature for the four configurations and the reference values gained at the prototype of Manzanares.

Good agreement between the current numerical model and the experimental results from Manzanares can be obtained. Best accordance shows configuration D for the case of the SCPP with the cone inside the transition section. It also can be seen that the temperature increase is too high for the numerical solution which leads to a difference in the velocity at the turbine plane as a consequence.

Figure 9.2 shows the grid of the numerical model where the three partitions can easily be distinguished.

Table 9.7: Final Grid Results

	max. Velocity (Outlet)	**max. Velocity (Turbine Plane)**	**max. Temperature (Collector)**	**max. Temperature (Ground)**	**Δ T**
A	15.87 m/s	13.04 m/s	326 K	327 K	27 K
B	18.21 m/s	14.46 m/s	317 K	331 K	33 K
C	16.05 m/s	13.09 m/s	327 K	325 K	27 K
D	14.81 m/s	13.20 m/s	327 K	326 K	32 K
[A.158]	15.00 m/s	12.00 m/s	-	-	20 K

Average value.

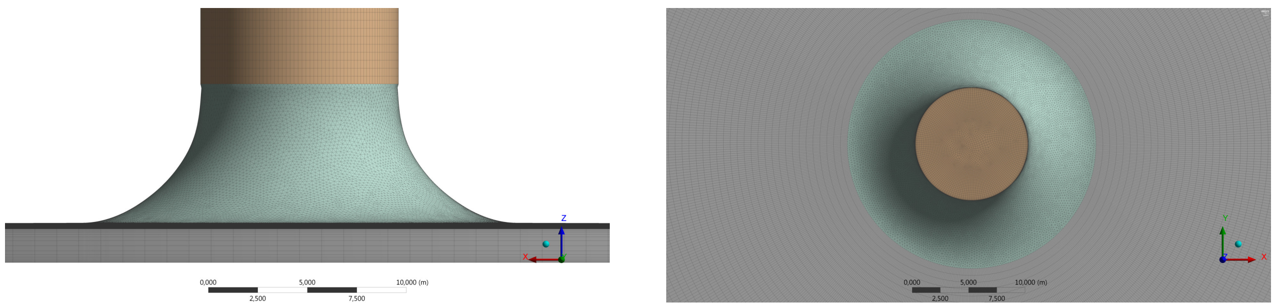

a) Side View b) Top View

Figure 9.2: Model With Grid

9.4 Results

In this section results will be presented for the four configurations. For all configurations temperature plots for three planes, namely the SC, the ground and for a height of z = 150 cm, will be presented. The level of z = 150 cm corresponds to a medium height underneath the SC. Plots for the configurations B, C and D can be found in appendix D. Also velocity and temperature plots for the turbine plane at z = 9.0 m are listed and will help the reader to interpret the results. As other authors have shown can it be helpful to show profile plots of the temperature and velocity development underneath the SC. Results will be given for radial distances from the center of the SCH of 121, 102, 82, 62, 42 and 22 m, respectively. y^+ values have been checked for all calculations and lie in an acceptable range.

9.4.1 Reference (A)

Temperature contour plots for the model without the cone structure inside the transition section and the S2S radiation model are shown in figure 9.3.

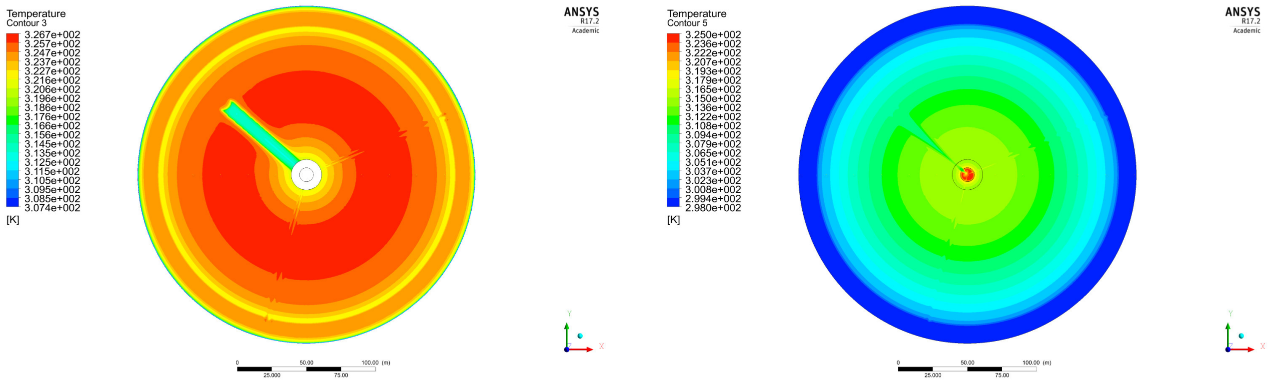

a) Temperature Contours at Solar Collector b) Temperature Contours at z = 150 cm

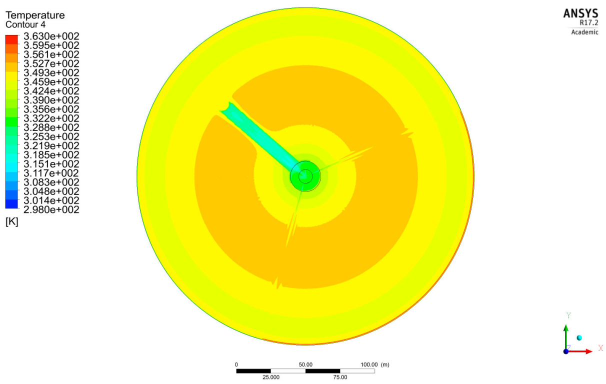

c) Temperature Contours at Ground

Figure 9.3: Temperature Contours (Solar Collector + Ground) (A)

All plots show a smooth distribution with some boundary disturbance where the course of temperature changes rapidly. Additionally, the influence of the tower shadow can be recognized in all three plots which is a more realistic scenario than the perfect symmetrical situation with the sun at the zenith. Figure 9.4 depicts the velocity contours at the turbine plane and the tower outlet.

The maximum velocities are 13.04 m/s and 15.87 m/s, respectively. For a better illustration, velocity and temperature profiles for several radial distances are given in figure 9.5.

We will distinguish between two locations, one close to the tower shadow and one in some distance. Both the velocity and temperature decreases for the location close to the tower shadow. Due to the inclination of the SC disturbances of the profile history at the upper boundary can be detected. Figure 9.6 shows the temperature and velocity contours at the middle plane of the SCPP.

The asymmetric behaviour due to the sun's position can be detected here, too.

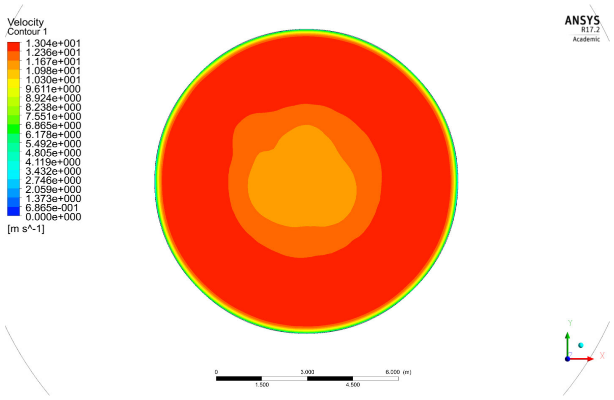

a) Velocity Contours at Turbine Plane

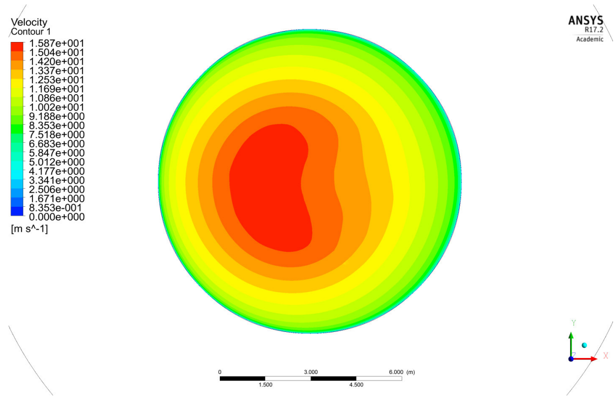

b) Velocity Contours at Solar Tower Outlet

Figure 9.4: Velocity Contours Inside the Solar Tower (A)

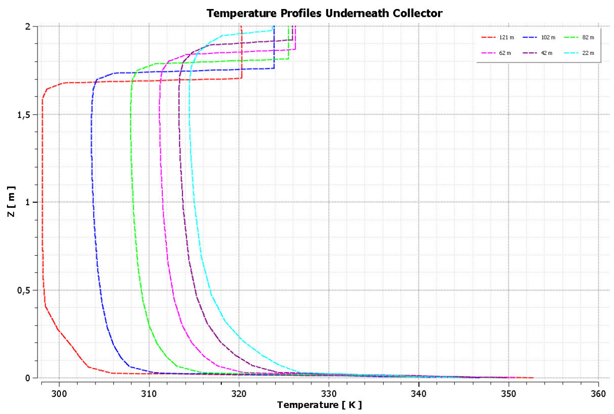

a) Temperature Profiles in Some Distance to the Tower Shadow

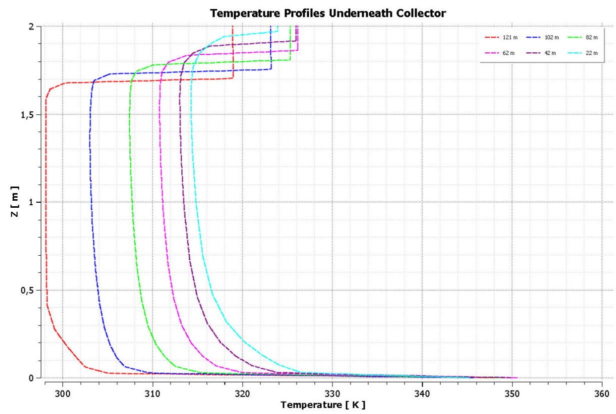

b) Temperature Profiles Close to the Tower Shadow

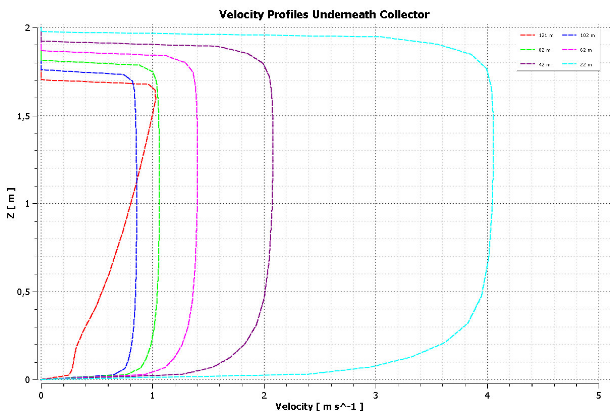

c) Velocity Profiles in Some Distance to the Tower Shadow

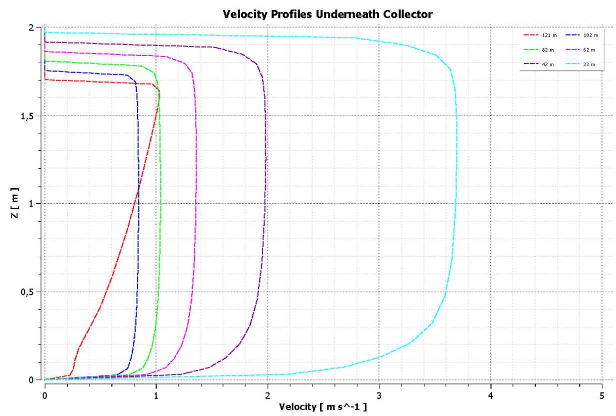

d) Velocity Profiles Close to the Tower Shadow

Figure 9.5: Temperature and Velocity Profiles Underneath the Solar Collector (A)

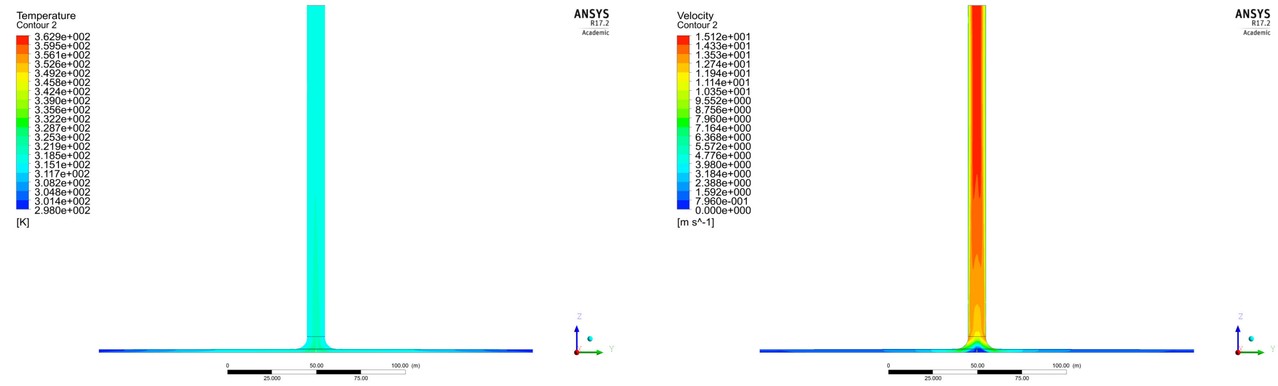

a) Temperature Contour at Middle Plane b) Velocity Contour at Middle Plane

Figure 9.6: Temperature and Velocity Contours at Middle Plane (A)

9.4.2 Without Installation and Without Radiation Model (B)

The calculations presented within this section include the SCPP model without the cone structure and without using the radiation model. Without the application of the S2S model the computing time and effort can be reduced due to the fact that no view factors are needed. Ignoring the process of radiation leads to higher temperatures at the ground and less at the SC. For the temperature beneath the SC and ground similar results can be obtained. Figure D.2 shows the received temperature plots.

The velocity contour plots show the highest values of all configurations and are depicted in figure D.1.

Maximum velocities are 14.46 m/s and 18.21 m/s which are at least 2.5 m/s higher than the reference values from Manzanares. The aforementioned effects can also be found in the profile plots in figure D.4.

The general trend is an increasing temperature and velocity towards the center of the SC. For the velocity plots the graph at a radial distance of 121 m shows a different trend due to the chosen boundary conditions at the outer rim of the SC. This effect does not influence the main flow behaviour underneath the SC and therefore is negligible.

Figure D.3 supports the general findings of increased temperatures and velocities for the case of no radiation modelling.

9.4.3 Without Installation and Without Shell Conduction Model (C)

As expected there is only a small influence of the 1D shell conduction model on the results presented in figure D.6.

The temperature contour plots show marginally different results compared to the reference case. For the velocity at the tower outlet, shown in figure D.5, the maximum value is 1 % higher than for the reference case.

The maximum detectable velocities for the turbine plane and at the tower outlet are 13.09

m/s and 16.05 m/s, respectively. This negligible effect of the shell conduction model on the power plant performance can also be found at the profile plots in figure D.8.

In the velocity contour plot of the middle plane, depicted in figure D.7, the aforementioned slightly higher values at the tower outlet can be found within the complete area of the SCH.

9.4.4 Model With Installation (D)

The best match between the experimental results from Manzanares and the current study can be found with configuration D. Figure D.10 shows the temperature contour plots.

The general temperature rise ΔT is higher than for Manzanares, which has been shown in table 9.7 before. It has to be mentioned that the current results do not allow a prediction of the average value as it is available for the prototype SCPP and therefore cannot be compared directly.

Due to the cone inside the SCH the velocity contour plots for three planes are shown in figure D.11 where z = 9.0 m corresponds to the height within the Prototype of Manzanares.

A marginal difference between the results for height z = 8.5 m and 9.0 m can be found with velocities of 13.20 m/s and 13.02 m/s, respectively, which is 1.5 % higher than for the reference case. The maximum velocity at the tower outlet amounts to 14.81 m/s, which is the lowest value for all investigated configurations. Figure D.9 shows the contours at the middle plane and figure D.12 the profiles of velocity and temperature underneath the SC with their typical course.

For a better understanding of the flow situation inside the transition section and the redirection of the flow via the placed cone, in figure 9.7 the velocity vectors for this section are depicted.

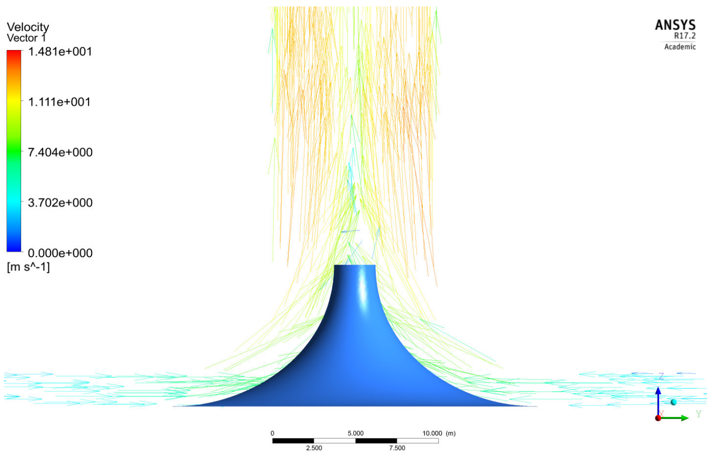

Figure 9.7: Velocity Vectors Inside the Transition Section

After the redirection, where the cone ends, a back-flow and highly turbulent region can be found. This is where the process of optimization needs to draw on.

9.5 Conclusion

The presented results show good agreement with former publications, which have also dealt with the numerical simulation of the prototype SCPP from Manzanares, cf. [A.3], [T.19]. A strong dependency on simulating the influence of radiation and the solar load has been found. On the other hand the usage of the shell conduction model for the SC has only a small, negligible effect on the velocity and temperature field within the whole power plant. The simulation on the basis of construction site parameters have shown that the general assumption of the symmetric case is only correct for perfect ambient conditions. Therefore it is of major importance to take these real flow and ambient parameters into account to get reliable results for the efficiency, power output, etc. Last but not least, the implementation of a cone within the transition section has led to the best performance of the power plant and most comparable results with full scale data gathered at Manzanares. Therefore special focus will be put on the asymmetric inflow conditions and the influence of a suitable variant of redirecting the flow within the transition section, which will be presented in part III at an improved model of the SCPP.

Chapter10

Structural Model with Finite Elements

Different concepts for the SCH and especially for the area of the transition region can be found in former publications. Here to mention are the column and shell concepts. The column concept, based on the design of CTs, leaves out the implementation of turbines in the transition section. For static reasons a shell concept should be favoured. This also considers fluid mechanic aspects for an improved flow behaviour through the turbines and inside the transition section. Additionally, many research on the static and dynamic behaviour of a SCH completely ignores the transition section, e.g. [T.7] and [T.17]. On the other side, speaking about the investigation on the fluid mechanic design, current experimental or numerical models do not take into account the static aspects. Therefore a model, which combines both the static and fluid mechanic properties, has been designed and will be presented in part III of this work.

10.1 Model Parameters

This section includes the model parameters of the constructed FE model and its different variants. The general concept of [A.72] has been utilized with some adaptations.

10.1.1 Material Properties

The material properties of the SCH made from RC are as following:

$$\begin{aligned} \rho &= 2{,}500\ kg/m^3 \\ \nu &= 0.2 \text{ (Poisson's Ratio)} \\ E &= 37{,}000\ N/m^2 \text{ for C50/60 (Young's Modulus)} \\ f_{cd} &= 28.3\ N/mm^2 \end{aligned}$$

10.1.2 Shape Profile of the Solar Chimney

The shape profile of the SCH follows the following function:

$$\frac{x^2}{42.5^2} - \frac{(z-350)^2}{219.4691^2} = 1 \tag{10.1}$$

For three configurations the diameter over height is listed in table 10.1, including a cone and two diffuser chimneys, with different shaped diffusers.

At least four more variants have been tested and the corresponding eigenfrequencies are given in section 10.7.

Table 10.1: Chimney Shape

z	*Diameter*[1]	*Diameter*[2]	*Diameter*[3]
m	m	m	m
0	79.000	80.000	80.000
50	71.081	71.981	71.670
100	63.621	64.420	63.928
150	56.775	57.500	56.966
200	50.828	51.478	51.035
250	46.126	46.704	46.443
300	43.089	43.589	43.511
350	42.500	42.500	42.500
750	42.500	61.109	61.000

[1] Cone chimney.
[2] Cone diffuser with enlarged hyperbolic curve (5% divergent).
[3] Hyperbolic diffuser divided at chimney throat.

10.1.3 Wall Thickness

The wall thickness as one of the major variables in the design process has been listed for two general concepts of the transition section of a SCH in table 10.2.

The column concept includes 18 turbine openings, the shell concept only 12, which is one explanation of the huge difference of wall thickness within the area close to the bottom. More on these two concepts follows in section 10.2.

10.1.4 Ring Stiffeners

Another element of the SCH, which is important for the dynamic behaviour, are the ring stiffeners distributed over height as can be seen in table 10.3.

Distribution and measures have been taken from [A.72] and have not been varied throughout this work.

Table 10.2: Wall Thickness

z	**Thickness**[1]	**Thickness**[2]
m	m	m
0	7.5 (**5.2**)	1.0
25	1.4	1.0
30	0.6	[3]
50	[3]	0.7
75	[3]	0.5
80	0.5	[3]
100	0.4	0.4
200	0.325	0.325
250	0.288	0.288
300	0.25	0.25
500	0.25	0.25
750	0.25	0.25

■ Minimal Possible Column Expansion in Radial Direction.
[1] Column Concept.
[2] Shell Concept.
[3] Values have been linearly interpolated.

Table 10.3: Details of Ring Stiffeners

No.	**z**	**Width**	**Height**	**Eccentricity**
-	m	m	m	m
1	100.0	3.0	0.6	none
2	200.0	3.0	0.6	none
3	300.0	5.0	1.0	none
4	400.0	6.0	1.0	none
5	500.0	5.0	1.0	none
6	600.0	6.0	1.0	none
7	750.0	6.0	0.6	none

10.2 Column vs. Shell Concept

A column and a shell concept have been investigated and both will be discussed in this section. Additionally, a comparison between two software packages, namely SOFiSTiK and ANSYS APDL, will be performed here. The FE models designed in ANSYS APDL and SOFiSTiK are shown in figure 10.1.

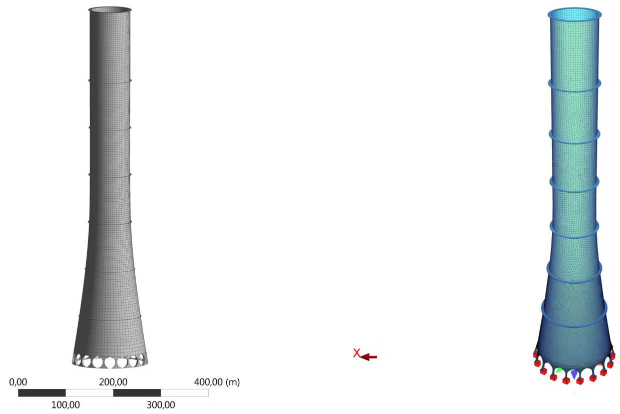

Figure 10.1: FE-Model in ANSYS APDL and SOFiSTiK [T.25] (both views are generic)

Three variants of columns and one shell design were built and their masses have been calculated for the sake of comparison, cf. figure 10.2.

The speciality of variant 1 and 2 is that the columns do not follow the chimney geometry which is only true for case 3, which can be seen in figure 10.2. It can be stated, that the major difference between both configurations lies in the quantity of turbine openings, 18 in case of the column and 12 in case of the shell concept. The ratio of open to closed area lies for the column concept in the range of 80 %, whereas the ratio diminishes to only 50 to 65 % in case of the shell concept. Due to a better static behaviour the masses of the shell concept do not exceed the masses of the column concept.

Column Concept

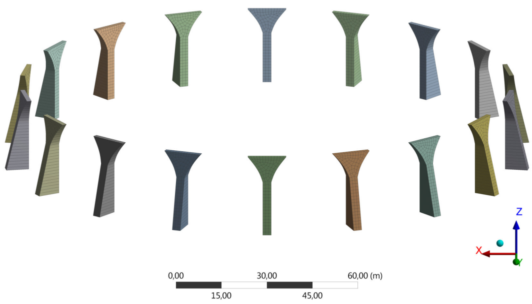

Variant 1

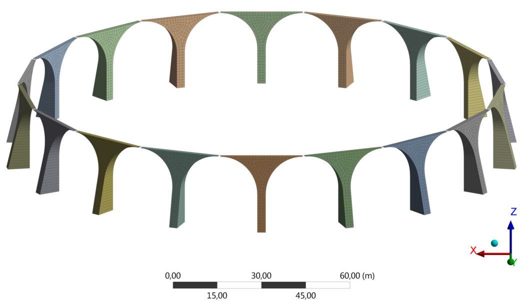

Variant 2

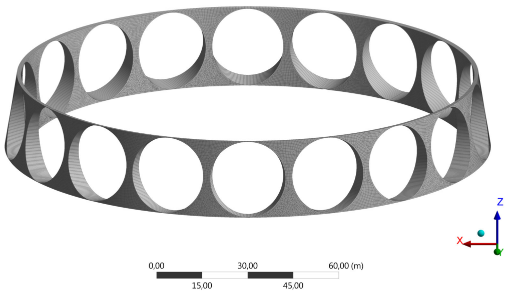

Variant 3 (18p. x 24.8m)

Variant 1: 169,210 kN
Variant 2: 204,230 kN
Variant 3: 397,920 kN
Variant 3.1 ($d = 5.2$ m): 294,140 kN

Shell Concept

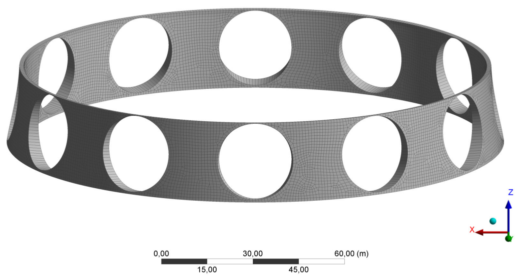

Variant 4 (12p. x 24.8m)

Variant 4: 170,210 kN

Figure 10.2: Column and Shell Concept with Masses

10.3 Grid Sensitivity Analysis

A grid sensitivity analysis has been performed to check for convergence of the gained results.

10.3.1 Convergence

The presented numerical model of the SCH consists of shell elements for the chimney and beam elements for the ring stiffeners. Table 10.4 gathers all tested configurations where the element size and the quantity of elements around the circumference for the ring stiffeners is given in column four.

Table 10.4: Grid Sensitivity

No.	Nodes	Elements	Size
	Shell181, Beam188[1]		
1	279,125	279,663	1.00m/360prt.
2	529,767	530,755	0.75m/540prt.
3	1,096,225	1,098,026	0.50m/720prt.
	Shell281, Beam189[2]		
4	832,685	279,667	1.00m/360prt.
5	1,582,801	530,749	0.75m/540prt.
6	3,280,019	1,098,031	0.50m/720prt.
6.1	1,641,697	547,757	0.50m/720prt.

■ Symmetrical case.
[1] Without middle nodes; Shell181 (4 nodes), Beam188 (2 nodes).
[2] With middle nodes; Shell281 (8 nodes), Beam189 (3 nodes).

The influence of middle nodes for the shell and beam elements on the eigenfrequency and modular form has been tested.

Taking into account the symmetry of the model does not change the static behaviour or interpretation, which is the red marked case. For the eigenfrequency analysis all twin eigenmodes for the second principal direction disappear and no torsion mode can be detected. As can be seen in table 10.5, this torsion mode can be neglected anyway.

Special attention has been given to the aspect ratio of each element to avoid shear locking which can cause a shear stress inside each element resulting in a stiffer behaviour than it actually is. Therefore an aspect ratio of 1:2 has been used for all elements as an upper boundary, also cf. [T.7].

10.3.2 Verification - Eigenfrequency and Modular Shape

Models 1 and 3 show identical eigenfrequencies and eigenmodes. Therefore no dependence on the chosen grid can be found. The use of shell and beam elements with middle nodes also shows no influence on the gained results. Table 10.5 gives the eigenfrequencies and modular shapes for variant 1 to 3, twin eigenmodes have been neglected.

In table 10.6 the eigenfrequencies for the column concept (variant 3.1) are compared to former research.

The major differences between the depicted configurations are that the outer measures for the ring stiffeners have been changed. Another difference is the expansion of the column in variant 2 of [T.25] which decreases from 2.50 m at the base to 1.00 m at the top. In the current model the thickness of the column at the top is 1.40 m.

Eigenmode 9 corresponds to a torsion mode which occurs due to soft columns under dynamic

Table 10.5: Eigenfrequency and Modular Shape

	Top View and Side View		
Modular Shape	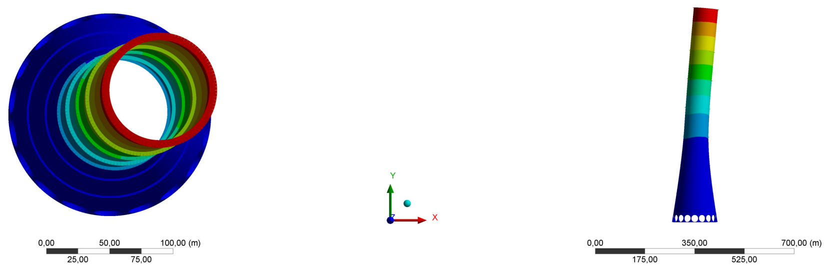		
Eigenfrequency in Hz	$f_{1,Var1} = 0.170$	$f_{1,Var2} = 0.171$	$f_{1,Var3} = 0.172$
Modular Shape	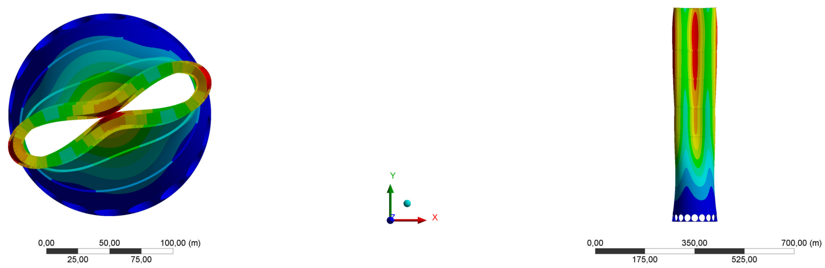		
Eigenfrequency in Hz	$f_{3,Var1} = 0.616$	$f_{3,Var2} = 0.617$	$f_{3,Var3} = 0.609$
Modular Shape	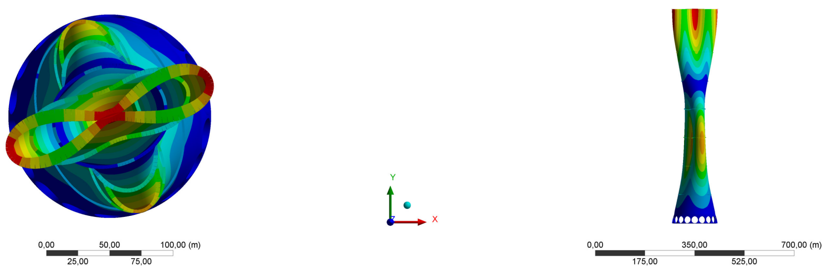		
Eigenfrequency in Hz	$f_{5,Var1} = 0.636$	$f_{5,Var2} = 0.643$	$f_{5,Var3} = 0.626$
Eigenfrequency in Hz	$f_{7,Var1} = 0.724$	$f_{7,Var2} = 0.735$	$f_{7,Var3} = 0.639$
	$f_{9,Var1} = 0.745$	$f_{9,Var2} = 0.766$	$f_{9,Var3} = 0.702$
	$f_{11,Var1} = 0.793$	$f_{11,Var2} = 0.801$	$f_{11,Var3} = 0.773$

Table 10.6: Eigenfrequency for Shell Concept

Mode	Witting[1] TAN	Witting[1] Var2	SCPP	Beam/Shell like
1	0.178	0.179	0.172	beam/beam/beam
2	0.178	0.179	0.172	beam/beam/beam
3	0.720	0.720	0.608	shell/shell/shell
4	0.720	0.720	0.608	shell/shell/shell
5	0.730	0.733	0.624	shell/shell/shell
6	0.731	0.733	0.624	shell/shell/shell
7	0.782	0.772	0.635	beam/beam/shell
8	0.782	0.772	0.635	beam/beam/shell
9	0.867	0.911	0.698	beam/shell/shell
10	0.922	0.911	0.698	shell/shell/shell
11	0.922	0.928	0.772	shell/beam/beam
12	0.950	0.950	0.772	shell/shell/beam

■ Beam Mode.
■ Shell Mode.
■ Torsion Mode.
[1] [T.25].

aspects. Overall the current design shows a softer behaviour than the model designed by [T.25].

Decreasing the wall thickness to 5.20 m, as it has been mentioned in table 10.2, leads to diminishing changes for the eigenfrequencies f_3 and f_6. The first and second eigenfrequencies are identical.

For the shell concept (variant 4) the first eigenfrequency is 0.173 and all following modes and eigenfrequencies change in the same magnitude.

10.3.3 Symmetry

Saving computing effort by taking into account the symmetry of the SCH model leads to a deviation of $< 2.9\%$ for the first twelve eigenfrequencies, six for the symmetrical case, even for a coarse and fine mesh. The decrease of rigidity of the model is negligible.

10.4 Load Cases

A linear mechanical analysis for the SCH under dead and wind load has been performed for variant 3.1.

10.4.1 Dead Load

The total dead load composes of the dead load for the SCH shell and the ring stiffeners respectively. Masses are given in table 10.7.

Table 10.7: Dead Load for Different Designs

Variant	Dead Load	ΔF_G
-	kN	%
Witting[1] TAN	2,393,036	10.9
Witting[1] Var 2	2,233,583	3.5
Var 3	2,340,200	8.5
Var 3.1	2,231,900	3.5
Var 4	2,157,300	-

■ Reference.
[1] [T.25].

The shell design provides the lightest model and saves ≈ 4 % of masses compared to the lightest column design. It has to be mentioned that no design optimization has been performed which could save additional material and finally save money.

10.4.2 Wind Load

The static wind load has been taken from [S.16] and has been applied onto the outer surface of the SCH. In ANSYS APDL a User Defined Function (UDF) has been written and implemented into the model code. The applied wind load follows curve K 1.5 from the guideline [S.16], for a SCH without ribs, and wind zone 2 and terrain category II have been taken as a reference. The reduction factor of ψ_λ, which accounts for the tip effect at the free end of the SCH, has not been considered in the current case. Figure 10.3 shows the circumferential distribution of the external pressure coefficient c_{pe} and the resulting wind pressure.

Also ANSYS gives the opportunity to calculate the wind load through a OneWay FSI, equivalent static loads have been applied to the structure, which is a very common approach in mechanical analysis of buildings. For more information compare results from [A.109], [A.74], [A.105], [A.129], [A.76], [A.58], [A.133], [A.134] and [A.72].

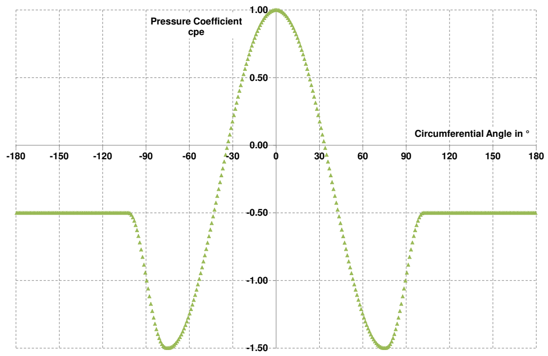

a) Pressure Coefficient c_{pe}

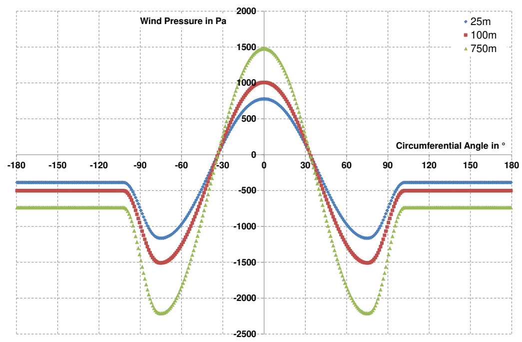

b) Wind Pressure in Pa

Figure 10.3: Wind Load

10.5 Results

Results have been obtained for different load combinations, including the single load cases for dead load (1.0 G) and wind load (1.0 W). As a general statement it can be said that the design value of compressive strength f_{cd} never exceeds its limit with a maximum value of 21.0 N/mm^2. What is not self evident for a 750 m high structure.

The impact of uncertainty quantification in structural analysis has not been discussed here but can be found in [A.110].

10.5.1 Displacements

The chimney displacements at different circumferential angles are depicted in table 10.8 for the current case compared with results from [T.25].

Table 10.8: Chimney Displacements K 1.5 - Single Load Case

Dead Load				**Wind Load**					
Direction of Gravity/Meridional $Direction^1$ **[mm]**									
0/180°	90/270°	0/180°[1]	90/270°[1]	0°	90/270°	180°	0°[1]	90/270°[1]	180°[1]
-159 (-159)	-159 (-159)	-170	-170	+36 (+36)	-2÷+2 (-2÷+1)	-36 (-36)	+42	-2÷+6	-43
Horizontal/Orthogonal Cell $Direction^1$ **[mm]**									
+10 (+10)	+8 (+8)	-22÷+5	-20÷+6	-451 (-453)	+68 (+68)	+327 (+329)	-450	-75	+530

■ Different sign for both results.

[1] As defined and found in [T.25] calculated with SOFiSTiK.

() Values in brackets have been obtained with Shell281 and Beam189 elements with middle nodes.

Angles are positive in clockwise direction. The definition of the displacements differs for both software packages. Whereas ANSYS APDL gives results for the direction of gravity and in horizontal direction, SOFiSTiK defines a meridional and orthogonal cell direction. Nevertheless, both results match each other very well. Positive values for the vertical direction z correspond to the case of extension, negative values to compression. For the horizontal directions direction x and y, positive values correspond to deformation of the shell to the outside, negative values in the opposite direction. Given values in brackets have been obtained with Shell281 and Beam189 elements with middle nodes. If the wall thickness is decreased to 5.2 m, the maximum deflection due to dead load increases by 1 mm to -160 mm. For the blue marked values no explanation could be found. Both models show similar values in magnitude with changed sign. There is also a big difference between the displacements for the horizontal direction for an circumferential angle of 180 °. For both aspects a deeper analysis of the implemented program code of both software packages could be helpful which has not been performed in the course of this work.

10.5.2 In-Plane Forces n_{22}, n_{11} and n_{12}

Two types of in-plane forces are characterised, n_{22} and n_{11}, respectively. n_{22} is the resultant in-plane force in the meridional direction while n_{11} is the resultant in-plane force in the circumferential direction. Especially n_{22} gives a lot of insight in the static response of the SCH and its ability to evenly distribute forces around the circumference. The stiffer the shell gets, the more cosine-like the distribution of the meridional forces around the circumference will be. The in-plane shearing stress resultants correspond to $n_{12} = n_{21}$. Figure 10.4 depicts n_{22} in meridional and circumferential direction.

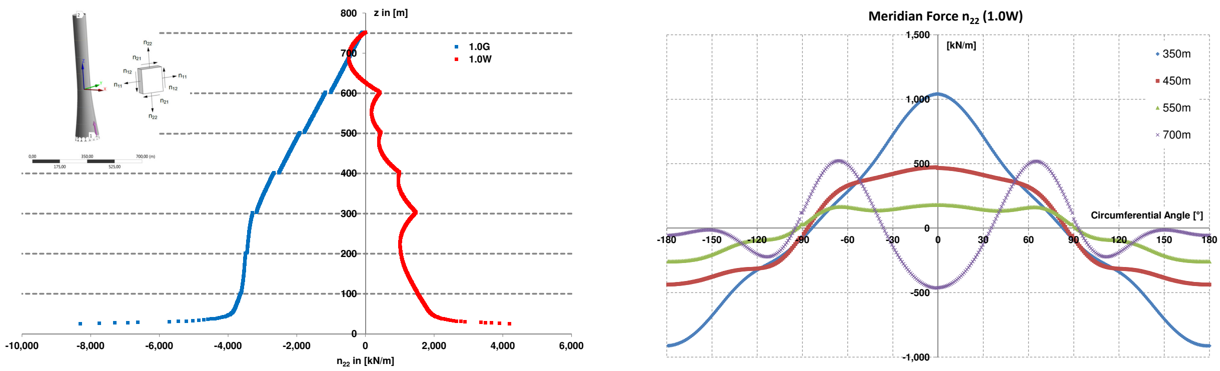

a) n_{22} Plotted Over Windward Meridian 0 ° b) n_{22} Plotted Over Circumference

Figure 10.4: n_{22} due to Wind Load

The values correspond well with results from [T.17]. For the load case of 1.0 W compression in the upper region can be found. Publications of [T.25] and [A.75] show a different behaviour. This corresponds to the findings presented in the previous subsection for the displacements.

10.5.3 Ring Stiffener Forces

Ring stiffener forces show reliable results over the circumferential angle for all eight rings and are depicted in figure 10.5 for the single load case of wind.

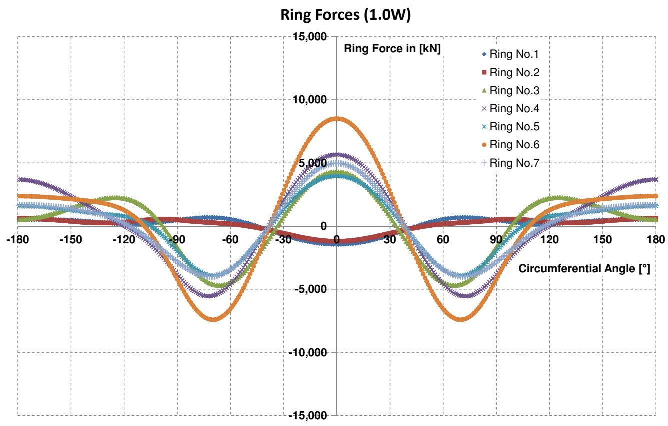

Figure 10.5: Ring Stiffener Forces Due to Wind Load

10.6 The Ultimate Limit State (ULS)

The structural Ultimate Limit State (ULS) represents the internal failure or the excessive deformation of the structure. Two load combinations will be discussed in this section, namely (1.0G+1.0W) and (1.0G+1.5W). Safety factors are taken from [S.16] and the Eurocode with National Annex.

10.6.1 Displacements

Table 10.9 shows the displacements for the load combination where values in brackets correspond to elements with middle nodes.

Table 10.9: Chimney Displacements K 1.5 - Load Combination

1.0D + 1.0W			**1.0D + 1.5W**		
Direction of Gravity [mm]					
0°	90/270°	180°	0°	90/270°	180°
-128 (-113)	-159 (-159)	-195 (-214)	-112 (-113)	-158 (-159)	-213 (-214)
Horizontal [mm]					
-451 (-680)	+69 (+103)	+327 (+494)	-677 (-680)	+103 (+103)	+491 (+494)

Differences can be found for the load combination with safety factors of 1.0. With increasing influence of the wind load nearly identical values can be obtained with both models.

10.6.2 Meridional Forces n_{22}

The meridional forces n_{22} are depicted in figure 10.6 for the meridional and circumferential direction.

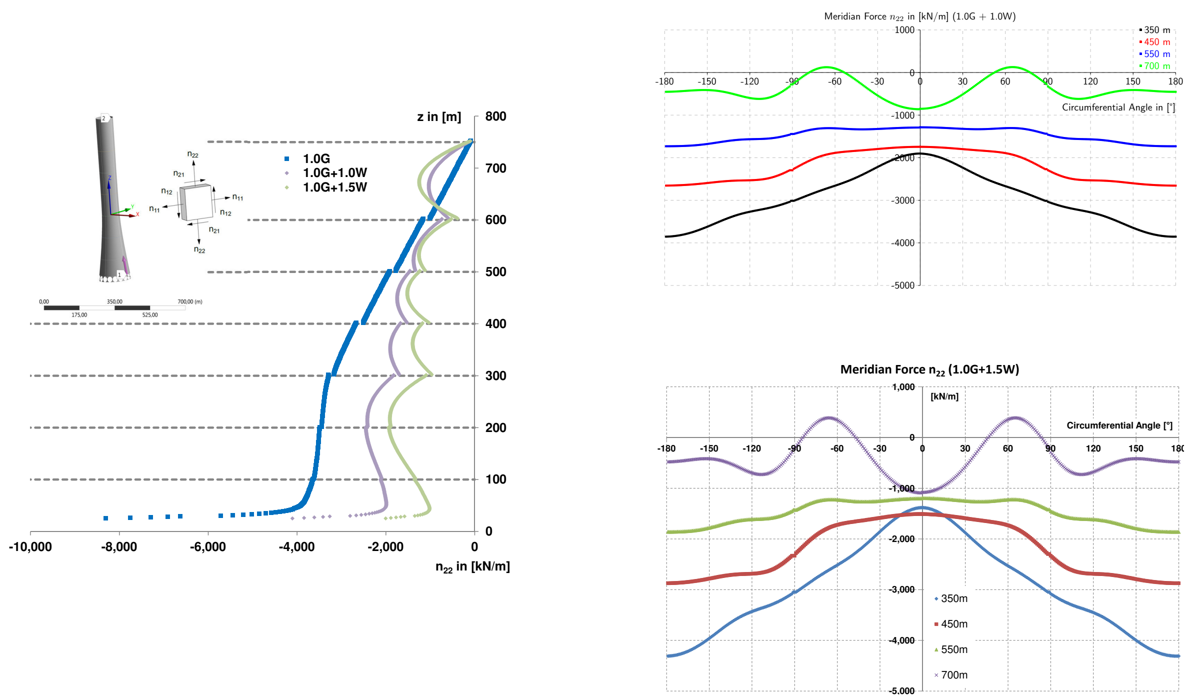

a) n_{22} Plotted Over Windward Meridian 0 ° b) n_{22} Plotted Over Circumference

Figure 10.6: n_{22} Due to Dead and Wind Load

Negative values indicate compression over the whole height of the SCH which corresponds well with the findings of [T.17].

10.6.3 Ring Stiffener Forces

Ring stiffener forces for both load combinations are shown in figure 10.7.

The typical distribution over the circumferential angle has been obtained for both load cases.

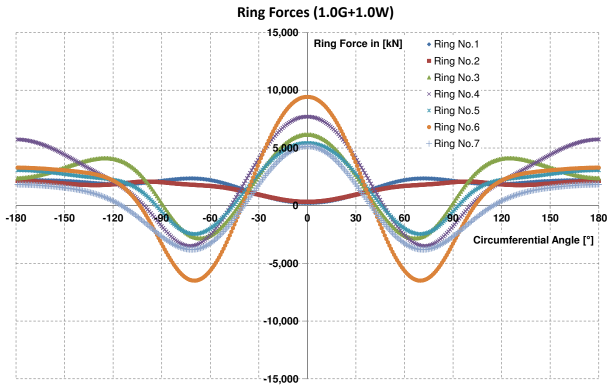

a) Ring Force for Load Combination (1.0G+1.0W)

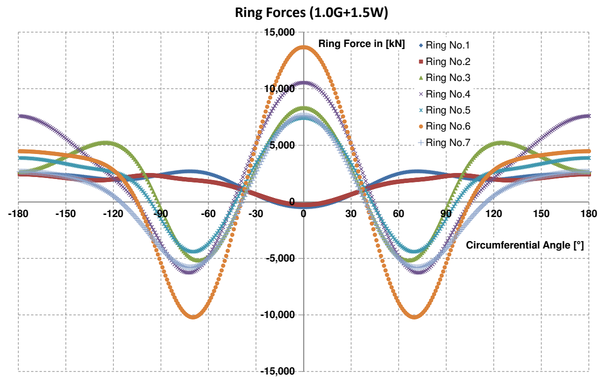

b) Ring Force for Load Combination (1.0G+1.5W)

Figure 10.7: Ring Stiffener Forces Due to Dead and Wind Load

10.7 Design Study for a Solar Chimney with Diffuser

In this section a design study for a SCH with a diffuser has been performed. Different general concepts have been considered and the optimum solution has been used to build an improved experimental and numerical model of the SCPP which will be explained within part III.

First, a cone diffuser with an opening ratio of 5 % and 10 % has been modelled on top of the hyperbolic shape profile defining the contour in the lower half. Due to the different opening ratios the cone starts at a height of z = 420 m for the 5 % and at a height of z = 500 m for the 10 % case. Hereby a seamless transition from the hyperbolic to the cone shape takes place. Second, a hyperbolic diffuser has been modelled following the equation established in appendix E. Due to the double hyperbolic shape small changes in the lower region occur from the cone design. The maximum radius at the top of the SCH has been taken from the cone variant. All profiles are depicted in figure 10.8.

A third variant with a straight diffuser starting at z = 400 m has been modelled and for all variants the first six eigenfrequencies have been calculated. A compilation of all results can be found in figure 10.9.

Someone can see that the eigenfrequencies may vary to a great extent for all variants which is due to a change in stiffness and changing masses in the upper region of the SCH.

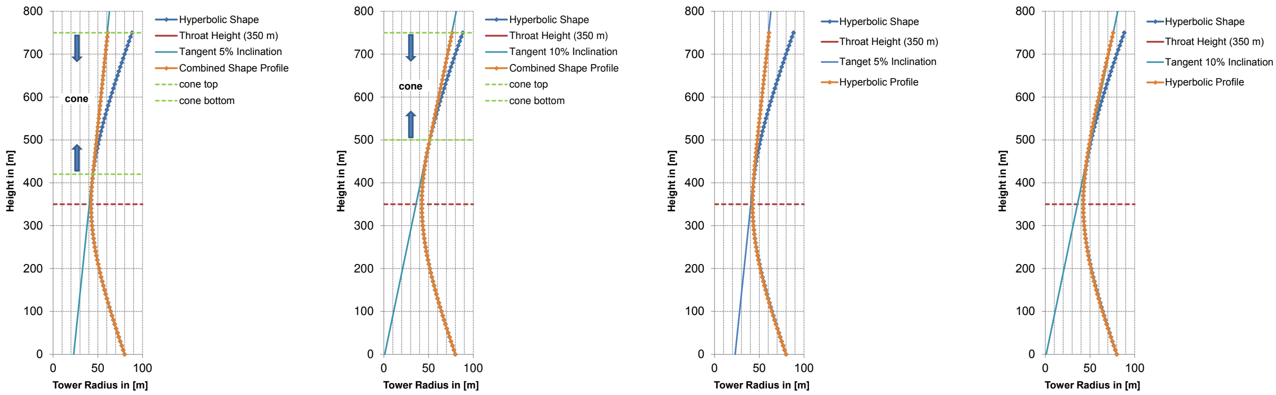

5% Cone 10% Cone 61 m hyperbolic 76 m hyperbolic

Figure 10.8: Solar Chimney Profile with Cone and Hyperbolic Diffuser

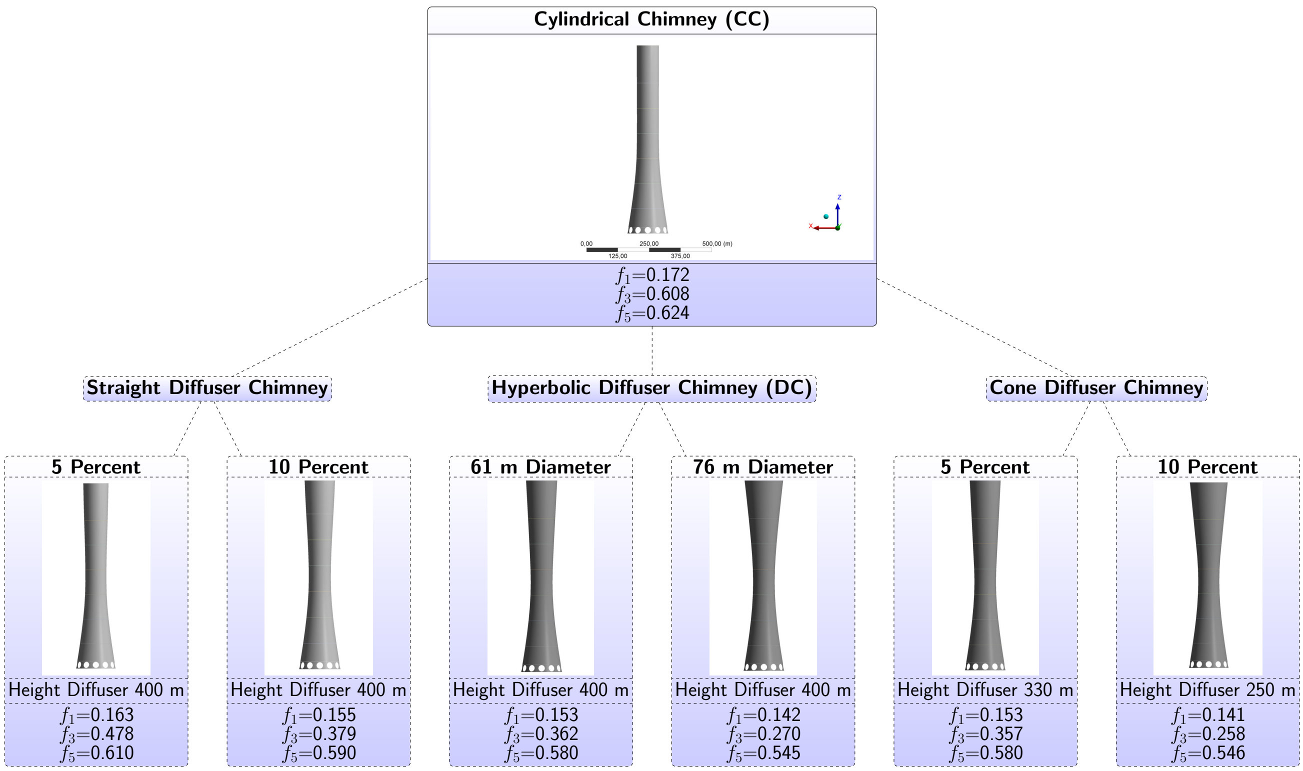

Figure 10.9: Design Study of a Solar Chimney with Diffuser

10.8 Conclusion

Two model concepts, namely a column and a shell concept, have been presented within this chapter. The intention of the performed FE analysis has been to find the best solution and set-up for tests on an improved model of the SCPP, which will be presented in part III of this work. The mass and eigenfrequency analysis have shown that the favoured shell concept gives good results for both which not only leads to a reduced material input in comparison to the column concept but shows a good performance for the dynamic excitation as well. Due to the structural analysis it has been proven that the designed models are reliable and can be used for further investigations. Last but not least the effect of a diffuser on top of the lower part of the SCH has been investigated and will be used for the build up of a second model, next to the one without a diffuser, to clarify its effect on the flow field and the efficiency of this improved model.

Part III

Improved Solar Chimney Power Plant Model

Chapter11

Wind Tunnel Studies at Bochum, Germany

This chapter deals with the experimental set-up and the wind tunnel study of a SCPP based on the improved structural model designed in chapter 10. The chimney base has been changed in that way that besides structural also fluid mechanic aspects have been taken into account for the improvement of the flow situation inside the transition section. All in all four chimney models have been built via 3D printing, two for CTA and two identically constructed for pressure measurements. Besides a Cylindrical Chimney (CC) with constant diameter above the chimney throat a Diffuser Chimney (DC) with a hyperbolic diffuser has been tested. For both models the influence of wind and buoyancy on the pressure distribution inside the chimney and on the velocities are gathered. Besides the influence of ambient parameters different redirecting variants, which have been implemented into the transition section, have been tested and their influence on the flow characteristics are also given. Additional tests have been performed to clarify the effect of changing inflow conditions into the SC due to installations and therefore a blockage effect on the lee and windward side. Also a serious consideration of experimentally modelling the influence of the turbines and their effect on the flow field has been performed and will be explained in appendix F.

11.1 Experimental Set-Up

The design of the improved wind tunnel model, the heat source to model the buoyancy effect, the turbine influence and the background to the assumption of different inflow conditions will be explained within this section. Details of the wind tunnel in Bochum can be taken from [T.16].

11.1.1 Model Design and Parameters

The part of the turbine area of the chimney model designed on the basis of the structural model from chapter 10 is depicted in figure 11.1.

Two design concepts for the chimney base and therefore of the location of the turbines situated in the circumference of the chimney are given, too. The upper one in figure 11.1 only takes into account structural aspects, light and efficient in material consumption. For the lower design in figure 11.1 additionally fluid mechanic aspects have been implemented to find a solution which satisfies both needs. One of these aspects, which has been taken into account is the drag coefficient.

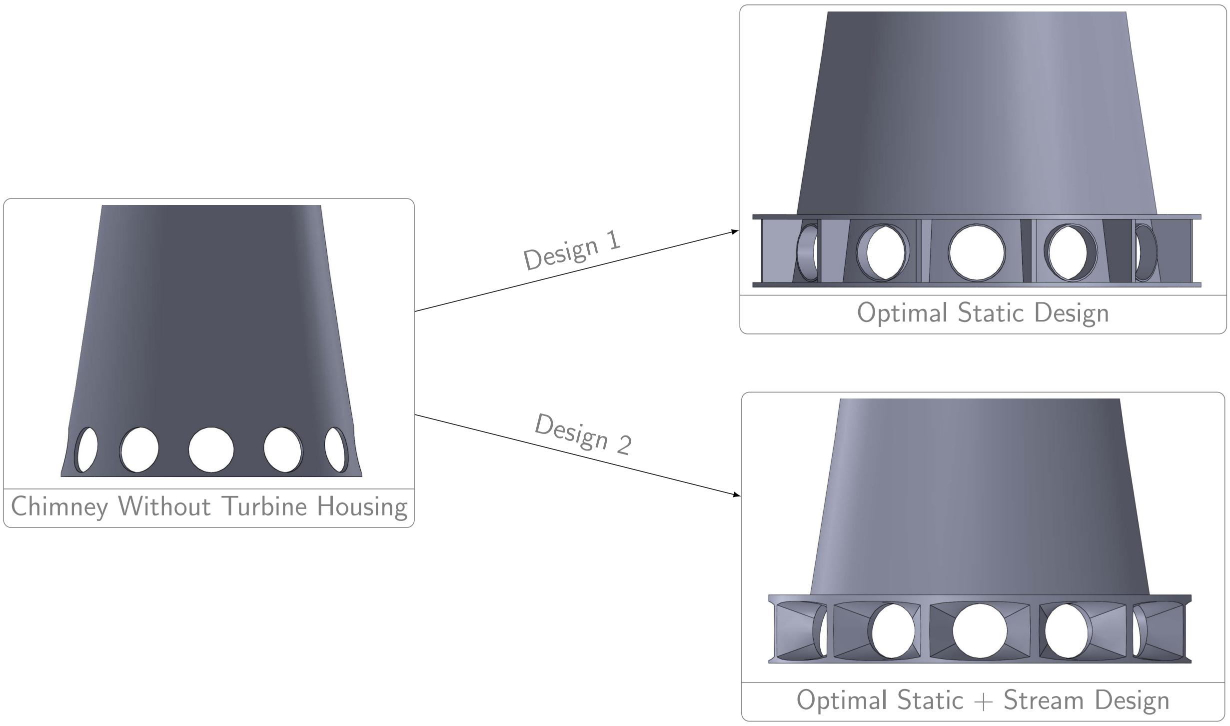

Figure 11.1: Design Variants of Turbine Area

Figure 11.2 shows the variation of the drag coefficient for flow in smooth and straight tubes of various cross sections.

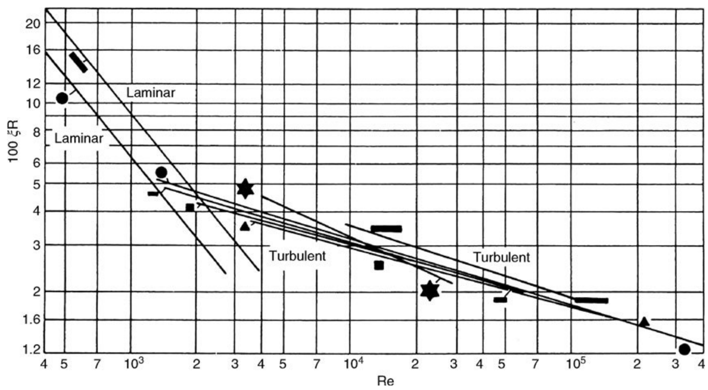

Figure 11.2: Drag Coefficient for Flow in Smooth Straight Tubes of Various Cross-Sections [B.43]

Due to the outer shape of the chimney base and limiting measures a compromise between structural costs, effort and the optimal circular shape for the smallest drag coefficient has led to the current design. This solution has been used to build the two CTA (white colour) and two pressure models (black colour) which are depicted in figure 11.3 with a cylindrical and a hyperbolic shape above the chimney throat, respectively.

The surface of all models exhibited a certain kind of roughness, on the outside much bigger than on the inside, which had to be smoothened before putting it into the wind tunnel. The roughness has been taken into account for the set-up of the numerical analysis which will be presented in the following chapter 12. The pressure model in the processed state is shown in figure 11.4, pictures of the unprocessed state can be found in appendix F.

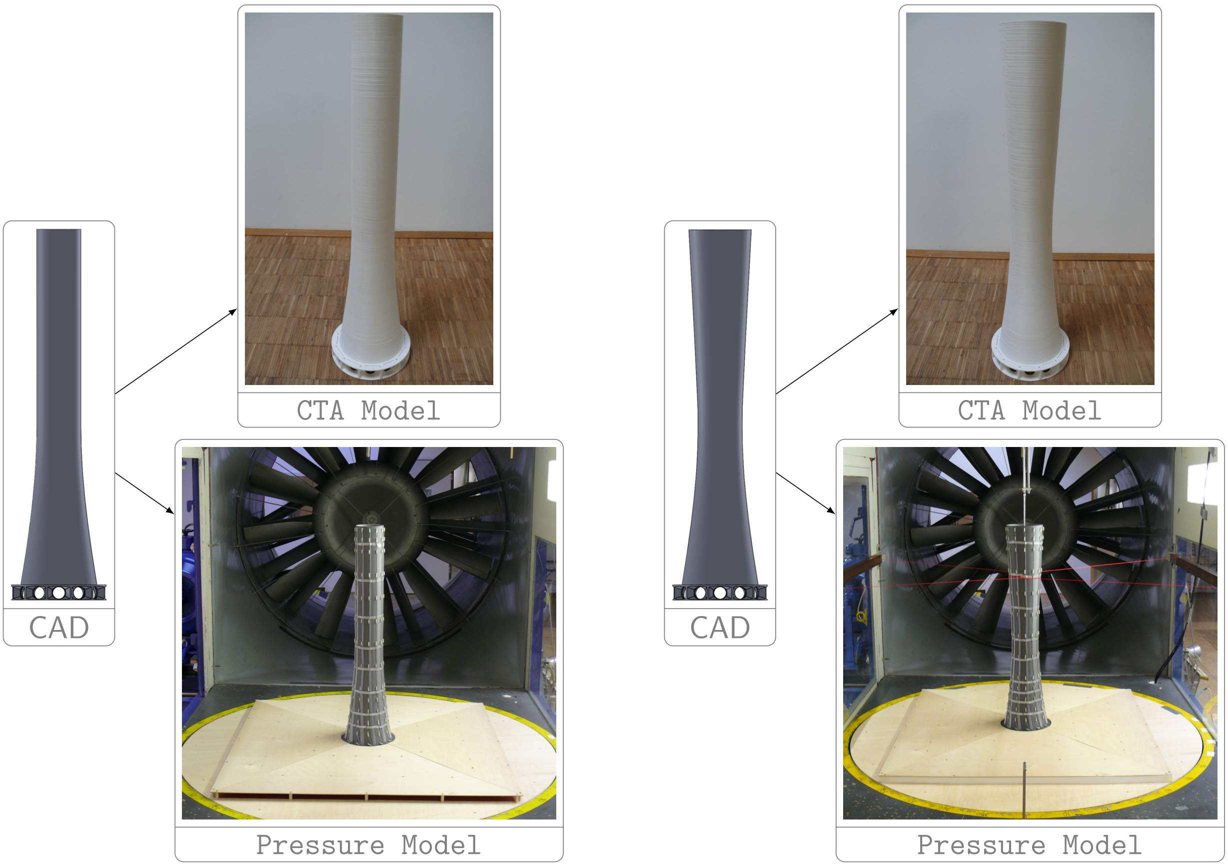

Figure 11.3: From Sketch to Model (Cylindrical Chimney (left), Diffuser Chimney (right))

Each brass tube connects the pressure point on the inside of the chimney model via PVC pipe with the pressure transducer located underneath the wind tunnel. Altogether 14 levels with 12 pressure points each, were prepared for all four models. Due to a limiting factor of 92 pressure transducers only this quantity of the 168 pressure points has been measured simultaneously. The configuration chosen for all measurements presented in this work can be found in table 11.1.

Material properties and dimensions of the chimney, collector, the turbine openings and the wind tunnel ground are gathered in table 11.2.

These properties are simultaneously the input parameters of the numerical model which will be presented within the next chapter.

11.1.2 Heat Source - Modelling of Buoyancy Effect

For the modelling of the buoyancy effect, namely natural convection, heating films made from silicon have been applied on the wind tunnel ground. With maximal temperatures of up to 200°C it will be possible to simulate the effect of heated up soil underneath the SC roof. Figure 11.5 shows the ten installed heating films, a PT 100 to measure the actual temperature of the corresponding heating film and a temperature control unit which has been located on the outside of the wind tunnel.

Another method to simulate the effect of temperature on the flow field of a SCPP model would

Processed State

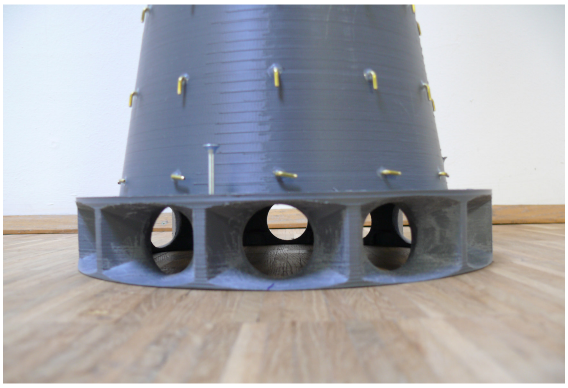

a) Transition Section (Turbine Area)

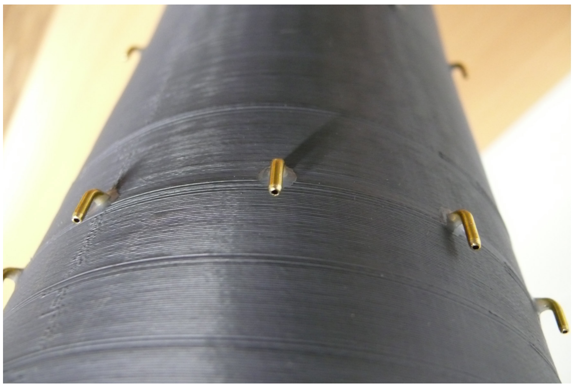

b) Pressure Tubes

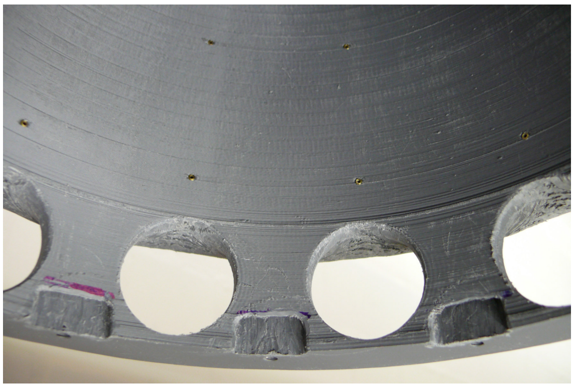

c) Recess for Pressure Tubes

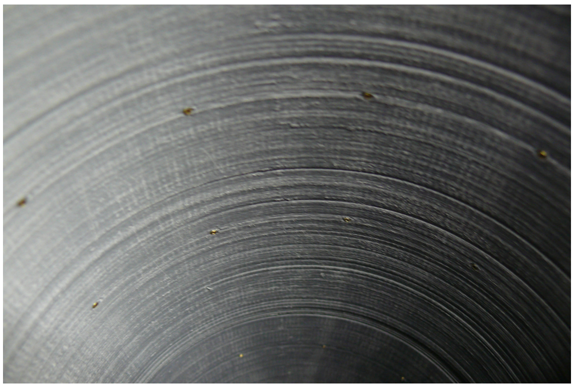

d) Inner Surface with Pressure Points

Figure 11.4: Pressure Model

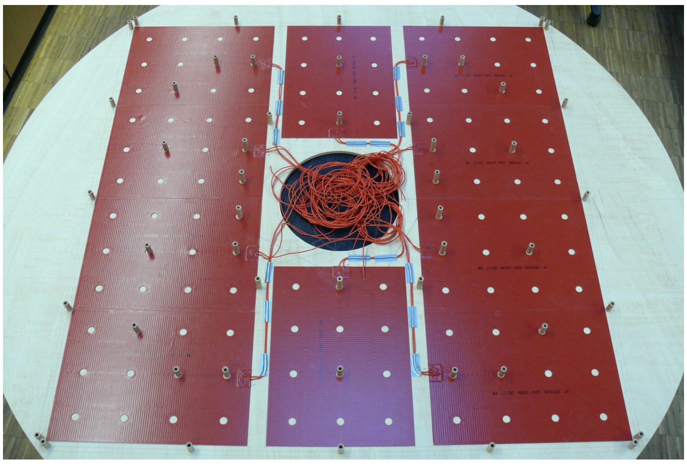

a) Heating Film

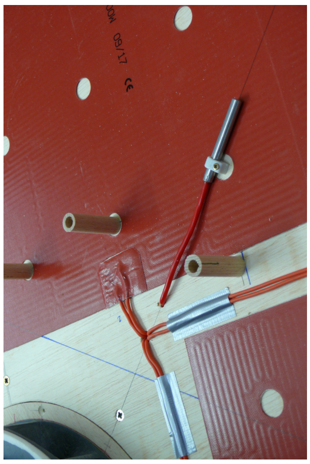

b) Temperature Sensor

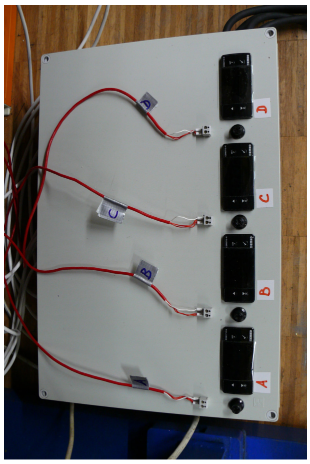

c) Temperature Control

Figure 11.5: Heating Film and Temperature Control

have been to simulate solar irradiance which can be found by [A.64] who used several types of lamps for his experimental set-up. For the current experiment the process of radiation has been neglected for the sake of simplicity.

Table 11.1: Pressure Points

Level	**Height**	**Quantity**	**Assigned**	**No.**[1]
-	mm	-	-	-
1	50	12	12	85÷96[2]
2	100	12	12	73÷84
3	150	12	12	61÷72
4	200	12	0	none
5	250	12	0	none
6	300	12	12	49÷60
7	400	12	0	none
8	500	12	12	37÷48
9	600	12	0	none
10	700	12	0	none
11	800	12	12	25÷36
12	900	12	0	none
13	950	12	12	13÷24
14	990	12	12	1÷12

[1] Measuring Point Numbers Clockwise starting at 0° (Stagnation Point).
[2] Measuring Points 87, 90, 93, 96 not assigned.

More information about the modelling of temperature effects and the process of buoyancy and natural convection can be found by [T.18], [B.31], [B.7], [A.120] and [A.153].

Table 11.2: Main Dimensions of Experimental Model

	Reference Values	**Unit**
Chimney		
Chimney Height	1.0	m
Chimney Diameter	variable[1]	m
Material	Industry Tec-B[2]	-
Collector		
Collector Height (Centre)	0.04	m
Collector Diameter	1.4	m
Collector Thickness	0.004	m
Collector Inclination	3	°
Material	plywood	-
Turbine Opening		
Turbine Diameter	0.033	m
Height Above Ground	0.02	m
Ground		
Material	fiberboard	-

[1] Profile of Chimney can be found in section 10.7.
[2] Material Properties in table F.1 of appendix F.

11.2 Redirecting Variants for the Transition Section

One of the main aims of this research is to find an optimal structural and therefore fluid mechanic solution for redirecting the flow inside the transition section and to improve the flow situation by reducing flow losses. In the standard case the redirection of the incoming flow streams after the turbine outlets happens due to the buoyancy effect and a suction effect due to the difference in density between the inlet of the SC and the SCH outlet. As it has been shown in chapter 9 this process can be improved by a conus structure inserted in the middle of the chimney base. This concept has been favoured by many authors so far but additional former research has shown that there are different concepts and five of them will be presented here. Two of them are well known from CTs where the main aim is not to increase the energy output but to diminish effects of wind on the cooling capability and the insertion of smoke gases into the main flow stream and to achieve a perfect mixing of the main and smoke gas stream.

11.2.1 Extension of Turbine Opening

Starting with a variant which extends the turbine outlets that the process of mixing of the fluid streams leaving each turbine will be spatially distributed inside the chimney base. Figure 11.6

shows this concept for a design study of a SCPP where only a quarter of the SC has been built to adapt to ambient conditions and to reduce material consumption and therefore costs.

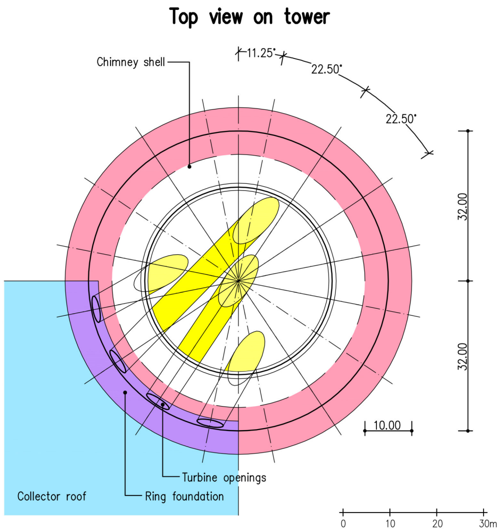

Figure 11.6: Extension of Turbine Opening [A.106] (courtesy of W.B. Krätzig)

Four turbines are situated in the quarter of the circumference, nearly the same quantity as it is the case for the designed wind tunnel model which will be presented in this chapter. In the CTs technology these ducts are used for the discharge of exhaust gas into the CT. This concept will become more challenging if not only four but 12 or 16 turbine flows need to be redirected. The arrangement of all ducts and therefore outlets is a classical process of optimization. The ducts in general have a cut end to allow the leaving fluid to relax and additional small guide vanes at the exit can improve the process of redirecting the flow. A further improvement of the flow situation via extensions of the turbine openings will lead to the case of a complete redirection of each flow stream, to the vertical direction, cf. variant of local redirection, facing the same problems of how to distribute 12 or 16 stream tubes within the SCH base.

11.2.2 Local Redirection

The following variant redirects each flow stream leaving the turbines separately directly after each turbine outlet. The process of mixing will not be guided by any structural measures as it has been the case by the first variant. To find the optimal solution, namely the right bend of each duct, for example [T.12] presents the streamline motions for different bend configurations.

"In a curved tube, fluid motion is not everywhere parallel to the curved axis of the tube (...), secondary motions are generated, the velocity profile is distorted, and there is increased energy dissipation. However, curving of a tube increases the stability of flow, and the critical Reynolds number increases significantly" [B.28].

Therefore figure 11.7 shows the process of flow separation and the development of a secondary flow inside a curved pipe.

One measure of this effect is the Dean number De which is the Reynolds number Re modified by the pipe curvature. For this reason the secondary motion appearing as counter-rotating vortices

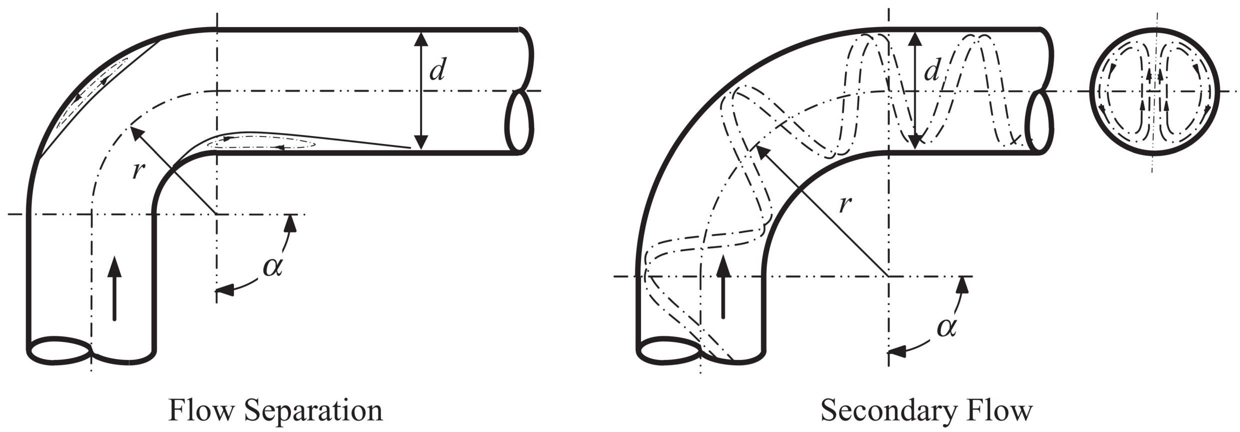

Figure 11.7: Curved Pipe Flow [B.37]

are called *Dean vortices*. In our case not only the formation of a secondary flow is of interest but also the losses accompanying this kind of tube flow.

"The pressure loss in pipe bends may be thought of as made up of three components. One component is the pressure loss due to ordinary surface friction that corresponds to fully developed flow in a straight pipe having the same length as the centreline of the bend. A second component is due to a twin-eddy secondary flow superimposed on the main or primary flow due to the combined action of centrifugal force and frictional resistance of the pipe walls. A third component is due to separation of the main flow from the inner and outer radius of the bend and subsequent expansion of the contracted stream. For bends of small radius of curvature, flow separation and secondary flow dominate. For bends of large radius of curvature, ordinary surface friction and secondary flow prevail" [B.37].

More on these effect can be found by [A.151], [A.8], [A.163], and [A.2].

11.2.3 Global Redirection

The most common variant is the cone structure known from the prototype SCPP of Manzanares. Flow streams leaving the turbine outlets can interact with each other before they are redirected as one big flow stream in the middle of the chimney base. This symmetric concept will be used as a reference in the course of this work. This concept only lacks of the ability to deal with asymmetric inflow conditions due to, e.g. ambient wind, which ensures that there is a typical velocity distribution on the in- and outside of the SCH. Improvements of this simple and efficient cone structure will be discussed in the following subsections. Figure 11.8 shows three concepts dating back to 1995 when an arrangement of several turbines with vertical axes had been favoured.

These pictures underline the importance of this investigation and the fact that still no perfect solution to redirect the flow with minimal losses has been found so far.

11.2.4 Windbreaker

The simplest structural way is the implementation of a windbreaker in shape of a wall right in the middle of the chimney base. This variant has nothing to do with the IGVs presented in former

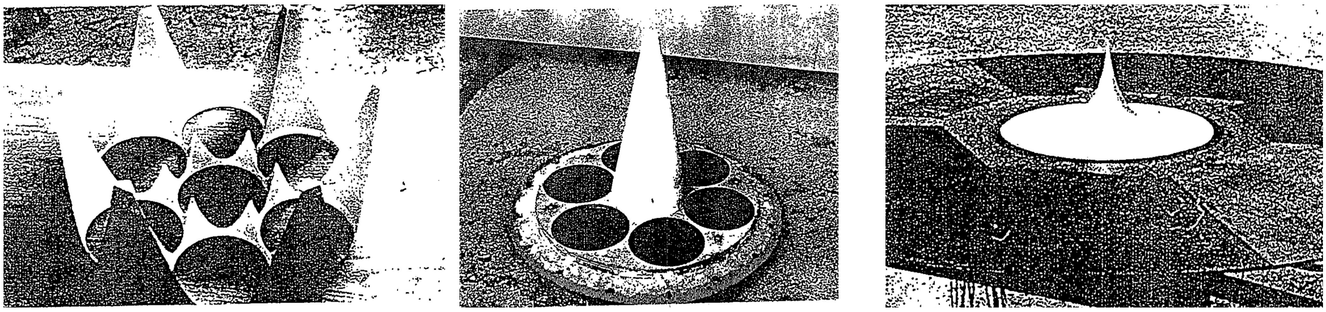

Figure 11.8: Wind Tunnel Models of Former Studies [A.160]

chapters which only guide the incoming flow stream into the SCH but in general do not cause a blocking of entering ambient wind or redirect the flow stream to the vertical direction. Here different variants divide the full circular area into two (180°), three (120°) or four (90°) parts. Besides the layout, the height plays an important role. Therefore Y- and X-shaped windbreakers with different heights have been built and investigated in the current wind tunnel study.

Some numerical analysis of the influence of windbreakers on the flow inside CTs can be found by [A.169] and [A.176].

11.2.5 Combination

The following variant combines the cone structure (global redirection) and the windbreaker. Structural simplicity and low material consumption are key figures to achieve an optimal solution for the flow situation inside the transition section. Figure 11.9 shows the combined structure for the application inside a CT with additional outer deflectors.

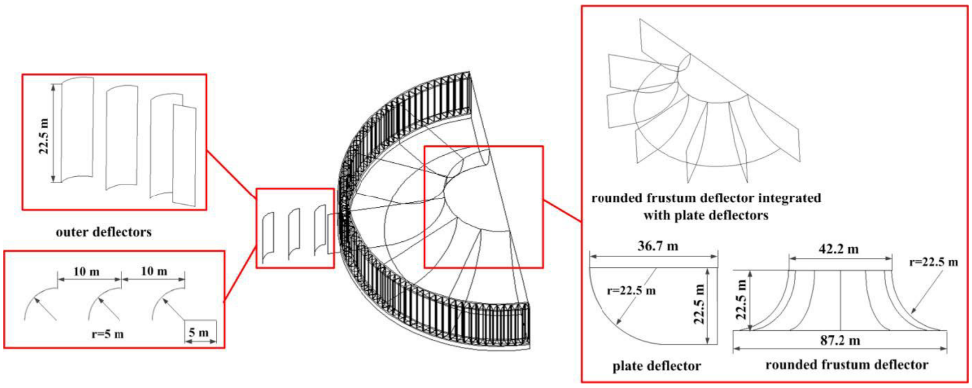

Figure 11.9: Installation for Cooling Towers [A.172]

11.2.6 Designed Variants

Figures 11.10 and 11.11 show the five concepts of redirecting structures which have been designed and built for the wind tunnel study presented within this chapter. All variants have been varied in outer measures like height, radius, angle and length as explained in the table notes.

I - Extension of Turbine Opening[1]

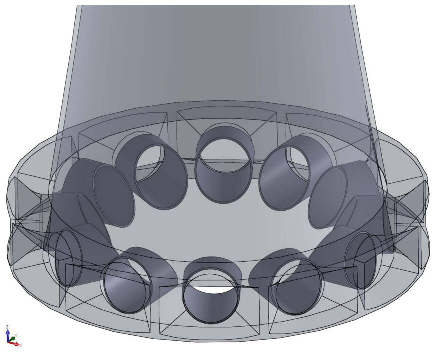
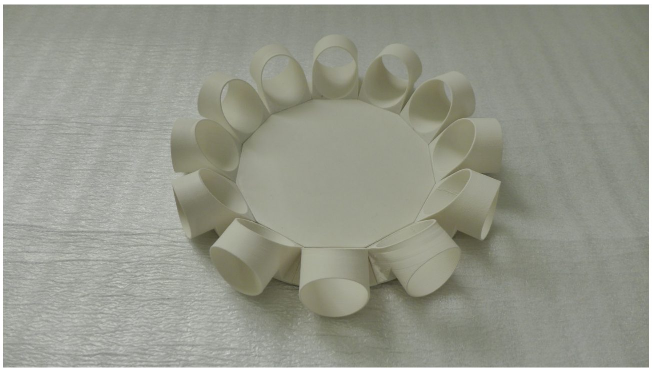

11: 40/30, **12**: 40/45, **13**: 47/30, **14**: 48/45

II - Local Redirection[2]

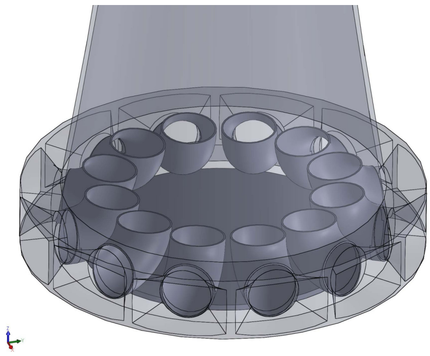
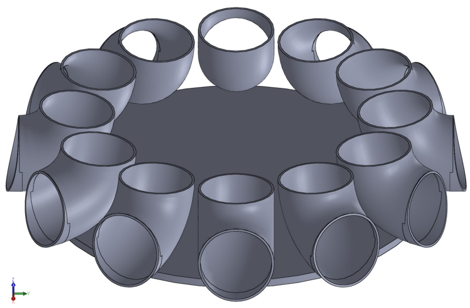

21: 40/40 (crooked), **22**: 43/60 (crooked), **23**: 43/80 (crooked),
24: 50/40, **25**: 50/60, **26**: 50/80

III - Global Redirection (Cone)[3]

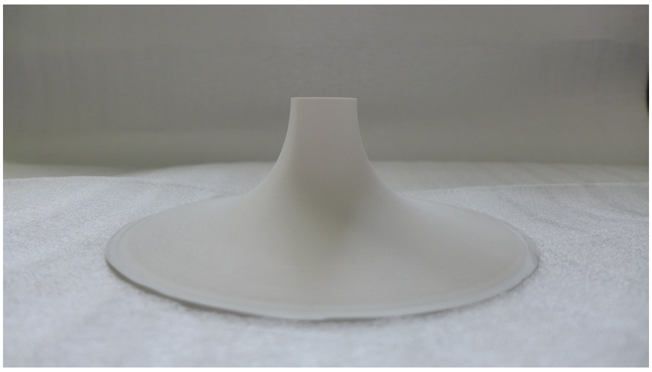
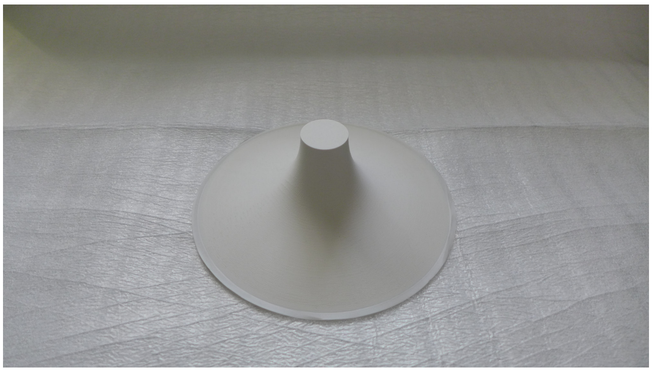

31: 40/10, **32**: 40/15, **33**: 40/20, **34**: 60/10, **35**: 60/15, **36**: 60/20, **37**: 80/10, **38**: 80/15,
39: 80/20, **310**: 120/10, **311**: 120/15, **312**: 120/20, **313**: 60/30, **314**: 60/45, **315**: 80/45

[1] Length in mm / Angle at the End in $^\circ$.
[2] Length in mm / Height in mm.
[3] Height in mm / Radius in mm, Height in mm / Angle in $^\circ$.

Figure 11.10: Configurations of Redirecting Variants - Part 1 of 2

IV - Windbreaker[4]

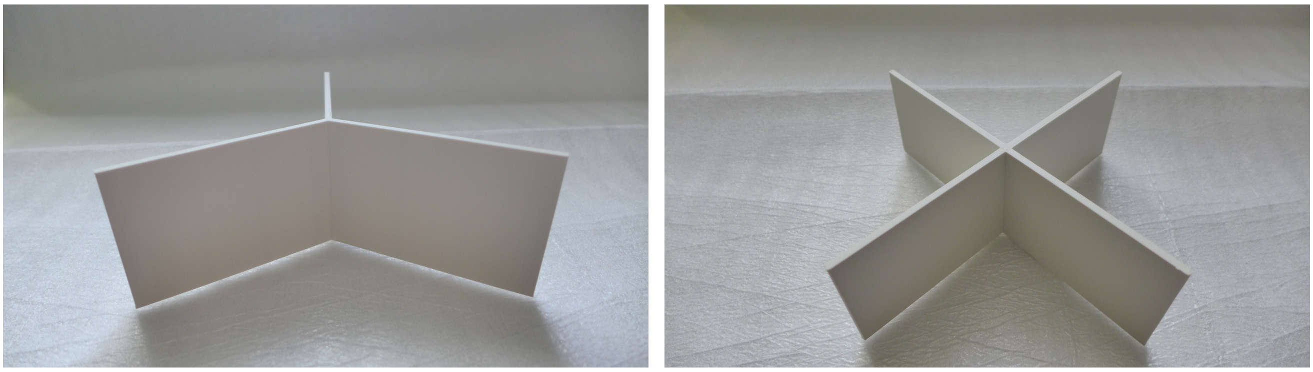

41: 40 (Y), **42**: 60 (Y), **43**: 80 (Y), **44**: 40 (X), **45**: 60 (X), **46**: 80 (X)

V - Combination[5]

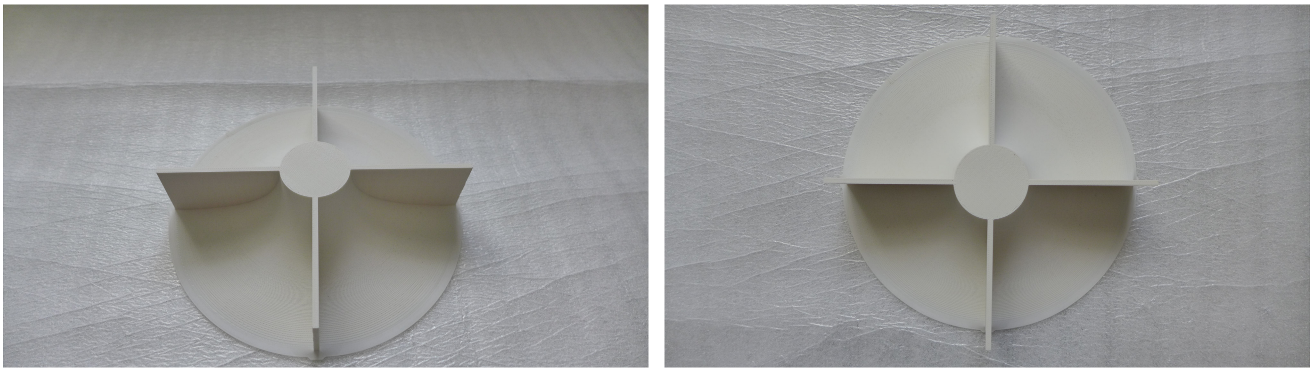

51: 40/10, **52**: 40/15, **53**: 40/20, **54**: 60/10, **55**: 60/15,
56: 60/20, **57**: 80/10, **58**: 80/15, **59**: 80/20

[4] Height in mm.
[5] Height in mm / Radius in mm.
[Y] Y-Shaped.
[X] Cross-Shaped.

Figure 11.11: Configurations of Redirecting Variants - Part 2 of 2

11.3 Asymmetric Inflow Conditions

The effect of asymmetric inflow conditions has already been discussed in the course of this work. Four situations where this needs to be taken into account are the influence of ambient wind (i), due to installations or flow barriers at the periphery of the SC (ii) and in the case of turbine malfunction or during the phase of construction or maintenance (iii). The fourth and always present case is the influence of the sun movement which can be seen in the numerical analysis of the prototype from Manzanares presented in chapter 9. The wind tunnel model will of course give some insight into the influence of wind on the flow field within the transition section and the SCH. [A.148] shows in his publication that due to wind a drop by 10% of annual plant power output can occur and therefore cannot be neglected. For the case of flow barriers at the periphery and the influence of maintenance a simple solution how to implement these effects into the wind tunnel model has been developed and will be explained here briefly.

11.3.1 Flow Barriers at the Periphery

Flow barriers at the periphery of the SC can have a natural reason like growing vegetation depicted in figure 2.3 or can be built like fences or wind breaking walls. Some research has been performed with a partially opened SC which diminishes the effect of wind on the flow situation underneath the SC roof. Flow vectors for such a configuration are shown in figure 11.12.

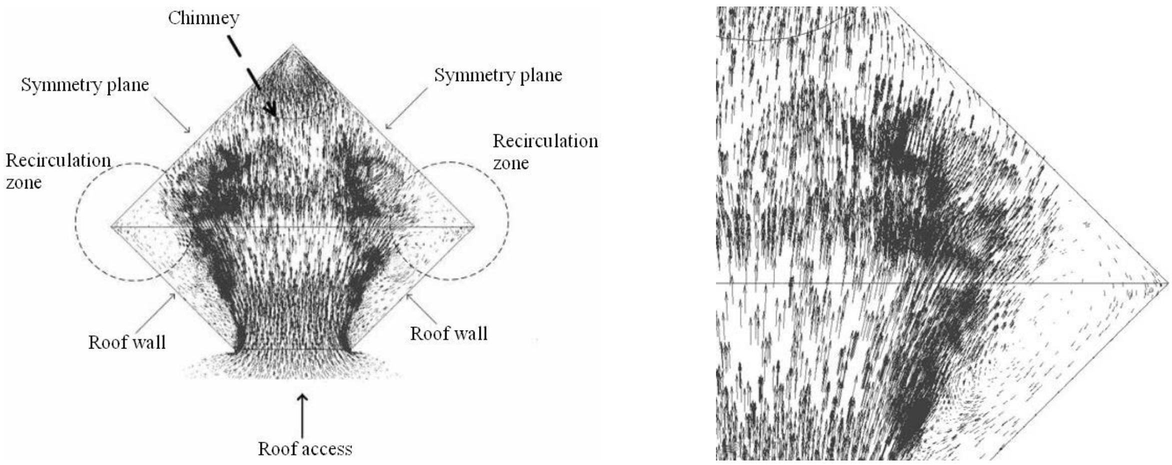

Figure 11.12: Partially Opened Solar Collector Inlet [T.15]

In a simplified manner this effect has been implemented into the wind tunnel study by closing one or more sides of the SC shown exemplarily in figure 11.13 for the current model.

All in all three variants have been tested. Closing the lee side of the SC entrance (i), closing the windward side (ii) and closing both (iii). Also a height adjustable air entrance has been part of former research [A.23] which could help to reduce the effect of wind on the flow field. A numerical analysis of airflow and particle collection by vegetative barriers where porous elements have been used to represent fences or even trees can be found by [A.61].

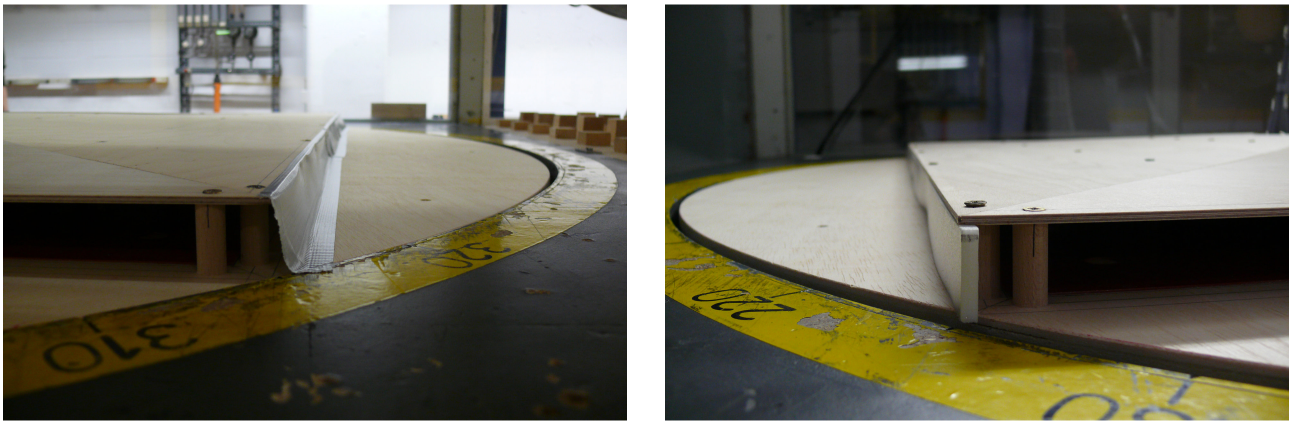

Figure 11.13: Closed Solar Collector Sides

11.3.2 Turbine Malfunction or During Phase of Construction or Maintenance

Another situation where highly asymmetric flow conditions can be found within the transition section is the case of malfunction of one or more turbine(s). In the phase of construction or maintenance an impact of the changed flow situation on the efficiency of the redirecting variants will be found and should be taken into account. For the current model a serious consideration of experimentally modelling the influence of the turbines and their effect on the flow field has been performed and will be explained in appendix F.

11.4 Measuring Devices

For the current wind tunnel study two measurement techniques, namely CTA with two 3D probes, commonly known as hot-wires, and pressure measurements have been used. The CTA technique inhibits the opportunity to measure point wise with a high sampling rate whereas pressure measurements can be used to measure at a huge quantity of pressure points simultaneously. Pressure measurements are always accompanied by pitot-static tube readings for measuring a reference velocity to develop pressure coefficients afterwards. A second pitot-static tube has been utilized for the gathering of the flow velocity underneath the SC to have a point of reference for the interpretation of the gained results.

The hot-wire probes used for the current study are two 3D probes of the type 55P95. "The sampling rate is determined by the maximum frequency component in the flow. The sampling theorem states that the sampling rate must be at least twice the highest frequency component in the input signal" [S.12]. Therefore a sampling rate of 2 kHz (default) and 10 kHz for high flow temperatures has been used throughout all presented measurements.

Figure 11.14 shows the traverse, the hot-wire probes have been attached to and their position inside the wind tunnel model.

The top one has been positioned in the middle of the chimney outlet 60 mm below the upper rim (z = 940 mm). The second one is placed close to the throat at a height of z = 500 mm.

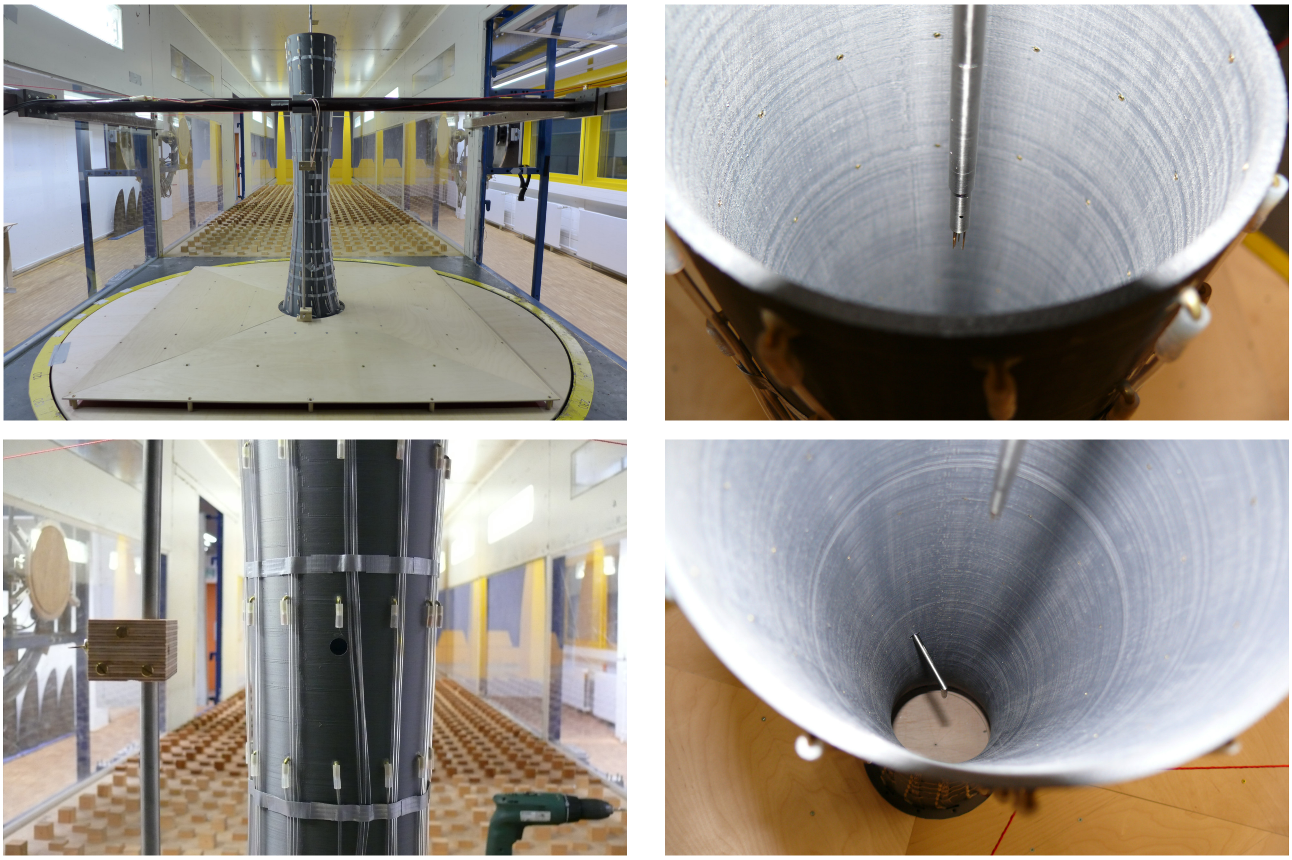

Figure 11.14: Hot-Wire Probes Installed Inside the Chimney Model

The orientation of the hot-wire probe has been kept constant throughout all measurements. A temperature correction has been performed with a temperature probe attached to the upper hot-wire probe.

More details on the pressure measurement technique used at the wind tunnel facility in Bochum can be found by [T.16] and in appendix F. For more information on different flow measurement techniques and their merits and demerits please see [B.41].

11.5 Results

The measuring program includes six investigations, namely:

I) Effect of ambient wind with different velocities without temperature.
II) Investigation of the buoyancy effect without the influence of ambient wind.
III) Combined effect of wind and temperature both are varied.
IV) Influence of closing one or two sides of the SC periphery.
V) Velocity measurements on the inside of the chimney model at different positions.
VI) Influence of the different configurations on the flow parameters.

Not all gained results will be presented within this chapter but in appendix F respectively.

11.5.1 Cylindrical Chimney (CC)

In this subsection the results for the CC model will be presented. Therefore figure F.6 shows the circumferential pressure distribution of the internal pressure coefficient c_{pi} for the mean and Root Mean Square (RMS) value. One result for each of the three main variants, namely the local redirection (No 39), the windbreaker (No 45) and the combination (No 57(2)) will be given here. All other results can be found in the appendix F.

The general distribution shows a distinct course for all tested variants both for the mean and RMS values. A perfect symmetric distribution due to a symmetric set-up cannot be obtained for any configuration. One of the main reasons is a slight perturbation of the wind profile within the wind tunnel. Also small deviations of the model itself cannot be ruled out. Both will not effect the general findings of this investigation but have been taken into account by the interpretation of the presented results. At the lower levels $(1 \div 3)$, the distribution shows an increase in pressure coefficients, reduction of the mean pressure coefficients and an increase for the RMS, for the area between 90 and 270 ° for most of the configurations. While levels $(6 \div 13)$ exhibit a nearly constant course for all configurations. The lowest coefficients and the most significant distribution for the mean and on the other hand the highest RMS values can be obtained at level 14 which is close to the upper rim of the chimney.

One of the main aims of a redirecting variant is to improve the flow situation inside the chimney for all levels. Someone can see that the smoothest results both for mean and RMS values have been obtained with the installation of the windbreaker (No 45) and the combination (No 57(2)), so special focus was put on these two configurations afterwards.

The last two plots of the pressure coefficient show the averaged course of $c_{pi,mean}$ and $c_{pi,sigma}$ for all tested variants. Additionally, the scattering found in this measurements is plotted. For the sake of clarity three selected levels, namely 1 (low z), 6 (medium z) and 11 (high z) are given. Someone can see that in the lower part of the chimney close to the transition section a large scattering is present. This is due to the effect of the redirecting variant and its impact on the pressure development inside the chimney. Already at level 6 no such dominant scattering can be found which is also true for level 11 close to the outlet of the chimney. The large variation in mean and RMS values prove the necessity of a well-chosen redirecting variant to reduce flow losses and improve the flow situation inside the chimney.

Table 11.3 gathers the measured mean velocities and their RMS values at the upper measuring point where u corresponds to the vertical velocity, v in streamwise direction and w perpendicular to it.

The velocity inside the chimney depends on the wind speed adjusted in the wind tunnel. Therefore the respective velocity at the pitot static tube v_{pra} is listed to show that the difference in velocities is not due to higher wind speed but due to the effect of the different variants on the fluid flow. Additionally, the ratio of the current value v_{mean}/v^1_{max} and v_{max} found the combination variant (No 57(2)) are listed. A maximal deviation of 10% from the maximum obtained velocity can be found.

Another aim of the improvement of the flow situation should be the reduction of the v and

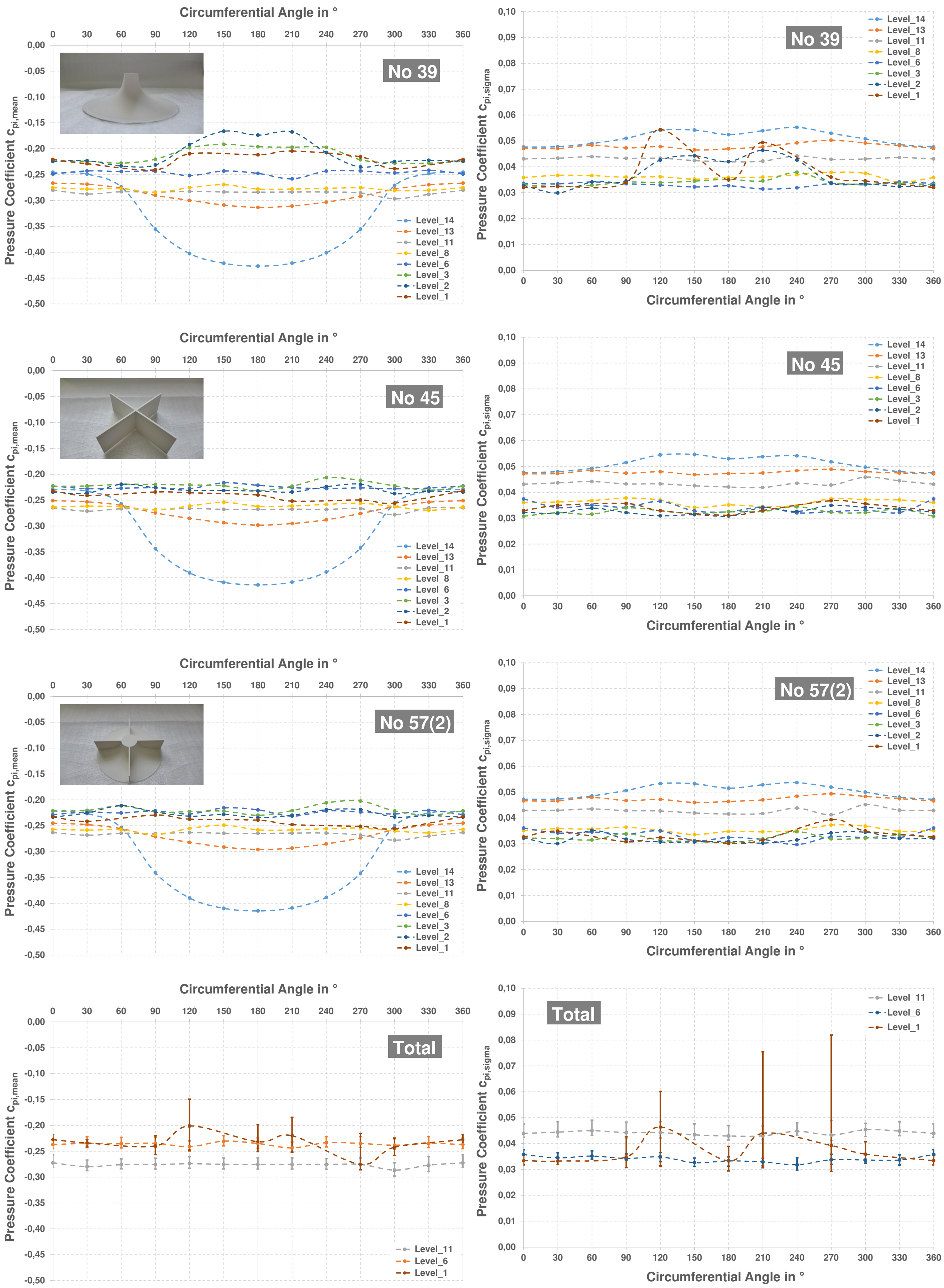

Figure 11.15: Circumferential Distribution of Internal Pressure Coefficient $c_{pi,mean}$ and $c_{pi,sigma}$ for Different Configurations

Table 11.3: Velocity Values at z = 940 mm for Different Configurations

Configuration No	$v_{u,mean}$ m/s	$v_{u,sigma}$ m/s	$v_{v,mean}$ m/s	$v_{w,mean}$ m/s	v_{Pra} m/s	v_{mean}/v^1_{max}
32	4.631	0.544	-0.433	-0.246	15.833	0.94
39	4.692	0.504	-0.502	-0.172	15.864	0.96
311	4.659	0.511	-0.694	0.003	15.748	0.95
313	4.542	0.568	-0.851	-0.170	15.891	0.93
43	4.588	0.528	-0.823	0.029	15.699	0.93
43(2)[3]	4.493	0.467	-0.390	-0.416	15.815	0.92
44	4.569	0.476	-0.677	-0.202	15.945	0.93
45	4.529	0.422	-0.967	0.064	15.846	0.92
51	4.405	0.478	-0.950	-0.208	15.860	0.90
55	4.665	0.432	-0.553	-0.132	15.673	0.95
55(2)[3]	4.445	0.441	-0.626	-0.174	15.337	0.91
57	4.739	0.428	-0.585	-0.074	15.714	0.97
57(2)[3]	**4.910 (4.962)**[2]	**0.421 (0.433)**[2]	**-0.556 (-0.542)**[2]	**-0.098 (-0.105)**[2]	**15.757 (16.013)**[2]	**1.00**
59	4.697	0.428	-0.754	-0.065	16.129	0.96

[1] Maximum velocity taken from the combination variant (No 57(2)).
[2] Values in brackets taken from repetition measurement.
[3] (2) marks a changed incident flow direction. Flow on the field between the variant walls.

w flow components to increase the performance of the SCH due to higher outflow velocities in the positive z direction. Someone can see that the implementation of the combination variant (No 57(2)) shows for both components low values compared to the others but not the lowest ones which led to a first selection process where configurations showing no good performance have been discarded for the ongoing research. Low material input, a general good performance, low RMS values, homogenizing of the pressure distribution, low turbulence, no anisotropy effects and high velocities have led to the decision of considering only selected configurations as can be seen in the subsection F.5.1 of the appendix.

The effect of closing one or two sides of the SC on the pressure distribution and the velocity inside the chimney will be discussed in a next step. Figure 11.16 shows the influence of different set-ups for the SC on the mean pressure coefficient distribution for the reference case without any redirecting variant inside the transition section.

All courses indicate an unstable pressure distribution for lower levels and a shift to higher (less

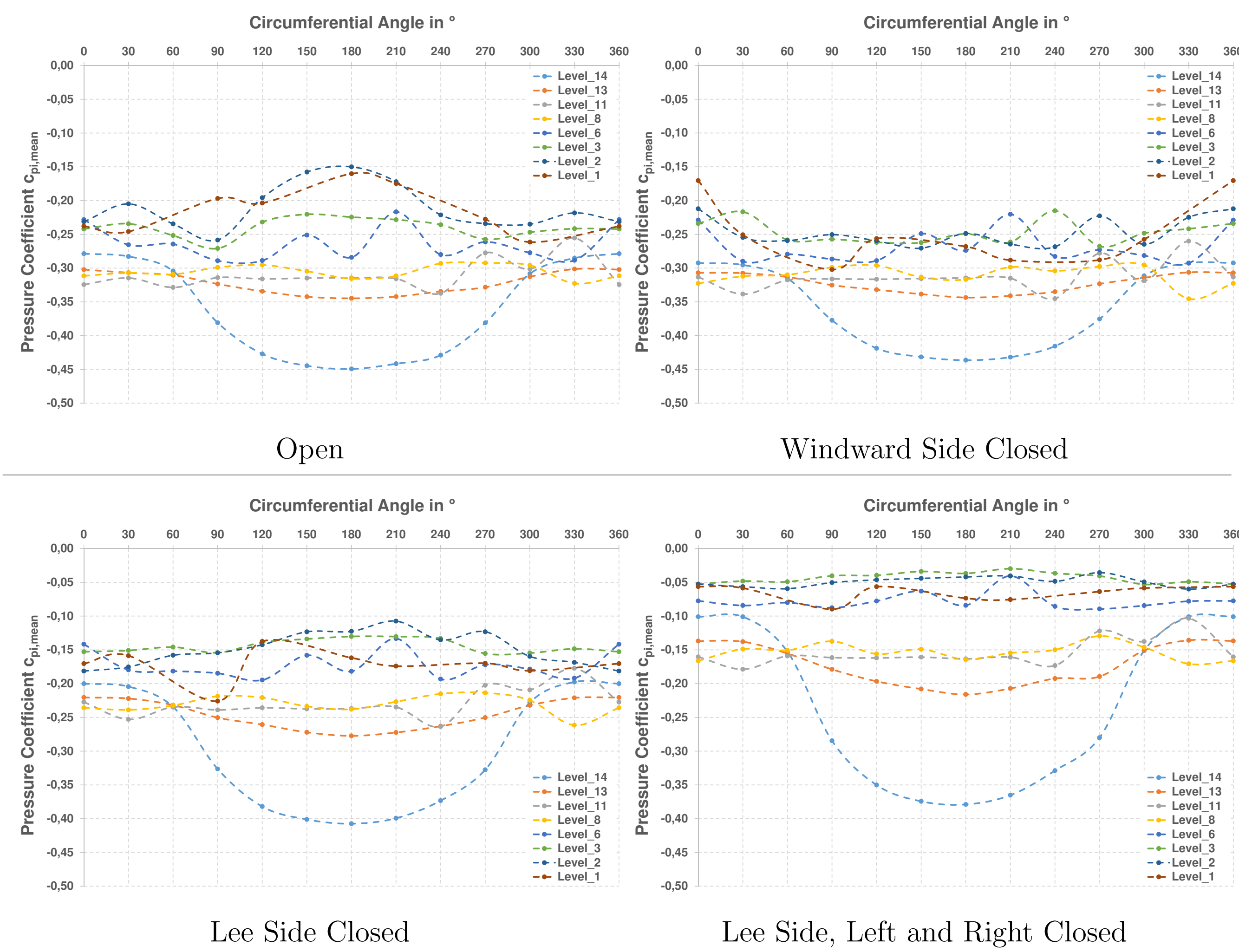

Figure 11.16: Circumferential Distribution of Pressure Coefficient $c_{pi,mean}$ for Open and Closed Case - Default Configuration Without Redirecting Variant

negative) coefficients caused by closing one or three sides of the SC entrance. The influence of unsymmetric inflow conditions as explained before can be detected throughout all results leading to nonsymmetric pressure distributions. Therefore the configuration with the combination variant (No 57(2)) has been chosen to illustrate this special set-up and its influence on the pressure distribution because the gained results have shown to be more efficient than the reference case.

Figure 11.17 shows the circumferential pressure distributions both for mean and RMS values.

The influence of closing the windward or lee side shifts the course of the distribution depending on the current situation. Whereas for closing the windward side the pressure coefficient shows more negative values for all levels except level 14 where the influence of the outer wind flow still dominates. The impact of closing the lee side of the SC is even more pronounced. The pressure coefficient rises to higher values for all levels. For the RMS values still a nearly constant distribution can be found for both situations. The instability in the RMS has been diminished compared to the reference situation with open SC sides.

The measured vertical velocity (u-component) indicates the strong influence of this set-up with the highest velocities found by closing the lee side of the SC due to the air trap effect. Table 11.4

Windward Side Closed

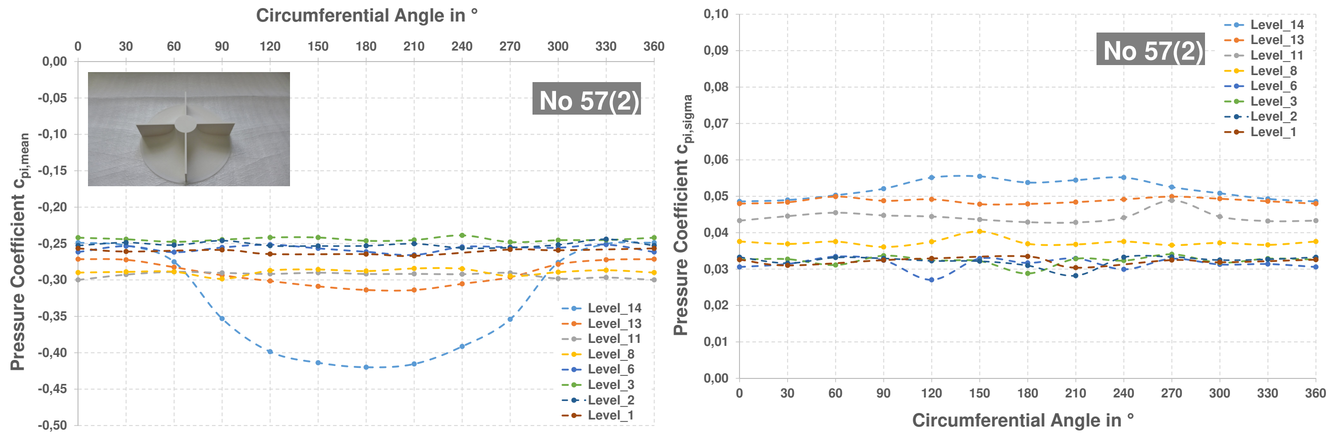

$$v_{mean} = \mathbf{4.570\ (4.529)}\ m/s,\ v_{sigma} = \mathbf{0.422\ (0.410)}\ m/s,\ v_{Pra} = \mathbf{15.813\ (15.757)}\ m/s$$

Lee Side Closed

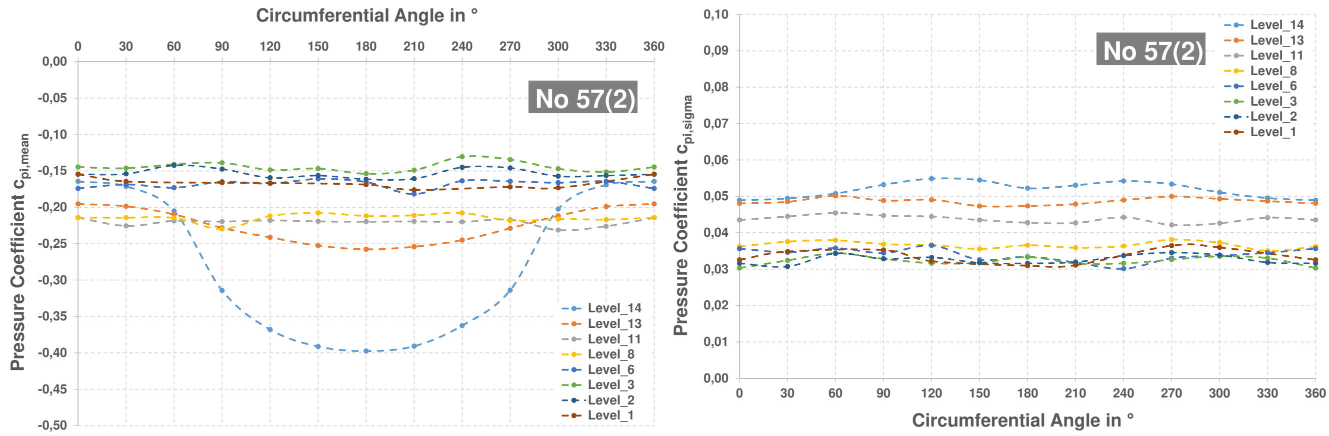

$$v_{mean} = \mathbf{5.482\ (5.583)}\ m/s,\ v_{sigma} = \mathbf{0.438\ (0.432)}\ m/s,\ v_{Pra} = \mathbf{15.534\ (15.799)}\ m/s$$

Figure 11.17: Results for Combination Variant (No 57(2)) - Closed Set-Up (Values in Brackets are for the Repetition Measurement)

gathers the measured velocities for three redirecting variants which confirms this statement.

Due to only small temperature gradients within the wind tunnel measurements for the cylindrical chimney no results for the influence of temperature and therefore buoyancy will be presented here. Instead a discussion on the impact of temperature on the performance of the diffuser chimney will be given within the next subsection.

Table 11.4: Velocity Values for Different Set-Ups

Configuration No	v_{mean} m/s	v_{sigma} m/s	v_{Pra} m/s
Windward Side Closed			
45	4.066	0.389	15.786
55	3.997	0.401	15.626
55(2)	4.343	0.425	15.726
Lee Side Closed			
45	4.922	0.403	15.678
55	4.927	0.426	15.636
55(2)	5.020	0.466	15.329

11.5.2 Diffuser Chimney (DC)

Results for the diffuser chimney will be presented within this subsection. Starting with the circumferential pressure distributions of the mean and RMS values of the pressure coefficient for different configurations. The mean pressure coefficients are given in figure F.13 and the RMS values in figure F.14 respectively.

As it has been the case for the cylindrical chimney, current results show the huge impact of the redirecting variants on the pressure distribution. The effect extends from the levels close to the transition section till level 6. At level 8, which corresponds to the chimney throat, an effect on both mean and RMS values cannot be found. The last two plots of the pressure coefficient show the averaged course of $c_{pi,mean}$ and $c_{pi,sigma}$ for all tested variants as it has been introduced by the cylindrical chimney. The scattering in the lower part of the chimney is way more pronounced than in the upper chimney region. Already at level 6 no such dominant scattering can be found which is also true for level 11 close to the outlet of the chimney. Windbreaker (No 45) and the combination variants (No 55), (No 57(2)) and (No 59) show good results for the pressure distributions whereas only the first three for the velocity values which are collected in table 11.5.

The highest mean velocity values can be obtained with the combination variant (No 57) and (No 57(2)) respectively. For the RMS value and the v-component either variant (No 45) or (No 57(2)) show the best results. Variant (No 55) exhibits the lowest w-velocity values but does not give any high values for the main vertical velocity component u.

The influence of temperature, namely the buoyancy effect, has been taken into account for the following measurements. Therefore a temperature gradient of $\Delta T = 115K$ has been generated. The ten installed heating films were heated up to 140°C which has led to the development of smoke in the first few minutes of this experiments due to a burning of the glue used for attaching the heating films to the wind tunnel floor. The smoke plume is depicted in figure 11.20 and has been a good indication, that the chimney effect worked fine.

The air temperature inside the chimney is given in figure F.12 (left) which shows the phases of heating and cooling down of the heating films for an exemplarily measuring time of 100 seconds.

This effect is due to the response time of the PT 100 probes attached to the heating films which transfer the necessary information about the current temperature to the control unit. A smaller response time would have led to a decrease in amplitude for the case without any ambient wind but would have been counter-productive in the case of additional wind because of the cooling of the heat films. One velocity history plot for the main investigation with $\Delta T = 115K$ is also given in figure F.12 (right) to show the influence of the temperature course on the gained velocity signals.

It can be seen that the velocity signal fluctuates corresponding to the fluctuations of the temperature. Due to thermodynamic effects a vertical velocity component in the size of 0.35 m/s even without any influence of temperature within the wind tunnel facility has been found and has not been filtered in the presented results.

Figure 11.22 shows the temperature distribution on top and underneath the SC and of the plume rising up from the chimney outlet.

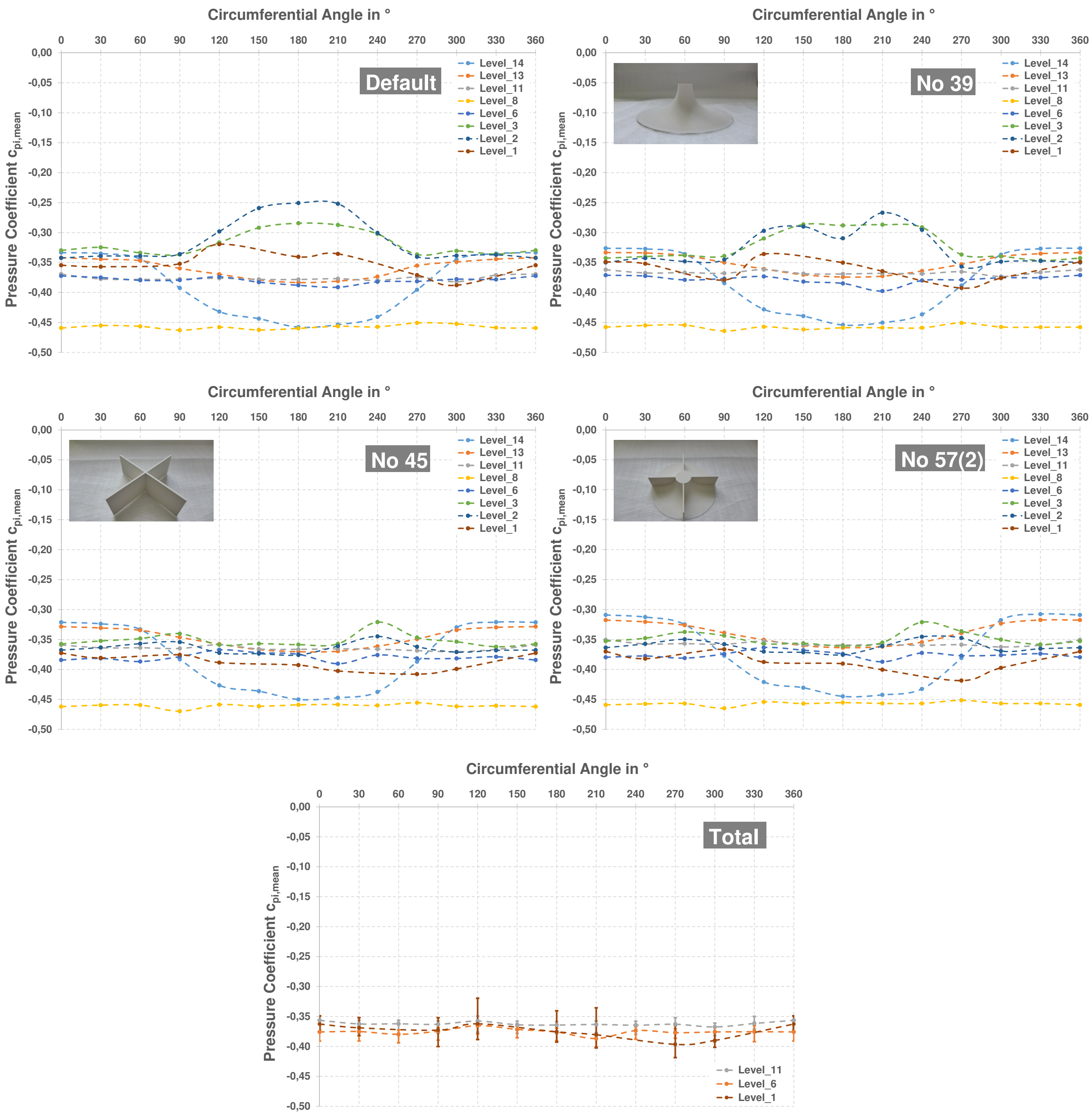

Figure 11.18: Circumferential Distribution of Internal Pressure Coefficient $c_{pi,mean}$ for Different Configurations

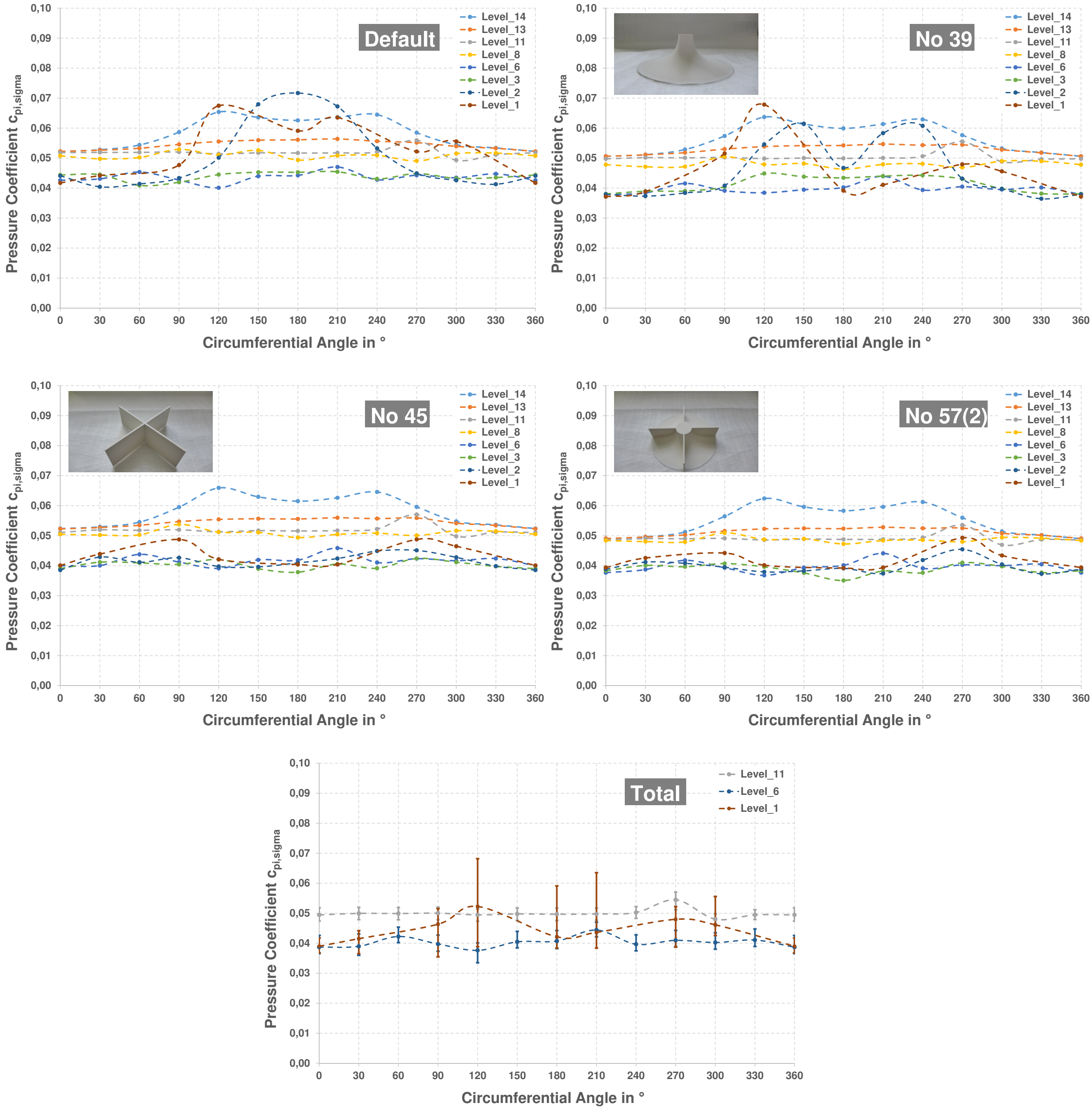

Figure 11.19: Circumferential Distribution of Internal Pressure Coefficient $c_{pi,sigma}$ for Different Configurations

Table 11.5: Velocity Values for Different Configurations and Set-Ups - Diffuser Chimney

Configuration No	$v_{u,mean}$ m/s	$v_{u,sigma}$ m/s	$v_{v,mean}$ m/s	$v_{w,mean}$ m/s	v_{Pra} m/s
			Open		
Default	3.383	0.831	-1.405	0.814	16.013
39	3.875	0.738	-0.406	-0.289	15.981
45	3.856	**0.554**	-0.627	-0.209	15.624
55	3.899	0.612	-0.729	**-0.146**	15.773
57	**4.172**	0.596	-0.399	-0.319	15.969
57(2)	3.512	0.683	**-0.278**	-0.484	15.773
59	3.450	0.705	-1.640	1.010	15.764
			Windward Side Closed		
Default	3.368	0.840	-0.368	-0.227	15.960
39	3.548	0.742	-0.318	-0.341	15.929
45	3.791	0.583	-0.352	**-0.218**	15.824
55	3.772	0.635	-0.457	-0.220	15.859
57	**4.199**	0.592	-0.297	-0.296	15.973
57(2)	4.028	**0.560**	**-0.273**	-0.368	16.070
59	3.303	0.640	-1.663	1.035	15.786
			Lee Side Closed		
Default	4.119	0.796	-0.764	-0.419	15.730
39	4.271	0.743	-0.611	-0.387	15.779
45	4.834	**0.624**	-0.660	-0.313	15.950
55	4.676	0.665	-0.777	**-0.236**	15.559
57	4.293	0.642	-0.421	-0.452	15.838
57(2)	**5.043**	0.658	**-0.394**	-0.516	15.724
59	4.015	0.784	-1.891	1.174	15.922

An investigation of the velocity distribution has been performed in a final step to clarify if the current findings of higher velocities with the implementation of redirecting variants compared

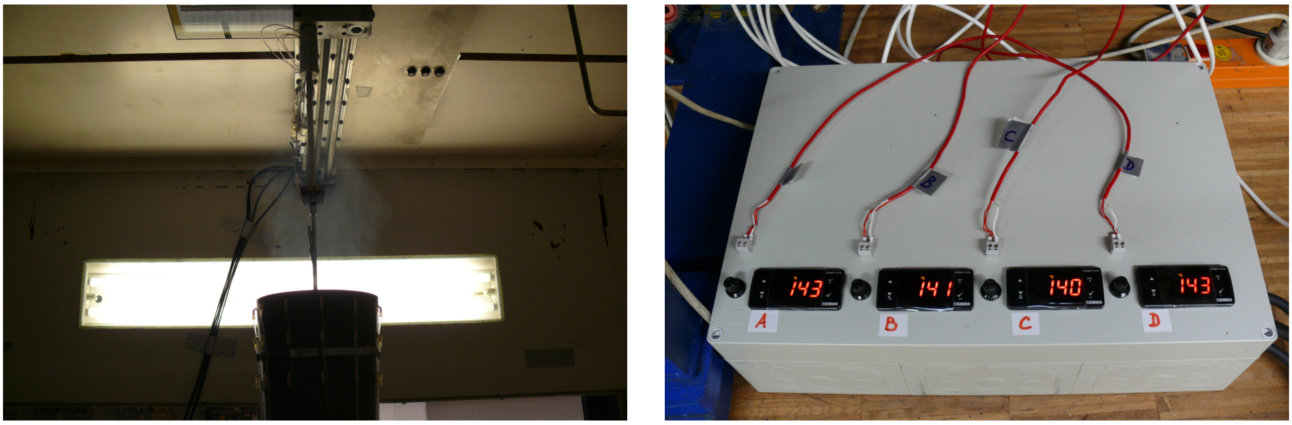

Figure 11.20: Smoke Development at High Heat Film Temperatures

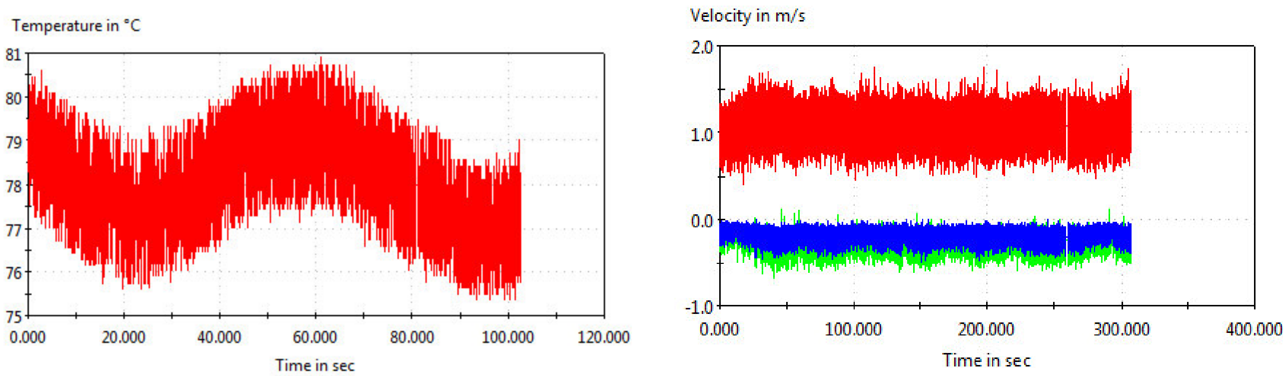

Detail View of Time Course $\Delta T = 115K$

Figure 11.21: Velocity History Inside Chimney Without Wind for $\Delta T = 115K$ (red - u component, blue - v component, green - w component)

to the reference situation can be hold for the whole area of the SCH or is only true for certain measuring points.

Figure F.15 shows the mean values for the vertical velocity and figure F.16 for the RMS values at a height z = 940 mm.

Only half of the cross-section has been measured due to the assumption of symmetry which will be checked via the numerical model presented within chapter 12.

Corresponding velocities at the throat level (z = 500 mm) are listed in table 11.6.

All configurations exhibit an improvement of the velocities at nearly all measuring points. The combination variant (No 57(2)) shows a uniformly distributed vertical velocity whereas variant (No 55), given in appendix F, performs slightly better. Surprisingly, even the windbreaker variant (No 45) gives good results also for the RMS values which decrease compared to the reference situation without any redirection. Variants (No 55) and (No 57(2)) perform well for the obtained RMS values and show comparable results.

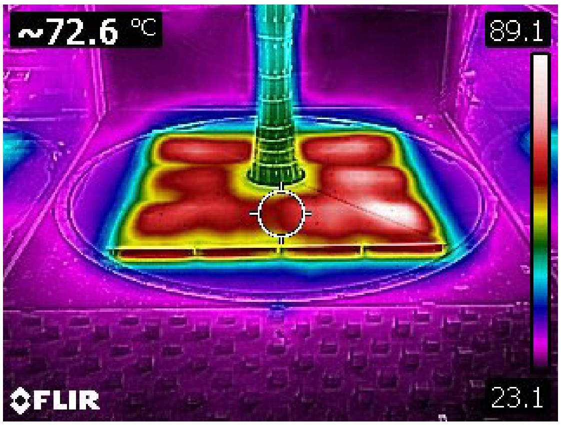

Temperature on Top of the Solar Collector

Temperature at Heating Films Without the Solar Collector

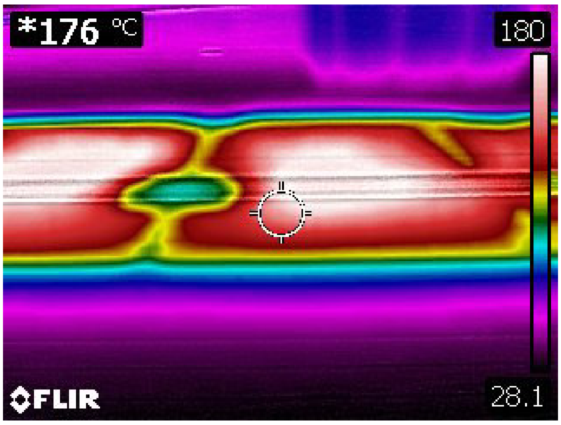

Temperature Underneath the Solar Collector

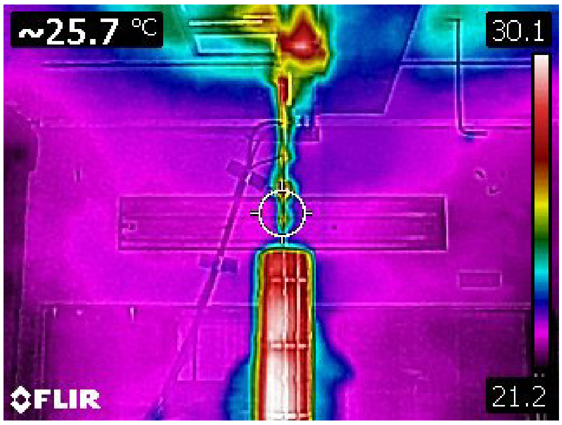

Chimney and Plume Temperature

Figure 11.22: Development of Buoyancy Effect

Table 11.6: Velocity Values at z = 500 mm

Configuration No	v_{mean} m/s	v_{sigma} m/s
Default	6.403	1.132
39	6.505	1.003
45	6.778	**0.994**
55	6.590	0.975
57(2)	**6.891**	1.051
311	6.514	0.997

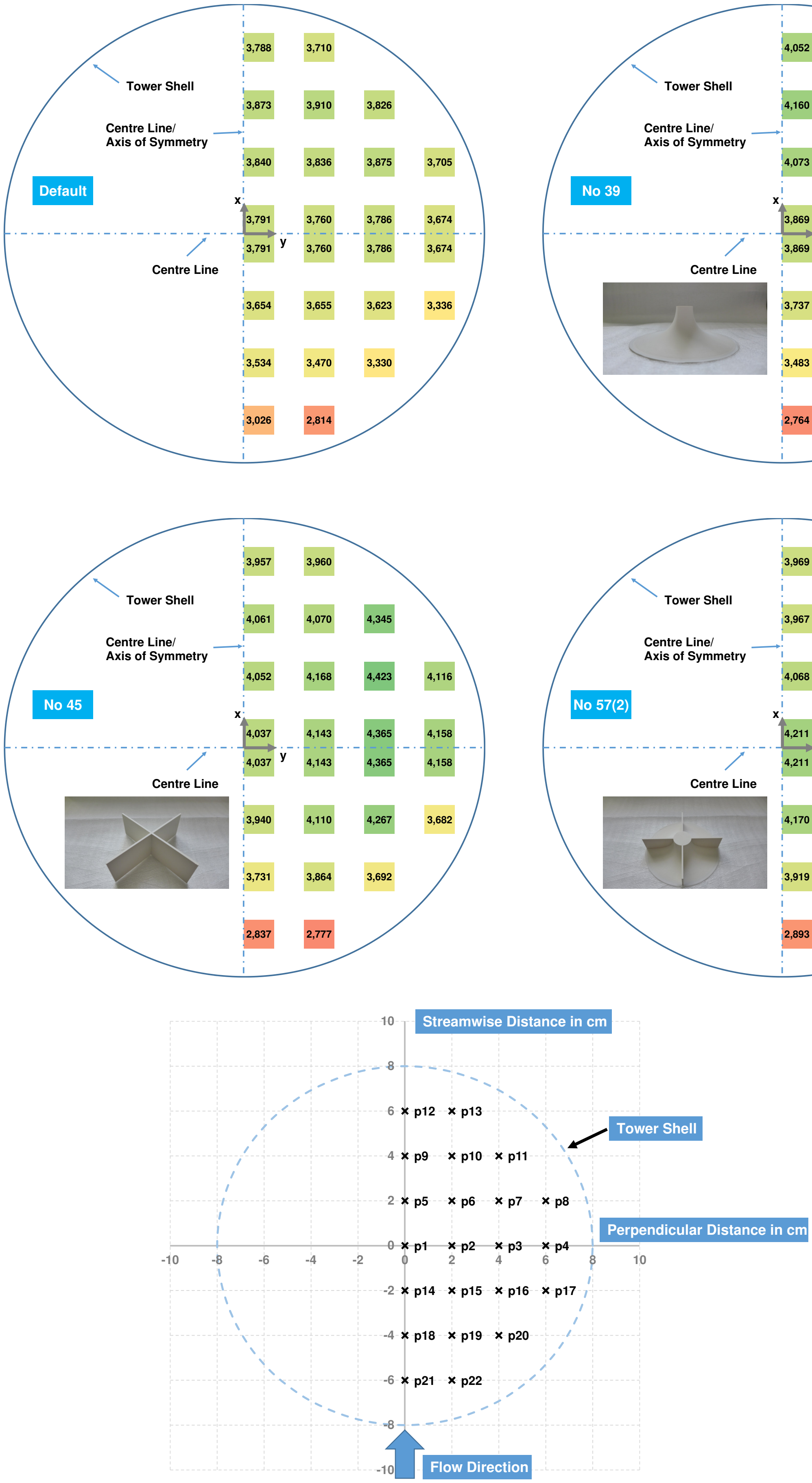

Figure 11.23: Distribution of Mean Velocity (Open, z = 940 mm)

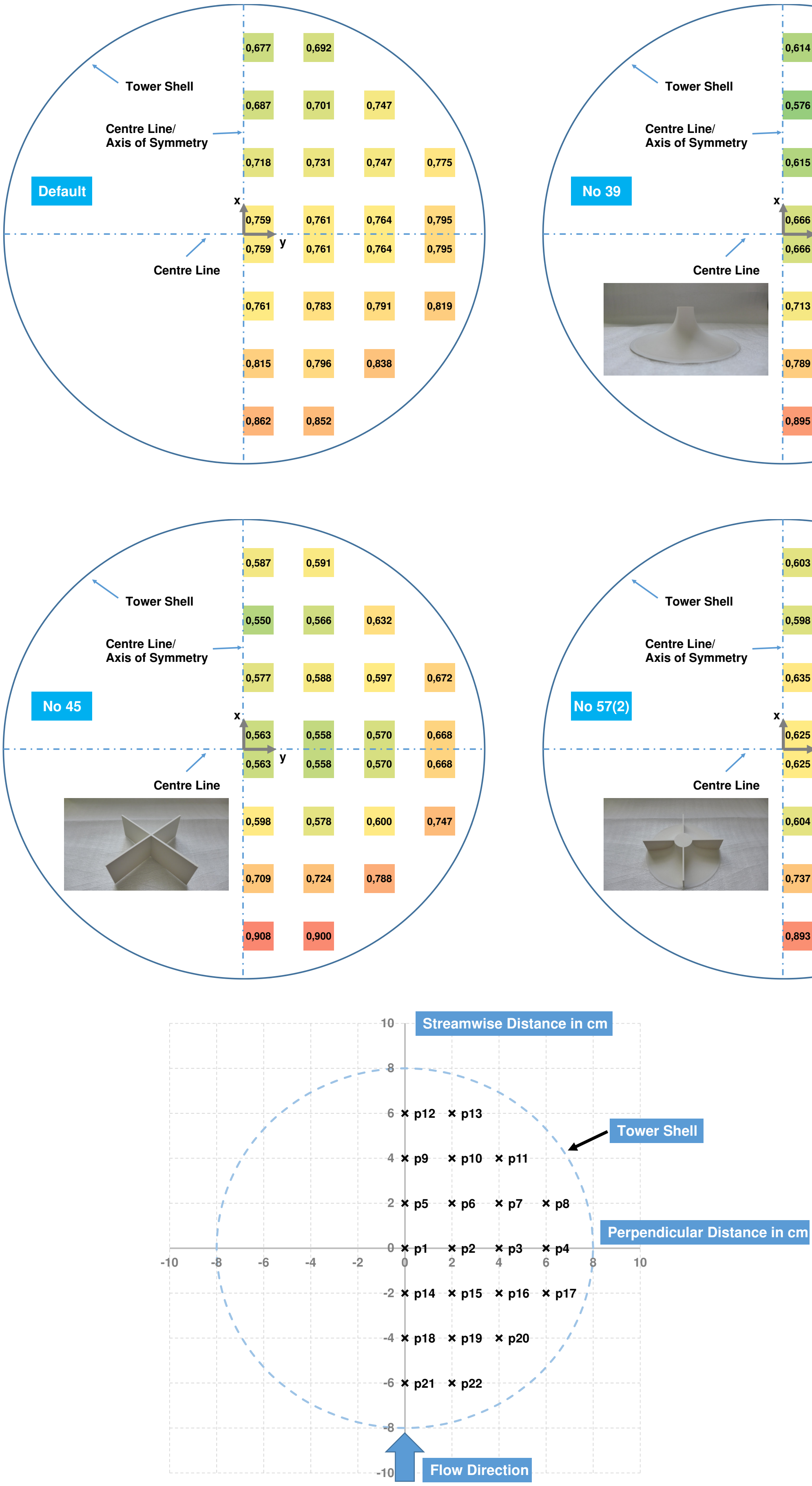

Figure 11.24: Distribution of RMS (Open, z = 940 mm)

11.6 Conclusion

Fourteen configurations for the cylindrical and seven selected ones for the diffuser chimney have been tested for different wind speeds and temperatures. While the wind speed was changed to rule out Re effects a maximal temperature gradient of $\Delta T = 115K$ has been generated. Both pressure and velocity measurements have been performed to gather information about the flow situation underneath the SC, inside the transition section and the SCH. Results have shown that there is a huge impact of the redirecting structure within the transition section on the performance of the SCPP.

For the cylindrical chimney, which depicts the reference design case for the SCH, all tested configurations show a maximal deviation of 10 % for the measured velocities. The best perfomance has been obtained with the combination variant (No 57(2)). Uniform pressure distributions with low RMS values for all levels (variable height z) and high vertical velocities with small velocity components in the horizontal directions have been the deciding factor to use these six configurations for the investigation on the diffuser chimney.

The results for the hyperbolic diffuser chimney have been more decisive. The best performance has been obtained with the combination variant (No 57) or (No 57(2)) respectively. This variant combines the merits of the wind breaker and the global redirection structure. The improved flow situation with higher vertical velocities at nearly all positions of the cross section and homogeneous pressure distributions at all heights will lead to higher mass flow rates. The increase in velocity over the whole cross section lies in the range of $2.2 \div 3.2$ % for the global redirection variant (No 39), 8.0 % for the windbreaker (No 45) and in the range of $10.4 \div 12.1$ % for the combination variant (No 55, No 57(2)). A quantification of the exact increase of the mass flow rates will be presented with the help of the numerical analysis on the current model given within chapter 12. The diffuser, which has been designed under aspects of structural and fluid mechanic optimization, as it has been explained in chapter 10, therefore exhibits an improvement on the flow situation, increased mean vertical velocities and comparable RMS values compared to the default case. A detailed quantification will be presented with the help of the numerical model results.

All findings compare very well with results from [A.83], [A.139], [A.128] and [A.140] for model tests and numerical analysis on SCPP models with a cylindrical or diffuser structure, varied in outer measures but for lower temperature gradients.

The modelling of the buoyancy effect has proven the functionality of the chimney with or without diffuser under thermal conditions. Results have shown an increase in vertical velocity with an increasing temperature gradient and the influence of the redirecting structure on the flow field under thermal and ambient wind conditions.

Last but not least has it been possible to prove the assumption that asymmetric or variable inflow conditions inhibit a strong influence on the flow field underneath the SC and within the SCH. Both the closing of the windward or lee side of the SC improve the vertical velocity inside the SCH. Due to the blockage of the wind in the first situation or the air trap situation in the latest higher velocities can be detected. The increase in mean velocities is accompanied by higher RMS values. Also higher temperatures of the updraft in the range of ≥ 5 % can be found by closing the windward side which shows the shelter effect of a flow barrier at the periphery of the SC on the main flow stream within the SCPP.

Chapter12

3D-CFD Analysis of the Wind Tunnel Model

This chapter deals with the numerical realization of the wind tunnel model presented within the previous chapter. No fully recalculation of all examined configurations will be given here. Instead six models are set up to investigate the influence of the chimney profile and combination variant (No 57) and (No 57(2)) within the transition section on the flow situation respectively. This configuration has shown best results for both chimney configurations and therefore will be used as a reference. Also a brief discussion about the importance of the combination of experimental and numerical studies will be given on the basis of the presented results.

12.1 Set-Up of the Numerical Model

The numerical model is an exact reproduction of the wind tunnel model presented in chapter 11 but without the modelling of the wind tunnel itself. Instead the boundary conditions are matched to the results obtained with the wind tunnel measurements. Default ambient conditions at the in- and outlets of the domain besides all walls are taken as adiabatic (no slip condition). For the simulation of the air overflow at the outlet of the SCH, which has a major impact on the gained results, to the main domain representing the inner flow field of the SCPP a second one has been added to the model. Special attention has been paid for the outer measures of this area to avoid numerical errors. The solver configuration with its parameters can be taken from chapter 9 without the usage of the radiation, shell conduction and solar load model. Results shown by [T.18], [A.14], [A.7] and [A.50] have been used for the right set-up of the model.

12.2 Results

Table 12.1 shows all six configurations which have been investigated in the course of this chapter. The following enumeration gives some criteria which can be used to describe the influence of the implemented configurations on the flow field. This enumeration is not intended to be exhaustive.

- Distance between turbine inlet and tube flow
- Position of *Vena contracta*
- Max. pressure inside the transition section
- Velocity values (max, min, average) at different levels
- Friction or flow losses (Darcy Friction Factor)

Table 12.1: Index

Configuration	**Index**
Cylindrical Chimney, Default	A
Cylindrical Chimney, No 57	B
Cylindrical Chimney, No 57(2)	C
Diffuser Chimney, Default	D
Diffuser Chimney, No 57	E
Diffuser Chimney, No 57(2)	F

- Forces on chimney shell and/or redirecting variant
- De number
- Turbulence kinetic energy
- Energy dissipation

Especially the TKE is used in many engineering fields to describe improved flow situations, e.g in car industry low values of TKE represent a better aerodynamic property, cf. [A.156].

For the set-up of the numerical model both pitot static tube readings for the velocity from the wind tunnel tests have been used as boundary conditions. Due to a reduced computational effort only the upper part of the ambient flow field has been modelled as can be seen in the results depicted in figure 12.1 for the velocity vectors in the centre axis of the numerical model.

The plots confirm on the one hand findings from the first wind tunnel study in Stellenbosch presented in chapter 7 and on the other hand the results from the second wind tunnel study in Bochum on the improved SCPP presented in chapter 11. The course of the velocity vectors in the transition section has the same characteristic for both the cylindrical and hyperbolic chimney without a redirecting structure. A diversion in the vertical direction is delayed compared to the situation with the combination variant (No 57) and (No 57(2)) respectively. The smoothest course has been found with the implementation of variant (No 57(2)) which can be verified with the results in table 12.2 gathering the TKE in the lower part of the SCH.

The depicted control volume represents an exemplarily chosen part of the internal flow field of the SCH, where the biggest influence of the redirecting variant will be determined. Average and maximal values are given for all six investigated configurations. A reduction in TKE by the implementation of variant (No 57) can be detected. The average values, which are more representative than the maximal values, show a distinct improvement of the flow situation with the lowest values for variant (No 57(2)) for the cylindrical and diffuser chimney. The found improvement lies in the range of 32.8 % for the cylindrical and of 24.7 % for the diffuser chimney. The maximal values of the TKE for the diffuser chimney and both alignments of variant (No 57) lead to a reduction in the found values. For the cylindrical chimney the maximal value increases which does not affect the general finding of an improved flow situation compared to the case

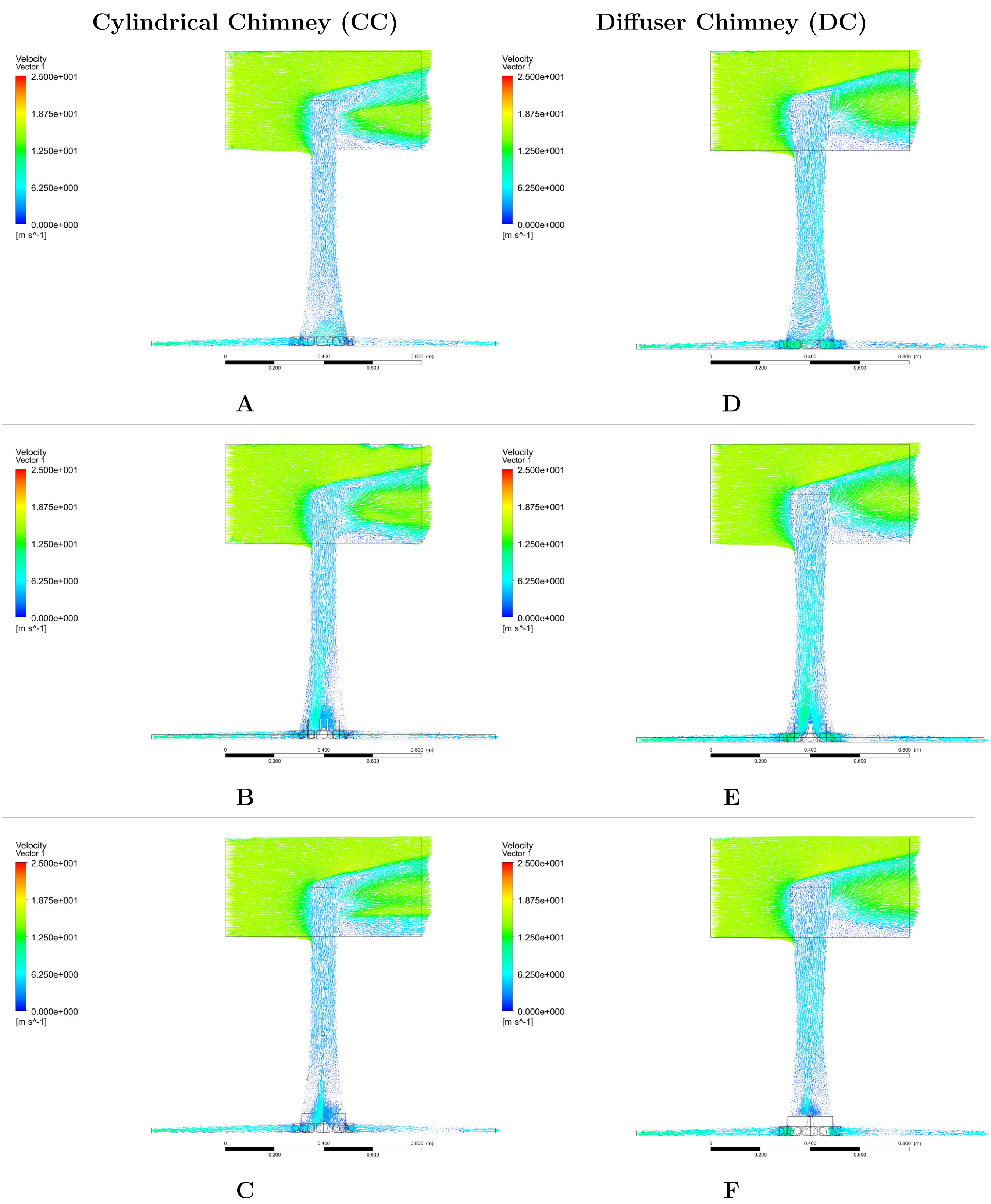

Figure 12.1: Velocity Vectors in the Vertical Centre Axis for Configurations A to F

without a redirecting variant with a distinct decrease of the average value. The increase in the maximal TKE could be caused by a local effect of the configuration on the flow field and can be

Table 12.2: TKE_{ave} and TKE_{max} at Chimney Base

Volume	Variant	CC		DC	
		TKE_{ave}	TKE_{max}	TKE_{ave}	TKE_{max}
	No	J/kg	J/kg	J/kg	J/kg
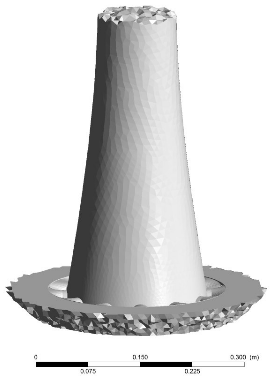	Default	1.89	**12.66**	2.39	16.15
	57	1.34	13.49	2.02	**14.47**
	57(2)	**1.27**	13.05	**1.80**	15.90

diminished by a detailed investigation of the flow situation at the edges of the configuration.

Velocity vector plots for the chimney base given in figure 12.2 confirm these findings of an improved and more structured flow field within this lower region of the SCH.

The flow streams of all turbine openings are clearly visible in all six plots. While both figures for the cylindrical and diffuser chimney without an installation show a really crowded and random distribution of the velocity vectors, variant (No 57) and (No 57(2)) for both chimney profiles reveal a more assorted one. Due to the implementation of variant (No 57) the air parcels are guided into the vertical direction and due to the four sectors formed by the additional wall of this configuration even flow streams from the turbine openings on the lee side exhibit a less random distribution.

Contour plots in figure 12.3 show the velocity distribution for z = 940 mm.

The wider cross section of the diffuser chimney model at the mentioned height is distinctive. The frayed outer shape of all plots is only due to numerical difficulties by displaying these results in the utilized software and does not affect the main findings. Also the maximal velocities at this level are listed here. For the cylindrical chimney both (No 57) and (No 57(2)) show an increase in the maximal velocity in the range of 13.3 % and for the diffuser chimney of 2.3 %. The same finding can be found at the throat level (z = 500 mm) of the chimney model gathered in table 12.3.

The higher maximal velocity comes along with an increased mass flow in the range of 18.9 % for the cylindrical and of 8.5 % for the diffuser chimney. Variant (No 57) shows the best performance for all three parameters. Results for the diffuser chimney exhibit a similar tendency. At throat height variant (No 57) shows the best performance while the highest velocity has been found at z = 940 mm for (No 57(2)). The current results confirm the findings of the wind tunnel tests with higher velocities at nearly all measuring points for variant (No 57(2)) compared to the reference case without any installation. The high velocity values obtained in the wind tunnel tests for (No

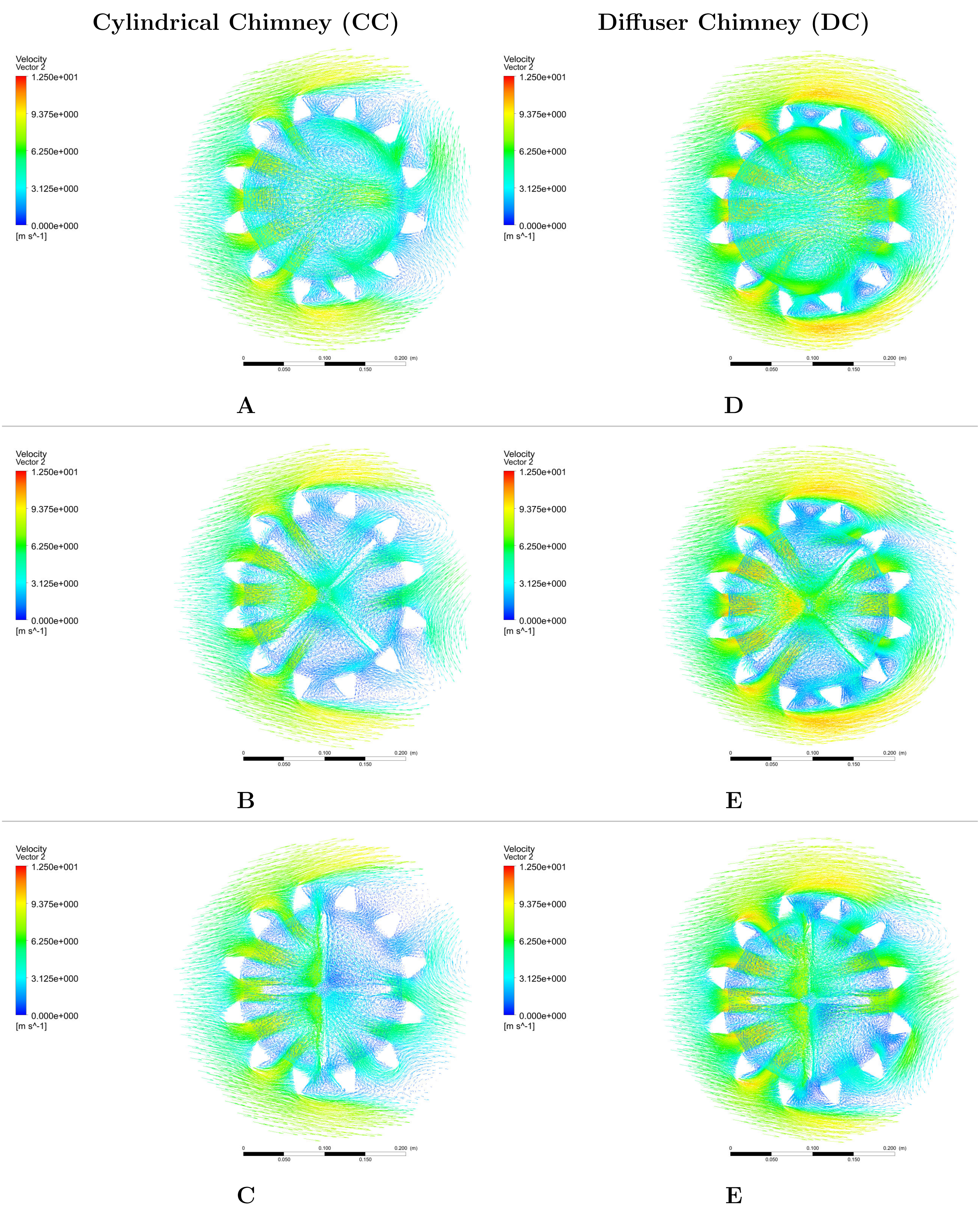

Figure 12.2: Top View of the Velocity Vectors in the Chimney Base for Configurations A to F

57(2)) cannot be found in the numerical analysis which may have several reasons and will be explained in the next section.

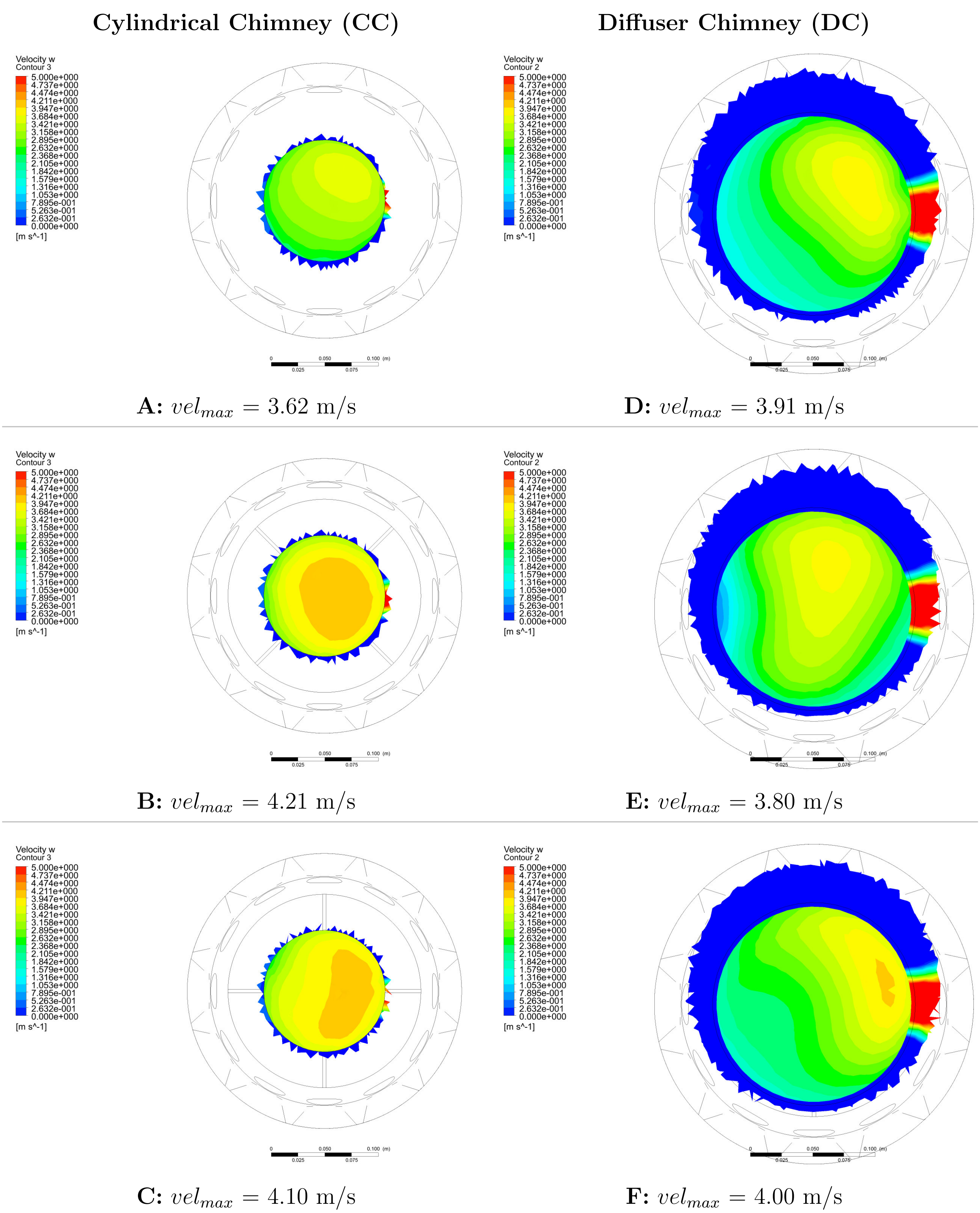

Figure 12.3: Velocity Contours (z = 940 mm) for Configurations A to F

Table 12.3: Mass Flows and vel_{max} at z = 500 mm

Configuration	**CC**		**DC**	
	$\dot{m}$	vel_{max}	$\dot{m}$	vel_{max}
-	kg/s	m/s	kg/s	m/s
Default	0.037	3.18	0.059	5.03
57	**0.044**	**3.78**	**0.064**	**5.43**
57(2)	0.044	3.73	0.064	5.39

12.3 Conclusion

The presented results confirm the general findings of the improved flow situation due to the implementation of the redirecting structure inside the transition section. Three configurations have been analysed numerically for both chimney models, namely the cylindrical and diffuser chimney, to give a brief overview about the velocity and TKE distribution inside the SCH and the mass flow respectively. Additionally, the current results are used for the verification and validation of the results obtained by the wind tunnel study. Only variants (No 57) and (No 57(2)), which have shown the best performance during the experiments, have been investigated. A comparison between both studies exhibit general similarities but also some differences. The general distribution of the velocity at the upper part of the SCH (z = 940 mm) are similar for both investigations. Findings for the TKE and the mass flow confirm the results obtained from the wind tunnel tests where the implementation of the redirecting structure improves the flow situation inside the transition section and therefore within the whole SCPP. The found improvement for the TKE lies in the range of 32.8 % for the cylindrical and of 24.7 % for the diffuser chimney. For the cylindrical chimney both (No 57) and (No 57(2)) show an increase in the maximal velocity in the range of 13.3 % and for the diffuser chimney of 2.3 %. The higher maximal velocity comes along with an increased mass flow in the range of 18.9 % for the cylindrical and of 8.5 % for the diffuser chimney. Additionally, the results of all three configurations, namely the default, (No 57) and (No 57(2)) show, that the improvement of the diffuser compared to the cylindrical chimney lies in the range of ≥ 30 % for the mass flow. The design study presented in chapter 10 has shown that there is still the opportunity to increase the opening angle of the diffuser without compromising the static behaviour and therefore increase the positive influence of the diffuser on the mass flow. The high velocity values from the wind tunnel study cannot be found within the numerical analysis. Two reasons for this deviation can be mentioned, namely the non-simultaneously acquisition of data during the wind tunnel study due to practical reasons and a possible blockage effect of the second hot-wire probe inserted at z = 500 mm, which perhaps caused a disturbance of the original and undisturbed flow field. Due to the unknown magnitude of disturbance within the wind tunnel study, the chosen boundary conditions for the current numerical analysis, which rely on the measured data at both pitot static tubes, could need some adjustment. Therefore a variation of the input parameters has been conducted but still no perfect matching between experimental and numerical results has been obtained. A simultaneous acquisition of the velocity distribution inside the chimney model would be the best solution to rule out possible measuring errors which either requires more hot-wire probes or a measuring technique which allows the spatial capturing of the velocity vectors, e.g. PIV.

Part IV

Final Remarks

Chapter13

Conclusion

The main objective of this dissertation was the better understanding of the flow situation inside a SCPP and especially inside the transition section. Former research generally left out either the structural or fluid mechanic aspects which causes unrealistic results. Therefore a holistic design approach on a structural and fluid mechanic optimized SCH model has been performed.

In Part I the fundamentals of the involved disciplines, namely the structural design, fluid mechanics, thermodynamics and the experimental and numerical modelling are presented in detail. The structural simplicity of the three main components SC, turbines and SCH comes along with complex fluid mechanic and thermodynamic processes involved. Driven by the buoyancy effect and the air overflow at the tower outlet the SCPP technology belongs to the renewable energies. Previous assumptions of symmetry in structure and of the flow situation and unrealistic model designs have led to the decision to develop an improved model of the SCH which includes a detailed investigation of redirecting structures integrated into the transition section.

Part II starts with the set-up of a mathematical 1D model to explain the influence of RH, the soil heat flux $Q_B(z,t)$ and minimal soil temperature T_0 on the annual energy output for four variants of a SCPP with defined outer measures. The designed model underlines the decisive influence of the store effect of soil on the energy output throughout a daily and diurnal cycle. This good approximation of the real world problem with simplifications both in structural and fluid mechanic aspects gave the impulse to set-up a new model taking into account 3D flow effects and to have a closer look at the transition section where the redirection of the air parcels take place.

A wind tunnel model reproducing the SC and SCH flow has been tested at the facility of Stellenbosch, South Africa. PIV and pressure measurements have been performed to visualize the flow situation underneath the SC, within the transition section and inside the SCH. The influence of the ratio between the wind velocity and the tower outflow v_{wind}/v_t has been tested. It has been shown that the assumption of symmetric flow inside the transition section only applies for a flow case without or merely small ambient wind velocities. The influence of a flow redirecting structure like a cone, which can be found in the prototype of Manzanares has not been tested in the course of this measuring program but afterwards on a separate model.

Due to the only available full-scale data on a SCPP, the prototype of Manzanares has been utilized for the set-up of a numerical model. On the basis of this model the influence of the thermal processes radiation, conduction and the solar load have been tested. Gained results for temperature and velocity profiles underneath the SC have shown a strong dependency on the influence of radiation and on the applied solar load. The effect of conduction has been negligible for the current study. Additional tests on the influence of an implemented cone structure inside the transition section, as it has been the case for the full-scale plant, have been conducted. As expected, the best results have been generated with this model and showed a good agreement with full-scale data from the Manzanares plant. These findings encouraged the author to look for a new model which combines the merits of structural and fluid mechanic aspects under the premise of economic efficiency.

A structural FE model with two concepts for the transition section, namely a column or a shell concept, has been designed. The eigenfrequencies and modular forms have been checked and different load cases have been applied to compare displacements and internal forces. Both a reduction in material input and improved eigenfrequencies have been obtained although no focus has been put on a fully process of optimization. A design study for a diffuser chimney with four different diffuser profiles has led to the decision to perform additional tests on two models, one with a cylindrical chimney and the other with a hyperbolic diffuser chimney, which follows the profile of the lower part of the SCH. In the area of the transition section an extension of the turbine openings has been added to the structural design to take care of an improved flow situation compared to the general SCH design.

Part III gathers the wind tunnel study in Bochum, Germany and the numerical analysis of an improved SCPP model designed under structural and fluid mechanic optimization. The effect of ambient wind and thermal effects underneath the SC on the main flow within the power plant have been part of this study. On the basis of pressure and hot-wire measurements the flow field of the SC and within the SCH have been captured for a cylindrical and a hyperbolic diffuser model respectively.

For the cylindrical chimney, which depicts the standard design case for the SCH, all tested configurations show a maximal deviation of 10 % for the measured velocities from the default case without any installation. Uniform pressure distributions with low RMS values and high vertical velocities with small velocity components in the horizontal directions have been a good indication of the improvement of the flow situation compared to the default case.

Results for the hyperbolic diffuser chimney have shown that the best performance can be found for both design cases with configurations which combine the merits of the wind breaker (wall) and the global redirection (cone) structure. The improved flow situation with higher vertical velocities will lead to higher mass flow rates and therefore a better efficiency of the SCPP. The wind tunnel study shows an increase in velocity over the whole cross section varying between 2.2 % and 12.1 % depending on the different configurations compared to the default case. For the mass flow, taken from the numerical analysis, the improvement is of the magnitude of 18.9 % for the cylindrical and of 8.5 % for the diffuser chimney and therefore even higher. Additionally, the results of the best variants, namely (No 57) or (No 57(2)) show, that the improvement of the diffuser compared to the cylindrical chimney lies in the range of ≥ 30 % for the mass flow. The design study presented in chapter 10 has shown that there is still the opportunity to increase the opening angle of the diffuser without compromising the static behaviour and therefore increase the positive influence of the diffuser on the mass flow. The found improvement for the TKE lies in the range of 32.8 % for the cylindrical and of 24.7 % for the diffuser chimney. This confirms the statement, that the redirecting structure improves the flow situation inside the transition section and diminishes flow

losses due to a better guidance of the incoming air parcels from the SC to the SCH.
It has also been found that configurations which exceed the height of the turbine openings by a factor of three (No 311) not necessarily lead to an improvement of the flow situation. Due to structural reasons and huge material input these configurations should not be taken into account for any further investigations.
Last but not least has it been proven that asymmetric or variable inflow conditions include a strong influence on the flow field underneath the SC and within the SCH. Both the closing of the windward or lee side of the SC improve the vertical velocity inside the SCH. Also higher temperatures of the updraft in the range of ≥ 5 % can be found by closing the windward side which confirms the shelter effect of a flow barrier at the periphery of the SC on the main flow stream within the SCPP.

Chapter14

Outlook

The current study has shown the importance of additional research on the SCPP technology and the design and construction of a full scale plant. Following recommendations and suggestions for future research should be taken into account to improve this technology and enable it to be compatible with current renewable energy concepts:

Redirecting variants: Subsequent to the investigation of the redirecting variants and their improving character a second design study on the process of optimization would be necessary. Aiming at the finding of an maximal efficiency for different measures of the variants and main dimensions of the SCPP. Additionally, the first two introduced configurations (extension of turbine openings) and (local redirection) may be investigated to prove their general efficiency. Also anisotropy effects for unsymmetrical variants and their influence on the flow situation shall be investigated. Simultaneously, the possible execution of movable variants which interact with the incoming flow streams inside the transition section shall be performed. This study is inevitably connected with full-scale tests to demonstrate their feasibility under real conditions.

Thermal effects: Due to limitations in scale and temperature for the presented experimental wind tunnel study a new model concept should be set up to achieve higher Ri numbers to reproduce full-scale conditions, especially for the case of implemented redirecting variants inside the transition section. Current tests have proven their practicability and can be taken as a reference.

Effect of asymmetric inflow conditions: The effect of asymmetry on the flow situation due to ambient or internal conditions has a strong influence on the mode of operation of a SCPP. As part of the current investigation results have been presented where the mentioned effect on flow parameters is depicted. Nevertheless additional tests should be run if these situation always inherits a positive and improving effect on the flow field within the SCPP or if there are situations where a negative effect can be observed. One way of diminishing this effect could be a regulation of the incoming fluid flows to achieve symmetric inflow conditions as it has been assumed in former research.

Influence of turbines and guide vanes: The influence of turbines on the flow field shall be included into future investigations either for full-scale or model tests. Due to the implementation of additional IGVs or Outlet Guide Vanes (OGVs) a swirl effect may influence the flow situation inside the transition section. For model test appendix G shows some results for the simulation of fan flow and general information about turbine modelling respectively. It has been found that only less information about this special application of turbines can be found which is one of the key figures that need to be resolved before planing a full-scale power plant.

Interface between ambience and the structure of the SCPP: At the interfaces between the ambience and the SCPP, predominantly at the periphery of the SC and the SCH outlet, special effects can occur. Cold inflows into the SCH as it was observed by CTs, the tip effect which is due to the air overflow at the SCH outlet, the thermal behaviour of the plume and possible shading effects and the influence of blockage at the periphery of the SC shall be investigated. Therefore a two-way FSI will help by the understanding of all processes involved.

Results of a prototype plant at Aswan, Egypt: A monitoring campaign on a prototype SCPP, which has been built from 2015 till 2017 for the location of Aswan, Egypt currently collects a huge amount of data, which will demonstrate the fully operational capability of this technology. The work has been part of a joint research project (ID: 01DH14006A D0101232A) between Egypt and Germany, financed by the Science and Technology Development Fund (STDF) and the Bundesministerium für Bildung und Forschung (BMBF), coordinated by the Deutsches Zentrum für Luft- und Raumfahrt (DLR). Major aim of this study is the design of small scale plants for limited households and the production of green energy. The implemented Structural Health Monitoring (SHM) system will give continuous readings for ambient parameters like wind velocity, solar irradiation, temperature and RH, for the SCH the acceleration, inclination and strains of the shell, for the flow inside the plant the pressure, velocity and temperature distributions at several measuring locations and for the turbine the produced electrical energy. The obtained results can be used for the interpretation of degradation processes during the life-time of the power plant and for the design and construction of new SCPP on a bigger scale. After a full annual cycle, the collected data can be used for further improvements of the structure and the ambient conditions, e.g. the preparation of the soil, to run the power plant 24 hours a day, 365 days a year, regardless of the daily conditions.

For more detailed information please see appendix H and the final research report.

List of References

Articles

[A.1] A., H.S., G., A., Shetta, M., and Hiremath, P. “CFD Analysis on Solar Chimney for Power Generation Application”. In: *Brahma Valley College of Engineering and Research Institute* (2012) (cit. on p. 109).

[A.2] Abdalla, H.A., EL Shenawy, E.A., Kabeel, A.E., and Omara, Z.M. “Experimental Performance Analysis of Annular Diffusers with and Without Swirl”. In: *Proceedings of ICFDP7, Seventh International Congres on Fluid Dynamics and Propulsion; Cairo, Egypt, pp.1-11* (2001) (cit. on p. 146).

[A.3] Agarwal, A. and Kumar, P. “Full-Scale Three-Dimensional Computational Analysis of Solar Updraft Tower in Manzanares, Spain for Power Generation”. In: (2016) (cit. on pp. 109, 118).

[A.4] Akbarzadeh, A., Johnson, P., and Singh, R. “Examining Potential Benefits of Combining a Chimney with a Salinity Gradient Solar Pond for Production of Power in Salt Affected Areas”. In: *Solar Energy, Volume 83, pp. 1345-1359* (2009) (cit. on p. A.6).

[A.5] Alduchov, O.A. and Eskridge, R.E. “Improved Magnus Form Approximation of Saturation Vapor Pressure”. In: *National Climatic Data Center - National Oceanic and Atmospheric Administration* (1997) (cit. on pp. 78, 79).

[A.6] Amirkhani, S., Nasirivatan, Sh., Kasaeian, A.B., and Hajinezhad, A. “ANN and ANFIS Models to Predict the Performance of Solar Chimney Power Plants”. In: *Renewable Energy, Volume 83, pp. 597-607* (2015) (cit. on p. A.3).

[A.7] Andreozzi, A., Buonomo, B., and Manca, O. “Numerical Study of Natural Convection in Vertical Channels with Adiabatic Extensions Downstream”. In: *Numerical Heat Transfer, Part A: Applications: An International Journal of Computation and Methodology 47, Issue 8, pp.741-762* (2005) (cit. on p. 169).

[A.8] Anwer, M. and So, R.M.C. “Swirling Turbulent Flow Through a Curved Pipe - Part I: Effect of Swirl and Bend Curvature”. In: *Experiments in Fluids, Volume 14, pp.85-96* (1993) (cit. on p. 146).

[A.9] Backström, T.W. von and Fluri, T.P. “Maximum Fluid Power Condition in Solar Chimney Power Plants - An Analytical Approach”. In: *Solar Energy 80, pp.1417-1423* (2006) (cit. on p. 25).

[A.10] Backström, T.W. von and Gannon, A.J. “Solar Chimney Turbine Characteristics”. In: *Solar Energy 76, pp.235-241* (2004) (cit. on pp. 24, 25).

[A.11] Backström, T.W. von and Gannon, A.J. “The Solar Chimney Air Standard Thermodynamic Cycle”. In: *R & D Journal 16(1), pp.16-24* (2000) (cit. on p. 45).

[A.12] Backström, T.W. von, Kirstein, C.F., and Pillay, L.A. “The Influence of Some Secondary Effects on Solar Chimney Power Plant Performance”. In: *R & D Journal 22(1) incorporated into The SA Mechanical Engineer, pp.5-10* (2006) (cit. on p. 14).

[A.13] Backström, T.W. von and Fluri, T.P. “Solar Chimney Turbine Layout and Design Considerations”. In: *SCPT 2010 - Solar Chimney Power Technology - International Conference, pp.239-246* (2010) (cit. on pp. 22, 23, 27).

[A.14] Barakos, G. and Mitsoulis, E. “Natural Convection Flow in a Square Cavity Revisited: Laminar and Turbulent Models with Wall Functions”. In: *International Journal for Numerical Methods in Fluids 18, pp.695-719* (1994) (cit. on p. 169).

[A.15] Becker, H.A. and Booth, B.D. “Mixing in the Interaction Zone of Two Free Jets”. In: *AiChE Journal 21, Issue 5, pp.949-958* (1975) (cit. on p. 36).

[A.16] Bernardes, M.A dos Santos, Valle, R.M., and Cortez, M.F.-B. “Numerical Analysis of Natural Laminar Convection in a Radial Solar Heater”. In: *International Journal of Thermodynamical Sciences 38, pp.42-50* (1999) (cit. on p. 29).

[A.17] Bernardes, M.A. dos S., Backström, T.W. von, and Kröger, D.G. “Critical Evaluation of Heat Transfer Coefficients Applicable to Solar Chimney Power Plant Collectors”. In: *Proceedings of ISES Solar World Congress, Solar Energy and Human Settlement, pp.1706-1713* (1997) (cit. on p. 50).

[A.18] Bernardes, M.A. dos Santos. “Convective Heat Transfer Coefficients for Solar Chimney Power Plant Collectors”. In: *Heat Transfer - Mathematical Modelling, Numerical Methods and Information Technology, pp.607-620* (2011) (cit. on pp. 19, 50).

[A.19] Bernardes, M.A. dos Santos, Backström, T.W. von, and Kröger, D.G. “Analysis of Some Available Heat Transfer Coefficients Applicable to Solar Chimney Power Plant Collectors”. In: *Solar Energy 83, pp.264-275* (2009) (cit. on pp. 50, 53).

[A.20] Bernardes, M.A. dos Santos, Voß, A., and Weinrebe, G. “Thermal and Technical Analyses of Solar Chimneys”. In: *Solar Energy 75, pp.511-524* (2003) (cit. on p. 2).

[A.21] Betz, A. “Wind-Energie und ihre Ausnutzung durch Windmühlen”. In: *Bandenhoed & Ruprecht, Göttingen, pp.1-38* (1926) (cit. on p. 25).

[A.22] Borri, C., Lupi, F., Niemann, H.-J., and Peil, U. “Non-Conventional Wind Loading on Ultra-High Towers in Solar Updraft Power Plants”. In: *IABSE-IASS Symposium, Taller, Longer, Lighter, London, England* (2011) (cit. on p. 33).

[A.23] Bugutekin, A. “An Experimental Investigation of the Effect of Periphery Height and Ground Temperature Changes on the Solar Chimney System”. In: *Journal of Thermal Science and Technology 32, Issue 1, pp.51-58* (2012) (cit. on p. 150).

[A.24] Bugutekin, A. “Experimental Study of Temperature Field in a Solar Chimney Plant in Adiyaman”. In: *Journal of Thermal Science and Technology 32, pp.73-80* (2012) (cit. on pp. 2, A.3).

[A.25] Cantrak, D., Jankovic, N., Ristic, S., and Ilic, D. “Influence of the Axial Fan Blade Angle on the Turbulent Swirl Flow Characteristics”. In: *Scientific Technical Review, Volume 64, pp.23-30* (2014) (cit. on p. G.9).

[A.26] Chaichan, M.T. and Kazem, H.A. “Thermal Storage Comparison for Variable Basement Kinds of a Solar Chimney Prototype in Baghdad - Iraq Weathers”. In: *International Journal of Applied Sciences 2, Issue 2, pp.12-20* (2010) (cit. on pp. 43, A.4).

[A.27] Cheng, N.-S. “Formulas for Friction Factor in Transitional Regimes”. In: *Journal of Hydraulic Engineering, ASCE, 134, Issue 9, pp.1357-1362* (2008) (cit. on p. 35).

[A.28] Chergui, T., Boualit, A.H., and Bouhdjar, A. “Finite Element Analysis of Laminar Flow in Solar Chimney”. In: *Seminaire International sur le Genie Climatique et l'Energetique, SIGCLE 2010, pp.1-6* (2010) (cit. on p. 29).

[A.29] Chergui, T., Bouhdjar, A., Boualit, H., and Larbi, S. “Entropy Generation Analysis of the Solar Chimney Power Plant”. In: *pp.1-6* (2012) (cit. on p. 29).

[A.30] Coetzee, H. “Design of a Solar Chimney to Generate Electricity Employing a Convergent Nozzle”. In: *Herman Coetzee, Botswana Technology Centre, Gaborone, Botswana, pp.1-15* (1999) (cit. on p. 2).

[A.31] Coetzee, H. and Oram, C. “Solar Chimney Exit Loss Control by Use of a Diffuser”. In: *pp.1-5* (2005) (cit. on pp. 33, A.6).

[A.32] Colebrook, C.F. “Turbulent Flow in Pipes with Particular Reference to the Transition Region between the Smooth and Rough Pipe Laws”. In: *No. 5204* (1939) (cit. on p. 34).

[A.33] Colebrook, C.F. and White, C.M. “Experiments with Fluid Friction in Roughened Pipes”. In: *Proceedings of the Royal Society of London* (1937) (cit. on p. 35).

[A.34] Cook, M., Ji, Y., and Hunt, G. "CFD Modelling of Buoyancy-Driven Natural Ventilation Opposed by Wind". In: *9th International IBPSA Conference* (2005) (cit. on p. 109).

[A.35] Cook, M.J. and Lomas, K.J. "Guidance on the Use of Computational Fluid Dynamics for Modelling Buoyancy Driven Flows". In: *pp. 1-8* (1997) (cit. on p. 109).

[A.36] Al-Dabbas, M.A. "A Performance Analysis of Solar Chimney Thermal Power Systems". In: *Thermal Science 15, No. 3, pp.619-642* (2011) (cit. on p. A.3).

[A.37] Al-Dabbas, M.A. "The First Pilot Demonstration: Solar Updraft Tower Power Plant in Jordan". In: *International Journal of Sustainable Energy 31, Issue 6, pp.399-410* (2012) (cit. on p. A.3).

[A.38] Deubener, J., Helsch, G., Moiseev, A., and Bornhöft, H. "Glasses for Solar Energy Conversion Systems". In: *Journal of the European Ceramic Society 29, pp.1203-1210* (2009) (cit. on p. 2).

[A.39] Dyk, C. van and Zijl, G.P.A.G. "Realisation of the Inlet Guide Vanes - an Integral Part of the Solar Chimney". In: *Progress in Structural Engineering, Mechanics and Computation, Zingoni, pp.315-320* (2004) (cit. on p. 2).

[A.40] Elsner, B. von, Briassoulis, D., Waaijenberg, D., Mistriotis, A., Zabeltitz, Chr. von, Gratraud, J., Russo, G., and R., Suay-Cortes. "Review of Structural and Functional Characteristics of Greenhouses in European Union Countries, Part I: Design Requirements". In: *Journal of Agricultural Engineering Resources, Vol. 75, pp.1-16* (2000) (cit. on p. 7).

[A.41] Elsner, B. von, Briassoulis, D., Waaijenberg, D., Mistriotis, A., Zabeltitz, Chr. von, Gratraud, J., Russo, G., and R., Suay-Cortes. "Review of Structural and Functional Characteristics of Greenhouses in European Union Countries, Part II: Typical Designs". In: *Journal of Agricultural Engineering Resources, Vol. 75, pp.111-126* (2000) (cit. on p. 7).

[A.42] Ferreira, A.G., Maia, C.B., Cortez, M.F.B., and Valle, R.M. "Technical Feasibility Assessment of a Solar Chimney for Food Drying". In: *Solar Energy 82, pp.198-205* (2008) (cit. on p. A.5).

[A.43] Figuerola, P.I. and Mazzeo, N.A. "An Analytical Model for the Prediction of Nocturnal and Dawn Surface Temperatures under Calm Clear Sky Conditions". In: *Agricultural and Forest Meteorology 85, pp.229-237* (1997) (cit. on p. 43).

[A.44] Fluri, T.P. and Backström, T.W. von. "Comparison of Modelling Approaches and Layouts for Solar Chimney Turbines". In: *Solar Energy 82, pp.239-246* (2008) (cit. on p. G.12).

[A.45] Fluri, T.P. and Backström, T.W. von. "Performance Analysis of the Power Conversion Unit of a Solar Chimney Power Plant". In: *Solar Energy 82, pp.999-1008* (2008) (cit. on pp. 2, 25–27, 29).

[A.46] Franke, J. "Evaluating FLUENT V6.2 with the German VDI Guideline for Obstacle Resolving Micro-Scale Models". In: *The Fourth International Symposium on Computational Wind Engineering, Yokohama, pp.793-796* (2006) (cit. on p. 70).

[A.47] Franke, J. and Thanh, H.P. "Analysis of Pressure Fluctuations from Large Eddy Simulation of the Flow Around a Surface Mounted Pyramid". In: *6th International Symposium on Computational Wind Engineering, pp.64-65* (2014) (cit. on p. 70).

[A.48] Freund, J.B. and Moin, P. "Jet Mixing Enhancement by High-Amplitude Fluidic Actuation". In: *American Institute of Aeronautics and Astronautics (AIAA), Journal 38, Issue 10, pp.1863-1870* (2000) (cit. on p. 36).

[A.49] Freund, J.B. and Moin, P. "Mixing Enhancement in Jet Exhaust using Fluidic Actuators: Direct Numerical Simulations". In: *Proceedings of Fluids Engineering Division Summer Meeting (FEDSM) 98, June 21-25, Washington, DC, USA* (1998) (cit. on p. 36).

[A.50] Gan, G. "Interaction Between Wind and Buoyancy Effects in Natural Ventilation of Buildings". In: *The Open Construction and Building Technology Journal, Volume 4, pp. 132-145* (2010) (cit. on p. 169).

[A.51] Gannon, A.J. and Backström, T.W. von. “Solar Chimney Turbine Performance”. In: *Journal of Solar Energy Engineering, Volume 125, pp.101-106* (2003) (cit. on p. G.12).

[A.52] Geographie für Sachsen, TERRA. “Schülerbuch”. In: *pp.48-49* (2008) (cit. on p. 78).

[A.53] Ghalamchi, M., Kasaeian, A., and Ghalamchi, M. “Experimental Study of Geometrical and Climate Effects on the Performance of a Small Solar Chimney”. In: *Renewable and Sustainable Energy Reviews, Volume 43, pp. 425-431* (2015) (cit. on p. A.1).

[A.54] Gholamalizadeh, E. and Chung, J.D. “Analysis of Fluid Flow and Heat Transfer on a Solar Updraft Tower Power Plant Coupled with a Wind Turbine Using Computational Fluid Dynamics”. In: *Applied Thermal Engineering, Volume 126, pp. 548-558* (2017) (cit. on p. 109).

[A.55] Gholamalizadeh, E. and Kim, M.-H. “Three-Dimensional CFD Analysis for Simulating the Greenhouse Effect in Solar Chimney Power Plants Using a Two-Band Radiation Model”. In: *Renewable Energy, Volume 63, pp. 498-506* (2014) (cit. on p. 109).

[A.56] Gholamalizadeh, E. and Mansouri, S.H. “A Study on the Optimization of Performance of a Small-Scale Prototype Solar Chimney Power Plant”. In: *Proceedings of the ASME 2011 5th International Conference on Energy Sustainability, August 7-10, Washington, DC, USA, pp.1-6* (2011) (cit. on p. A.4).

[A.57] Ghosal, M.K., Tiwari, G.N., Das, D.K., and Pandey, K.P. “Modeling and Comparative Thermal Performance of Ground Air Collector and Earth Air Heat Exchanger for Heating of Greenhouse”. In: *Energy and Buildings 37, pp.613-621* (2005) (cit. on p. 43).

[A.58] Graffmann, M., Harte, R., Krätzig, W.B., and Montag, U. “Sturmbeanspruchte dünne Stahlbetonschalen im Ingenieurbau”. In: *Festschrift zum 65. Geburtstag von Prof. Dr.-Ing. Friedhelm Stangenberg, Ruhr-Universität Bochum, pp.1-13* (2007) (cit. on p. 129).

[A.59] Greet, R.J. “Maximum Windmill Efficiency”. In: *Journal of Applied Physics 51, pp.4680-4681* (1980) (cit. on p. 25).

[A.60] Group, Elioth - Iosis. “The Solar Mountains - An Introduction to the Solar Updraft Mountains”. In: (2010) (cit. on pp. A.4, A.5).

[A.61] Guo, L. and Maghirang, R.G. “Numerical Simulation of Airflow and Particle Collection by Vegetative Barriers”. In: *Engineering Applications of Computational Fluid Mechanics, Vol. 6, No. 1. pp.110-122* (2012) (cit. on p. 150).

[A.62] Guo, P., Li, J., Wang, Y., and Liu, Y. “Numerical Analysis of the Optimal Turbine Pressure Drop Ratio in a Solar Chimney Power Plant”. In: *Solar Energy 98, pp.42-48* (2013) (cit. on p. 25).

[A.63] Guo, P., Li, J., Wang, Y., and Wang, Y. “Evaluation of the Optimal Turbine Pressure Drop Ratio for a Solar Chimney Power Plant”. In: *Energy Conversion and Management, Volume 108, pp. 14-22* (2016) (cit. on p. 109).

[A.64] Guo, P., Wang, Y., Meng, Q., and Li, J. “Experimental Study on an Indoor Scale Solar Chimney Setup in an Artificial Environment Simulation Laboratory”. In: *Applied Thermal Engineering, Volume 107, pp. 818-826* (2016) (cit. on pp. 142, A.2).

[A.65] Gurevich, E. and Likov, M. “Fan Outlet Velocity Distributions and Calculations”. In: (2012) (cit. on p. G.2).

[A.66] Haaf, W. “Solar Chimneys Part II: Preliminary Test Results from the Manzanares Pilot Plant”. In: *International Journal of Solar Energy, Volume 2, pp.141-161* (1983) (cit. on p. 109).

[A.67] Haaf, W., Friedrich, K., Mayr, G., and Schlaich, J. “Solar Chimneys Part I: Principle and Construction of the Pilot Plant in Manzanares”. In: *International Journal of Solar Energy, Volume 2, pp.3-20* (1983) (cit. on p. 109).

[A.68] Haarhuis, K. “Maximum Transparent Barrel-Vaulted Glass Roof”. In: *IABSE-IASS Symposium, Taller, Longer, Lighter, London, England* (2011) (cit. on p. 2).

[A.69] Hamdan, M.O. “Analysis of a Solar Chimney Power Plant in the Arabian Gulf Region”. In: *Renewable Energy 36, Issue 10, pp.2593-2598* (2011) (cit. on p. 2).

[A.70] Hamdan, M.O. and Rabbata, O. “Experimental Solar Chimney Data with Analytical Model Prediction”. In: *pp.1-6* (2011) (cit. on p. A.3).

[A.71] Hardy, B. “ITS-90 Formulations for Vapor Pressure, Frostpoint Temperature, Dewpoint Temperature, and Enhancement Factors in the Range -100 to +100 C”. In: *Third International Symposium on Humidity and Moisture* (1998) (cit. on p. 78).

[A.72] Harte, R., Graffmann, M., and Krätzig, W.B. “Optimization of Solar Updraft Chimneys by Nonlinear Response Analysis”. In: *Applied Mechanics and Materials 283, pp.25-34* (2013) (cit. on pp. 12, 121, 122, 129).

[A.73] Harte, R., Höffer, R., Krätzig, W.B., Mark, P., and Niemann, H.-J. “Solar Updraft Power Plants: Engineering Structures for Sustainable Energy Generation”. In: *Engineering Structures 56, pp.1698-1706* (2013) (cit. on pp. 2, 20).

[A.74] Harte, R., Höffer, R., Krätzig, W.B., and Niemann, H.-J. “Solare Aufwindkraftwerke: Ein Beitrag der Bautechnik zur nachhaltigen und wirtschaftlichen Energieerzeugung”. In: *Bautechnik 89, Heft 3, pp.173-181* (2012) (cit. on p. 129).

[A.75] Harte, R. and Krätzig, W.B. “State-of-the-Art of Structural Design of Cooling and Solar Updraft Towers”. In: *Taller, Longer, Lighter. Proceedings of IABSE-IASS Symposium, London, England* (2011) (cit. on p. 131).

[A.76] Harte, R. and Zijl, G.P.A.G. “Renewable Energy for Sub-Saharan Africa - Structural Aspects of Classical Wind Turbines and Innovative Solar Chimney Concept”. In: *4th European & African Conference on Wind Engineering, ITAM ASCR Prague 2005, pp.136-137* (2005) (cit. on p. 129).

[A.77] Hassan, A., Ali, M., and Waqas, A. “Three Dimensional CFD Analysis of Solar Chimney Power Plant”. In: *Proceedings of the 3rd International Conference on Engineering and Emerging Technologies* (2016) (cit. on p. 109).

[A.78] Hilgers, A. “Control and Optimization of Turbulent Jet Mixing”. In: *Center for Turbulence Research, Annual Research Briefs, pp.45-54* (2000) (cit. on p. 36).

[A.79] Höffer, R., Tewolde, S., Bogoevska, S., and Dumova-Jovanoska, E. “Vibration-Based Health Monitoring of Slender Structures”. In: *International Symposium on Industrial Chimneys and Cooling Towers* (2016) (cit. on p. H.8).

[A.80] Höffer, R., Wevers, C., and Görnandt, V. “Transport and Deposition of Dust on the Collector Surface”. In: *SCPT 2010 - Solar Chimney Power Technology - International Conference, pp.325-335* (2010) (cit. on pp. 8, 20).

[A.81] Hooff, T. van and Blocken, B. “Coupled Urban Wind Flow and Indoor Natural Ventilation Modelling on a High-Resolution Grid - A Case Study for the Amsterdam ArenA Stadium”. In: *Environmental Modelling and Software, Volume 25, pp.51-65* (2010) (cit. on p. 65).

[A.82] Hu, S. and Leung, D.Y.C. “Mathematical Modelling of the Performance of a Solar Chimney Power Plant with Divergent Chimneys”. In: *Energy Procedia, Volume 110, pp.440-445* (2017) (cit. on p. 2).

[A.83] Hu, S., Leung, D.Y.C., Chen, M.Z.Q., and Chan, J.C.Y. “Effect of Guide Wall on the Potential of a Solar Chimney Power Plant”. In: *Renewable Energy, Volume 96, pp. 209-219* (2016) (cit. on pp. 2, 167, A.2).

[A.84] Huang, H., Li, G., and Zhang, H. “Experimental Performance of a Solar Collector in Solar Chimney Power Plant System”. In: *International Conference on Electrical and Control Engineering, pp.3718-3721* (2010) (cit. on p. 43).

[A.85] Huang, H.L., Zhang, H., Huang, Y., and Lu, F. "Simulation Calculation on Solar Chimney Power Plant System". In: *International Conference on Power Engineering, October 23-27, Hangzhou, China* (2007) (cit. on pp. 67, 109).

[A.86] Huleihil, M. and Mazor, G. "Wind Turbine Power: The Betz Limit and Beyond". In: *INTECH, Chapter 1, pp.1-28* (2002) (cit. on p. 25).

[A.87] Ingram, G. "Wind Turbine Blade Analysis Using the Blade Element Momentum Method". In: • (2011) (cit. on pp. G.9, G.10).

[A.88] Jain, D. and Tiwari, G.N. "Modeling and Optimal Design of Ground Air Collector for Heating in Controlled Environment Greenhouse". In: *Energy and Conversion Management 44, pp.1357-1372* (2003) (cit. on p. 43).

[A.89] Jamieson, P. "Beating Betz - Energy Extraction Limits in a Uniform Flow Field". In: *pp.1-10* (2008) (cit. on p. 25).

[A.90] Jankovic, N.Z. "Investigation of the Free Turbulent Swirl Jet Behind the Axial Fan". In: *Thermal Science, Volume 20, pp.1-12* (2016) (cit. on p. G.9).

[A.91] Jemli, M.R., Naili, N., and Farhat, A. "Experimental Investigation of Solar Tower with Chimney Effect Installed in CRTEn, Tunisia". In: *International Journal of Hydrogen Energy, pp. 1-11* (2016) (cit. on p. A.2).

[A.92] Kalantar, V. and Zare, M. "Simulation of Flow and Heat Transfer in 3D Solar Chimney Power Plants - Numerical Analysis". In: *Jordan International Energy Conference 2011, Amman, Jordan, pp.1-9* (2011) (cit. on p. 109).

[A.93] Kalash, S., Naimeh, W., and Ajib, S. "Experimental Investigation of the Solar Collector Temperature Field of a Slope Solar Updraft Power Plant Prototype". In: *Solar Energy, Volume 98, pp. 70-77* (2013) (cit. on p. A.3).

[A.94] Kasaeian, A.B., Heidari, E., and Vatan, Sh.N. "Experimental Investigation of Climatic Effects on the Efficiency of a Solar Chimney Pilot Power Plant". In: *Renewable and Sustainable Energy Reviews, Volume 15, pp. 5202-5206* (2011) (cit. on p. A.3).

[A.95] Kasaeian, A.B., Molana, Sh., Rahmani, K., and Wen, D. "A Review on Solar Chimney Systems". In: *Renewable and Sustainable Energy Reviews, Volume 67, pp. 954-987* (2017) (cit. on p. A.2).

[A.96] Al-Khalidy, N. "Design Optimisation of Industrial Ducts Using Computational Fluid Dynamics". In: *Third International Conference on CFD in the Minerals and Process Industries. Melbourne, Australia.* (2003) (cit. on p. G.9).

[A.97] Kiijärvi, J. "Darcy Friction Factor Formulae in Turbulent Pipe Flow". In: *pp.1-11* (2011) (cit. on p. 35).

[A.98] Kirstein, C.F. and Backström, T.W. von. "Flow Through a Solar Chimney Power Plant Collector-to-Chimney Transition Section". In: *Journal of Solar Energy Engineering 128, pp.312-317* (2006) (cit. on p. 29).

[A.99] Kirstein, C.F., Backström, T.W. von, and Kröger, D.G. "Flow Phenomena in the Transition Section of a Solar Chimney Model". In: *4th International Conference on Heat Transfer, Fluid Mechanics and Thermodynamics, HEFAT 2005, Cairo, Egypt, pp.1-6* (2005) (cit. on p. 29).

[A.100] Klarin, B., Nizetic, S., and Roje, J. "Basic Solar Chimney Flow Improvements". In: *Strojarstvo 51, Issue 5, pp.465-472* (2009) (cit. on pp. 24, 109).

[A.101] Koonsrisuk, A. "Mathematical Modeling of Sloped Solar Chimney Power Plants". In: *Energy 47, pp.582-589* (2012) (cit. on p. 67).

[A.102] Koonsrisuk, A. and Chitsomboon, T. "Dynamic Similarity in Solar Chimney Modeling". In: *pp.1-8* (2007) (cit. on p. 28).

[A.103] Koonsrisuk, A. and Chitsomboon, T. "Partial Geometric Similarity for Solar Chimney Power Plant Modeling". In: *Solar Energy 83, pp.1611-1618* (2009) (cit. on p. 66).

[A.104] Krätzig, W.B. "An Integrated Computer Model of a Solar Updraft Power Plant". In: *Advances in Engineering Software 62-62, pp.33-38* (2013) (cit. on pp. 44, 73).

[A.105] Krätzig, W.B., Harte, R., Montag, U., and Wörmann, R. "From Large Natural Draft Cooling Tower Shells to Chimneys of Solar Upwind Power Plants". In: *Proceedings of the International Association for Shell and Spatial Structures (IASS) Symposium 2009, Valencia, Evolution and Trends in Design, Analysis and Construction of Shell and Spatial Structures, pp.1-16* (2009) (cit. on p. 129).

[A.106] Krätzig, W.B., Niemann, H.-J., Harte, R., and Höffer, R. "Solar Updraft Power Plants - Experimental Prototype with 350 m Solar Chimney and Square Collector of 1 km2 of Area". In: (2015) (cit. on p. 145).

[A.107] Kuck, J., Ziller, C., Schnatbaum-Laumann, L., and Gladen, H. "Methodical Approach to Design the Solar Collector of a Solar Chimney Power Plant". In: *SCPT 2010 - Solar Chimney Power Technology - International Conference, pp.293-300* (2010) (cit. on pp. 8, 9).

[A.108] Kühnen, J., Holzner, M., Hof, B., and Kuhlmann, H. "Time-Resolved 3D-PIV Measurements of Travelling Waves in a Torus". In: *16th International Symposium of Laser Techniques to Fluid Mechanics* (2012) (cit. on p. 92).

[A.109] Kulkarni, S. and Student, P.G. "Wind and Buckling Analysis of Natural Draught Cooling Towers Using ANSYS". In: *First International Conference on Recent Advances in Science and Engineering* (2014) (cit. on p. 129).

[A.110] Laermann, K.-H. "On the Impact of Uncertainty Quantification in Structural Analysis". In: *International Symposium on Experimental Methods and Numerical Simulation in Engineering Sciences* (2016) (cit. on p. 130).

[A.111] Larbi, S., Bouhdjar, A., and Chergui, T. "Contribution to the Thermo-Fluid Aspect Analysis in Solar Chimney Power Plants". In: *SCPT 2010 - Solar Chimney Power Technology - International Conference, pp.257-266* (2010) (cit. on p. 50).

[A.112] Laurantzon, F., Örlü, R., Tillmark, N., and Alfredsson, P.H. "Response of Common Flowmeters to Unsteady Flow". In: (2010) (cit. on p. B.5).

[A.113] Liu, W., Ming, T.-Z., and Yang, K. "Simulation of Characteristics of Heat Transfer and Flow for MW Grade Solar Chimney Power Plant". In: *Proceedings of International Solar Energy Conference ISEC 2005, August 6-12, Orlando, Florida, USA, pp.1-6* (2005) (cit. on p. 29).

[A.114] Love, E.S., Grigsby, C.E., Lee, L.P., and Woodling, M.J. "Experimental and Theoretical Studies of Axisymmetric Free Jets". In: *National Aeronautics and Space Administration - Technical Report R-6, pp.1-298* (1959) (cit. on p. 36).

[A.115] Maia, C.B., Ferreira, A.G., Valle, R.M., and Cortez, M.F.B. "Analysis of the Airflow in a Prototype of a Solar Chimney Dryer". In: *Heat Transfer Engineering 30, Issue 5, pp.393-399* (2009) (cit. on p. 43).

[A.116] Maia, C.B., Ferreira, A.G., Valle, R.M., and Cortez, M.F.B. "Theoretical Evaluation of the Influence of Geometric Parameters and Materials on the Behavior of the Airflow in a Solar Chimney". In: *Computers & Fluids, pp.1-12* (2008) (cit. on p. A.5).

[A.117] Mattern, P., Sieber, S., Dues, M., Caglar, S., and Gabi, M. "Simultaneous High Speed Stereo PIV and LDA Measurements in the Highly Transient Vortical Wake of an Axial Fan". In: *16th International Symposium on Applications of Laser Techniques* (2012) (cit. on p. G.9).

[A.118] Mehla, N., Makade, R., and Thakur, N.S. "Experimental Analysis of a Velocity Field Using Variable Chimney Diameter for Solar Updraft Tower". In: *International Journal of Engineering Science and Technology 3, No. 4, pp.3167-3171* (2011) (cit. on p. A.4).

[A.119] Mekhail, T., Rekaby, A., Fathy, M., Bassily, M., and Harte, R. "Experimental and Theoretical Investigations of Mini Solar Chimney Power Plant". In: *Journal of Clean Energy Technologies, Volume 5, pp.294-298* (2017) (cit. on p. A.1).

[A.120] Melbourne, W.H. and Aust, M.I.E. "Wind Tunnel Modelling of Buoyant Chimney Plumes". In: *Conference on Hydraulics and Fluid Mechanics, pp. 81-85* (1968) (cit. on p. 143).

[A.121] Meng, F., Ming, T., and Pan, Y. "A Method of Decreasing Power Output Fluctuation of Solar Chimney Power Generating Systems". In: *Third International Conference on Measuring Technology and Mechatronics Automation, pp.114-118* (2011) (cit. on p. 43).

[A.122] Ming, T., Gui, J., Richter, R.K. de, Pan, Y., and Xu, G. "Numerical Analysis on the Solar Updraft Power Plant System with a Blockage". In: *Solar Energy, pp.1-12* (2013) (cit. on p. 109).

[A.123] Ming, T., Liu, W., Xu, G., Xiong, Y., Guan, X., and Pan, Y. "Numerical Simulation of the Solar Chimney Power Plant Systems Coupled with Turbine". In: *Renewable Energy 33, pp.897-905* (2008) (cit. on p. 2).

[A.124] Ming, T., Meng, F., Liu, W., Pan, Y., and Richter, R.K. de. "Analysis of Output Power Smoothing Method of the Solar Chimney Power Generating System". In: *International Journal of Energy Research, pp.1-12* (2012) (cit. on p. 43).

[A.125] Miyasato, N., Okada, A., Miyake, Y., Nomoto, K., and Saitoh, M. "An Applicability Evaluation of Hybrid Glass Beam as Structural Member". In: *IABSE-IASS Symposium, Taller, Longer, Lighter, London, England* (2011) (cit. on p. 2).

[A.126] Mohamed, A.E.-E.A., El-Hadidy, M., Deif, A., and Elenean, K.A. "Seismic Hazard Studies in Egypt". In: *Journal of Astronomy and Geophysics, Volume 1, pp. 119-140* (2012) (cit. on p. H.4).

[A.127] Moore, F.K. and Garde, M.A. "Aerodynamic Losses of Highly Flared Natural Draft Cooling Towers". In: *Third Waste Heat Management and Utilization Conference, Miami, 1981* (1981) (cit. on p. 34).

[A.128] Motoyama, M., Sugitani, K., Ohya, Y., Karasudani, T., Nagai, T., and Okada, S. "Improving the Power Generation Performance of a Solar Tower Using Thermal Updraft Wind". In: *Energy and Power Engineering, Volume 6, pp. 362-370* (2014) (cit. on pp. 2, 167).

[A.129] Mungan, I. "Applicability of BSS Approach to Solar Chimneys". In: *IABSE-IASS Symposium, Taller, Longer, Lighter, London, England* (2011) (cit. on p. 129).

[A.130] Najmi, M., Nazari, A., and Mansouri, H. "Feasibility Study on Optimization of a Typical Solar Chimney Power Plant". In: *Heat Mass Transfer 48, pp.475-485* (2012) (cit. on p. A.4).

[A.131] Nasirivatan, S., Kasaeian, A., Ghalamchi, M., and Ghalamchi, M. "Performance Optimization of Solar Chimney Power Plant Using Electric-Corona Wind". In: *Journal of Electrostatics, Volume 78, pp.22-30* (2015) (cit. on p. A.1).

[A.132] Neuhaus, C. "Numerische frequenzabhängige Kalibrierung langer Druckmessschlauchsysteme". In: *Internal Paper, Chair of Wind Engineering and Fluid Mechanics, University of Bochum. IB-2010-0001-0* (2010) (cit. on p. B.5).

[A.133] Niemann, H.-J. and Höffer, R. "Wind Loading for the Design of the Solar Tower". In: *Structural Engineering, Mechanics and Computation 3, pp.890-895* (2007) (cit. on p. 129).

[A.134] Niemann, H.-J., Lupi, F., Höffer, R., Hubert, W., and Borri, C. "The Solar Updraft Power Plant - Design and Optimization of the Tower for Wind Effects". In: *EACWE 5, Florence, Italy. 19th - 23rd July 2009, pp.1-12* (2009) (cit. on p. 129).

[A.135] Nijsse, R. and Wenting, R. "The all Glass Cube in Haarlem (NL)". In: *IABSE-IASS Symposium, Taller, Longer, Lighter, London, England* (2011) (cit. on p. 2).

[A.136] Ninic, N. "Available Energy of the Air in Solar Chimneys and the Possibility of its Ground-Level Concentration". In: *Solar Energy 80, pp.804-811* (2006) (cit. on p. 2).

[A.137] Nizetic, S., Ninic, N., and Klarin, B. “Analysis and Feasibility of Implementing Solar Chimney Power Plants in the Mediterranean Region”. In: *Energy 33, pp.1680-1690* (2008) (cit. on pp. 34, 35).

[A.138] Oberkampf, W.L. and Trucano, T.G. “Verification and Validation in Computational Fluid Dynamics”. In: *Sandia National Laboratories* (2002) (cit. on p. 68).

[A.139] Ohya, Y., Wataka, M., Watanabe, K., and Uchida, T. “Laboratory Experiment and Numerical Analysis of a New Type of Solar Tower Efficiently Generating a Thermal Updraft”. In: *Energies, Volume 9, pp. 1-14* (2016) (cit. on pp. 2, 167).

[A.140] Okada, S., Uchida, T., Karasudani, T., and Ohya, Y. “Improvement in a Solar Chimney Power Generation by Using a Diffuser Tower”. In: *Journal of Solar Energy Engineering, Volume 137, pp. 1-9* (2015) (cit. on pp. 2, 167).

[A.141] Papageorgiou, C.D. “Enclosed Solar Chimney Power Plant Technology”. In: *Open Access Library Journal, Volume 3, pp.1-18* (2016) (cit. on p. A.3).

[A.142] Pastohr, H., Kornadt, O., and Gürlebeck, K. “Numerical and Analytical Calculations of the Temperature and Flow Field in the Upwind Power Plant”. In: *International Journal of Energy Research 28, pp.495-510* (2004) (cit. on pp. 51, 66, 109).

[A.143] Pasumarthi, N. and Sherif, S.A. “Experimental and Theoretical Performance of a Demonstration Solar Chimney Model - Part I: Mathematical Model Development”. In: *International Journal of Energy Research 22, pp.277-288* (1998) (cit. on pp. 8, A.6).

[A.144] Pasumarthi, N. and Sherif, S.A. “Experimental and Theoretical Performance of a Demonstration Solar Chimney Model - Part II: Experimental and Theoretical Results and Economic Analysis”. In: *International Journal of Energy Research 22, pp.443-461* (1998) (cit. on pp. 2, A.6).

[A.145] Pretorius, J.P. and Kröger, D.G. “Critical Evaluation of Solar Chimney Power Plant Performance”. In: *Solar Energy 80, pp.535-544* (2006) (cit. on pp. 2, 17, 40).

[A.146] Pretorius, J.P. and Kröger, D.G. “Sensitivity Analysis of the Operating and Technical Specifications of a Solar Chimney Power Plant”. In: *Journal of Solar Energy Engineering 129, pp.171-178* (2007) (cit. on pp. 40, 43).

[A.147] Pretorius, J.P. and Kröger, D.G. “Solar Chimney Power Plant Performance”. In: *Journal of Solar Energy Engineering 128, pp.302-311* (2006) (cit. on pp. 17, 40, 43, 73).

[A.148] Pretorius, J.P. and Kröger, D.G. “The Influence of Environment on Solar Chimney Power Plant Performance”. In: *R & D Journal of the South African Institution of Mechanical Engineering 25, pp.1-9* (2009) (cit. on p. 150).

[A.149] Pretorius, J.P., Kröger, D.G., Buys, J.D., and Backström, T.W. von. “Solar Tower Power Plant Performance Characteristics”. In: (2003) (cit. on pp. 16, 35, 40).

[A.150] Promet. “Satellitenmeteorologie II”. In: *Meteorologische Fortbildung, Heft 3* (1972) (cit. on p. 78).

[A.151] Pruvost, J., Legrand, J., and Legentilhomme, P. “Numerical Investigation of Bend and Torus Flows, Part I: Effect of Swirl Motion on Flow Structure in U-Bend”. In: *Chemical Engineering Science, Volume 59, pp. 3345-3357* (2004) (cit. on p. 146).

[A.152] Ragheb, M. and Ragheb, A.M. “Wind Turbines Theory - The Betz Equation and Optimal Rotor Tip Speed Ratio”. In: *Fundamental and Advanced Topics in Wind Power, pp.19-38* (2011) (cit. on p. 25).

[A.153] Rey, C., Schon, J.P., and Mathieu, J. “Buoyancy Effects in a Wind Tunnel Simulation of the Atmospheric Boundary Layer”. In: *Phyiscs of Fluids, Volume 22, pp. 1020-1028* (1979) (cit. on p. 143).

[A.154] Roache, P.J. “Quantification of Uncertainty in Computational Fluid Dynamics”. In: *Annual Review of Fluid Mechanics, Volume 29, pp.123-160* (1997) (cit. on p. 68).

[A.155] Ruth, von J. and Gumpp, R. "Solar Power Plant - Studenten der Bauhaus-Universität Weimar bauen das größte Aufwindkraftwerk Deutschlands". In: *Schriftenreihe Konstruktion und Gestalt, pp.1-49* (2008) (cit. on p. A.5).

[A.156] Savli, M. "Turbulence Kinetic Energy - TKE". In: (2012) (cit. on p. 170).

[A.157] Schlaich, J., Bergermann, R., Friedrich, K., Haaf, W., and Lautenschlager, H. "Baureife Planung und Bau einer Demonstrationsanlage eines atmosphärenthermischen Aufwindkraftwerkes - Anwendungsnahe Auslegung größerer Einheiten und erweitertes Meßprogramm". In: *Forschungsbericht T86-208, Bundesministerium für Forschung und Technologie, pp.1-400* (1986) (cit. on pp. 10, 11, 21, 22, 79, 109).

[A.158] Schlaich, J., Bergermann, R., Schiel, W., and Weinrebe, G. "Design of Commercial Solar Updraft Tower Systems - Utilization of Solar Induced Convective Flows for Power Generation". In: *Journal of Solar Energy Engineering 127, pp.117-124* (2005) (cit. on p. 114).

[A.159] Schlaich, J. and Schiel, W. "Solar Chimneys". In: *Encyclopedia of Physical Science and Technology, Third Edition, pp.0-10* (2000) (cit. on pp. 2, A.6).

[A.160] Schlaich, Bergermann, and Partner. "The Solar Chimney - Transferability of Results from the Manzanares Solar Chimney Plant to Larger Scale-Plants". In: (1995) (cit. on pp. 75, 82, 109, 147).

[A.161] Schlünzen, K.H., Baechlin, W., Brünger, H., Eichhorn, J., Grawe, D., Schenk, R., and Winkler, C. "An Evaluation Guideline for Prognostic Microscale Wind Field Models". In: *9th International Conference on Harmonisation within Atmospheric Dispersion Modelling for Regulatory Purposes, Garmisch-Partenkirchen, Germany* (2004) (cit. on p. 70).

[A.162] Smith, D.J.L., Johnston, I.H., and Fullbrook, D.J. "Investigations on an Experimental Single-Stage Turbine of Conservative Design". In: *Aeronautical Research Council - Reports and Memoranda, No. 3541* (1967) (cit. on p. G.12).

[A.163] So, R.M.C. and Anwer, M. "Swirling Turbulent Flow Through a Curved Pipe - Part 2: Recovery from Swirl and Bend Curvature". In: *Experiments in Fluids, Volume 14, pp.169-177* (1993) (cit. on p. 146).

[A.164] Ströher, G.R., Martins, C.A., and Andrade, C.R. de. "Numerical and Experimental Study of a Free Incompressible Isothermal Turbulent Coaxial Jet". In: *Thermal Engineering 9, Issue 1 und 2, pp.98-107* (2010) (cit. on p. 36).

[A.165] Tamburello, D.A. and Amitay, M. "Interaction of a Free Jet with a Perpendicular Control Jet". In: *Journal of Turbulence 8, Issue 21, pp.1-27* (2007) (cit. on p. 37).

[A.166] Tamburello, D.A. and Amitay, M. "Three-Dimensional Interactions of a Free Jet with a Perpendicular Synthetic Jet". In: *Journal of Turbulence 8, Issue 38, pp.1-21* (2007) (cit. on p. 36).

[A.167] Ücgül, I. and Koyun, A. "Experimental Investigations on Performance and Design Parameters of Solar Chimney". In: *pp.255-265* (2010) (cit. on p. A.6).

[A.168] Vieira, R.S., Petry, A.P., Rocha, L.A.O., Isoldi, L.A., and Santos, E.D. dos. "Numerical Evaluation of a Solar Chimney Geometry for Different Ground Temperatures by Means of Constructural Design". In: *Renewable Energy, Volume 109, pp.222.234* (2017) (cit. on p. 2).

[A.169] Al-Waked, R. and Behnia, M. "The Performance of Natural Draft Dry Cooling Towers Under Crosswind: CFD Study". In: *International Journal of Energy Research 28, pp.147-161* (2004) (cit. on p. 147).

[A.170] Wang, H.J. and Davidson, M.J. "Jet Interaction in a Still Ambient Fluid". In: *Journal of Hydraulic Engineering 129, Issue 5, pp.349-357* (2003) (cit. on pp. 35, 36).

[A.171] Wang, Q., Jiang, Z., and Wei, Y. "Experimental and Numerical Study of a Novel Updraft Tower Power Plant Based on Wind and Solar Energy". In: (2016) (cit. on pp. 7, A.4).

[A.172] Wang, W., Chen, L., Huang, X., Yang, L., and Du, X. "Performance Recovery of Natural Draft Dry Cooling Systems by Combined Air Leading Strategies". In: *Energies 2017, Volume 10, pp.1-18* (2017) (cit. on p. 147).

[A.173] Weinrebe, G. “Das Aufwindkraftwerk - Wasserkraftwerk der Wüste”. In: *Aufsatz zum Vortrag anlässlich der Jahresversammlung der Leopoldina am 18.10.2003 in Halle, pp.1-31* (2003) (cit. on p. 14).

[A.174] Weinrebe, G. and Schiel, W. “Up-Draught Solar Chimney and Down-Draught Energy Tower - A Comparison”. In: *ISES 2001 Solar World Congress* (2001) (cit. on p. 109).

[A.175] Yamaji, B., Szijarto, R., and Aszodi, A. “Study of Thermal Stratification and Mixing Using PIV”. In: (2008) (cit. on p. 92).

[A.176] Zavaragh, H.G., Ceviz, M.A., and Tabar, M.T.S. “Analysis of Windbreaker Combinations on Steam Power Plant Natural Draft Dry Cooling Towers”. In: *Applied Thermal Engineering, Volume 99, pp. 550-559* (2016) (cit. on p. 147).

[A.177] Zheng, Y., Ming, T.Z., Zhou, Z., Yu, X.F., Wang, H.Y., Pan, Y., and Liu, W. “Unsteady Numerical Simulation of Solar Chimney Power Plant System with Energy Storage Layer”. In: *Journal of the Energy Institute 83, Issue 2, pp.86-92* (2010) (cit. on pp. 43, 109).

[A.178] Zhou, X., Wang, F., Fan, J., and Ochieng, R.C. “Performance of Solar Chimney Power Plant in Qinghai-Tibet Plateau”. In: *Renewable and Sustainable Energy Reviews 14, pp.2249-2255* (2010) (cit. on p. 2).

[A.179] Zhou, X., Wang, F., and Ochieng, R.M. “A Review of Solar Chimney Power Technology”. In: *Renewable and Sustainable Energy Reviews 14, pp.2315-2338* (2010) (cit. on p. A.6).

[A.180] Zhou, X., Xiao, B., Liu, W., Guo, X., Yang, J., and Fan, J. “Comparison of Classical Solar Chimney Power System and Combined Solar Chimney System for Power Generation and Seawater Desalination”. In: *Desalination 250, pp.249-256* (2010) (cit. on p. 2).

[A.181] Zhou, X., Yang, J., Xiao, B., and Hou, G. “Experimental Study of Temperature Field in a Solar Chimney Power Setup”. In: *Applied Thermal Engineering, Volume 27, pp. 2044-2050* (2007) (cit. on p. A.6).

Books

[B.1] Baehr, H.D. and Stephan, K. *Wärme- und Stoffübertragung (7. Auflage)*. 2010 (cit. on pp. 35, 50).

[B.2] Burton, T., Jenkins, N., Sharpe, D., and Bossanyi, E. *Wind Energy Handbook - Second Edition*. 2011 (cit. on pp. 81, G.10).

[B.3] Carriveau, R. *Fundamental and Advanced Topics in Wind Power*. 2011 (cit. on p. G.10).

[B.4] Casey, M. and Wintergerste, T. *ERCOFTAC Special Interest Group on Quality and Trust in Industrial CFD*. 2000 (cit. on pp. 68, 69).

[B.5] Cengel, Y.A. *Heat Transfer - A Practical Approach - Second Edition*. 1998 (cit. on pp. 48–50).

[B.6] Cengel, Y.A. and Boles, M.A. *Thermodynamics - An Engineering Approach (Fifth Edition)*. 2008 (cit. on p. 45).

[B.7] Chenvidyakarn, T. *Buoyancy Effects on Natural Ventilation*. 2013 (cit. on p. 143).

[B.8] Cory, W.T.W.B. *Fans and Ventilation - A Practical Guide*. 2005 (cit. on pp. G.3, G.10, G.11).

[B.9] Dixon, S.L. *Fluid Mechanics and Thermodynamics of Turbomachinery (Fifth Edition)*. 2005 (cit. on pp. 27, 44–46, G.10).

[B.10] Duffie, J.A. and Beckman, W.A. *Solar Engineering of Thermal Processes (Second Edition)*. 1991 (cit. on pp. 50, 51).

[B.11] Dyke, M. van. *An Album of Fluid Motion*. 1982 (cit. on p. 35).

[B.12] Etling, D. *Theoretische Meteorologie*. 2008 (cit. on pp. 15, 19, 41, 42).

[B.13] Franke, J., Hellsten, A., Schlünzen, H., and Carissimo, B. *Best Practice Guideline for the CFD Simulation of Flows in the Urban Environment - Quality Assurance and Improvement of Microscale Meteorological Models (Cost Action 732)*. 2007 (cit. on p. 69).

[B.14] Fried, E. and Idelchik, I.E. *Flow Resistance - A Design Guide for Engineers*. 1989 (cit. on p. 24).

[B.15] Fröhlich, J. *Large Eddy Simulation turbulenter Strömungen*. 2006 (cit. on pp. 57, 60–62).

[B.16] Gasch, R. and Twele, J. *Wind Power Plants - Fundamentals, Design, Construction and Operation (Second Edition)*. 2012 (cit. on p. G.12).

[B.17] Hansen, M.O.L. *Aerodynamics of Wind Turbines - Second Edition*. 2008 (cit. on p. 22).

[B.18] Hau, E. *Windkraftanlagen - Grundlagen, Technik, Einsatz, Wirtschaftlichkeit - Fifth Edition*. 2014 (cit. on p. 81).

[B.19] Hillel, D. *Environmental Soil Physics*. 1998 (cit. on pp. 81, 84).

[B.20] Hirsch, C. *Numerical Computation of Internal and External Flows - Volume 1 - The Fundamentals of Computational Fluid Dynamics (Second Edition)*. 2007 (cit. on pp. 58, 65, 66).

[B.21] Idelchik, I.E. *Handbook of Hydraulic Resistance - 4th Revised and Augmented Edition*. 2007 (cit. on pp. 29–32, F.3).

[B.22] Idelchik, I.E. *Handbook of Hydraulic Resistance - Coefficients of Local Resistance and of Friction*. 1960 (cit. on pp. 17, 21, 23, 24, 28–30, 32, 33, 35).

[B.23] Incropera, Dewitt, Bergman, and Lavine. *Fundamentals of Heat and Mass Transfer - Supplemental Material (Sixth Edition)*. 2007 (cit. on pp. 20, 50).

[B.24] Jiji, L.M. *Heat Convection (Second Edition)*. 2009 (cit. on p. 50).

[B.25] Kraus, H. *Grundlagen der Grenzschicht - Meteorologie, Einführung in die Physik der atmosphärischen Grenzschicht und in die Mikrometeorologie*. 2008 (cit. on pp. 41, 43).

[B.26] Kröger, D.G. *Air-Cooled Heat Exchangers and Cooling Towers - Thermal Flow Performance Evaluation and Design - Volume I*. 2004 (cit. on p. 34).

[B.27] Kröger, D.G. *Air-Cooled Heat Exchangers and Cooling Towers - Thermal Flow Performance Evaluation and Design - Volume II*. 2004 (cit. on p. 34).

[B.28] Kundu, P.K., Cohen, I.M., and Dowling, D.R. *Fluid Mechanics - Fifth Edition*. 2012 (cit. on p. 145).

[B.29] Lal, R. and Shukla, M.K. *Principles of Soil Physics*. 2004 (cit. on p. 43).

[B.30] Malberg, H. *Meteorologie und Klimatologie - Eine Einführung (Fifth Edition)*. 2007 (cit. on pp. 76, 77, 81).

[B.31] Ming, T. *Solar Chimney Power Plant Generating Technology*. 2016 (cit. on p. 143).

[B.32] Mohseni, K. and Mittal, R. *Synthetic Jets - Fundamentals and Applications*. 2015 (cit. on p. 36).

[B.33] Monteith, J.L. and Unsworth, M.H. *Principles of Environmental Physics - Second Edition*. 1990 (cit. on p. 84).

[B.34] Petersen, C. *Dynamik der Baukonstruktion*. 2000 (cit. on p. 13).

[B.35] Pope, S.B. *Turbulent Flows*. 2000 (cit. on p. 61).

[B.36] Raffel, M., Willert, C., Wereley, S., and Kompenhans, J. *Particle Image Velocimetry - A Practical Guide - Second Edition*. 2007 (cit. on p. 92).

[B.37] Rennels, D.C. and Hudson, H.M. *Pipe Flow - A Practical and Comprehensive Guide*. 2012 (cit. on p. 146).

[B.38] Roache, P.J. *Verification and Validation in Computational Science and Engineering*. 1998 (cit. on p. 68).

[B.39] Schaffarczyk, A.P. *Introduction to Wind Turbine Aerodynamics*. 2014 (cit. on p. 22).

[B.40] Schlichting, H. and Gersten, K. *Grenzschicht-Theorie (10 Auflage)*. 2006 (cit. on pp. 18, 44).

[B.41] Tropea, C., Yarin, A.L., and Foss, J.F. *Springer Handbook of Experimental Fluid Mechanics*. 2007 (cit. on pp. 152, G.9).

[B.42] Union, European. *Soil Atlas of Africa*. 2013 (cit. on pp. H.2, H.3).

[B.43] VDI. *VDI Heat Atlas - Second Edition*. 2010 (cit. on p. 140).

[B.44] Versteeg, H.K. and Malalasekera, W. *An Introduction to Computational Fluid Dynamics - The Finite Volume Method (Second Edition)*. 2007 (cit. on pp. 56, 57, 60, 61, 63, 65, 69).

[B.45] Vismann, U. *Wendehorst Bautechnische Zahlentafeln - 35 Edition*. 2015 (cit. on p. 80).

[B.46] White, F.M. *Fluid Mechanics (Seventh Edition)*. 2009 (cit. on p. 20).

Presentations

[P.1] Kadem, L. *Particle Image Velocimetry for Fluid Dynamics Measurements [Power Point Slides]*. 2012 (cit. on p. 92).

[P.2] Kiger, K. *Introduction of Particle Image Velocimetry [Power Point Slides]. Burgers Program for Fluid Dynamics Turbulence School*. 2014 (cit. on p. 92).

[P.3] Pastohr, H. *Studie Umlenkung [Power Point Slides]. Solar Millenium AG*. 2008 (cit. on p. 47).

[P.4] Sturm, M. and Franke, J. *Evaluation of OpenFOAM with the German VDI Guideline 3783/9 for Environmental Meteorology [Power Point Slides]*. 2010 (cit. on p. 70).

Standards and Guidelines

[S.1] ANSYS Inc., 2016. *ANSYS Fluent Theory Guide 17.2*. 2016 (cit. on pp. 64, 65).

[S.2] ANSYS Inc., 2016. *ANSYS Fluent Tutorial Guide 17.2*. 2016 (cit. on p. 69).

[S.3] ANSYS Inc., 2016. *ANSYS Meshing Users Guide 17.2*. 2016 (cit. on p. 67).

[S.4] ANSYS Inc., 2016. *ANSYS Users Guide 17.2*. 2016 (cit. on p. 65).

[S.5] DIN EN ISO, 5167-1. *DIN EN ISO 5167-1 Durchflussmessung von Fluiden mit Drosselgeräten in voll durchströmten Leitungen mit Kreisquerschnitt - Teil 1: Allgemeine Grundlagen und Anforderungen (ISO 5167-1:2003). Deutsche Fassung EN ISO 5167-1:2003, 01-2004*. 2004 (cit. on p. 93).

[S.6] DIN EN ISO, 5167-3. *DIN EN ISO 5167-3 Durchflussmessung von Fluiden mit Drosselgeräten in voll durchströmten Leitungen mit Kreisquerschnitt - Teil 3: Düsen und Venturidüsen (ISO 5167-3:2003). Deutsche Fassung EN ISO 5167-1:2003, 01-2004*. 2004 (cit. on p. 93).

[S.7] DIN EN ISO, 5167-4. *DIN EN ISO 5167-4 Durchflussmessung von Fluiden mit Drosselgeräten in voll durchströmten Leitungen mit Kreisquerschnitt - Teil 4: Venturirohre (ISO 5167-4:2003). Deutsche Fassung EN ISO 5167-4:2003, 01-2004*. 2004 (cit. on p. 93).

[S.8] DIN EN, 13031-1. *DIN EN 13031-1 Gewächshäuser - Bemessung und Konstruktion - Teil 1: Kulturgewächshäuser. Deutsche Fassung EN 13031-1:2001, 09-2003*. 2003 (cit. on p. 7).

[S.9] DIN, 24163-1. *Ventilatoren, Leistungsmessung und Normkennlinien. 01-1985*. 1985 (cit. on p. G.10).

[S.10] DIN, 24163-2. *Ventilatoren, Leistungsmessung und Normprüfstände. 01-1985*. 1985 (cit. on p. G.10).

[S.11] DIN, 24163-3. *Ventilatoren, Leistungsmessung an Kleinventilatoren und Normprüfstände. 01-1985*. 1985 (cit. on p. G.10).

[S.12] Dynamics, Dantec. *StreamWare Basic - Installation and User Guide 6.00.* 2016 (cit. on p. 151).

[S.13] Movement, Air and Control Association International, Inc. *AMCA 210-99 Laboratory Methods of Testing Fans for Aerodynamic Performance Rating.* 1999 (cit. on p. G.10).

[S.14] Movement, Air and Control Association International, Inc. *AMCA 802-02 (R2008) Industrial Process/Power Generation. Fans: Establishing Performance Using Laboratory Models.* 2008 (cit. on p. G.10).

[S.15] V, ASME and V, 20-2009. *Standard for Verification and Validation in Computational Fluid Dynamics and Heat Transfer.* 2009 (cit. on p. 68).

[S.16] VGB PowerTech e.V., 2010. *VGB-R 610 U. Structural Design of Cooling Towers - VGB Guideline on the Structural Design, Calculation, Engineering and Construction of Cooling Towers.* (Cit. on pp. 129, 132).

Theses

[T.1] Backström, T.W. von. "From Turbo-Machines to Solar Chimneys". PhD Thesis. University of Stellenbosch, Department of Mechanical and Mechatronic Engineering. Stellenbosch, South Africa, 2012 (cit. on pp. 24, 25, 35).

[T.2] Bayer, A. "Modellierung der Temperaturentwicklung oberflächennaher Boden- und Gesteinsschichten arider Gebiete unter Berücksichtigung der solaren Einstrahlung und der Topographie". Master Thesis. Universität Stuttgart, Stuttgart, Germany, 2008 (cit. on pp. 84, 88).

[T.3] Bernardes, M.A. dos Santos. "Technische, ökonomische und ökologische Analyse von Aufwindkraftwerken". PhD Thesis. Institut für Energiewirtschaft und Rationelle Energieanwendung, Abteilung Neue Energietechnologien und Technikanalyse. Stuttgart, Deutschland, 2004 (cit. on p. 85).

[T.4] Blackiston Jr., H.S. "Tip Effects on Fluctuating Lift and Drag Forces Acting on a Circular Cylinder Perpendicular to an Air Flow". Master Thesis. California Institute of Technology. Pasadena, California, 1963 (cit. on p. 33).

[T.5] Burger, A.A.S. "Numerical Analysis of Flow Around Infinite and Finite Cylinders at Trans-Critical Reynolds Numbers with and without Surface Roughness". Master Thesis. University of Stellenbosch, Department of Mechanical Mechatronic Engineering. Stellenbosch, South Africa, 2015 (cit. on pp. 56, B.2).

[T.6] Dyk, C. van. "The Realisation of the Solar Chimney Inlet Guide Vanes". Master Thesis. University of Stellenbosch, Department of Civil Engineering. Stellenbosch, South Africa, 2004 (cit. on p. 14).

[T.7] Eck, S. R. G. van. "Solar Updraft Tower - Structural Optimisation Under Dynamic Wind Action". Master Thesis. Delft University of Technology, Delft, The Netherlands, 2014 (cit. on pp. 13, 121, 126).

[T.8] Fluri, T.P. "Turbine Layout for and Optimization of Solar Chimney Power Conversion Units". PhD Thesis. University of Stellenbosch, Department of Mechanical and Mechatronic Engineering. Stellenbosch, South Africa, 2008 (cit. on pp. 11, G.9, G.11, G.12).

[T.9] Gannon, A.J. "Solar Chimney Turbine Performance". PhD Thesis. University of Stellenbosch, Department of Mechanical Engineering. Stellenbosch, South Africa, 2002 (cit. on pp. A.6, G.9, G.11, G.12, G.13).

[T.10] Goldack, A. "Tragverhalten und Aussteifung hoher Stahlbetonröhren für Aufwindkraftwerke". PhD Thesis. Universität Stuttgart, Institut für Leichtbau Entwerfen und Konstruieren. Stuttgart, Germany, 2004 (cit. on p. 13).

[T.11] Harris, R.L. "A Numerical Analysis of the Flow Field Surrounding a Solar Chimney Power Plant". Master Thesis. University of Stellenbosch, Department of Mechanical Engineering. Stellenbosch, South Africa, 2004 (cit. on p. 66).

[T.12] Kalpakli, A. “Experimental Study of Turbulent Flows Through Pipe Bends”. PhD Thesis. Royal Institute of Technology, Stockholm, Sweden, 2012 (cit. on p. 145).

[T.13] Kirstein, C.F. “Flow Through a Solar Chimney Power Plant Collector-to-Chimney Transition Section”. Master Thesis. University of Stellenbosch, Department of Mechanical Engineering. Stellenbosch, South Africa, 2004 (cit. on pp. 2, G.12).

[T.14] Kistner, B. “Modellierung und numerische Simulation der Nachlaufstruktur von Turbomachinen am Beispiel einer Axialturbinenstufe”. PhD Thesis. Technische Universität Darmstadt, Darmstadt, Germany, 1999 (cit. on p. G.9).

[T.15] Koonsrisuk, A. “Analysis of Flow in Solar Chimney for an Optimal Design Purpose”. PhD Thesis. Suranaree University of Technology, Department of Mechanical Engineering. Thailand, 2009 (cit. on pp. 150, A.4, A.5).

[T.16] Lupi, F. “Stochastic Aerodynamic Effects in the Design of Ultra-High Towers exposed to the Atmospheric Flow”. PhD Thesis. Department of Architecture, Civil Engineering and Environmental Sciences, University of Braunschweig. Braunschweig, Germany, 2013 (cit. on pp. 139, 152, A.4).

[T.17] Lupi, F. “Structural Behaviour, Optimization and Design of a Solar Chimney Prototype under Wind Loading and other Actions”. Master Thesis. Ruhr Universität Bochum and Universita degli Studi die Firenze. Florence, Italy, 2009 (cit. on pp. 121, 131, 133).

[T.18] Meunders, A. “A Study on Buoyancy-Driven Flows - Using Particle Image Velocimetry for Validating the Fire Dynamics Simulator”. PhD Thesis. Bergische Universität Wuppertal, Wuppertal, Germany, 2016 (cit. on pp. 143, 169).

[T.19] Pastohr, H. “Thermodynamische Modellierung eines Aufwindkraftwerks”. PhD Thesis. Bauhaus-Universität Weimar, Fakultät Bauingenieurwesen. Weimar, Deutschland, 2004 (cit. on pp. 2, 36, 118).

[T.20] Pretorius, J.P. “Optimization and Control of a Large-Scale Solar Chimney Power Plant”. PhD Thesis. University of Stellenbosch, Department of Mechanical Engineering. Stellenbosch, South Africa, 2007 (cit. on pp. 34, 50, 53, 75, 80).

[T.21] Spuy, S.J. van der. “Perimeter Fan Performance in Forced Draught Air-Cooled Steam Condensers”. PhD Thesis. University of Stellenbosch, Department of Mechanical and Mechatronic Engineering. Stellenbosch, South Africa, 2011 (cit. on p. 27).

[T.22] Thiart, G.D. “A Numerical Procedure for Predicting the Effects of Distorted Inflow Conditions on the Performance of Axial Flow Fans”. PhD Thesis. University of Stellenbosch, Department of Mechanical Engineering. Stellenbosch, South Africa, 1990 (cit. on p. 25).

[T.23] Wald, J.-F. “Lois de paroi adaptatives pour un modèle de fermeture du second ordre dans un contexte industriel”. PhD Thesis. Universitè de Pau et des Pays de L’adour, 2016 (cit. on p. 58).

[T.24] Weersink, R. “Experimental Study of the Oscillatory Interaction between Two Free Opposed Turbulent Round Jets”. Master Thesis. Syracuse University and University of Twente. New York, USA, 2010 (cit. on p. 36).

[T.25] Witting, D. “Numerische Umsetzung und Untersuchung verschiedenartig modellierter Varianten eines SCPP in SOFiSTiK”. Master Thesis. Bergische Universität Wuppertal, Fakultät für Architektur und Bauingenieurwesen. Wuppertal, Germany, 2016 (cit. on pp. 124, 126, 128–131).

[T.26] Yabuz, Z.R. “The Study on the Constructional Improvements and the Research of Methods to Increase the Performance of the Solar Chimney”. Master Thesis. Süleyman Demirel University Graduate School of Applied and Natural Sciences, Mechanical Engineering Department, Isparta, 2009 (cit. on p. A.5).

URL

[U.1] *www.airfoiltools.com*. [accessed 28-July-2017] (cit. on p. G.12).

[U.2] *www.arch.mcgill.ca*. [accessed 07-November-2014] (cit. on p. 8).

[U.3] *www.cfd-online.com*. [accessed 09-June-2017] (cit. on pp. 63, 69).

[U.4] *www.ercoftac.org*. [accessed 11-June-2017] (cit. on p. 68).

[U.5] *www.floodmap.net*. [accessed 12-January-2015] (cit. on p. H.2).

[U.6] *www.greenhousegnome.com*. [accessed 20-September-2014] (cit. on p. 8).

[U.7] *www.pmfias.com*. [accessed 01-January-2018] (cit. on p. 77).

[U.8] *www.sbp.de*. [accessed 01-January-2018] (cit. on p. 12).

[U.9] *www.uttei.enea.it*. [accessed 06-June-2017] (cit. on p. 59).

[U.10] *www.weather-and-climate.com*. [accessed 16-December-2016] (cit. on pp. H.2, H.3, H.4).

[U.11] *www.wikipedia.com*. [accessed 07-November-2014] (cit. on pp. 8, 11).

[U.12] *www.windfinder.com*. [accessed 16-December-2016] (cit. on p. H.4).

Part V

Appendices

AppendixA

Former Research on the Solar Chimney Power Plant

Following figures A.1, A.2, A.3, A.4, A.5 and A.6 show all acquainted to the author known former prototypes of a SCPP within the last 37 years in descending chronological order.

solar tower:	20.1 m tall with constant diameter of 1 m, steel pipe
solar collector:	27.5 m side length, inclination angle of 3°, glass cover
turbine:	yes
others:	no ground preparation, structural health monitoring (SHM) concept

a) 2017 - Aswan, Egypt

solar tower:	4.0 m tall with variable diameter of 0.24 to 0.40 m (outlet) and 0.10 to 0.12 m (throat), steel pipe
solar collector:	3.2 m in diameter, inclination angle of 7°, 6 mm perspex cover
turbine:	none
others:	guyed mast, ground preparation (see above)

b) 2017 - Suva, Fiji (A833)

solar tower:	6.0 m tall and 0.15 m in diameter, PVC pipe
solar collector:	6.0 m in diameter, inclination from 0.25 to 0.50 m, plastic cover
turbine:	single vertical axis turbine with 0.144 m in diameter
others:	none

c) 2016 - Aswan, Egypt [A.119]

solar tower:	2.0 m of height and 0.2 m in diameter, PVC tube
solar collector:	3.0 m in diameter, glass elements, 0.06 m collector height
turbine:	unknown
others:	absorber made of steel and chipboard wood covered with black colour, electric corona wind effect has been utilized

d) 2016 - Teheran, Iran [A.131], [A.53]

Figure A.1: Physical Models of a Solar Chimney Power Plant - Part 1 of 6

solar tower:	2.0 to 4.0 m of height and a diameter of 0.3 m, PVC tube
solar collector:	8.0 m in diameter, PC sheets, inclination from appr. 0.2 to 0.5 m
turbine:	none
others:	ground made of concrete painted black

e) 2016 - Borj Cedria, Tunisia [A.91]

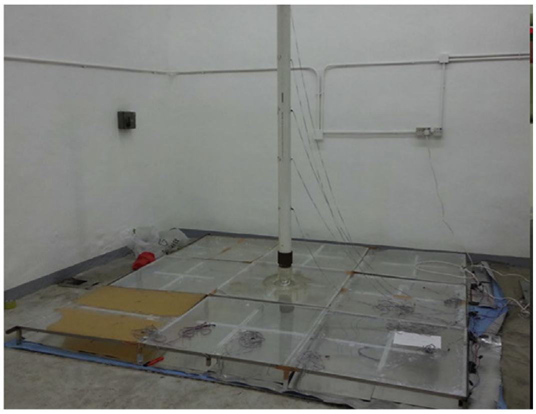

solar tower:	2.0 m of height and 0.1 m in entrance diameter, a second divergent chimney with an outlet diameter of 0.2 m has been investigated, PVC tube
solar collector:	square collector, 3.0 m x 3.0 m x 0.1 m, steel frame with organic glass
turbine:	none
others:	electrical infra-radiation film heater, fixed total power of 1520 W, overlaid the bottom of the collector and covered by several thin aluminium sheets for producing a more uniform heating surface

f) 2016 - Hong Kong, China [A.83]

solar tower:	0.2 m to 1.0 m of height, variable, flange connections
solar collector:	1.22 m in diameter, made of PC
turbine:	none
others:	400-W metal halide gas discharge lamp as light source for the solar simulator, 188 pieces, adjustable height

g) 2016 - Xian, China [A.64]

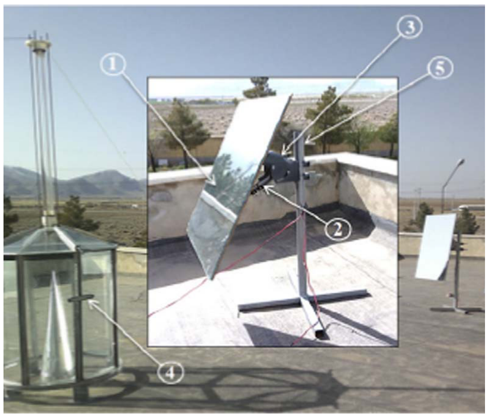

solar tower:	2.4 m of height and 0.16 m in diameter, glass tube
solar collector:	none, box of 0.92 m in diameter and 1.1 m of height, metal frame and glass sheets, octagonal shaped
turbine:	none
others:	intensifiers to focus the solar irradiation

h) 2015 - Isfahan, Iran [A.95]

Figure A.2: Physical Models of a Solar Chimney Power Plant - Part 2 of 6

solar tower: 25.0 m of height and 2.5 m of diameter, light metal skeleton permanently wrapped with a thermally insulated plastic
solar collector: 1020 m^2 made of plastic, square shaped, situated to one side of the tower
turbine: 1.12 m in diameter, situated at the periphery of the collector
others: enclosed periphery of collector, ground was covered by black plastic sheets

i) 2013 - Compotades, Greece [A.141]

solar tower: 9.0 m of height and 0.31 m in diameter, PVC tubes
solar collector: 4 mm glass sheet, insulated metallic box, 3.65 m x 6.04 m (converging), collector is tilted by 35°
turbine: none
others: absorption layer (soil) underneath the glass sheet

j) 2013 - Damascus, Syria [A.93]

solar tower: 17.15 m tall, 0.8 m in diameter, made of metal plate covered with aluminium foil and glass wool
solar collector: 27 m in diameter, slope of 6°, adjustable inlet from 0.05 to 0.35 m, plastic sheet
turbine: none
others: 0.5 m of ground is covered with Asphalt - Glass - Sand - Gravel - Glass Wool with Aluminium Foil

k) 2012 - Adiyaman, Turkey [A.24]

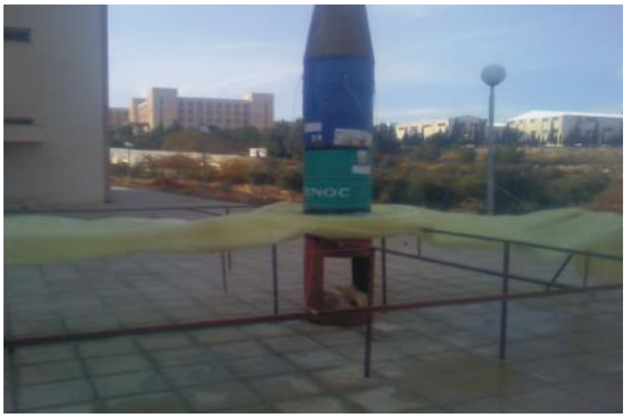

solar tower: 4.0 m of height and a diverging diameter of 0.57 to 0.58 m, steel tube
solar collector: 6.8 m in diameter, plastic sheets, roof height of 1.0 m
turbine: none
others: none

l) 2011 - Mutah, Jordan [A.36], [A.37]

solar tower: 12.0 m of height and 0.5 m in diameter, PE pipe
solar collector: 20.0 m in diameter, inclination from 0.15 to 1.0 m, PC sheets
turbine: none
others: ground was covered by black films of PE

m) 2011 - Zanjan, Iran [A.94], [A.6]

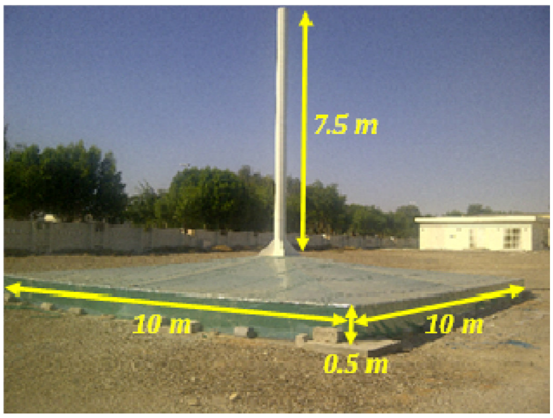

solar tower: 8.25 m tall and 0.24 m in diameter, steel pipe
solar collector: 10 m in diameter (square), collector with plastic cover, inclination of collector from 0.50 to 075 m
turbine: none
others: none

n) 2011 - Al-Ain, UAE [A.70]

Figure A.3: Physical Models of a Solar Chimney Power Plant - Part 3 of 6

solar tower:	0.8 m tall and 0.08 to 0.12 m in diameter, made of metal sheet
solar collector:	1.40 m in diameter, 0.10 m above ground, plastic sheet
turbine:	none
others:	none

o) 2011 - Himachal Pradesh, India [A.118]

solar tower:	60 m tall and 3.0 m in diameter, guyed and encased steel tube
solar collector:	40.0 m in diameter, inclination to the centre, plastic cover
turbine:	none
others:	none

p) 2011 - Kerman, Iran [A.56], [A.130]

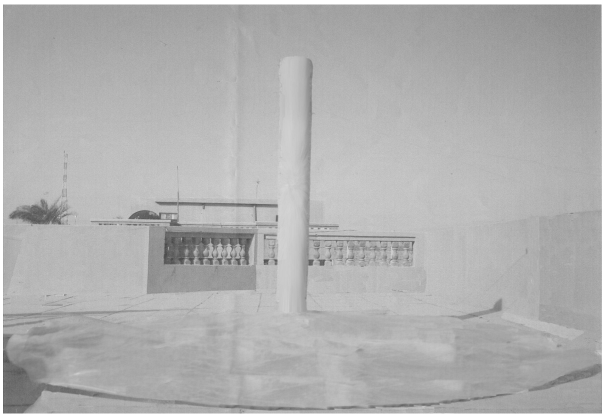

solar tower:	4.02 m tall and 0.20 m in diameter
solar collector:	6.0 m in diameter, plastic cover, inclination from 0.02 to 0.10 m
turbine:	none
others:	three kinds of ground (concrete, black coloured concrete, black coloured pebbles) were studied

q) 2010 - Baghdad (Saydia City), Irag [A.26]

solar tower:	53.0 m tall and 18.5 m in diameter, five tower entrances for turbines with 8.2 m in diameter, made of cement, steel and bricks
solar collector:	6,170 m^2 covered area, tempered glass
turbine:	five horizontal axis turbines with three blades each, blade length 4.0 m
others:	none

r) 2010 - Wuhai Desert, China [T.16], [A.171]

solar tower:	appr. 5.0 m of height and 0.5 in diameter
solar collector:	100 m^2, plastic cover, one quarter of a full circle, no plain area
turbine:	none
others:	prototype to prove reliability of concept

s) 2010 - France [A.60]

solar tower:	8.0 m tall and 2.0 m in diameter, tower made of metal sheet
solar collector:	8.0 m in diameter (octagonal shaped), plastic sheet, adjustable roof height from 0.06 to 0.50 m, convergent to centre
turbine:	none
others:	none

t) 2009 - Suranaree, Thailand [T.15]

Figure A.4: Physical Models of a Solar Chimney Power Plant - Part 4 of 6

solar tower:	8.0 m tall and divergent chimney from 2.0 to 2.82 m, tower made of metal sheet
solar collector:	8.0 m in diameter (octagonal shaped), plastic sheet, adjustable roof height from 0.06 to 0.50 m
turbine:	none
others:	none

u) 2009 - Suranaree, Thailand [T.15]

solar tower:	8.0 m tall and 1.0 m in diameter, tower made of metal sheet
solar collector:	3.36 in diameter (octagonal shaped), plastic sheet, adjustable roof entry 0.04 to 0.25 m
turbine:	none
others:	none

v) 2009 - Suranaree, Thailand [T.15]

solar tower:	8.0 m tall and 2.0 m in diameter, tower made of metal sheet
solar collector:	8.2 m side length (square), divergent to the centre, plastic sheet, 0.5 m above ground
turbine:	none
others:	partially opened at the edges

w) 2009 - Suranaree, Thailand [T.15]

solar tower:	appr. 100 m in length mounted to the ground, plastic sheet, 1.5 m in diameter
solar collector:	section of a full circle, plastic cover
turbine:	yes
others:	none

x) 2009 - Cerro Canela, Chile [A.60]

solar tower:	12.0 m of height, wooden frame with red tarpaulin
solar collector:	pyramid shaped square with 420 m^2
turbine:	yes, design studies have been performed
others:	a prototype plant has been erected made of a guyed PVC tube and a plastic sheet covered collector

y) 2008 - Weimar, Germany [A.155], [T.26]

solar tower:	12.3 m tall and 1.0 m in diameter, made from metal
solar collector:	25.0 m in diameter, plastic cover, adjustable roof from 0.05 to 0.50 m
turbine:	none
others:	none

z) 2008 - Minas Gerais, Brazil [A.116], [A.42]

Figure A.5: Physical Models of a Solar Chimney Power Plant - Part 5 of 6

solar tower:	8.85 m tall with a diameter of 0.3 m, PVC tubes, wind shield on top
solar collector:	10.0 m in diameter, glass elements, inclination from 0.05 to 0.8 m
turbine:	yes, blade length 0.14 m
others:	ground was covered with insulation material and mixed asphalt with black gravel on top

aa) 2006 - Wuhan, China [A.181]

solar tower:	15.0 m of height, steel tube, 1.22 m in diameter
solar collector:	16.0 m in diameter, glass elements
turbine:	yes
others:	installation in transition section, concrete foundation covering ground underneath collector

ab) 2005 - Turkey [A.167]

solar tower:	22.0 m of height and 2.0 m in diameter, guyed GRP pipes
solar collector:	15.0 m side length, square pyramidal shaped, glass elements
turbine:	1.1 m diameter
others:	granite as ground material

ac) 2004 - Gaborone, Botswana [A.31]

solar tower:	8.0 m of height and a diameter of 0.35 m, flexible material
solar collector:	no collector, therefore a solar pond, 4.2 m in diameter and a depth of 1.85 m
turbine:	no turbine, therefore a water to air heat exchanger
others:	none

ad) 2003 - Melbourne, Australia [A.4], [A.179]

solar tower:	7.92 m tall, converging from 2.28 to 0.61 m, made of Lexan sheets, polygonal shaped
solar collector:	9.15 m in diameter, Lexan roof, additional tests with clear visqueen, slope of 23.27°, polygonal shaped
turbine:	none
others:	ground was covered with different absorbers (aluminium plate with styrofoam insulation, black visqueen, canvas absorber)

ae) 1997 - Gainesville, USA [T.9], [A.144], [A.143]

solar tower:	194.6 m tall and 5.08 m in diameter, guyed steel tower
solar collector:	122.0 m in diameter, glass and plastic elements, inclination of roof from 1.7 to 2.0 m
turbine:	8.0 m in diameter, 4 blades
others:	none

af) 1986 - Manzanares, Spain [A.159]

Figure A.6: Physical Models of a Solar Chimney Power Plant - Part 6 of 6

AppendixB

Wind Tunnel Studies at Stellenbosch, South Africa

B.1 Wind Tunnel at Stellenbosch, SA

The wind tunnel at the University of Stellenbosch, South Africa has been used for tests at a model of a SCPP. The main details about the wind tunnel are collected in table B.1.

Table B.1: Properties of Wind Tunnel

	Range	**Unit**
Measures		
Length of Inlet Passage	4.0	m
Area of Inlet Passage	12.3	m^2
Testing Section Width	1.4	m
Testing Section Height	1.0	m
Testing Section Length	1.9	m
Outlet Passage	15.4	m
Flow		
x-Velocity	up to 100	m/s
Turbulence Intensity	unknown	-
Turbulence Length Scale	unknown	m
Fan		
Fan Diameter Span	2.7	m

The shape of the testing section and outlet passage is octagonal with a pitot static tube located close to the testing section to get the wind speed as a reference. An array of guide vanes situated in the inlet passage right after the flow is turned by 90 degrees to get into the testing section. The sucking fan is powered by a 373 kW motor. Figure B.1 shows a sketch of the wind tunnel.

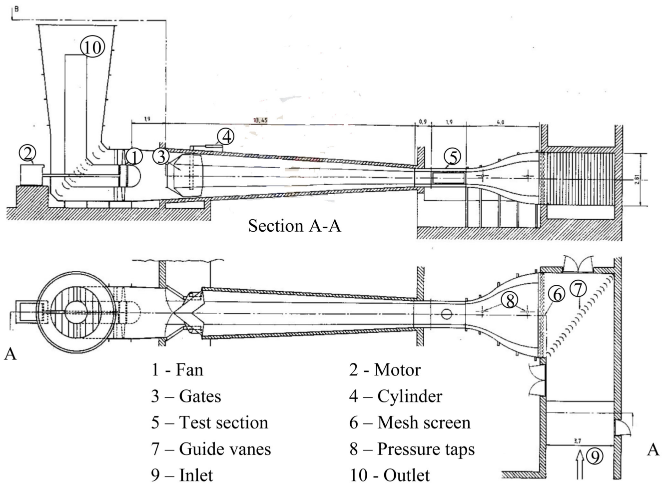

Figure B.1: Wind Tunnel at Stellenbosch [T.5]

B.2 Wind Tunnel Models I and II

Two wind tunnel models have been tested and the main model dimensions are listed in table B.2.

Table B.2: Main Model Dimensions

	Model I	**Model II**	**Unit**
Tower			
Height	1.2	0.9	m
Diameter	150	150	mm
Thickness	3	3	mm
Material	Perspex	Perspex	-
Collector			
Length	1.9	0.7	m
Width	1.4	0.875	m
Height	40	40	mm
Thickness	5	5	mm
Material	Perspex	Perspex	-
Openings			
Diameter	32	32	mm
Quantity	8	8	-

Model I was mounted on a bottom section which was placed inside the testing section of the wind tunnel. The bottom section served as the ground of a real SCPP representing the soil surface. For the wind tunnel studies pressure tabs were installed into it to measure the pressure underneath the collector roof. Figure B.2 shows the drawing of Model I for different views with the description of the main parts.

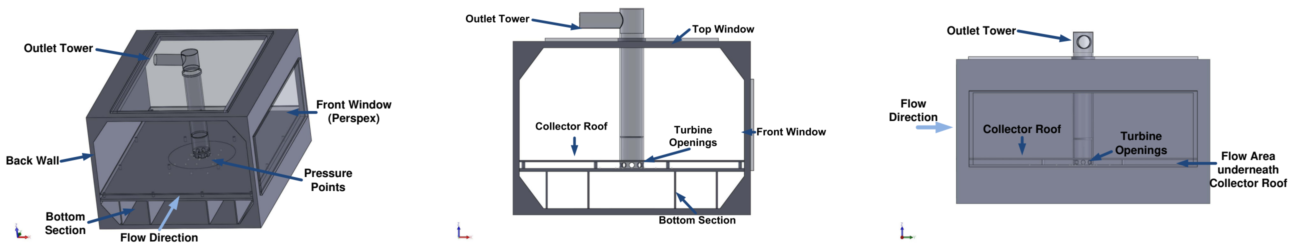

a) Iso View b) Stream-Wise View c) Side View

Figure B.2: Wind Tunnel Model I (Drawings)

Figure B.3 gives a collection of Model I in the phase of construction and placing it inside the wind tunnel.

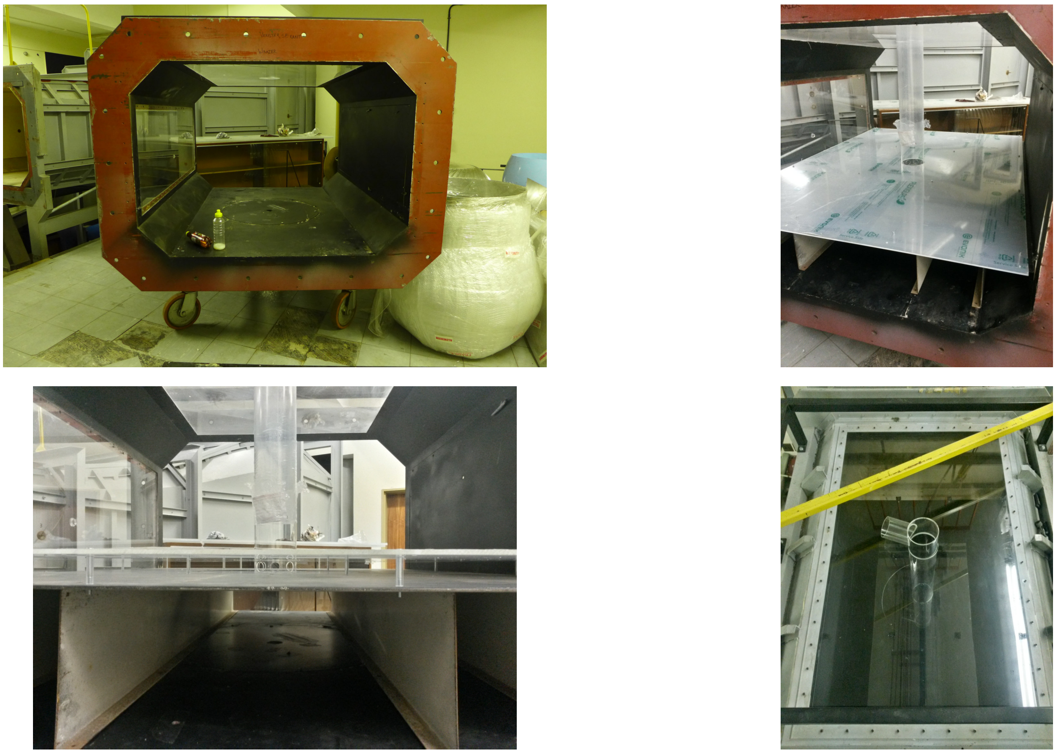

Figure B.3: Wind Tunnel Model I - Preparation

The bottom section, the collector and the turbine openings, and the tower outlet on top of the wind tunnel ceiling are depicted, respectively.

Due to problems with the calibration of the PIV system and the analysis of the measured data a second model had to be built. The general concept of the model was retained which lead to Model II. Two horizontal and one vertical layer has been measured for Model II which required an adaptation of the model on the measuring direction. Therefore figure B.4 and figure B.5 depict the final design for the measurement of the horizontal and vertical layers respectively.

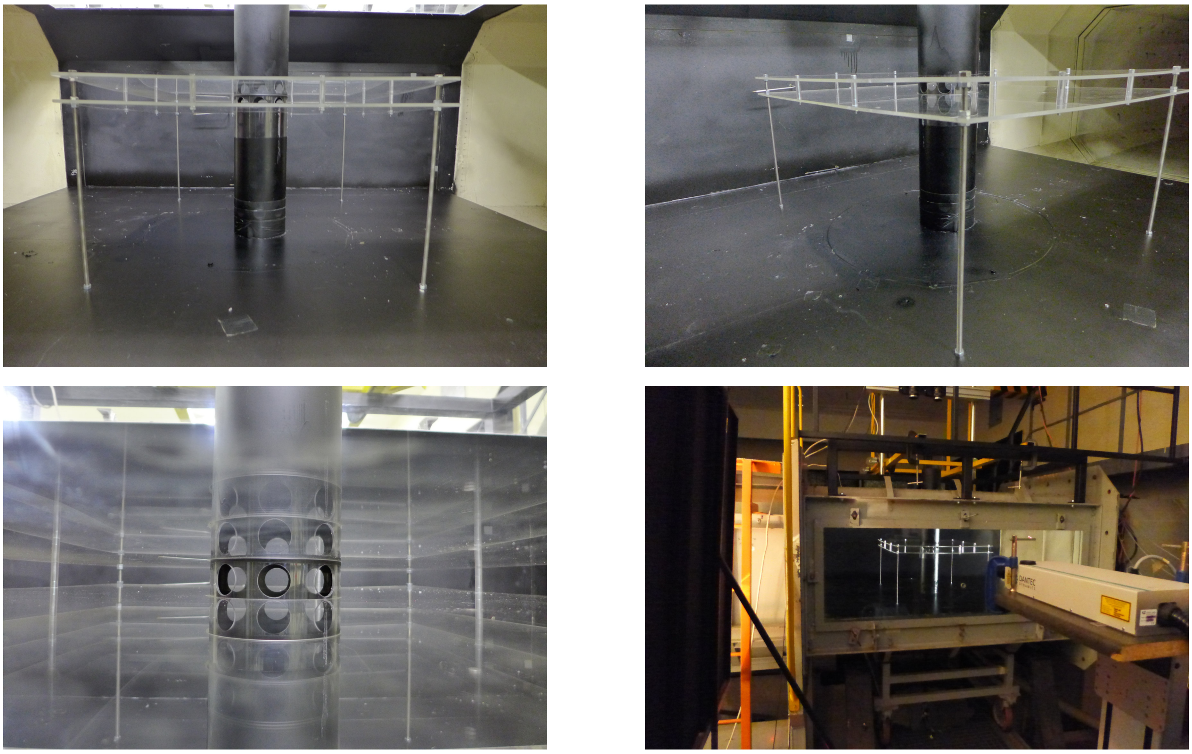

Figure B.4: Wind Tunnel Model II (Final Design) - Horizontal Layer

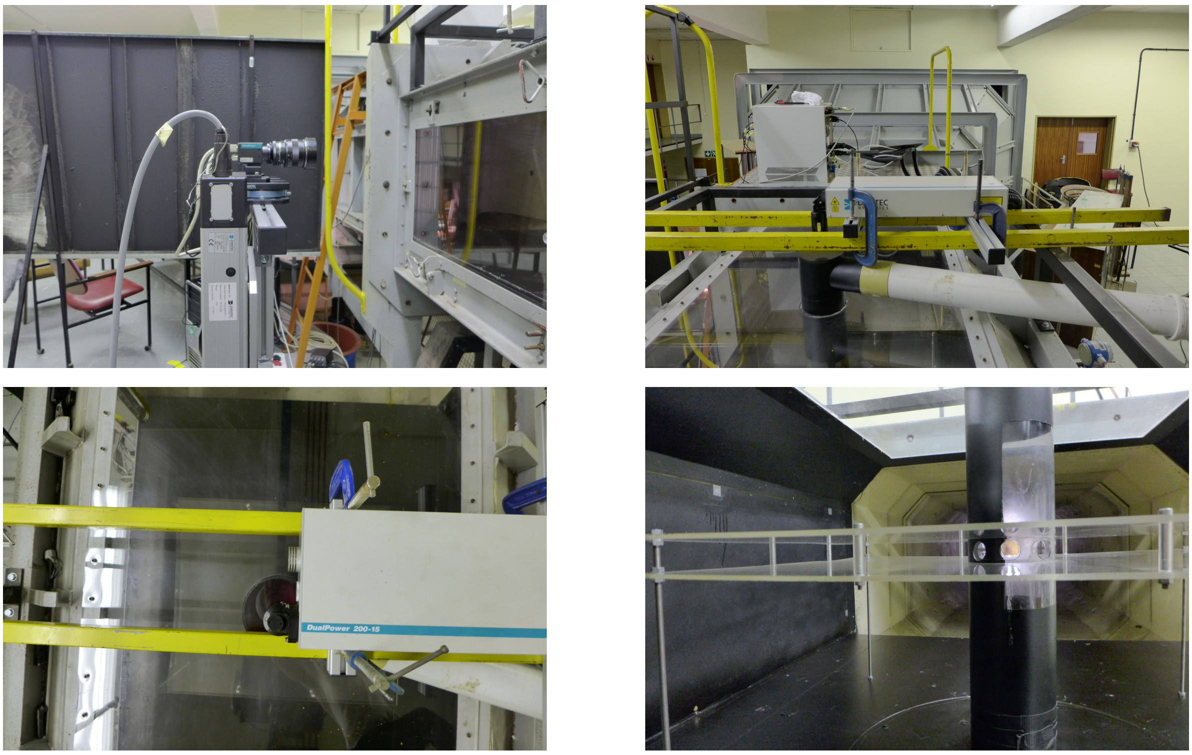

Figure B.5: Wind Tunnel Model II (Final Design) - Vertical Layer

B.3 Measurement Equipment

The following section gathers information about the equipment and measuring program for measuring the volume/mass flow, the pressure, the pitot static tube and the PIV system.

B.3.1 Volume/Mass Flow Measurements

Figure B.6 shows the standard *venturi flow meter* as can be found in industrial application. The right picture depicts the simple but efficient and reliable construction used at Stellenbosch.

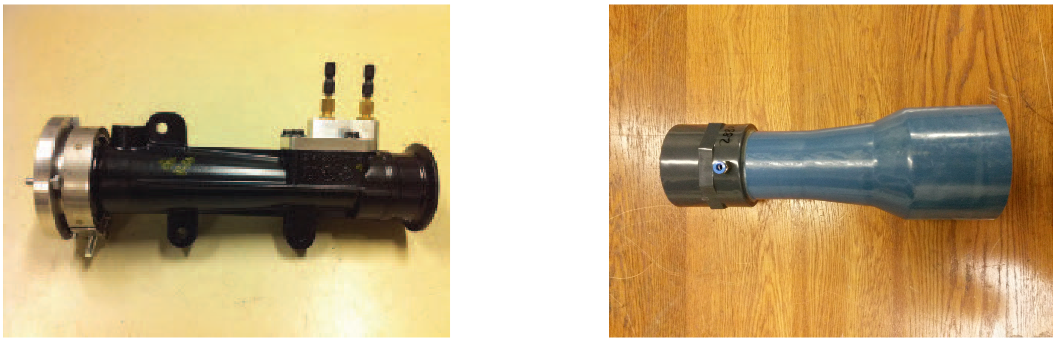

a) Standard b) Designed at Stellenbosch

Figure B.6: Venturi Flow Meter [A.112]

B.3.2 Pressure Measurements

The measuring program includes the gathering of the spatial distribution of velocity and pressure measurements underneath the collector, at the inlets of the transition section and inside the tower. Figure B.7 shows the pressure points at the three positions installed for Model I and figure B.8 the preparation and installation within the wind tunnel.

The pressure holes were mounted flush to the corresponding surfaces and have been connected with optimized tubes, cf. [A.132] to the pressure transducers shown in the picture. All in all 40 pressure points have been installed and had to be measured one by one. For Model II no pressure measurements have been performed. The results will not presented in the course of this work.

B.3.3 Pitot Static Tube

The *Pitot Static Tube* was mounted within the test section of the wind tunnel at medium height. Figure B.9 shows the front and back view of the installed pitot static tube.

B.3.4 PIV System

The PIV system with both cameras for the vertical and horizontal arrangement are depicted in figure B.10.

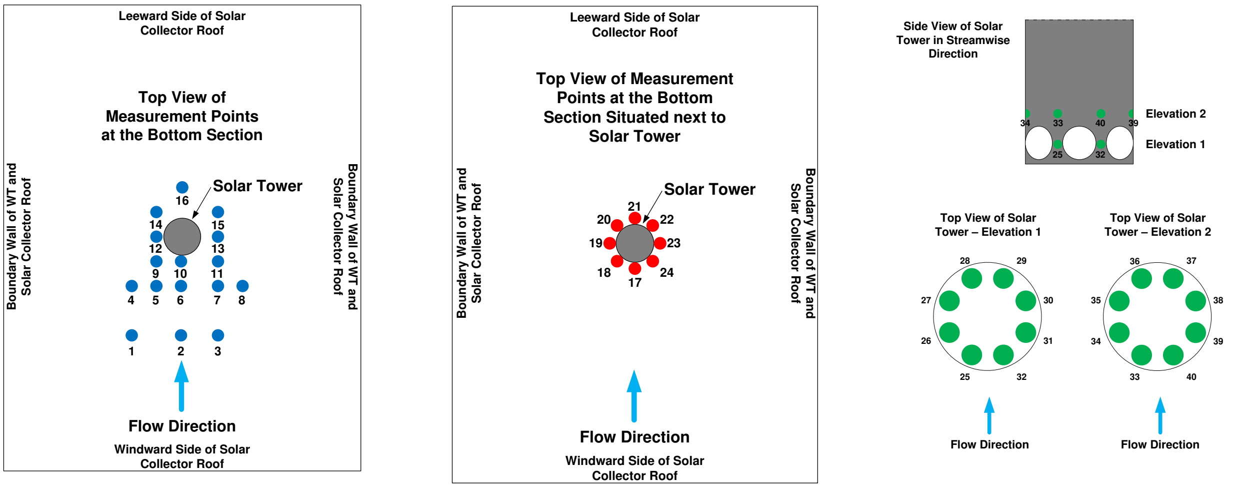

a) Pressure Points at Bottom Section

b) Pressure Points at Inlets of Solar Tower

c) Pressure Points Inside Solar Tower

Figure B.7: Pressure Measurement Points (Scheme)

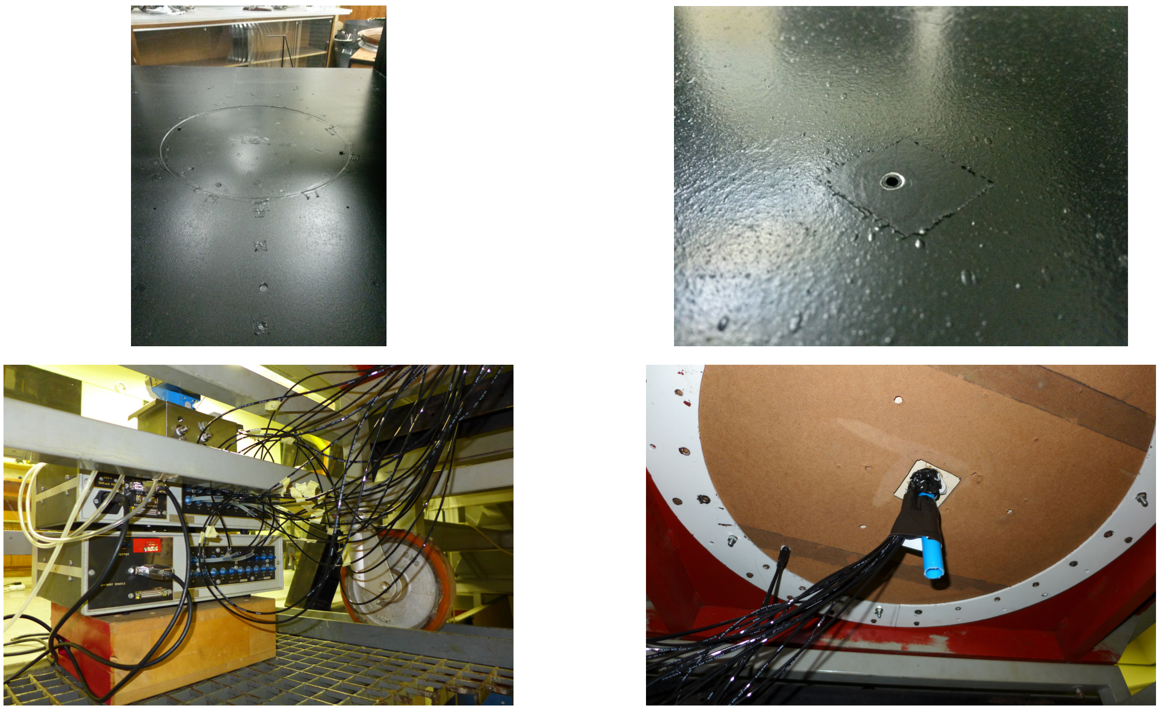

Figure B.8: Pressure Measurement Points - Preparation and Installation

The calibration procedure had to be repeated several times to get the perfect alignment and to reduce the negative influence of the reflections of the perspex sheets on the measurements.

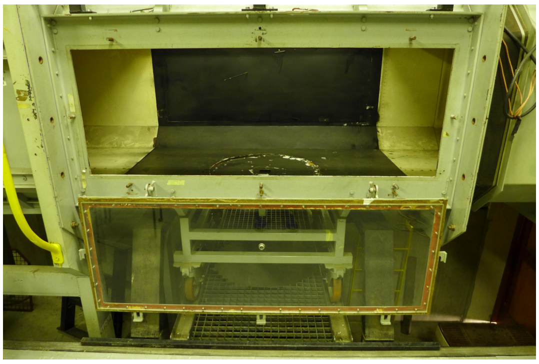
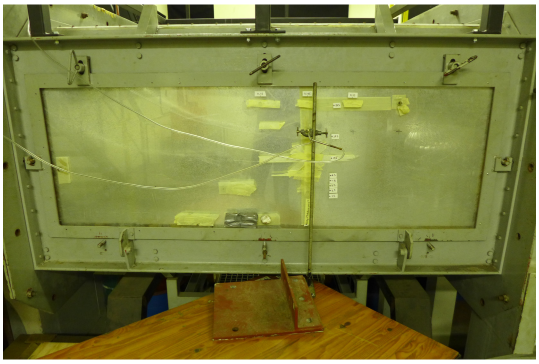

Figure B.9: Pitot Static Tube Inside the Measuring Section

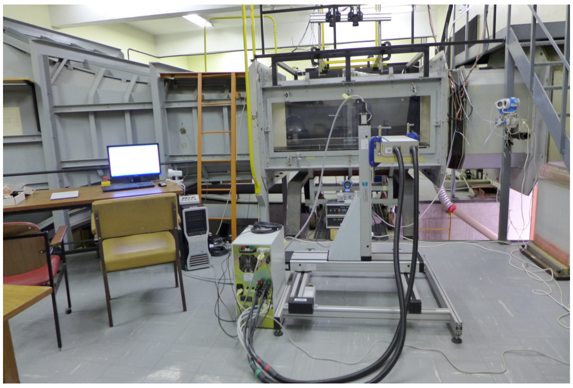
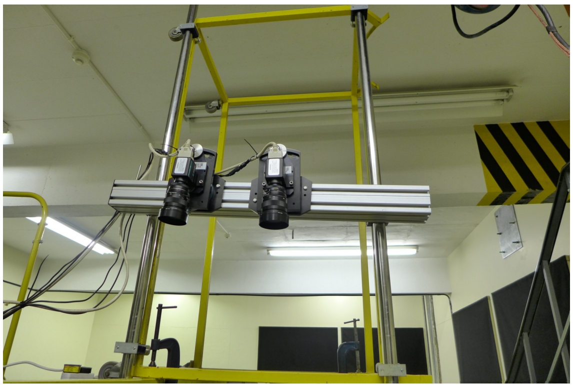

Figure B.10: PIV System

B.4 Calibration Data

Tables B.3, B.4, B.5, B.6, B.7 and figure B.11 show the calibration data of all used pressure transducers, the pitot static tube and the diagrams of calibration, respectively.

Table B.3: Calibration Data of Venturi Flow Meter

Fan Frequency Hz	**Pressure Transducer 1 Pa**	**Pressure Transducer 2 Pa**
50.00	285	1.380
44.97	230	1.110
40.07	180	0.851
35.05	131	0.623
30.00	81	0.369
25.02	57	0.250
20.06	57	0.250
15.01	34	0.136
10.06	18	0.057
5.00	8	0.006

Table B.4: Calibration Data of Pressure Transducer No 2

Voltmeter V	**Pressure Transducer kPa**	**Water Level mm**
3.00	0.004	0
3.16	0.018	2
3.30	0.037	4
3.44	0.058	6
3.58	0.078	8
3.72	0.098	10
3.85	0.118	12
4.13	0.158	16

Table B.5: Calibration Data of Pressure Transducer No 3

Voltmeter	**Pressure Transducer**	**Water Level**
V	**Pa**	**mm**
1.992	4	0
2.059	25	2
2.127	45	4
2.188	64	6
2.255	86	8
2.323	107	10
2.392	132	12

Table B.6: Calibration Data of Pitot Tube

Voltmeter	**Pressure Transducer**	**Water Level**
V	**Pa**	**mm**
1.986	18	0
2.001	0	2
2.017	20	4
2.033	40	6
2.049	61	8
2.066	82	10
2.083	104	12
2.223	280	29

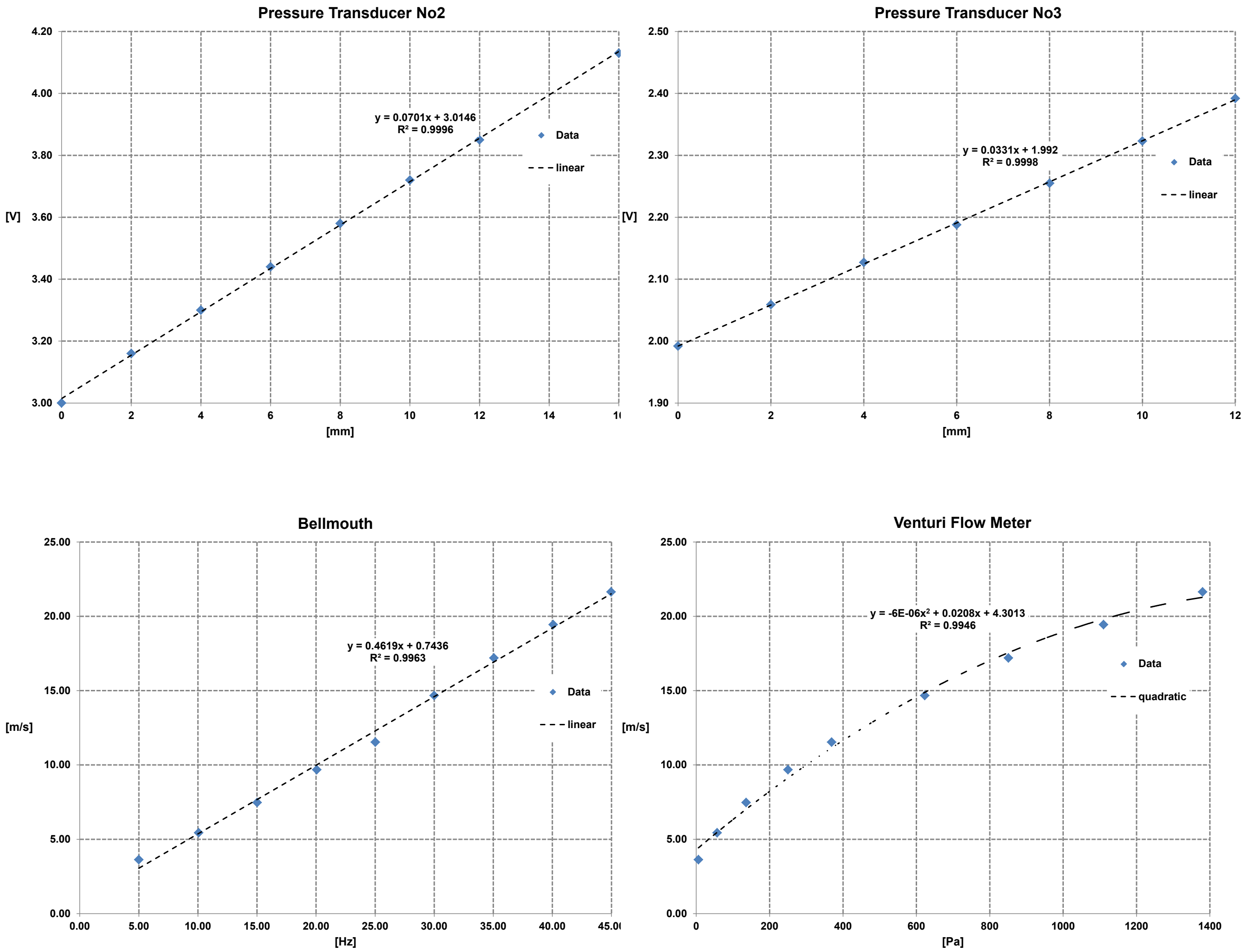

Figure B.11: Diagrams of Calibration

Table B.7: Calibration Data of Pressure Transducer (fixed)

Voltmeter V	**Pressure Transducer** kPa	**Water Level** mm
22.17	-0.010	1
	0.008	2
22.15	0.027	4
22.13	0.048	6
	0.068	8
	0.089	10
22.08	0.108	12
	0.138	15
	0.187	20
	0.197	21

B.5 Details of Measuring Equipment

Tables B.8, B.9 and B.10 show the general properties of the seeding generator, both cameras and the dual power laser used for the wind tunnel studies.

Table B.8: High Volume Liquid Droplet Seeding Generator by Dantec Dynamics

Maximum particles/second	Approximate 1013 particles/second seed output per jet (nominal value)
Operating period	can be run non-stop
Maximum Working Pressure	3 bar absolute
Compressed-air supply	max. 5 bar
Compressed-air flow	approx. 43.5 l/min at 5 bar (20.9 l/min at 2 bar) (when bypass closed)
Vessel capacity	max. 5 litres of spray fluid
Average droplet size	2 μm
Droplet size range	1-3 μm
Weight	approx. 7.2 kg (when empty)
Length x width x height	305 x 200 x 390 mm
Suitable fluids	liquid paraffin, vegetable oils (e.g. olive oil), gear lubricant oils

Table B.9: Flow Sense M4 by Dantec Dynamics

Dimensions (LxWxH)	Camera house 85x 51 x 51 mm excl. cable connectors
Lens mount	C-mount
CCD type	Progressive scan interline
Active pixels	2048 by 2048 pixel
Camera bit resolution	12-bit, 10-bit or 8-bit mode
Pixel pitch	7.4 x 7.4 μm
Signal to noise	>58dB
Pixel clock rate	40 MHz
Max. single-frame rate	14.5 Hz full frame Higher rate at partial readout up to 80 Hz.
PIV correlation mode	Yes
Pulse interval range	<1.0 μS
Double-frame rate	7.25 Hz full frame. Higher with partial readout up to 40 Hz.

Table B.10: Dual Power Laser 200-15 by Dantec Dynamics

Laser head structure	Mono-block aluminum
Configuration	Dual Cavity (type 2)
Max Repetition rate per cavity	15 Hz
Pulse Energy @ 532 nm (per cavity)	200 mJ
Beam diameter	6.5 mm
Beam divergence	3 mrad
Pulse length @ 1064 nm	6-9 ns
Pulse stability	±2%
Pointing stability	<100 μrad
Timing jitter (ns)	<0.5
Resonator type	Stable
Lamp life (pulses)	>5x10^7
Voltage	90-250 VAC
Frequency	47-63 Hz
Power	Single Phase
Ambient	18-30 °C
Consumption	<2.5kW
Power supply	LPU 550

B.6 Preliminary Tests

The model was made from transparent perspex for the tower and collector, which was the main property which lead to this decision. Former research has shown that it is possible to get PIV results from flow inside a circular and transparent structure like the one presented here. Nevertheless there is still the problem of flashing up of the complete structure when it got hit by the laser sheet due to reflections. For Model I we tried to reduce this effect by performing different test runs with different ground materials and coatings of the ground and tower. The six test runs are gathered in figure B.12.

Unfortunately it was not possible to diminish the effect of flashing up with this configurations. Another solution could have been to use special lenses for both cameras to filter out the unwanted spectral range. Although Model I failed for the PIV tests, the process of learning and understanding of the whole measuring system helped us to set-up Model II. It became apparent as the right decision afterwards.

Figure B.12: Tested Configurations with Different Coating of Model I

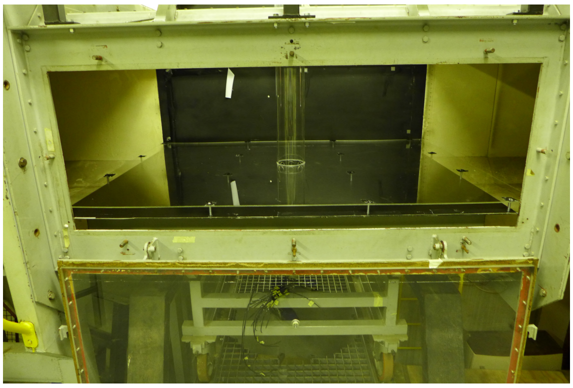

Test 1.1[1]

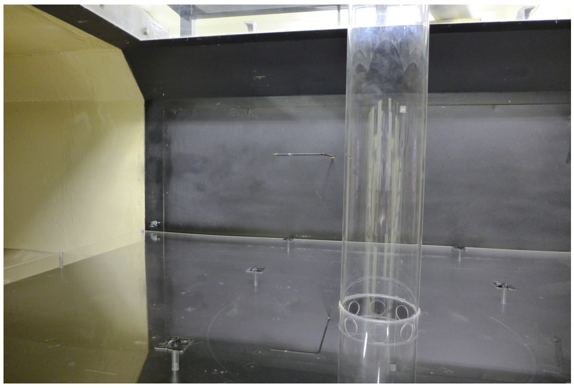

Test 1.2[1]

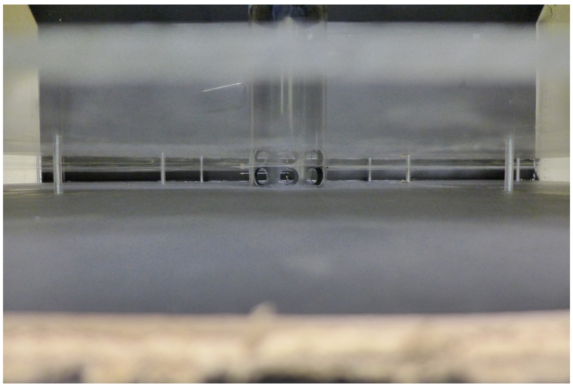

Test 2.1[2]

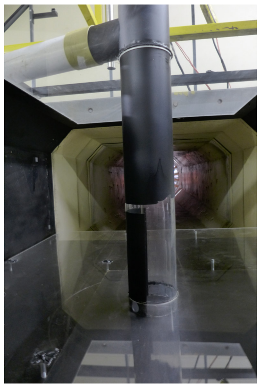

Test 2.2[2]

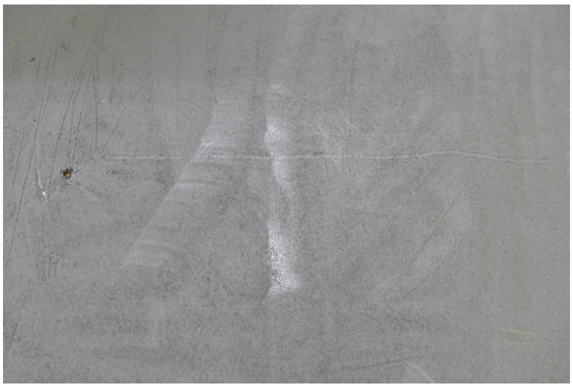

Test 3[3]

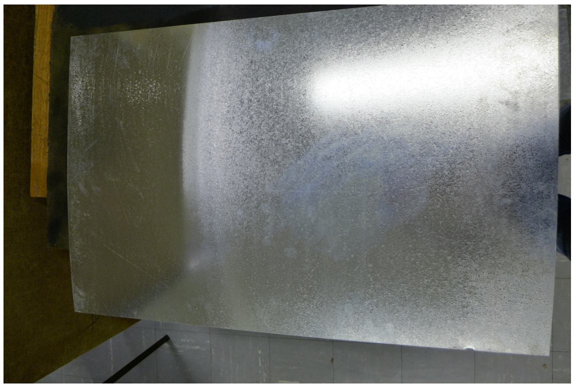

Test 4[4]

Test 5[5]

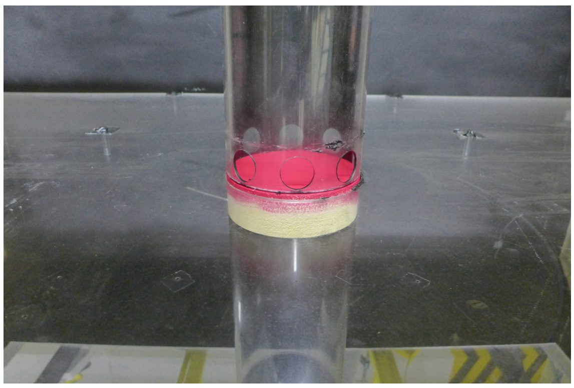

Test 6[6]

[1] 1: Clear Perspex Tube.
[2] 2: Black Sprayed Perspex Tube.
[3] 3: Black (matt) Painted Cardboard Bottom Section; Dulux Acrylic PVA.
[4] 4: Black (matt) Painted Metal Bottom Section; Dulux Acrylic PVA.
[5] 5: Fluro Rose (156) Painted Cardboard Bottom Section; Iris Fine Acrylic.
[6] 6: Fluro Rose (156) Painted Wooden Bottom Section; Iris Fine Acrylic.

B.7 Results

Results for the PIV measurements on Model II are presented in the following figures. Figure B.13 shows the upstream velocity distribution for the horizontal measuring plane of 0 mm.

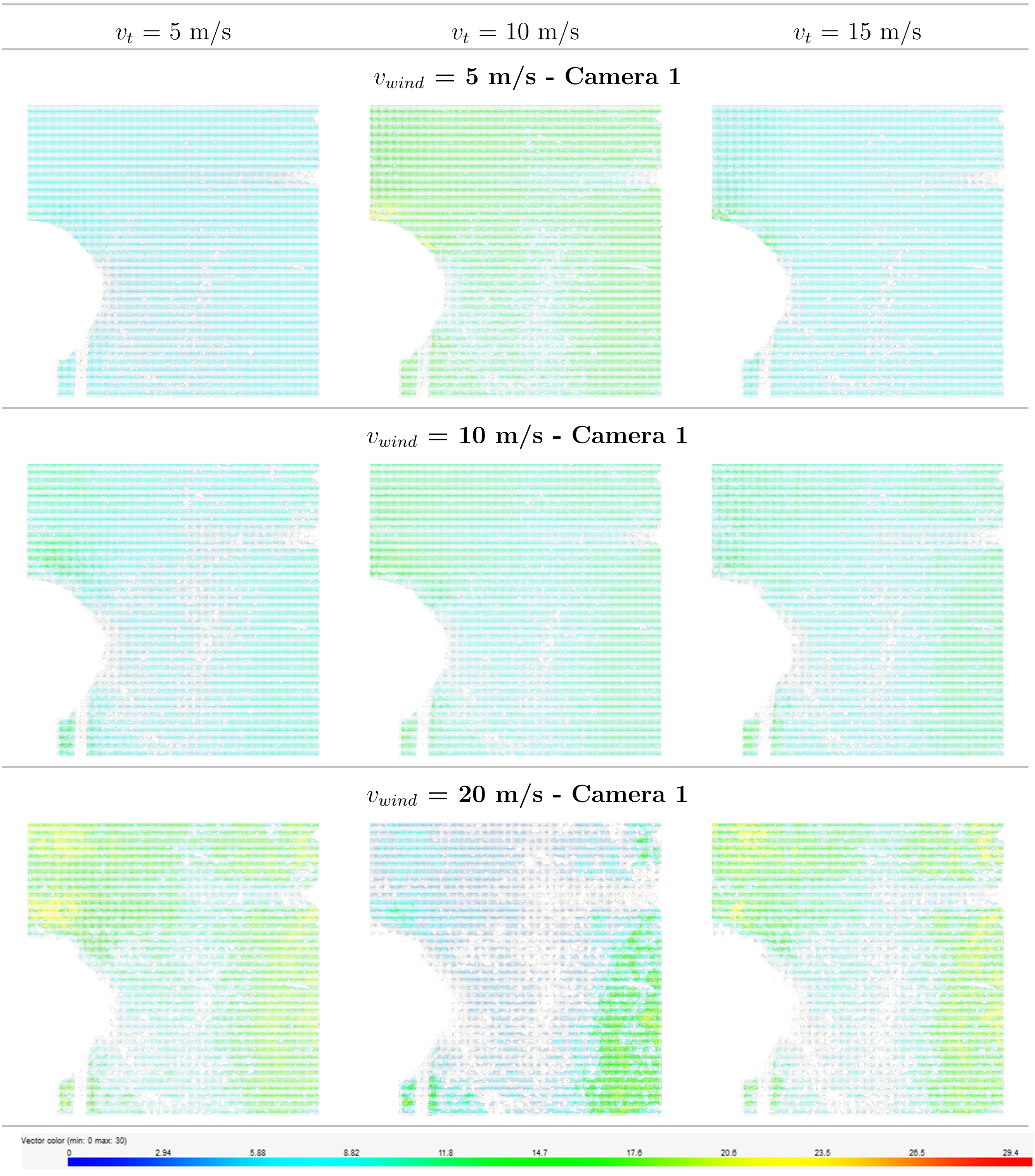

Figure B.13: Results Horizontal Level 0 mm (Upstream, Flow From Right to Left)

Figures B.14, B.15 and B.16 present the complete results for different ratios of the velocity streams for the horizontal level of 0 mm.

Measurement	**First Repetition**	**Second Repetition**
m/s	m/s	m/s

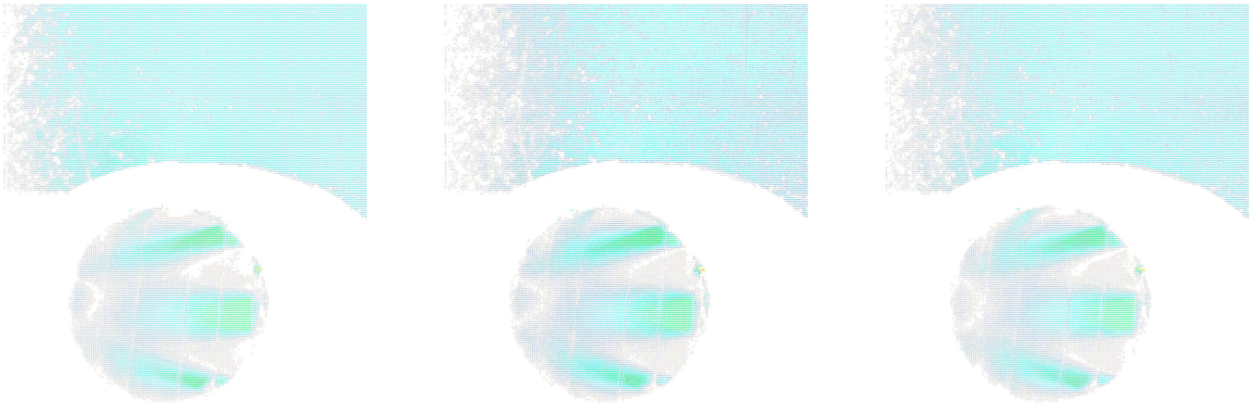

v_t = **5 m/s**, v_{wind} = **5 m/s**

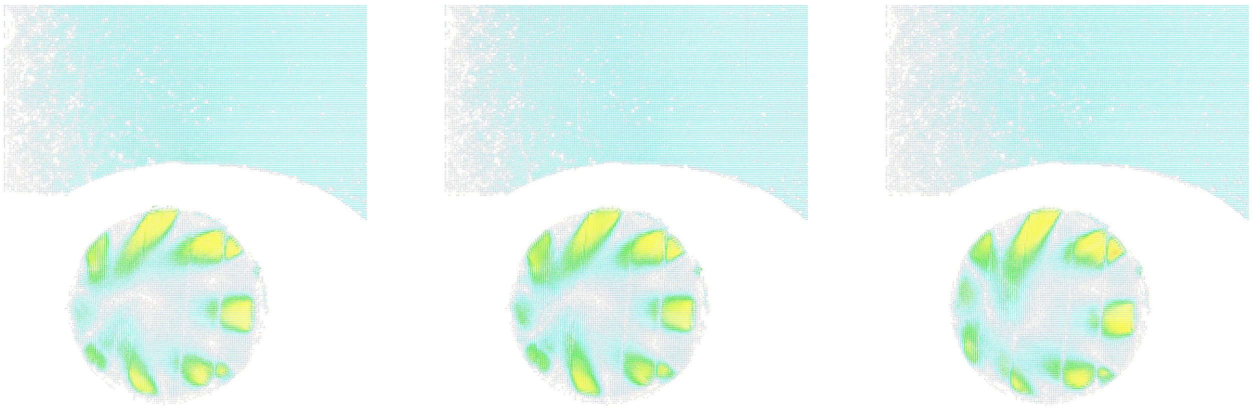

v_t = **10 m/s**, v_{wind} = **5 m/s**

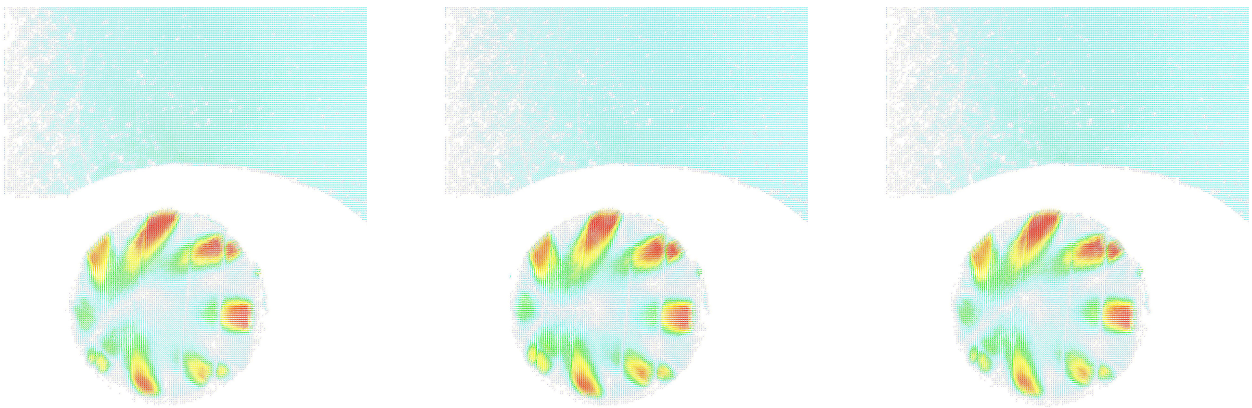

v_t = **15 m/s**, v_{wind} = **5 m/s**

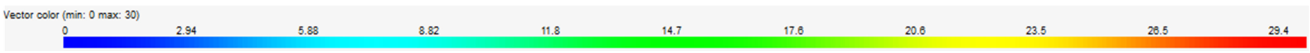

Figure B.14: Results Horizontal Level 0 mm (Flow From Right to Left) - Part 1 of 3

Measurement	**First Repetition**	**Second Repetition**
m/s	m/s	m/s

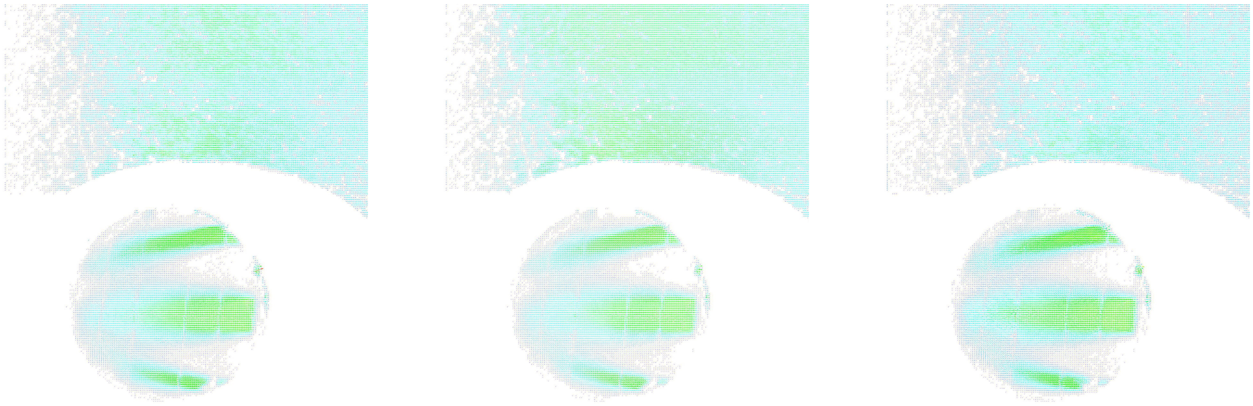

v_t **= 5 m/s,** v_{wind} **= 10 m/s**

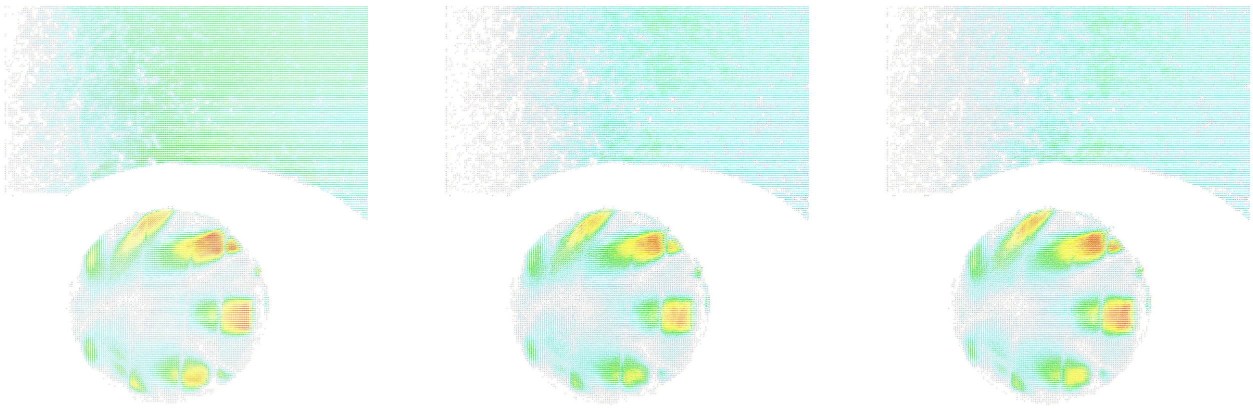

v_t **= 10 m/s,** v_{wind} **= 10 m/s**

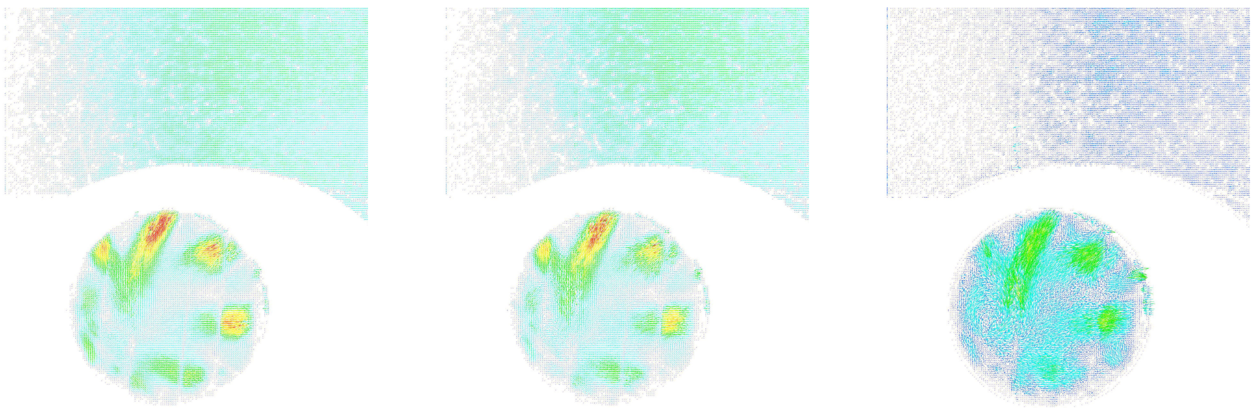

v_t **= 15 m/s,** v_{wind} **= 10 m/s**

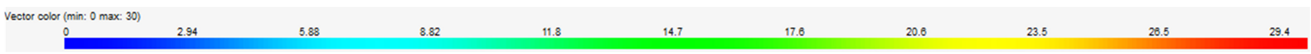

Figure B.15: Results Horizontal Level 0 mm (Flow From Right to Left) - Part 2 of 3

Measurement m/s	**First Repetition** m/s	**Second Repetition** m/s

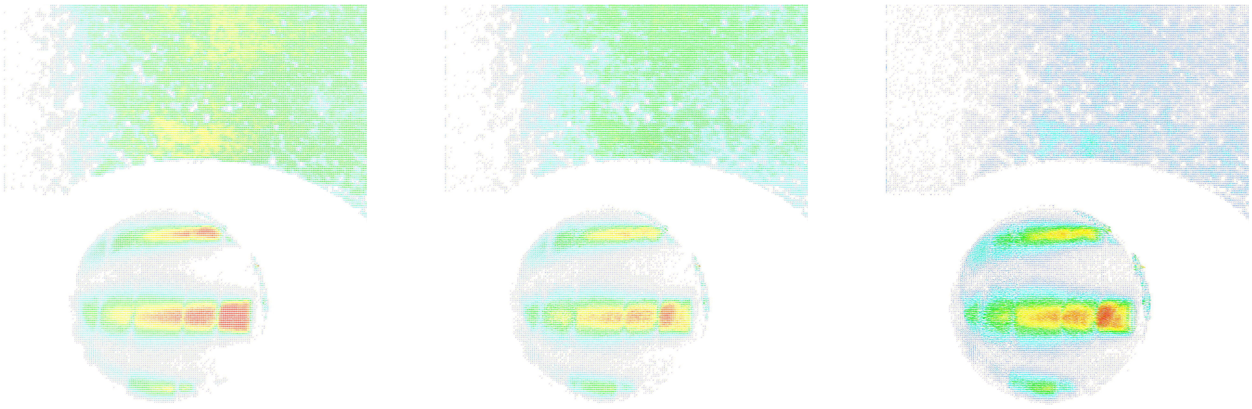

v_t = **5 m/s,** v_{wind} = **20 m/s**

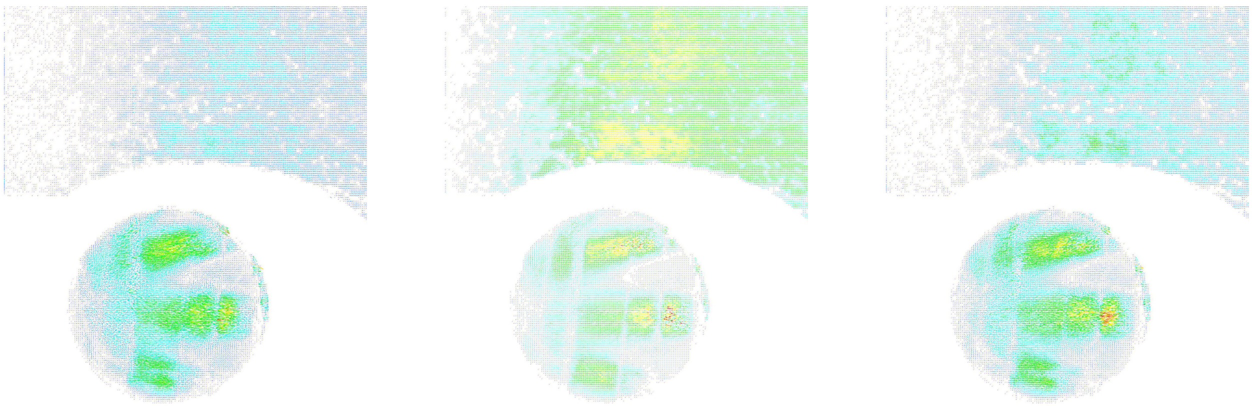

v_t = **10 m/s,** v_{wind} = **20 m/s**

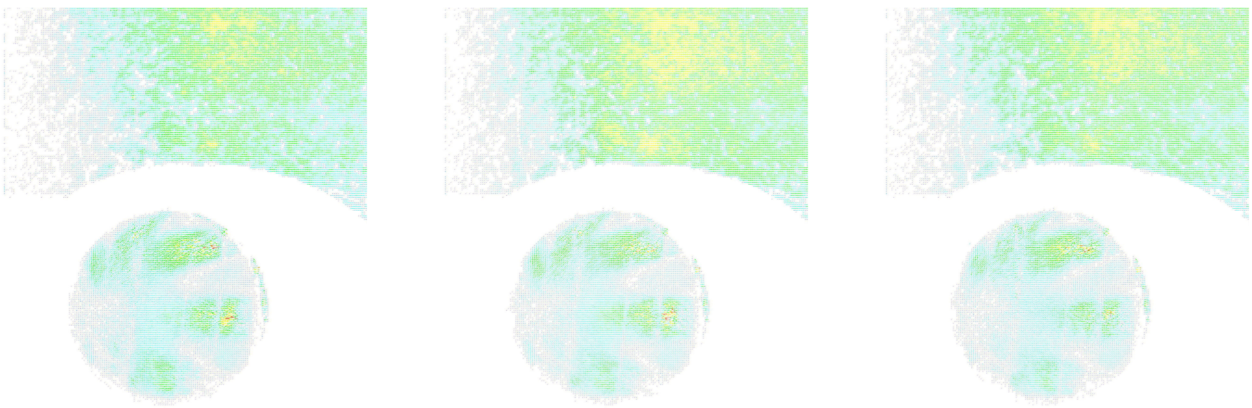

v_t = **15 m/s,** v_{wind} = **20 m/s**

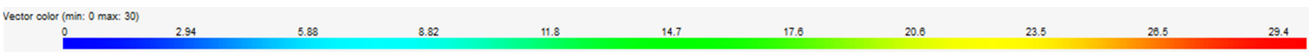

Figure B.16: Results Horizontal Level 0 mm (Flow From Right to Left) - Part 3 of 3

AppendixC

CFD Analysis of the Wind Tunnel Model from Stellenbosch

In this appendix results for different ratios of v_{wind}/v_{tube} are given in figures C.1, C.2, C.3 and C.4.

Horizontal Level 0 mm

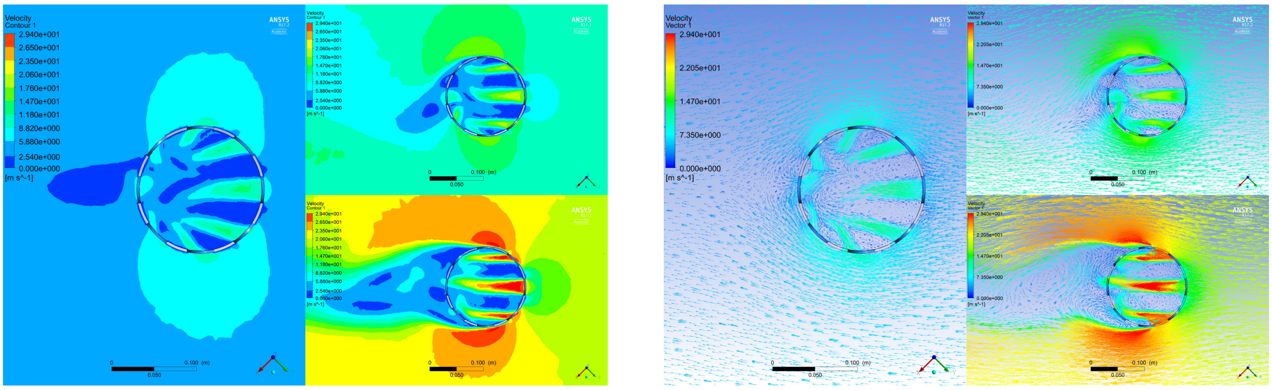

$v_{max,5}$= 12.41 m/s (left); $v_{max,10}$= 20.69 m/s (right top); $v_{max,20}$= 34.03 m/s (right bottom)

Horizontal Level 12 mm

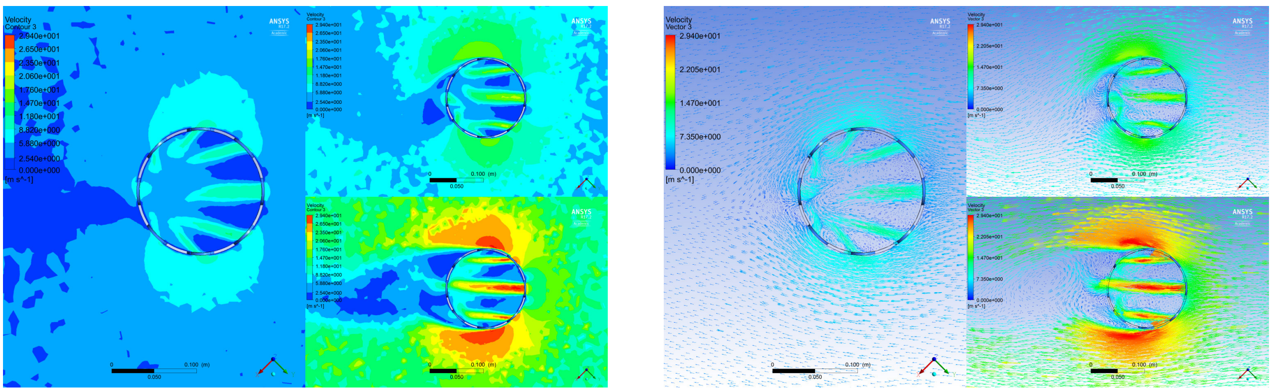

$v_{max,5}$= 12.32 m/s (left); $v_{max,10}$= 19.42 m/s (right top); $v_{max,20}$= 31.60 m/s (right bottom)

Figure C.1: Results for v_{wind} = 5, 10, 20 m/s and $\dot{m}_{venturi}$ = 0.042 kg/s (Flow From Right to Left) - Part 1 of 2

Vertical Centre

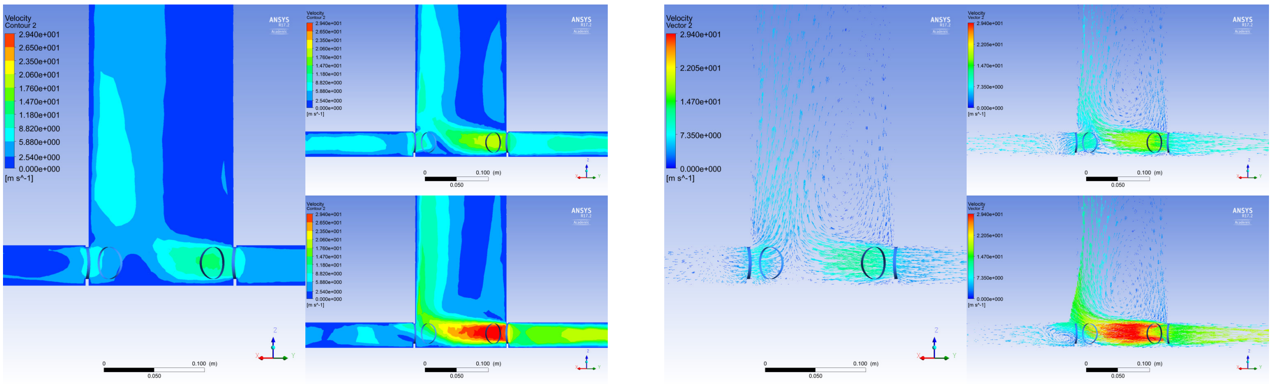

$v_{max,5}$= 12.27 m/s (left); $v_{max,10}$= 19.42 m/s (right top); $v_{max,20}$= 31.70 m/s (right bottom)

Figure C.2: Results for v_{wind} = 5, 10, 20 m/s and $\dot{m}_{venturi}$ = 0.042 kg/s (Flow From Right to Left) - Part 2 of 2

Horizontal Level 0 mm

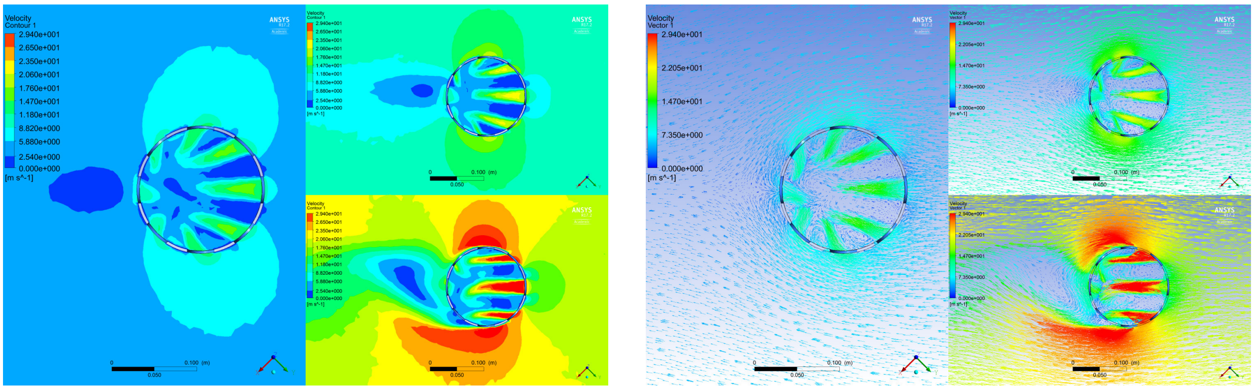

$v_{max,5}$= 15.94 m/s (left); $v_{max,10}$= 22.15 m/s (right top); $v_{max,20}$= 38.56 m/s (right bottom)

Horizontal Level 12 mm

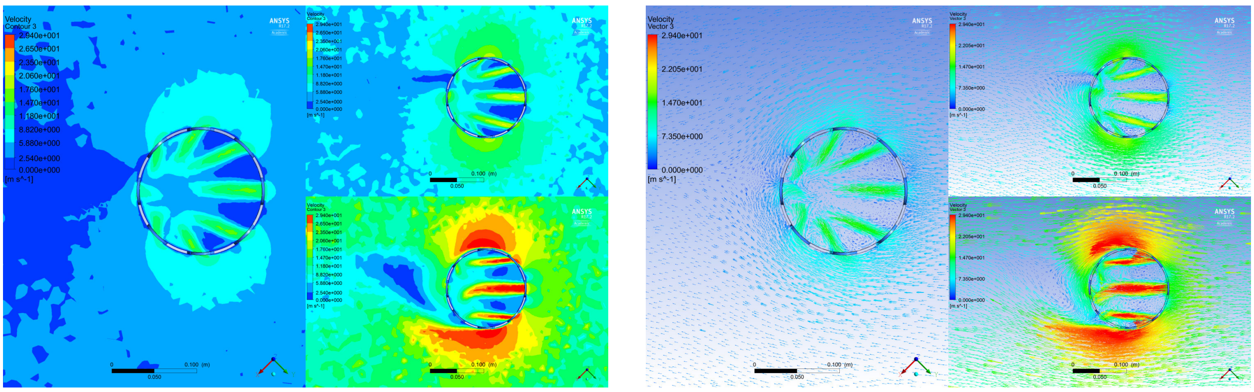

$v_{max,5}$= 16.50 m/s (left); $v_{max,10}$= 21.84 m/s (right top); $v_{max,20}$= 35.34 m/s (right bottom)

Figure C.3: Results for v_{wind} = 5, 10, 20 m/s and $\dot{m}_{venturi}$ = 0.063 kg/s (Flow From Right to Left) - Part 1 of 2

Vertical Centre

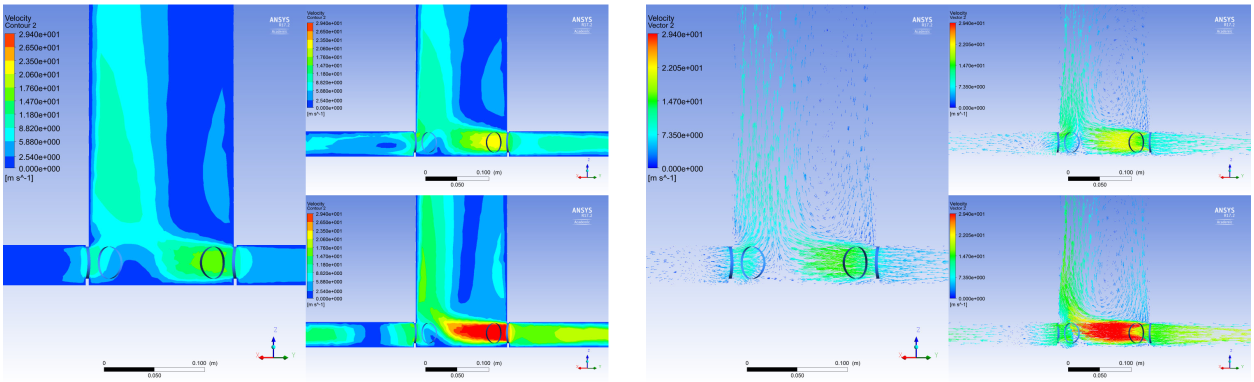

$v_{max,5}$= 15.89 m/s (left); $v_{max,10}$= 21.84 m/s (right top); $v_{max,20}$= 34.67 m/s (right bottom)

Figure C.4: Results for v_{wind} = 5, 10, 20 m/s and $\dot{m}_{venturi}$ = 0.063 kg/s (Flow From Right to Left) - Part 2 of 2

AppendixD

Stationary 3D-CFD Model of the Prototype of Manzanares, Spain

In this appendix the ambient conditions for Manzanares, Spain, which have been implemented into the program code for the solar ray tracing model, are given in table D.1.

Table D.1: Construction Site (Manzanares, Spain)

Parameter	Range	Unit
latitude	38.99915	deg
longitude	-3.36991	deg
height amsl	750	m
solar irradiation (direct)	1,200	W/m^2
solar irradiation (diffuse)	200	W/m^2
date	08.06	-
time	12:00	-
time zone	+1	GMT

In the following the numerical results for temperature and velocity contours for configuration B, C and D are listed in the corresponding sections.

D.1 Results for Configuration B

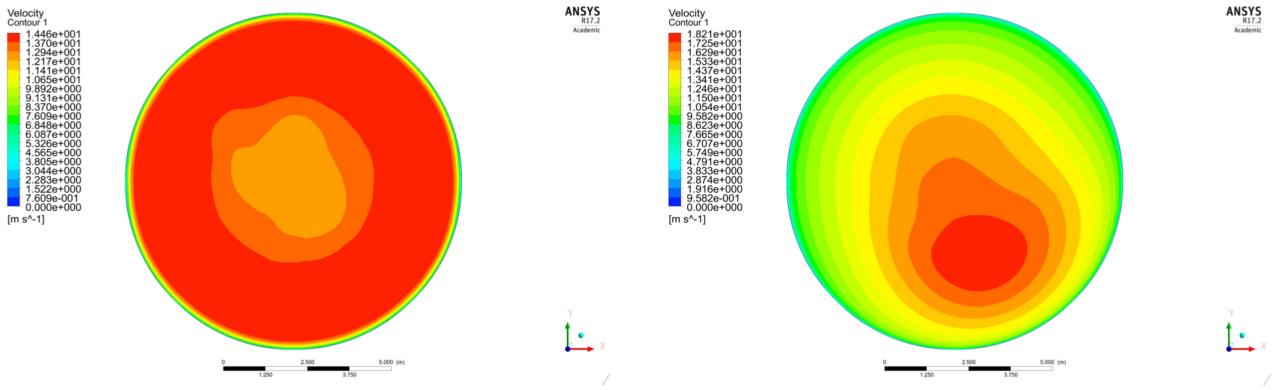

a) Velocity Contours at Turbine Plane b) Velocity Contours at Solar Tower Outlet

Figure D.1: Velocity Contours Inside Solar Tower (B)

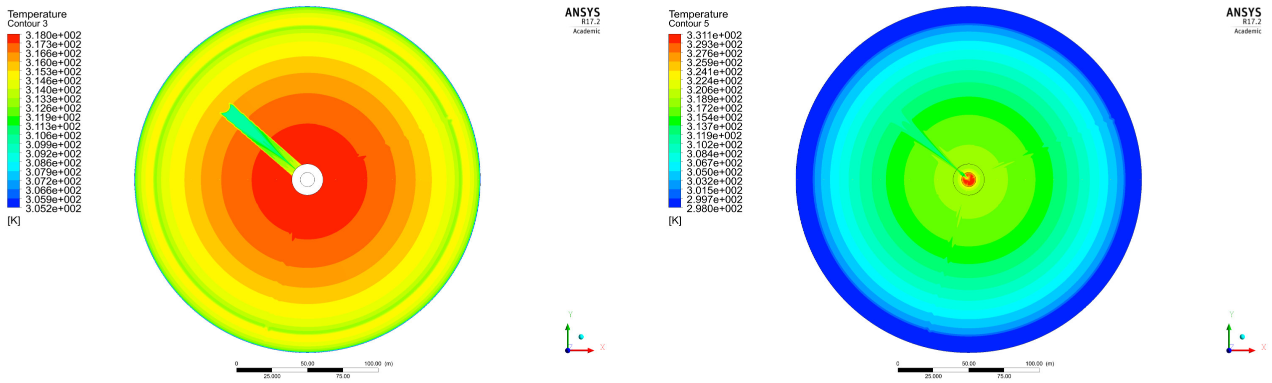

a) Temperature Contours at Solar Collector b) Temperature Contours at z = 150 cm

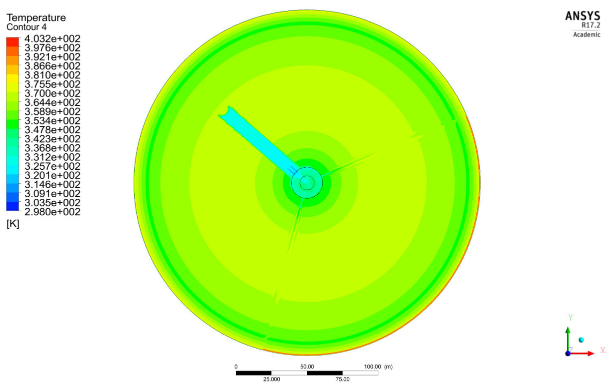

c) Temperature Contours at Ground

Figure D.2: Temperature Contours (Solar Collector + Ground) (B)

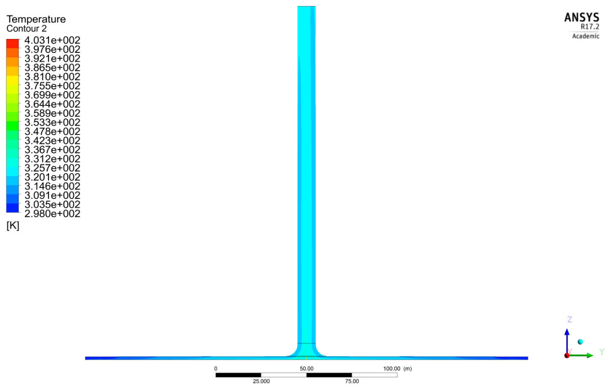

a) Temperature Contour at Middle Plane

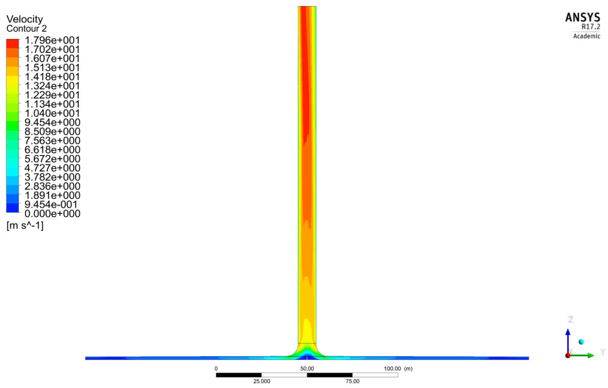

b) Velocity Contour at Middle Plane

Figure D.3: Temperature and Velocity Contours at Middle Plane (B)

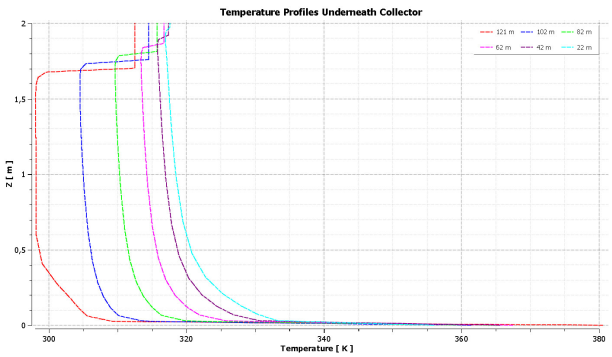

a) Temperature Profiles in Some Distance to the Tower Shadow

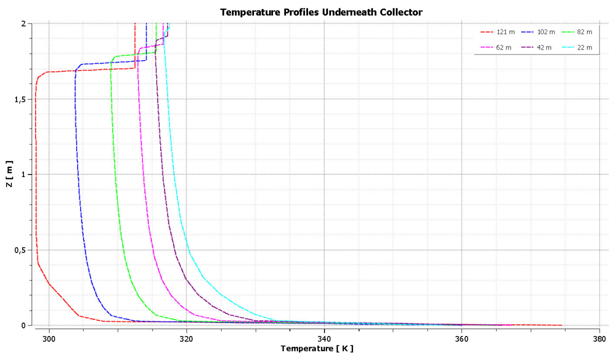

b) Temperature Profiles Close to the Tower Shadow

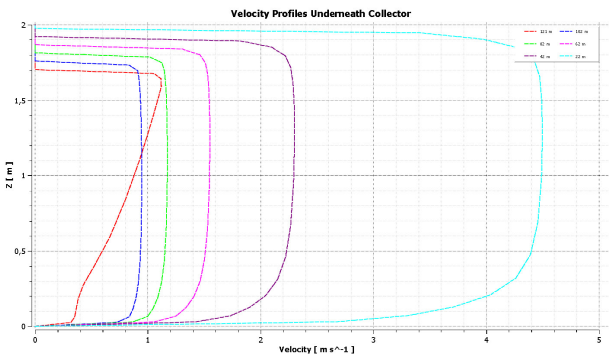

c) Velocity Profiles in Some Distance to the Tower Shadow

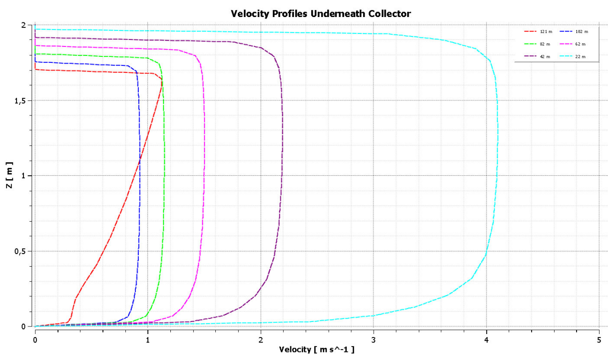

d) Velocity Profiles Close to the Tower Shadow

Figure D.4: Temperature and Velocity Profiles Underneath the Solar Collector (B)

D.2 Results for Configuration C

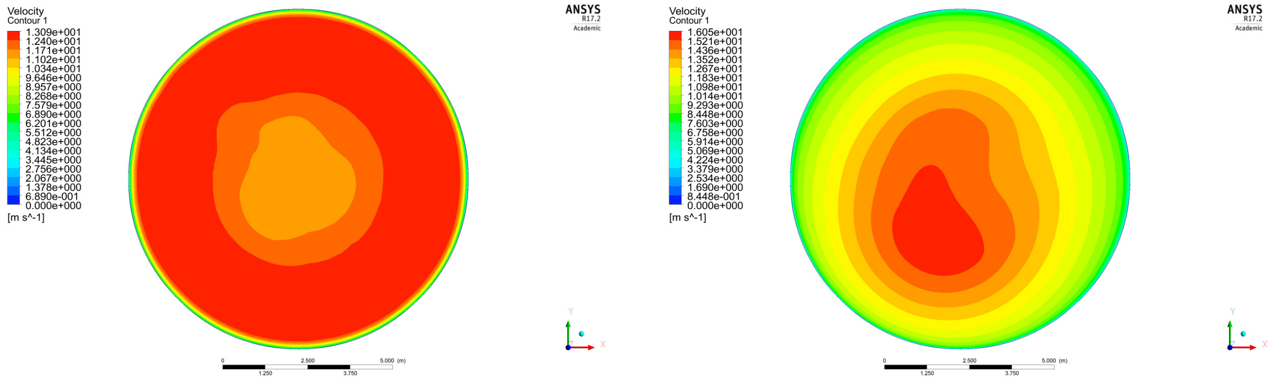

a) Velocity Contours at Turbine Plane b) Velocity Contours at Tower Outlet

Figure D.5: Velocity Contours Inside Solar Tower (C)

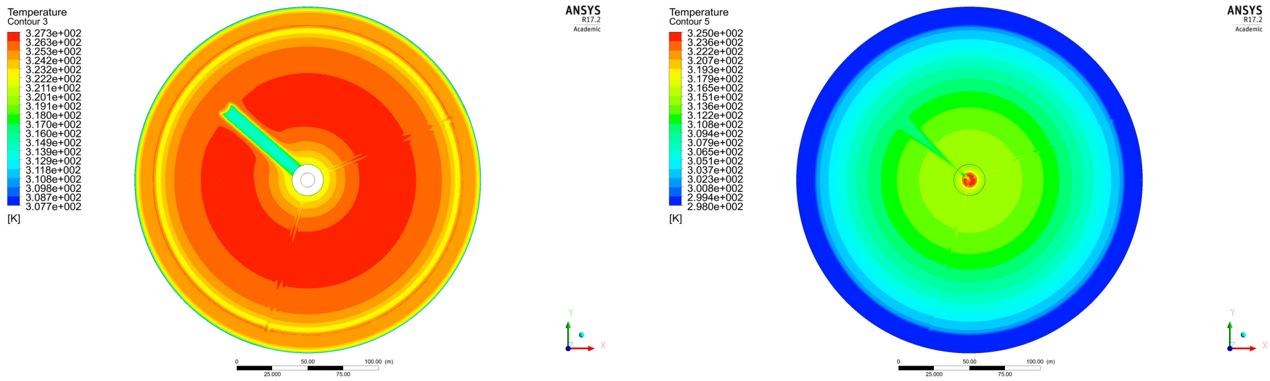

a) Temperature Contours at Solar Collector b) Temperature Contours at z = 150 cm

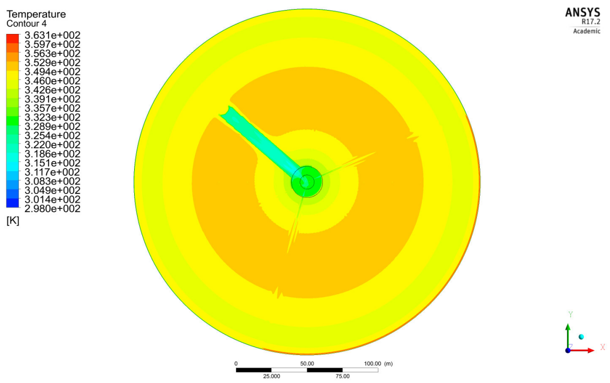

c) Temperature Contours at Ground

Figure D.6: Temperature Contours (Solar Collector + Ground) (C)

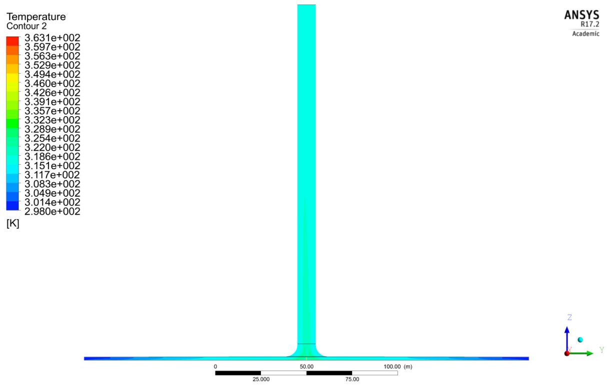

a) Temperature Contour at Middle Plane

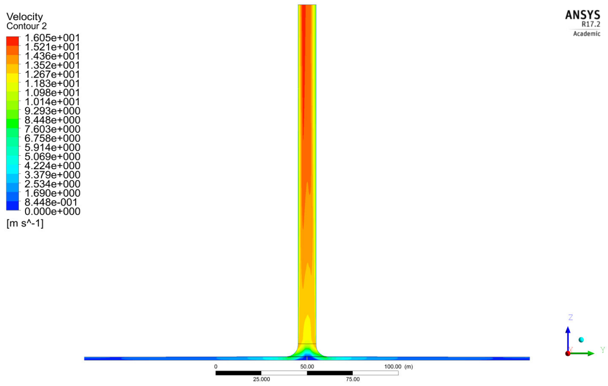

b) Velocity Contour at Middle Plane

Figure D.7: Temperature and Velocity Contours at Middle Plane (C)

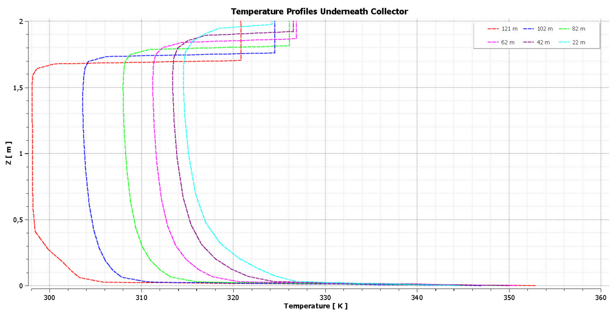

a) Temperature Profiles in Some Distance to the Tower Shadow

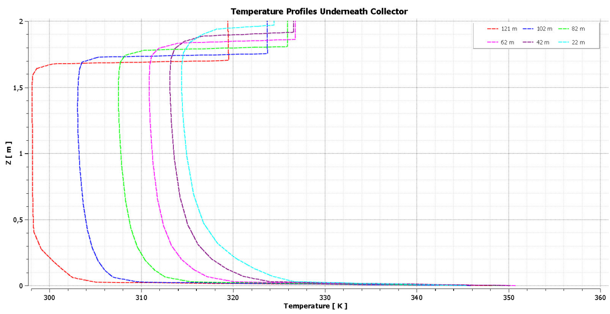

b) Temperature Profiles Close to the Tower Shadow

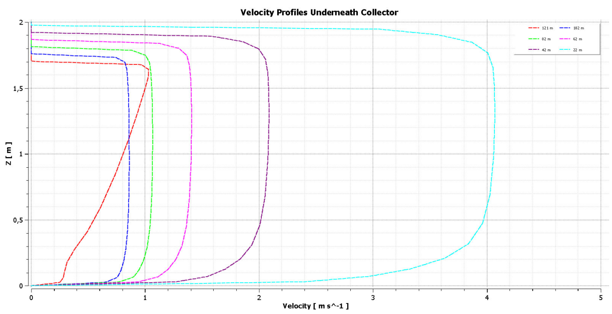

c) Velocity Profiles in Some Distance to the Tower Shadow

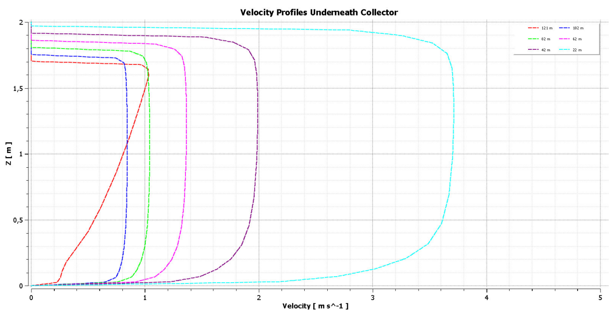

d) Velocity Profiles Close to the Tower Shadow

Figure D.8: Temperature and Velocity Profiles Underneath the Solar Collector (C)

D.3 Results for Configuration D

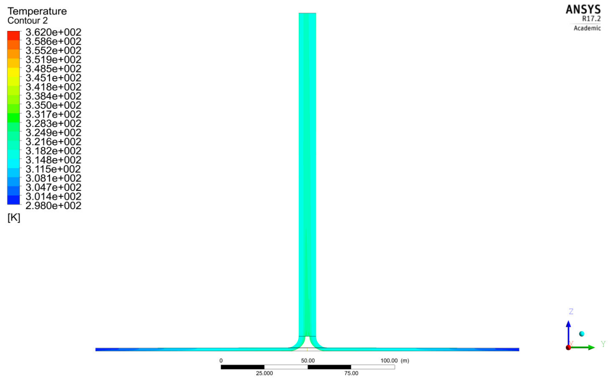

a) Temperature Contour at Middle Plane

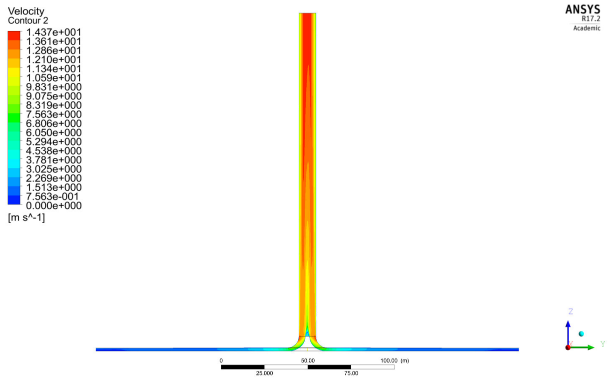

b) Velocity Contour at Middle Plane

Figure D.9: Temperature and Velocity Contours at Middle Plane (D)

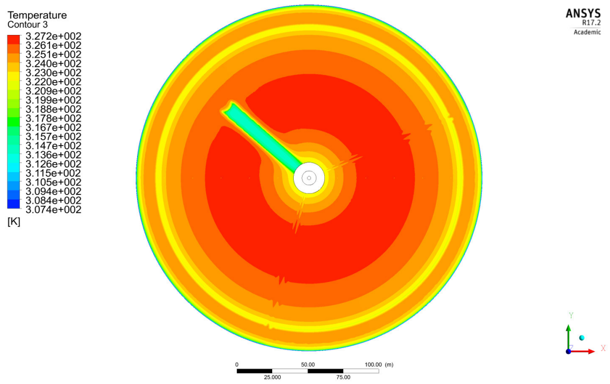

a) Temperature Contours at Solar Collector

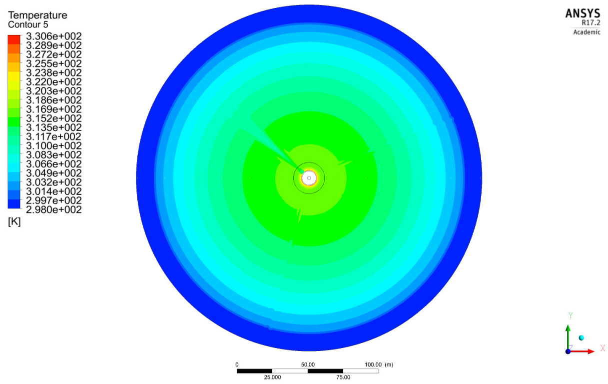

b) Temperature Contours at z = 150 cm

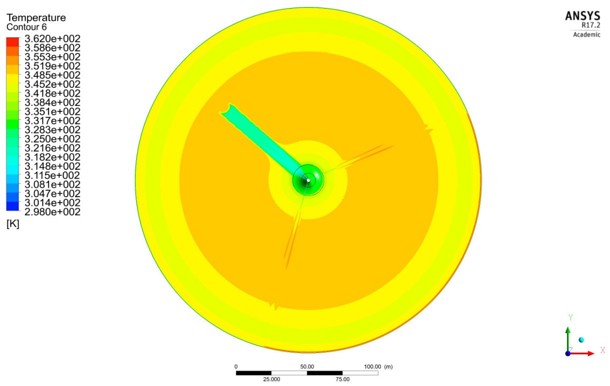

c) Temperature Contours at Ground

Figure D.10: Temperature Contours (Solar Collector + Ground) (D)

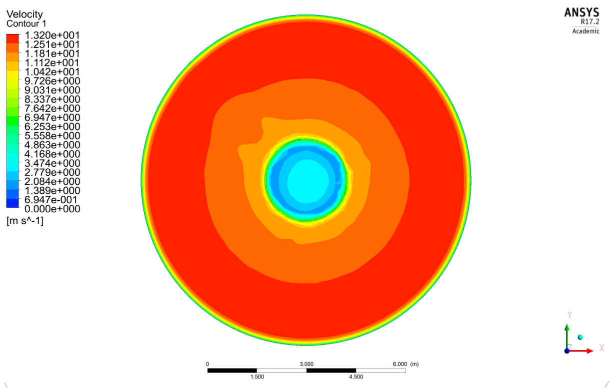

a) Velocity Contours at Turbine Plane (z = 8.5 m)

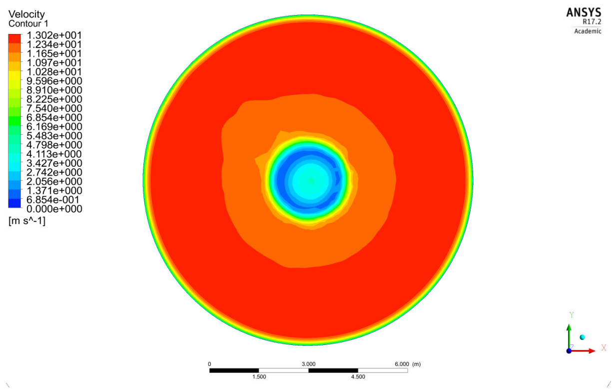

b) Velocity Contours at Turbine Plane (z = 9.0 m)

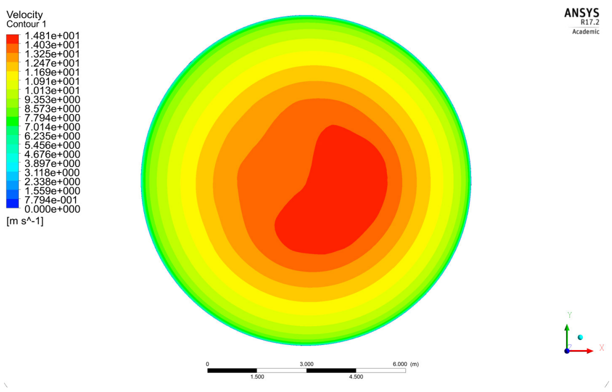

c) Velocity Contours at Tower Outlet

Figure D.11: Velocity Contours Inside Solar Tower (D)

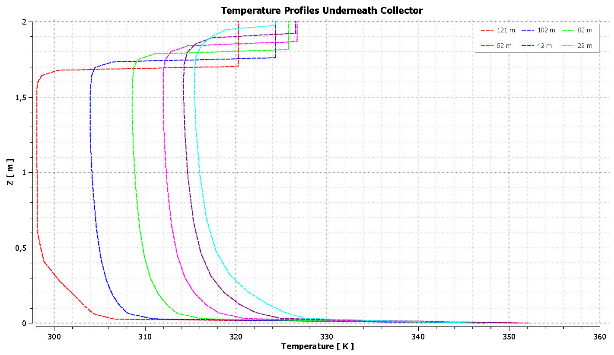

a) Temperature Profiles in Some Distance to the Tower Shadow

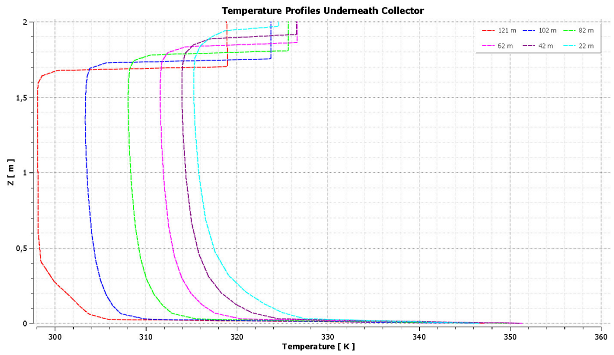

b) Temperature Profiles Close to the Tower Shadow

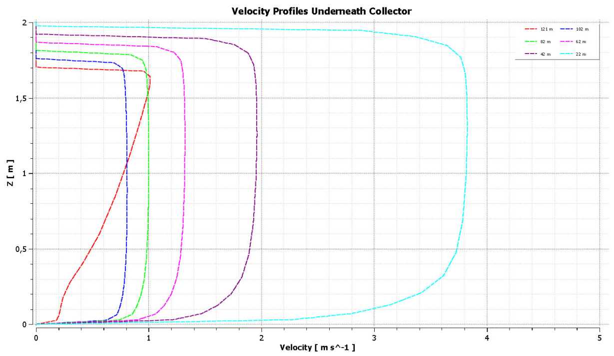

c) Velocity Profiles in Some Distance to the Tower Shadow

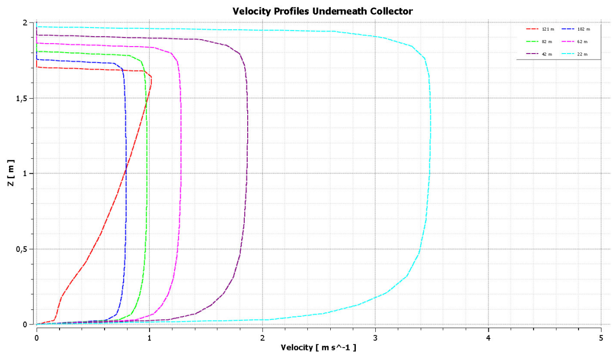

d) Velocity Profiles Close to the Tower Shadow

Figure D.12: Temperature and Velocity Profiles Underneath the Solar Collector (D)

AppendixE

Derivation of Hyperbola Equation

In the following appendix, the derivation of the hyperbola equation used within chapter 10 for the development of the improved experimental and numerical model from part III of this work, will be presented.

$$r = \Delta r + A\sqrt{1 + z^2/B^2} \tag{E.1}$$

$$r' = A\frac{1}{\sqrt{1 + z^2/B^2}}z/B^2 \tag{E.2}$$

with

Boundary Condition:

I) z = 0: r = Δ r + A = r_0

II) z = H: r = Δ r + A $\sqrt{1 + H^2/B^2} = r_1$

III) z = H: $r' =$ A $\dfrac{1}{\sqrt{1 + H^2/B^2}}$ H/$B^2 = r_1'$

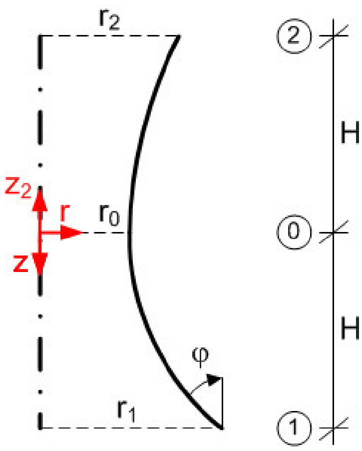

Figure E.1: Hyperbola

$$\text{as a consequence of I) : } \boxed{\Delta r = r_0 - A}$$

$$\text{as a consequence of II) : } r_1 = r_0 - A + A\sqrt{1 + H^2/B^2}$$

$$r_1 - r_0 = A(\sqrt{1 + H^2/B^2} - 1)$$

$$\boxed{A = \frac{r_1 - r_0}{\sqrt{1 + H^2/B^2} - 1}}$$

$$\text{as a consequence of III) : } r_1' = \frac{r_1 - r_0}{\sqrt{1 + H^2/B^2} - 1} \frac{1}{\sqrt{1 + H^2/B^2}} \frac{H}{B^2}$$

$$= \frac{r_1 - r_0}{1 + H^2/B^2 - \sqrt{1 + H^2/B^2}} \frac{H}{B^2}$$

$$\frac{r_1'}{H(r_1 - r_0)} = \frac{1}{(1 + H^2/B^2 - \sqrt{1 + H^2/B^2})B^2}$$

$$\frac{H(r_1 - r_0)}{r_1'} = B^2 + H^2 - B\sqrt{B^2 + H^2}$$

$$\left(-\frac{H(r_1 - r_0)}{r_1'} + H^2 + B^2\right)^2 = B^2\sqrt{B^2 + H^2}^2$$

$$K = \frac{-H(r_1 - r_0)}{r_1'} + H^2$$

$$K^2 + 2KB^2 + B^4 = B^4 + B^2H^2$$

$$K^2 + 2KB^2 = B^2H^2$$

$$B^2(2K - H^2) = -K^2$$

$$\boxed{B = \pm\sqrt{-K^2/(2K - H^2)}}$$

$$\boxed{K = -\frac{H(r_1 - r_0)}{r_1'} + H^2}$$

curvature:

$$r'' = \left(\frac{(A/B^2)z}{\sqrt{1 + z^2/B^2}}\right)'$$

$$= \frac{A/B^2\sqrt{1 + z^2/B^2} - A/B^2 \times z \times z/B^2/\sqrt{1 + z^2/B^2}}{1 + z^2/B^2}$$

$$= \frac{A}{B^2} \frac{1 + z^2/B^2 - z^2/B^2}{(1 + z^2/B^2)^{3/2}}$$

$$= \frac{A}{B^2}(1 + z^2/B^2)^{-3/2}$$

$$r''(0) = \frac{A}{B^2}$$

top hyperbola shape:

$z_2 = 0$: curvature r''_0 identical for top and bottom hyperbola part

$$r'' = \frac{A_2}{B_2^2}(1 + z_2^2/B_2^2)^{-3/2}$$

$$r''_0 = \frac{A_2}{B_2^2} = \frac{A_1}{B_1^2}$$

$$\Rightarrow B_2^2 = A_2/r''_0$$

$$A_2 = \frac{r_2 - r_0}{\sqrt{1 + r''_0 H^2/A_2} - 1}$$

$$A_2\sqrt{1 + r''_0 H^2/A_2} = r_2 - r_0 + A_2$$

$$\sqrt{A_2^2 + r''_0 H^2 A_2}^{\,2} = [(r_2 - r_0) + A_2]^2$$

$$A_2^2 + r''_0 H^2 A_2 = (r_2 - r_0)^2 + 2(r_2 - r_0)A_2 + A_2^2$$

$$[r''_0 H^2 - 2(r_2 + r_0)]A_2 = (r_2 - r_0)^2$$

$$\boxed{A_2 = \frac{(r_2 - r_0)^2}{r''_0 H^2 - 2(r_2 - r_0)}} = \frac{(r_2 - r_0)^2}{A_1 H^2/B_1^2 - 2(r_2 - r_0)}$$

$$\boxed{B_2 = \sqrt{A_2/r''_0}}$$

$$\boxed{\Delta r_2 = r_0 - A_2}$$

$$= \sqrt{(A_2/A_1)B_1^2}$$

here:

$$K = -183831.776$$

$$B = \pm 262.573$$

$$A = 56.275$$

$$\Delta r = -13.775$$

$$r = -13.775 + 56.275\sqrt{1 + z^2/262.573^2}$$

AppendixF

Wind Tunnel Studies at Bochum, Germany

F.1 Wind Tunnel Model

Figure F.1 shows one of the CTA models in the unprocessed state.

Unprocessed State

Transition Section Solar Collector to Turbines

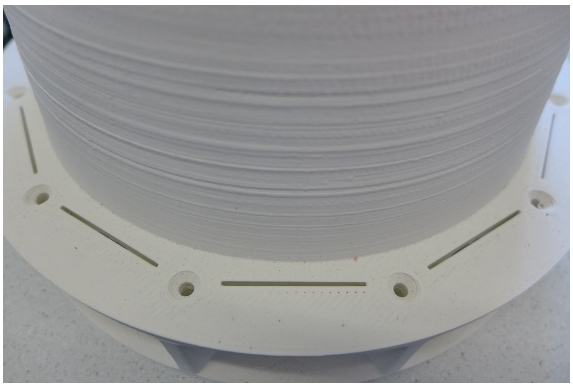

Slot for Simulation of Turbine Effect

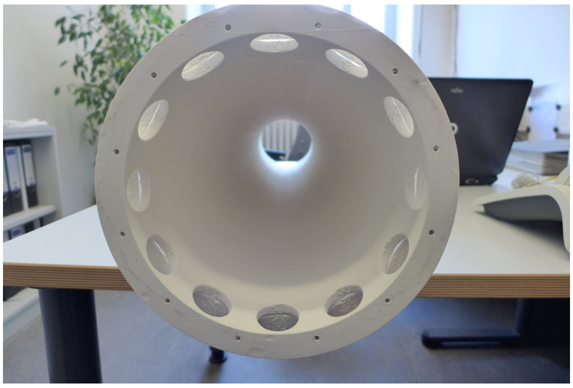

Inside View

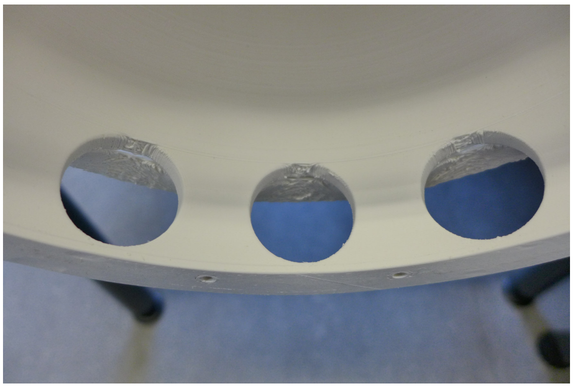

Turbine Openings

Figure F.1: CTA Model

Before the model was placed inside the wind tunnel the surface had to be smoothened to diminish the effect of roughness. After the preparations all models still had a certain roughness which has been taken into account by the interpretation of all measurements.

F.2 Measuring Equipment

Figure F.2 shows the measuring equipment for the CTA measurements and both triple sensor probes.

All used probes have been calibrated manually with a two-point calibration method.

F.2.1 Pressure Transducers

Figure F.3 shows the pressure tubes and transducers placed underneath the wind tunnel floor.

The red cables in the figures are for the temperature control unit and the heating films respectively.

F.2.2 Pitot-Static Tubes

Two pitot-static tubes have been utilized to measure a reference velocity in the undisturbed flow area right in front of the test section and below the model of the SC. Both positions are depicted in figure F.4 for a better understanding of the presented results.

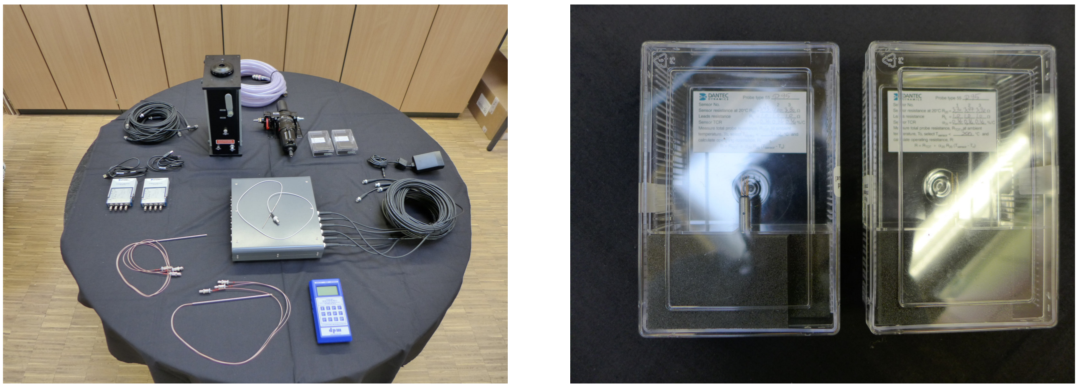

a) CTA Equipment b) Hot-Wire Probe

Figure F.2: Measuring Equipment for Constant Temperature Anemometer (CTA)

Figure F.3: Pressure Transducer Underneath the Wind Tunnel Floor

Figure F.4: Pitot-Static Tubes for Reference and Velocity Measurement Below Solar Collector

F.3 Modelling of Turbine Influence

The author has found a way to investigate the influence of the turbines on the flow field inside the transition section in a simplified way. Figure F.5 shows two approaches how to model the influence by closing or just blocking the slots which have been cut into the wind tunnel models to insert a flow barrier.

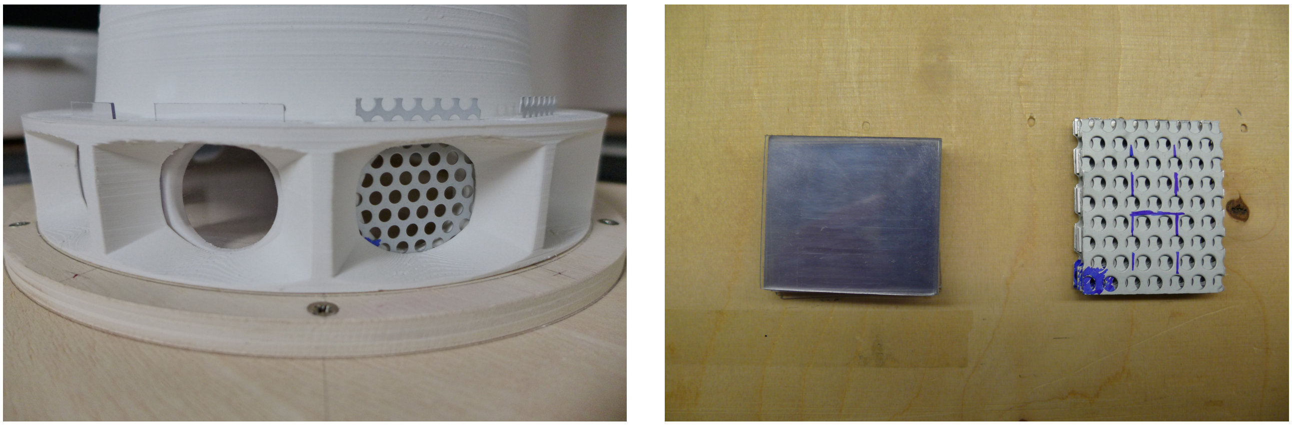

Figure F.5: Simulation of Turbine Effect

Due to the effect of closing or just blocking several turbine openings the influence of an asymmetric inflow condition, different ratios of turbulence or allowed mass flows through the openings can be investigated. The effect of swirl cannot be simulated by these two approaches but someone can rethink about other variants to reproduce this and other effects. Resistance coefficients of screens, grids and porous layers can be found in [B.21]. Also see appendix G for more information about influence and modelling of turbines in scaled model tests.

F.4 Material Properties

Table F.1 and F.2 show the material properties of the biocompound used for the design of the enhanced wind tunnel model and all variants of installations and of the heating film, respectively.

Table F.1: Industry Tec-B Material Properties

Tensile Stress	44 MPa
Tensile Elongation	5.3 %
Flexural Modulus	2,600 MPa
Flexural Strength	24 MPa
Izod Impact Strength	217.7 kJ/m^2
VST A 120	115 $°C$
MVR (190 $°C$/2.16 kg)	4 $cm^3/10min$
Shrinkage	0.54 %

Table F.2: Heating Film Properties

Material	Silicone
Thickness	0.8 $\div$ 3.0 mm
Length	400 mm
Width	290 mm
Current	230 V
Temperature	-60$°C\div$ 200 $°C$
Radiant Power per cm^2	0.02 $W/cm^2\div$ 3.0 W/cm^2
Performance	1000 W
Temperature Control	PT 100

F.5 Results

In the following section some additional results of the wind tunnel study will be presented.

F.5.1 Cylindrical Chimney (CC)

Figures F.6 and F.7 give the circumferential distribution of the mean pressure coefficient for all tested variants. Figures F.8 and F.9 show the corresponding RMS values.

Results for closing the windward or lee side of the SC for variant (No 39) with measured vertical velocities and its effect on the pressure distribution are given in figure F.10.

Figure F.11 shows the velocity history inside the chimney for different modelled temperatures without ambient wind.

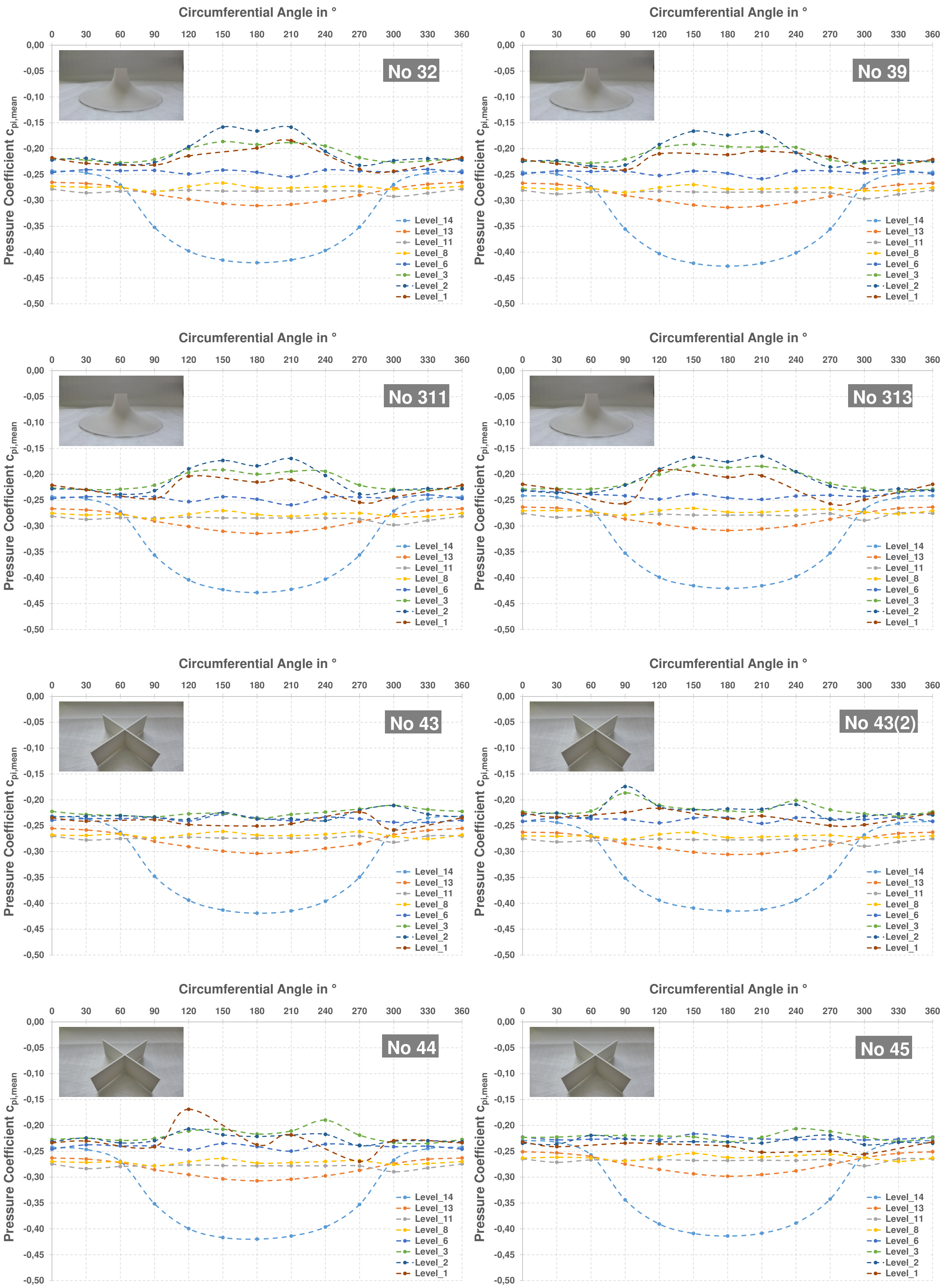

Figure F.6: Circumferential Distribution of Pressure Coefficient $c_{pi,mean}$ for Different Configurations - Part 1 of 2

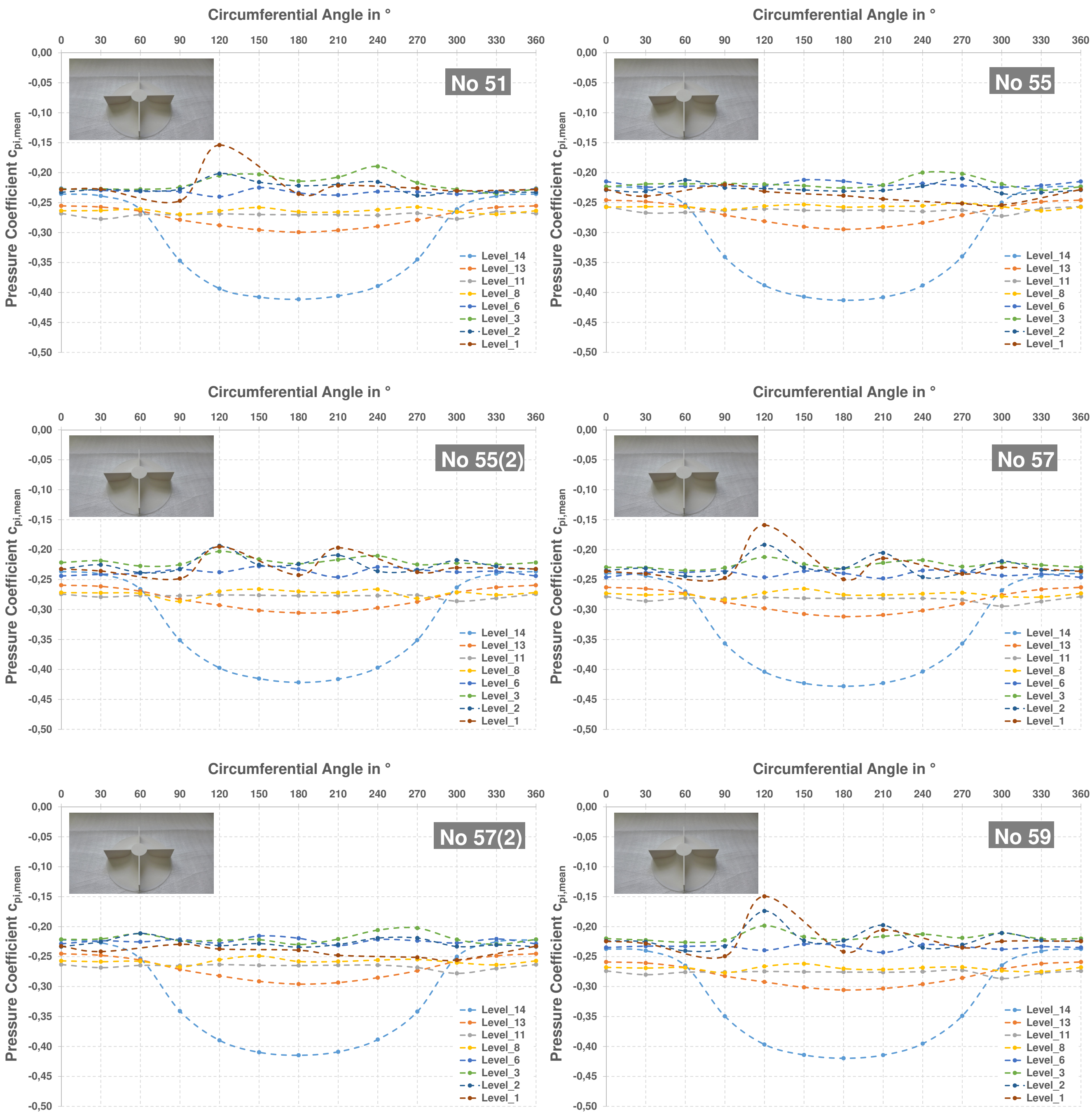

Figure F.7: Circumferential Distribution of Pressure Coefficient $c_{pi,mean}$ for Different Configurations - Part 2 of 2

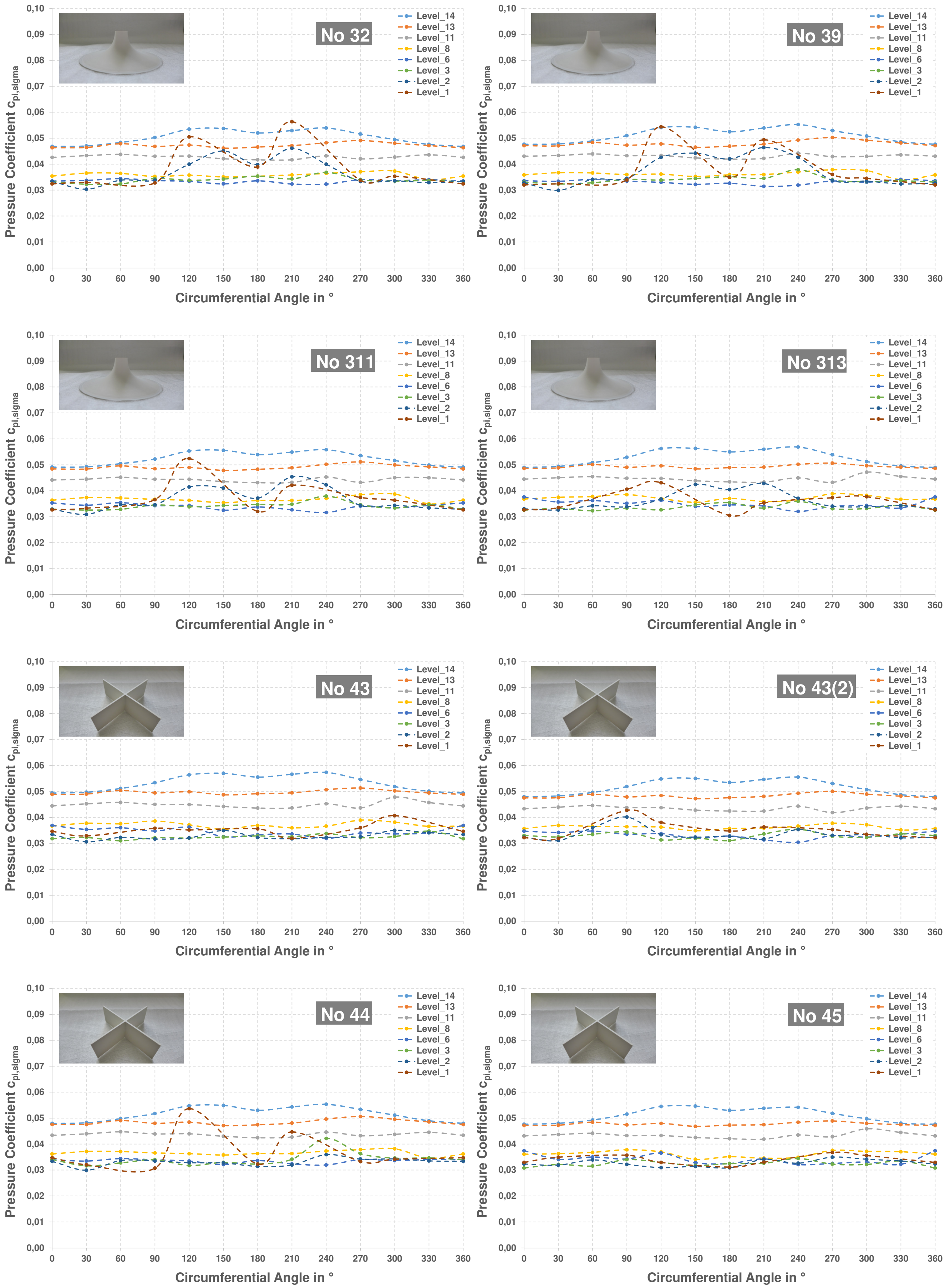

Figure F.8: Circumferential Distribution of Pressure Coefficient $c_{pi,sigma}$ for Different Configurations - Part 1 of 2

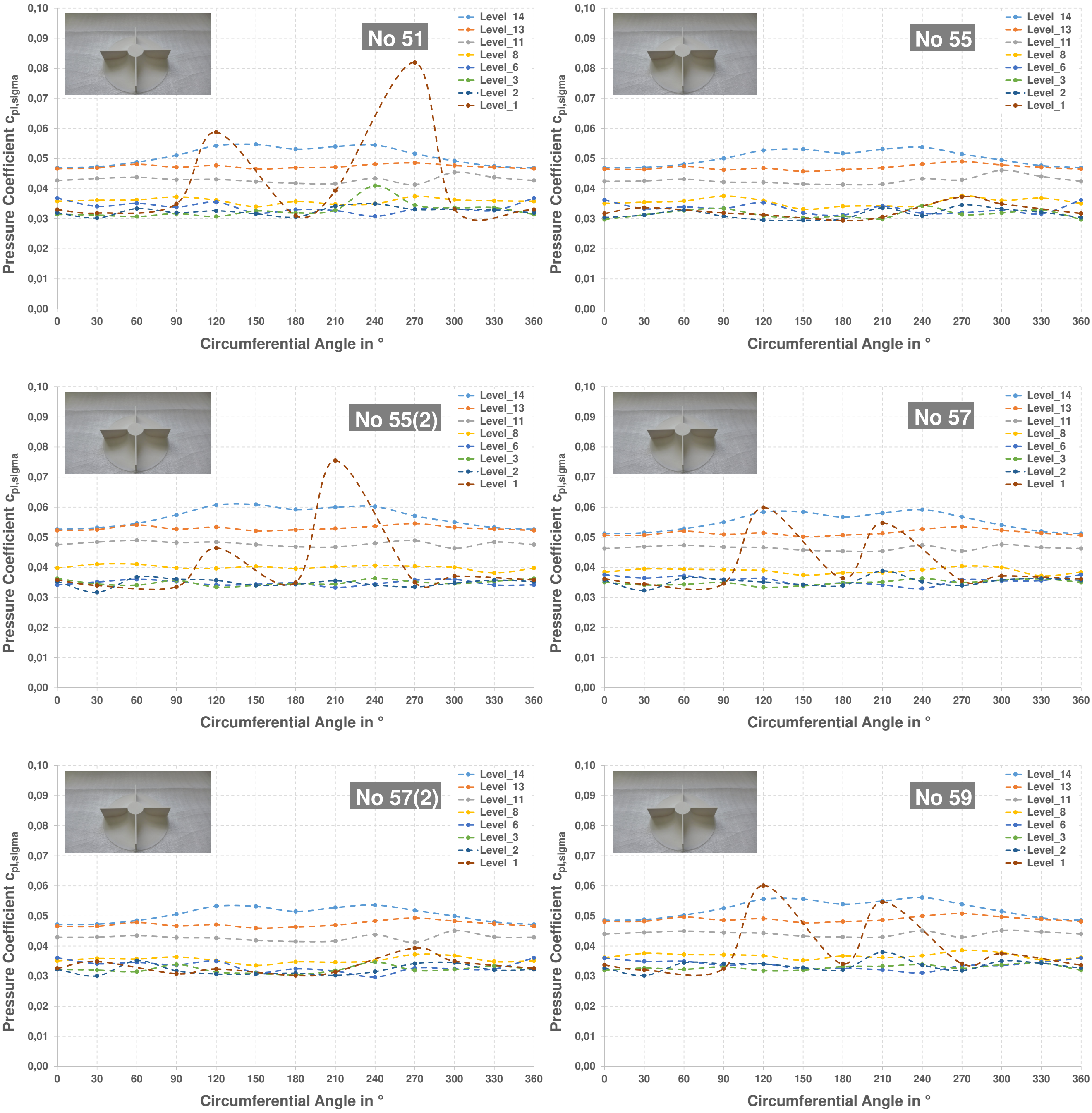

Figure F.9: Circumferential Distribution of Pressure Coefficient $c_{pi,sigma}$ for Different Configurations - Part 2 of 2

Windward Side Closed

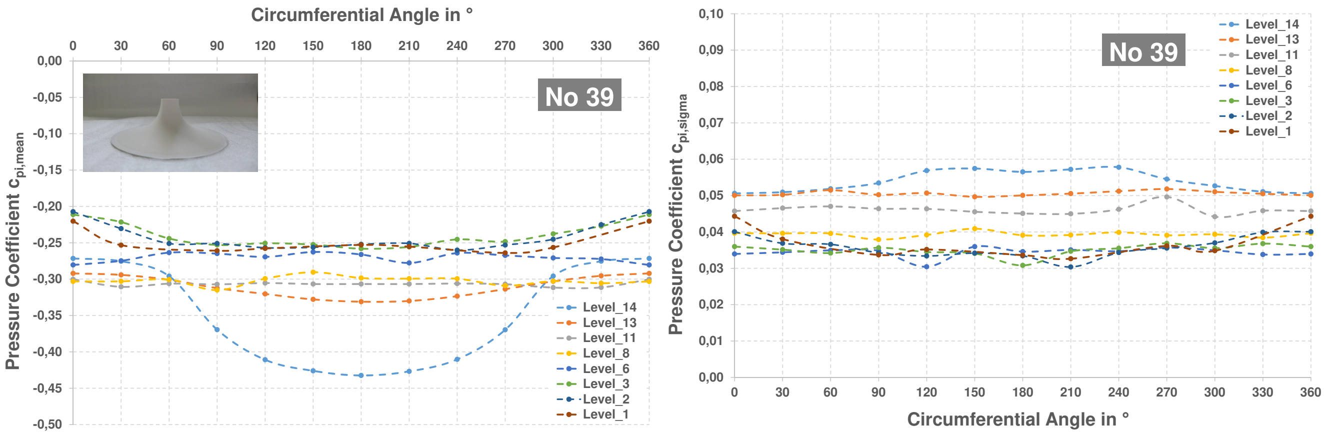

v_{mean} = **4.298 (4.381)** m/s, v_{sigma} = **0.545 (0.554)** m/s, v_{Pra} = **15.505 (15.870)** m/s

Lee Side Closed

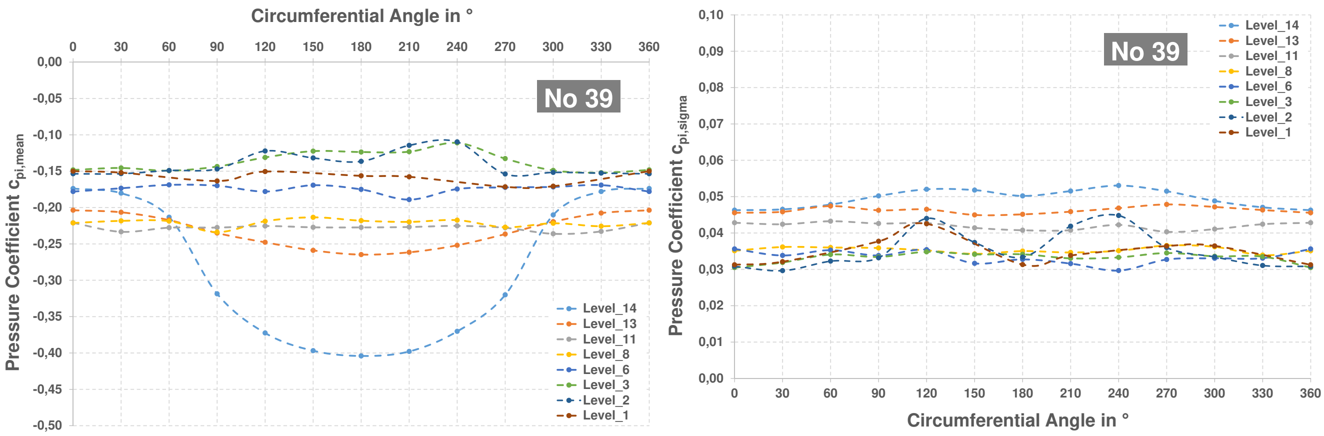

v_{mean} = **5.408 (5.440)** m/s, v_{sigma} = **0.519 (0.527)** m/s, v_{Pra} = **15.715 (15.911)** m/s

Figure F.10: Results for Configuration 39 - Closed Set-Up (Results in Brackets are for the Repetition Measurement)

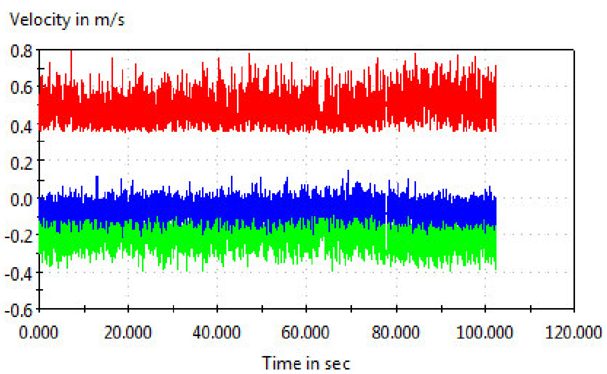

$\Delta T = 70°C$

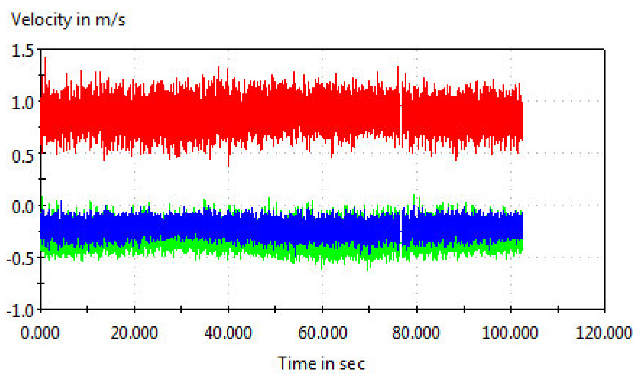

$\Delta T = 120°C$

Figure F.11: Velocity History Inside Chimney Without Wind for T = 70 and 120°C

F.5.2 Diffuser Chimney (DC)

Time history plots for the velocity inside the diffuser chimney without wind are shown for two temperature values in figure F.12.

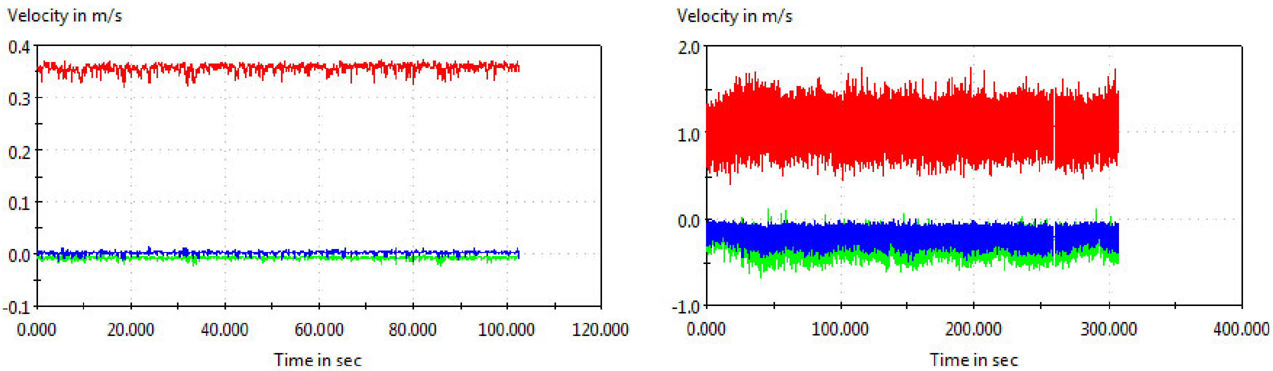

$\Delta T = 0K$ $\Delta T = 115K$

Figure F.12: Velocity History Inside Chimney Without Wind - Default Value and for T = 140°C (red - u component, blue - v component, green - w component)

Figures F.13 and F.14 show the circumferential distribution of the pressure coefficient for the tested variants for the diffuser chimney.

Results for the vertical velocity distribution at z = 940 mm are presented for all tested variants for the mean and RMS values in figures F.15 and F.16 respectively.

For the measurements with the implemented temperature effect figure F.17 shows the course of the velocity and the temperature for the reference case (default) and variant (No 55).

Someone can see the rise in the vertical velocity throughout the whole course of the measurement for variant (No 55) compared to the reference situation. The decrease in fluctuation for all three velocity components can clearly be seen for both cases of an open or on the windward side closed SC. The rise in temperature is for the open case in the range of $1 \div 2$ °C and when the windward side is closed $4 \div 5$ °C. That shows that the buoyancy effect and the rising of hot air inside the SCH can be improved with the implementation of a redirecting variant. Unfortunately not all tested configurations gave such clear results.

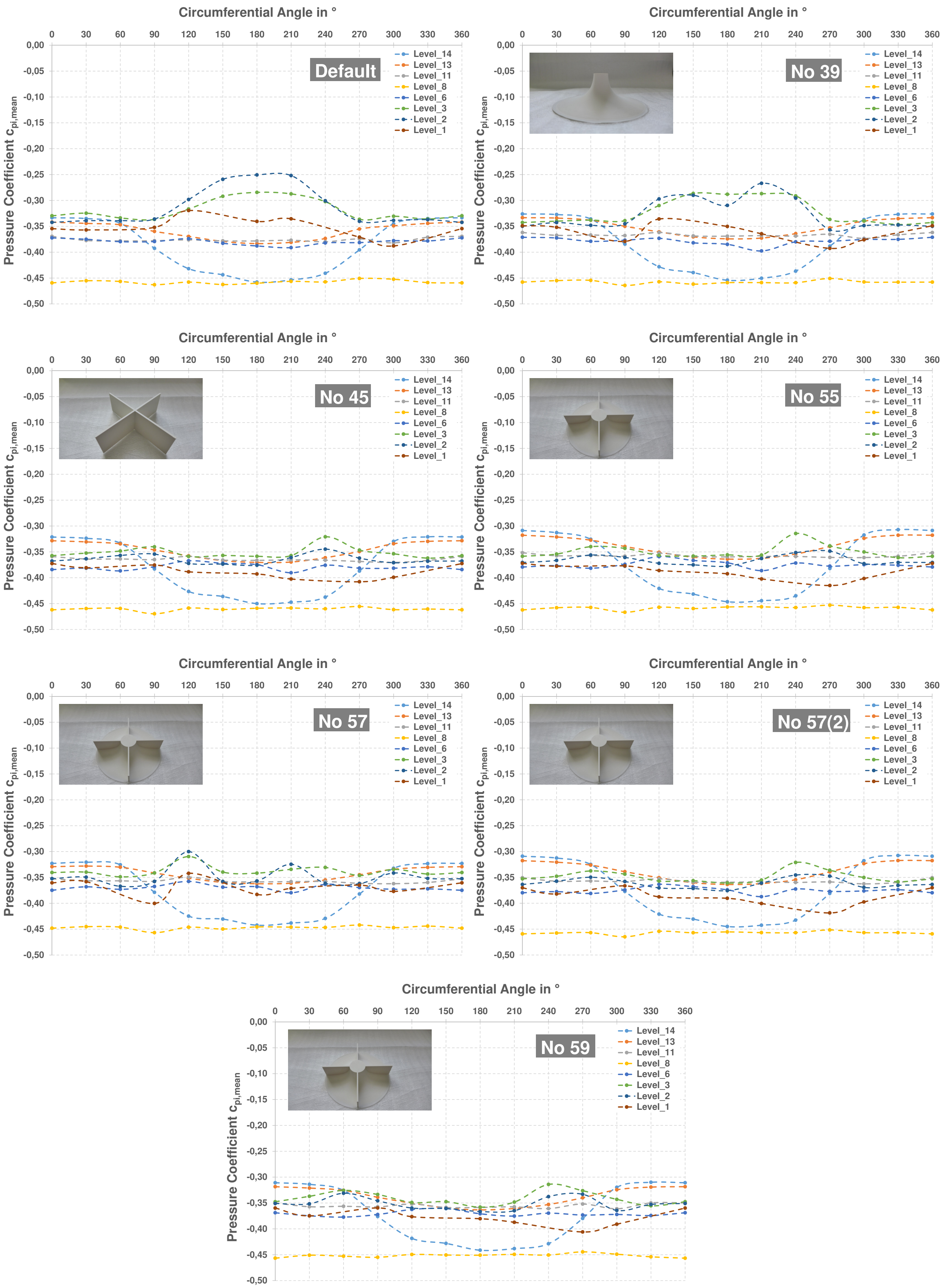

Figure F.13: Circumferential Distribution of Pressure Coefficient $c_{pi,mean}$ for Different Configurations - Diffuser Chimney

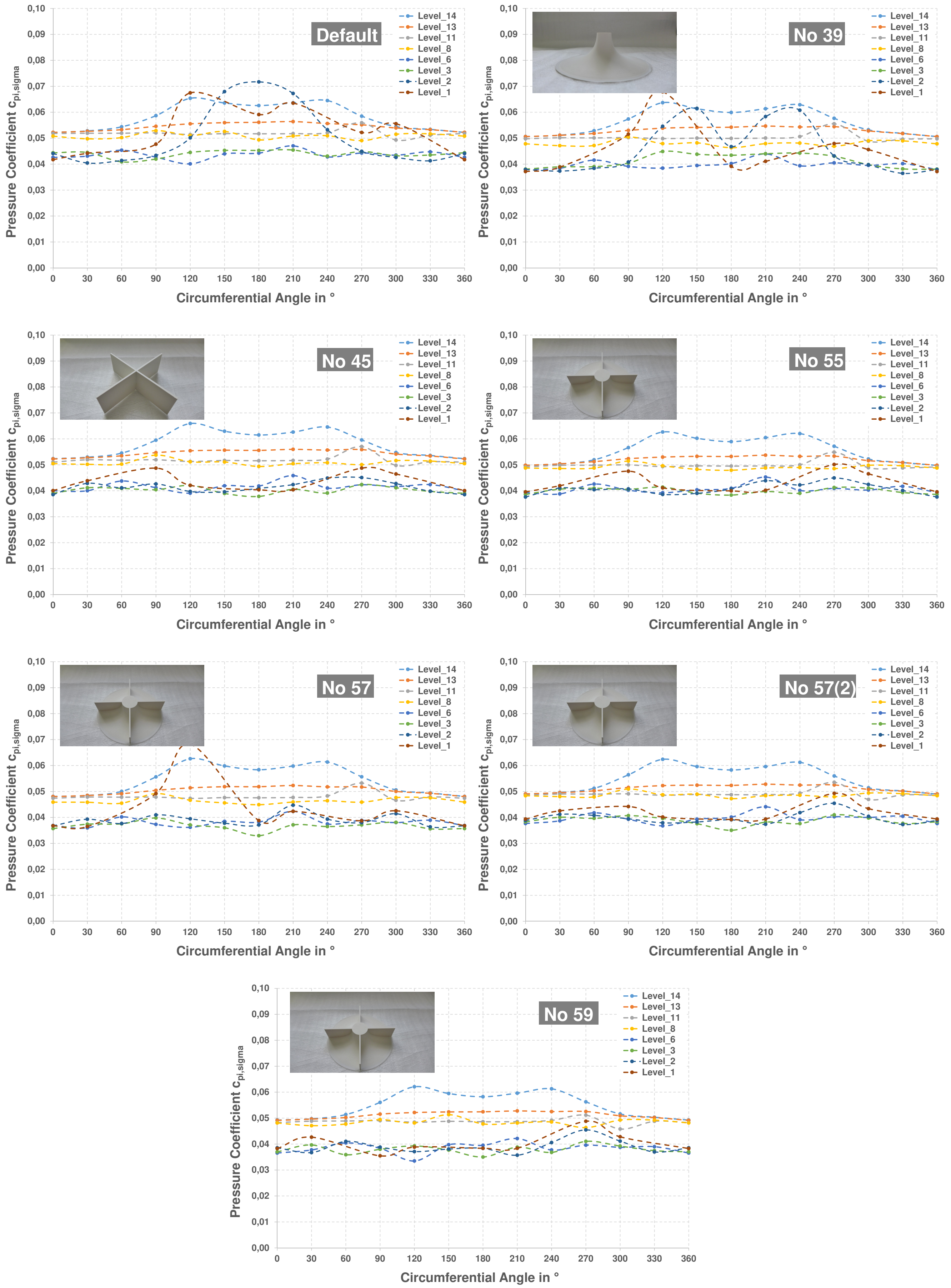

Figure F.14: Circumferential Distribution of Pressure Coefficient $c_{pi,sigma}$ for Different Configurations - Diffuser Chimney

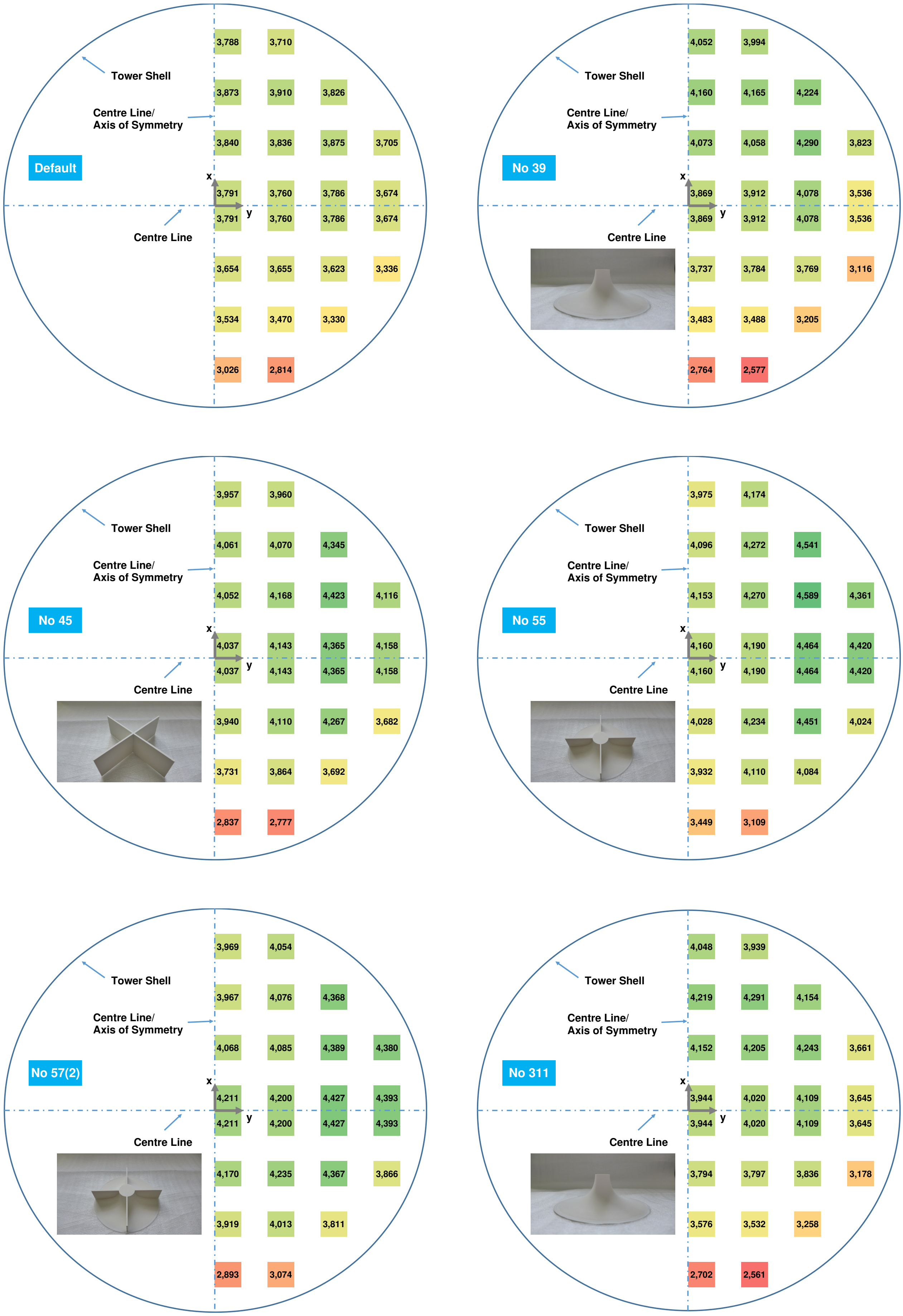

Figure F.15: Mean Velocity Distribution (Open, z = 940 mm, ⇑ Flow Direction)

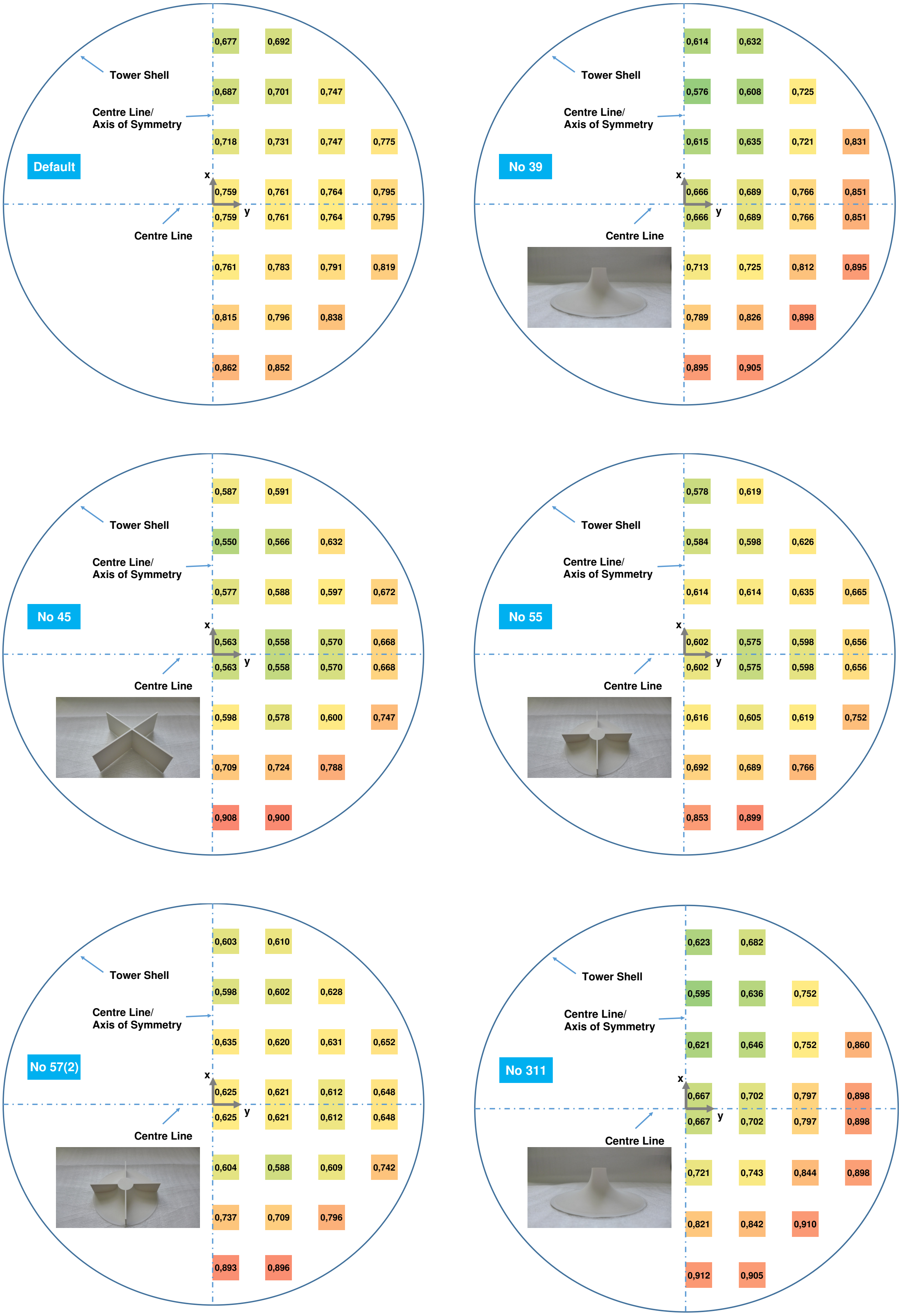

Figure F.16: Distribution of RMS (Open, z = 940 mm, ⇑ Flow Direction)

Default **Configuration 55**

Open

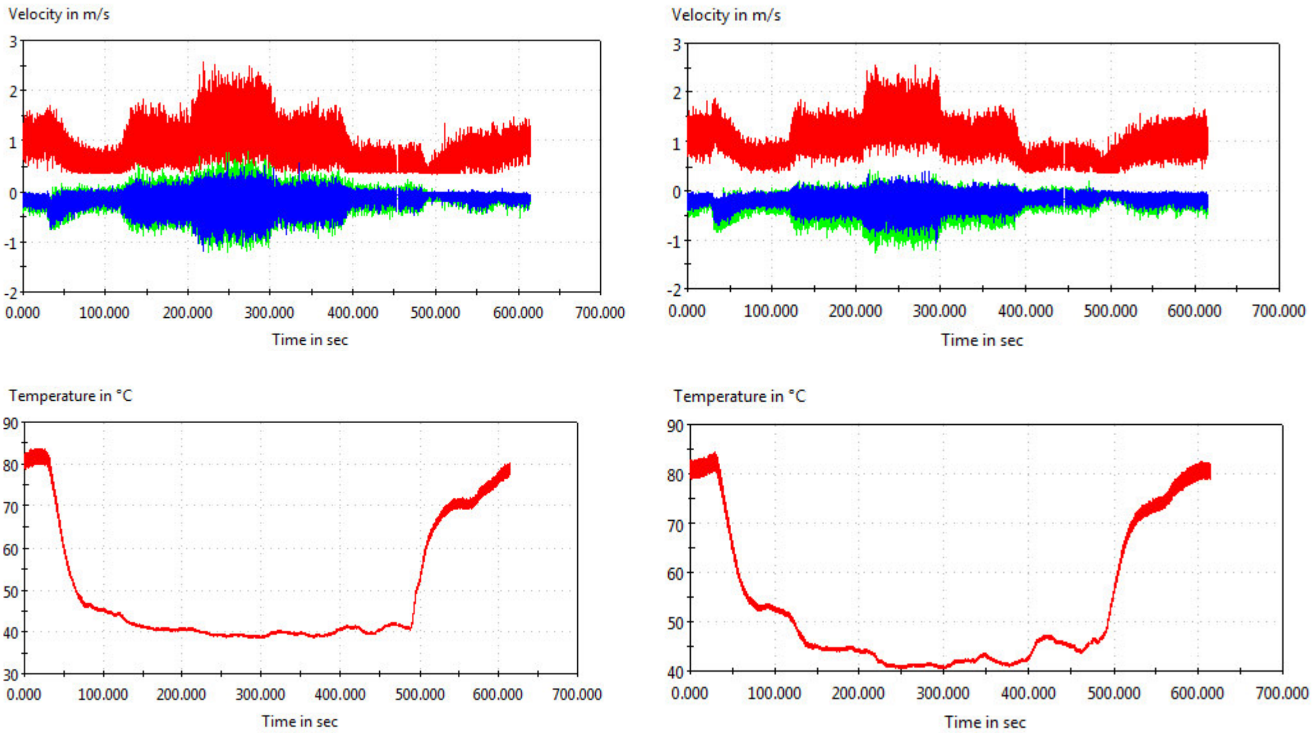

Windward Side Closed

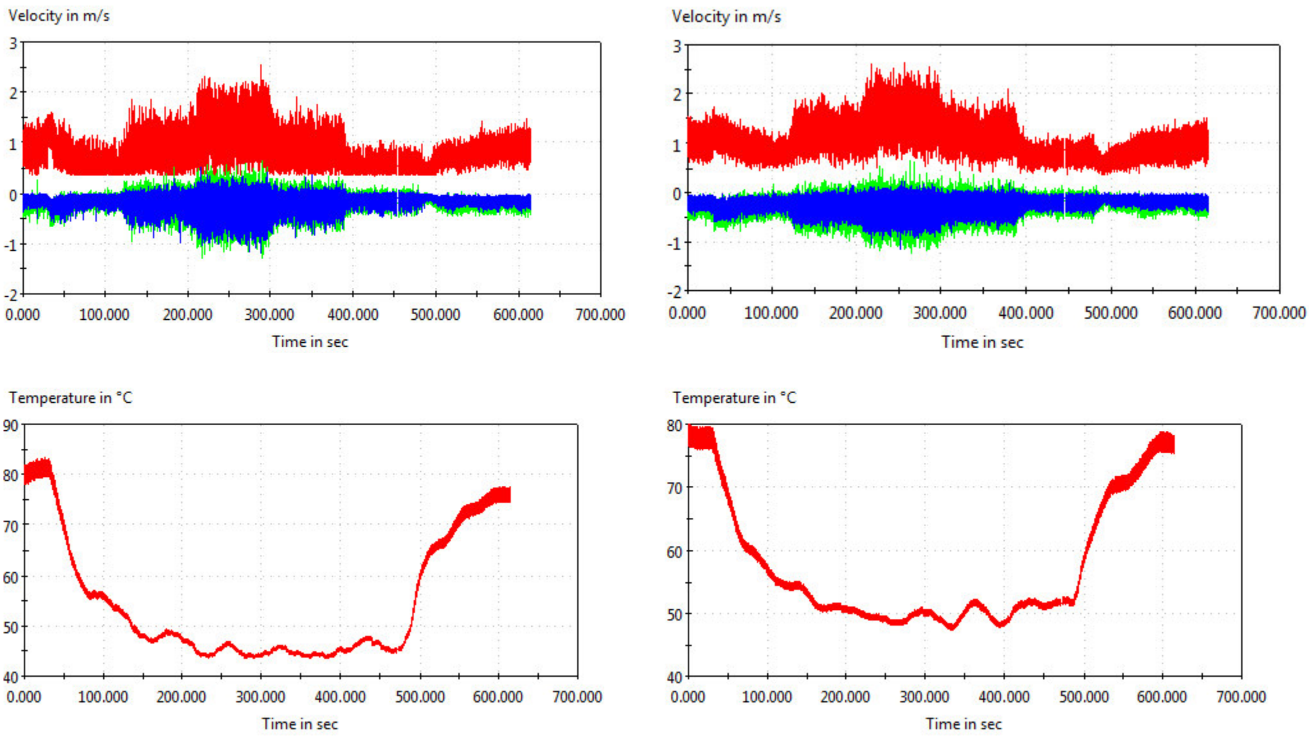

Figure F.17: Course of Velocity and Temperature - Default and Configuration 55

AppendixG

Fan Flow Simulation and Turbine Influence Modelling

G.1 Intention

In this appendix the flow situation inside the turbine - transition region of a SCPP has been investigated with a simplified fan model. Based on these tests the interaction of flow streams leaving the turbines has been captured visually with a high-speed camera. Different fan configurations shall give the reader an impression of the highly turbulent flow field and the importance of an exact reproduction of this part of the SCPP. This qualitative analysis has led to the wind tunnel tests described in chapter 7 on a more advanced model. Also the influence of the turbine(s) within a SCPP on the flow field has been investigated. The blade element momentum theory (BEM) will be explained and the concept of fan similarity. The latter one is important for the exact modelling of full scale axial turbines in scaled model tests. Two turbine layouts are briefly explained, taken from former research on SCPP turbines with their inflow and outflow conditions, respectively. The outflow conditions will be used for the model tests on an improved SCPP, which will be presented in part III of this work.

G.2 High-Speed Camera Testing

Model tests with a high-speed camera have been performed to get some insight about the influence of turbines on the flow situation inside a SCPP. Therefore a simple model has been designed and build.

The turbines have been modelled with conventional fans which can be found in computers to keep the model costs moderate and ensure a simple and fast build up of the model. Although the transfer from stream characteristics from a turbine, which can be found within the real SCPP to a fan is not that simple. Therefore it will be only possible to give a general statement and interpretation of the flow situation inside the transition section.

The tests will start with the investigation of the flow situation of an isolated fan and will be carried on with a small model of the turbine and transition section of the SCPP with or without a tower model. The visualization will be realized with smoke matches and will be explained within the next subsections.

G.2.1 Fan Model

The velocity distribution of a fan flow with its typical characteristics with two velocity peaks close to the hub where the velocity decreases rapidly is depicted in figure G.1 for a fan flow. As a reference the nozzle flow with its characteristic velocity profile is also shown.

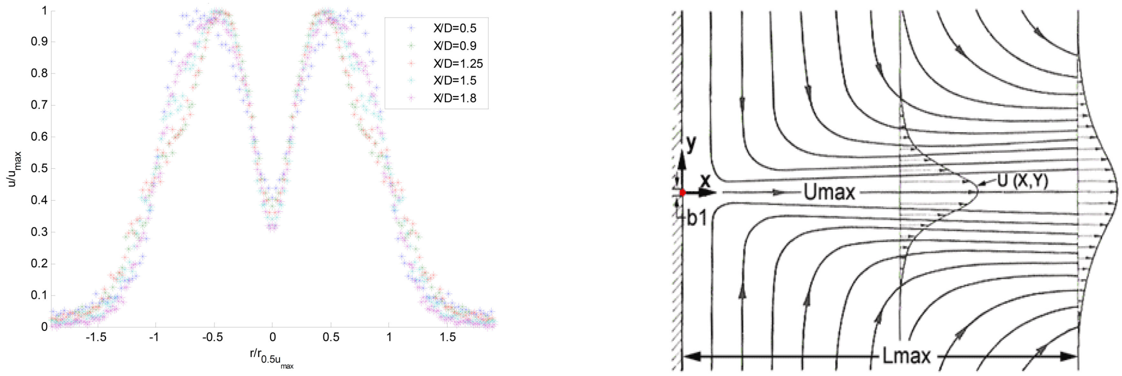

a) Fan Flow b) Nozzle Flow

Figure G.1: Fan Flow vs. Nozzle Flow [A.65]

The influence of the fan hub on the velocity profile can still be detected in a distance to the fan axis shown in figure G.2 for different normalized distances X/D where D is the diameter of the fan.

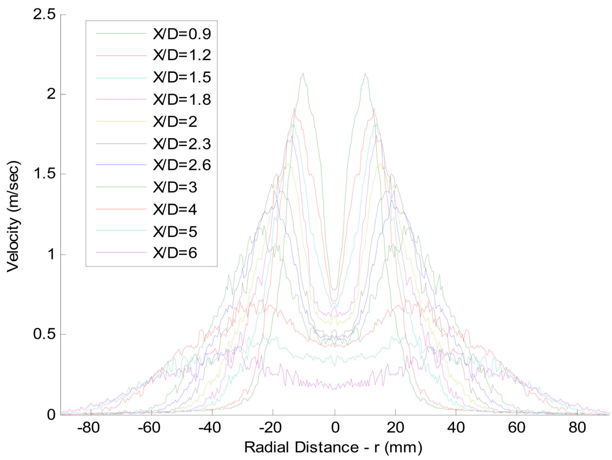

Figure G.2: Fan Flow at Different Distances to the Fan Axis [A.65]

G.2.2 Set-Up and Equipment of High-Speed Camera

The geometric scale of the model is nearly 1 : 400 for the transition section and the turbines and relies on the design of the SCPP shown in section 2.5. The transition section has a diameter of 0.28 m whereas the SCH with a height of 0.37 m is reduced in scale for the sake of simplicity. Figure G.3 shows the different set-ups, the tested fan model including the regulation module, the used high-speed camera and some views of the investigated model.

The configuration details for the measuring program are listed in table G.1.

a) Setup - View 1

b) Setup - View 2

c) Tested Fan

d) Turbine Arrangement with Tower (Side View)

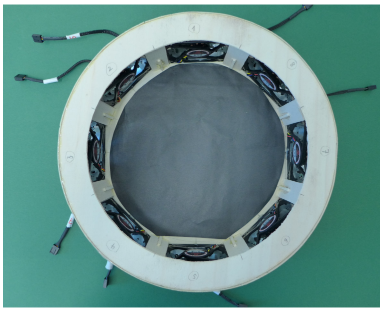

e) Turbine Arrangement (Top View)

f) Turbine Arrangement (Side View)

Figure G.3: Set-Up of Fan Flow Simulation

Details on fan similarity (geometric, kinematic and dynamic) will be explained in subsection G.4.3 and in [B.8].

G.2.3 Results

Results for the isolated fan flow are depicted in figures G.4 and G.5.

For a better visualization the main flow streams are marked throughout all results. The time stamp for each picture is given, where the interval is kept constant for a measurement but may vary between different configurations to get the best pictures of each configuration.

For all three isolated fan flow configurations the expected flow structure can be found on the pictures. Even the rotation and the widening of the flow field can be seen, where the best visualization is in the front view. A measure has been inserted to get a feeling of the widening angle.

Table G.1: Configurations

Suffix	Frequency	Shutter Time	Measuring Time	Distance Fan-Objective	RPM	Resolution
-	Hz	μs	sec	cm	-	PPI
1	400	1139	5.0	35.0	1000	844x608
2	875	1139	2.286	35.0	1000	844x608
3	1107	633	1.807	63.5	1000	584x480
4	200	1708	6.0	90.0	500	1024x960
5	200	1708	6.0	90.0	500	1024x960
6	200	1708	6.0	90.0	500	1024x960
7	200	423	2.837	90.0	1000(F3), 500(F7)	1024x960
8	200	1708	6.0	90.0	500	1024x960
9	200	1708	6.0	90.0	500	1024x960
10	200	1202	6.0	90.0	500	1024x960
11	200	844	6.0	90.0	500	1024x960
12	200	556	6.0	90.0	500	1024x960
13	200	2493	6.0	60.0	500	788x864

Obliquely From Front [1]

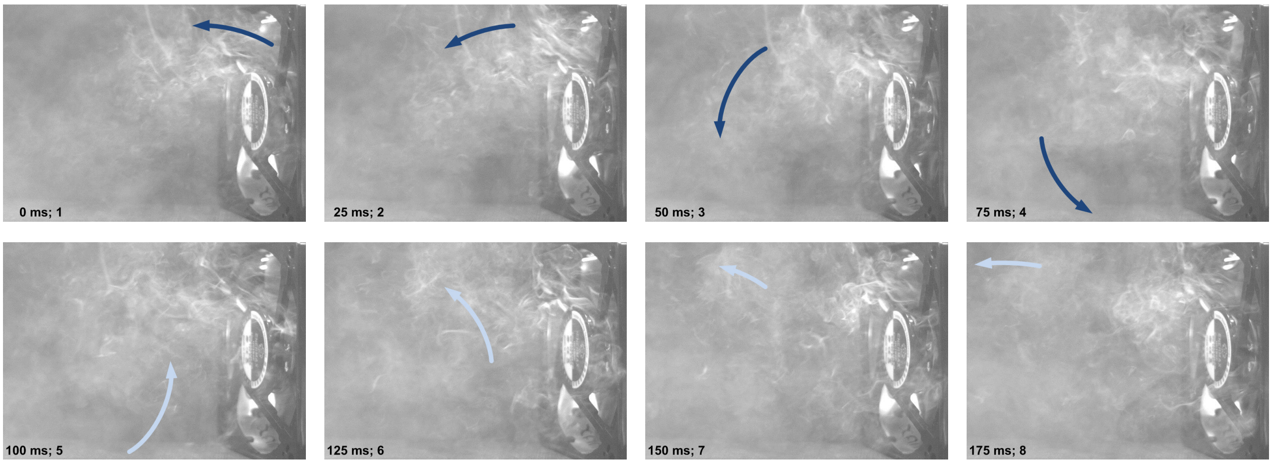

Figure G.4: Smoke View of Isolated Fan Flow - Part 1 of 2

The interaction between two or more fan flows in a typical SCPP arrangement has been investigated based on nine configurations where different flow scenarios have been tested. For the tower flow figure G.6 gathers the flow situation for one fan working. In figures G.7 and G.8 the flow situation only for the transition section is depicted.

For all configurations only the marked fans have been working while the others were standing still and only one of the working fan flows has been highlighted with smoke. Three findings were

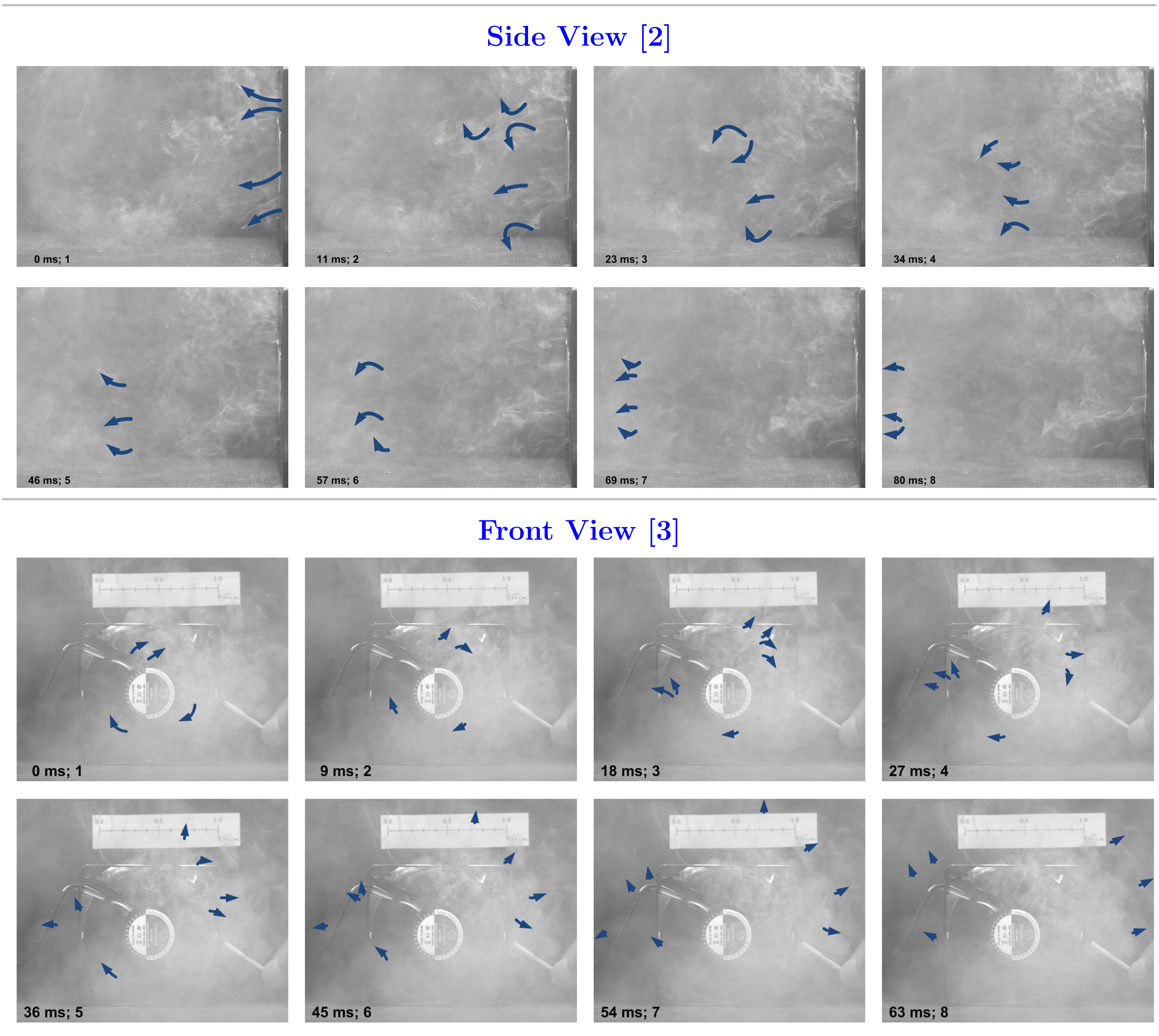

Figure G.5: Smoke View of Isolated Fan Flow - Part 2 of 2

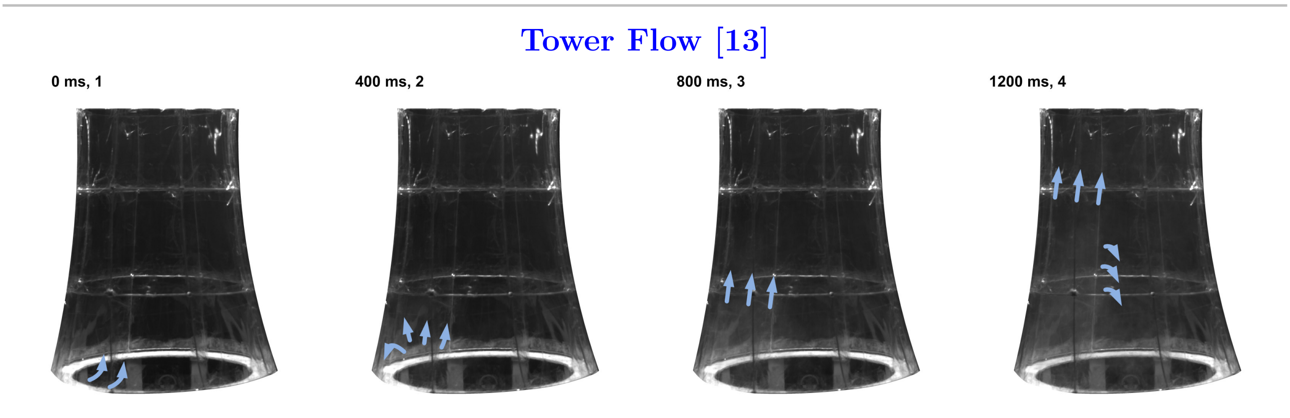

Figure G.6: Flow Situation Under Different Operating Conditions - Part 1 of 3

made:

- The speed (rpm) of opposing fans have an influence on the flow length of a stream from the fan axis to the inside of the transition section.
- Streams slanted to each other lead to a diversion of the main stream into a resultant direction.
- For the case of four to eight working fans the findings show that a highly turbulent and mixing flow field can be found. The formation of single flow streams is only true close to the outlets of the fans and is eliminated very fast afterwards.

For the tower it can be found that the produced smoke rises up inside the tower and diminishes close to the upper rim. Due to the complexity of the flow field additional tests have not been performed with this model but have been carried on at an improved model presented in part III.

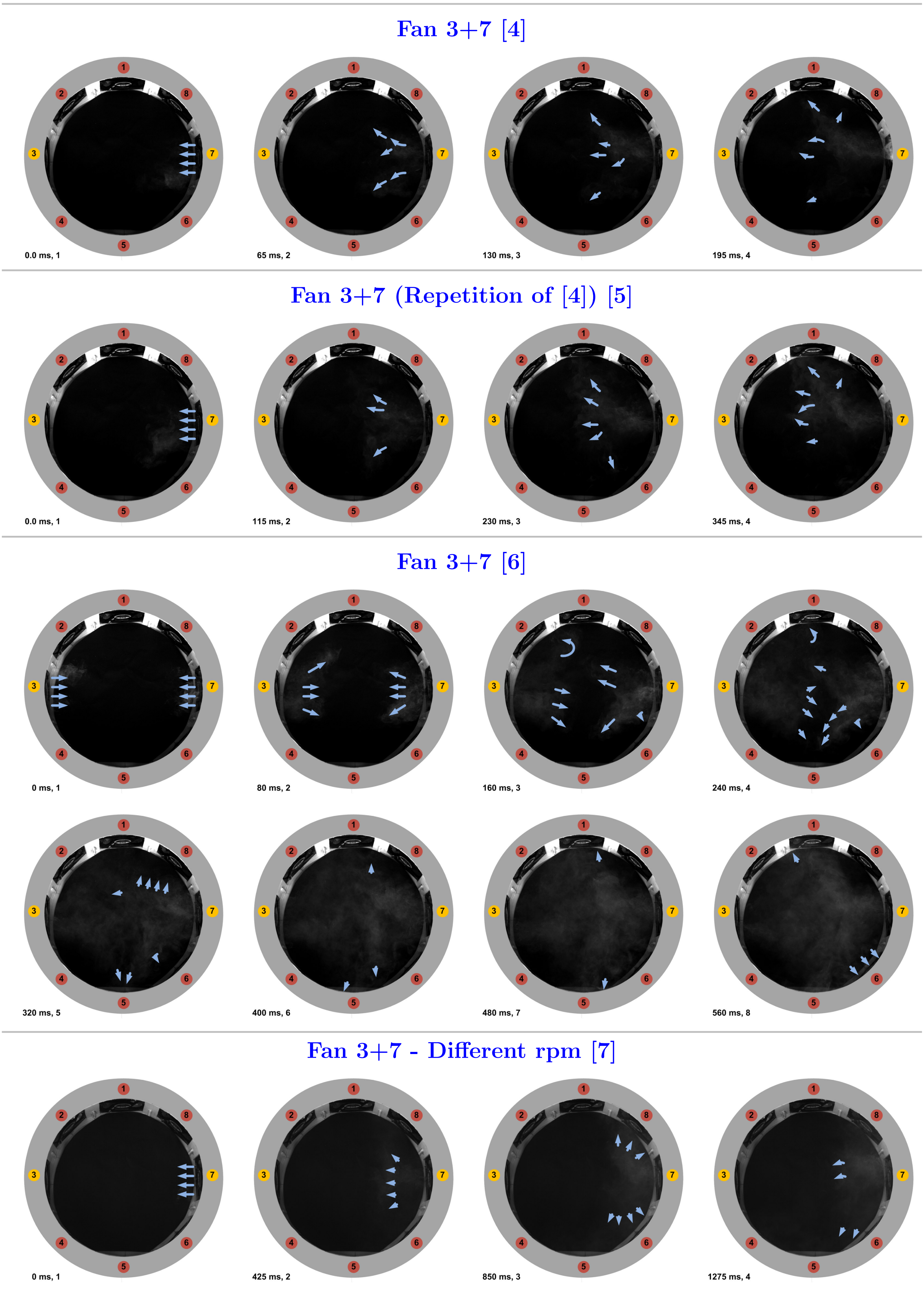

Figure G.7: Flow Situation Under Different Operating Conditions - Part 2 of 3

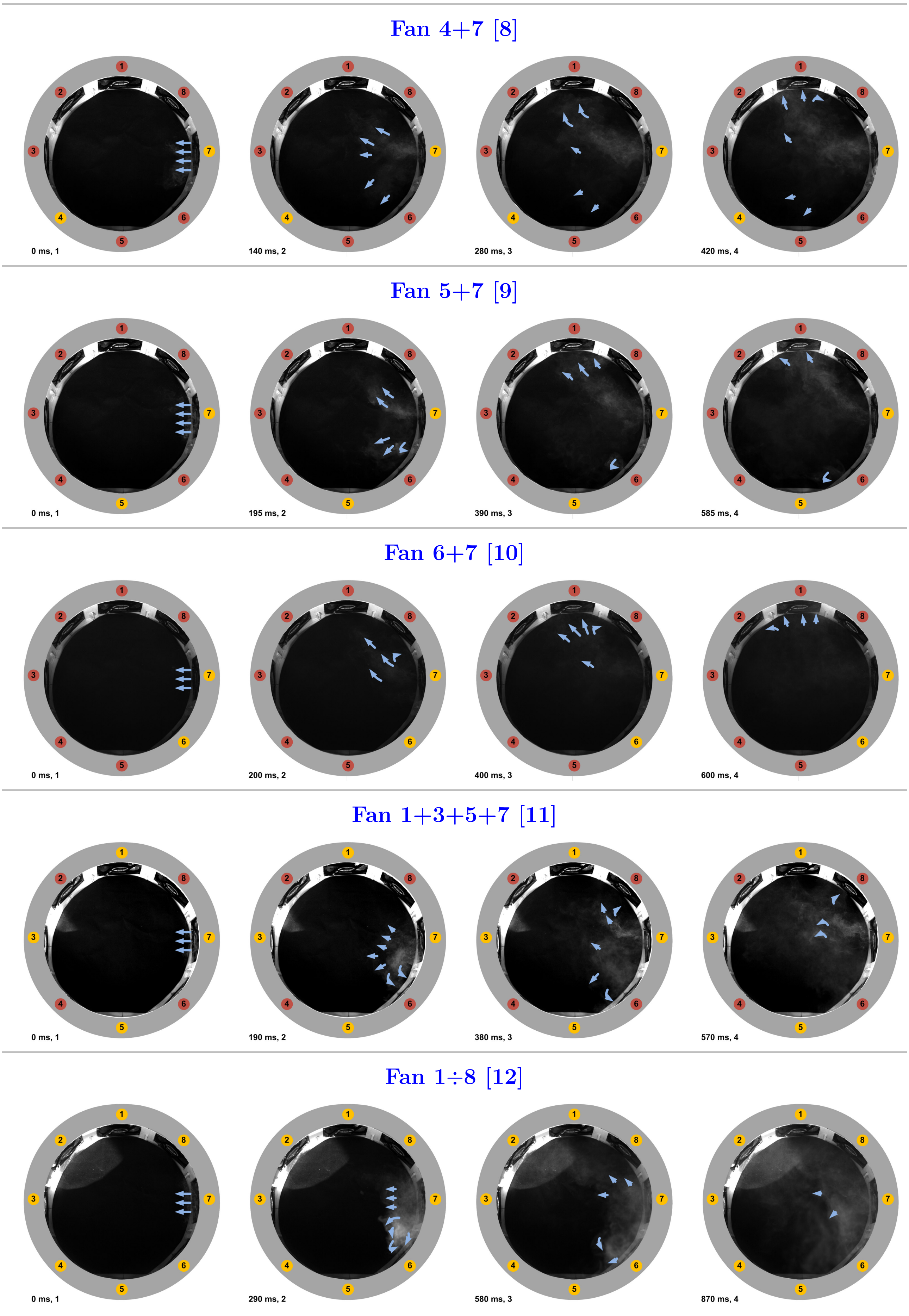

Figure G.8: Flow Situation Under Different Operating Conditions - Part 3 of 3

G.3 Basics of Axial Turbines

For a better understanding of the influence of axial turbines on the flow field figure G.9 depicts the velocity diagram of an axial turbine compared with an axial fan.

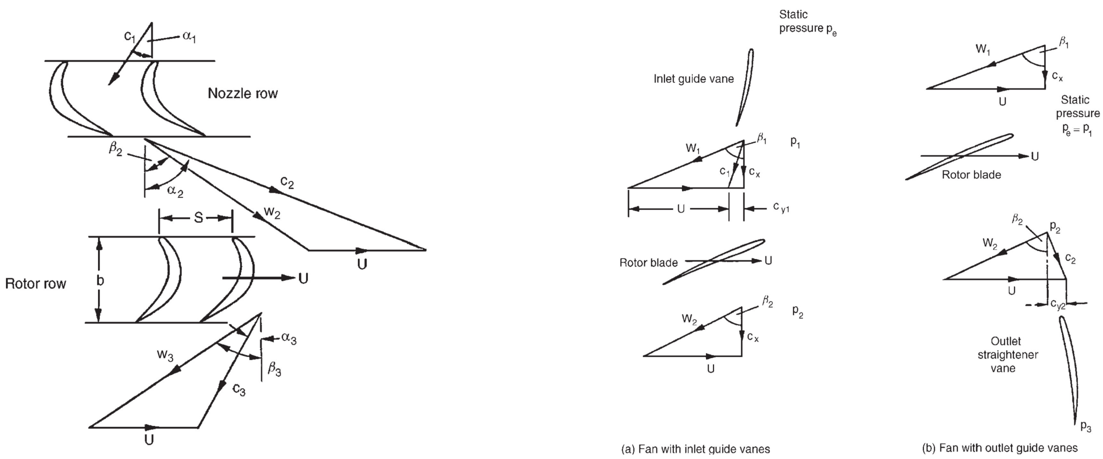

a) Axial-Flow Turbine b) Axial-Flow Fan

Figure G.9: Velocity Diagrams of an Axial-Flow Turbine and Fan [T.9]

In this case a nozzle row, also known as stator or IGV, has been installed in front of the rotor. *Absolute velocities* are named with a c and w for *relative velocities*. The relative velocity is found by subtracting, vectorially, the blade speed U from the absolute velocity c_i.

For a fan, as it has been used in section G.2, the velocity diagram is given for the case with an IGV and OGV, respectively. The axial-flow fan as a single-stage compressor of low-pressure and temperature rise shows a similar behaviour like the axial-turbine.

For both turbo machines the general aim is equivalent, namely to reduce the swirl of the flow at the outlet and to minimize the flow resistance.

Measuring techniques for turbomachinery flow are described in [B.41]. More research can be found by [A.117], [A.25] and [A.90].

Former research on the modelling of axial turbines both experimentally and numerically can be found by [T.8], who modelled a single vertical axis turbine. [T.9], who modelled 32 horizontal axis turbines and [T.14], who performed a numerical simulation of the wake region of an axial turbine stage. Last but not least see [A.96], where the fan was simulated as a vector flow with varied radial and tangential components.

G.4 Blade Element Momentum Theory (BEM)

"Blade Element Momentum Theory equates two methods of examining how a wind turbine operates. The first method is to use a momentum balance on a rotating annular stream tube passing through a turbine. The second is to examine the forces generated by the aerofoil lift and drag coefficients at various sections along the blade. These two methods then give a series of equations that can be solved iteratively" [A.87].

Details of the flow over aerofoils, e.g. the tip loss correction, will not be discussed here.

G.4.1 Blade Element Theory

"A blade element at a given radius can be defined as an aerofoil of vanishingly small span. In fan-design theory it is commonly assumed that each such element operates as a two-dimensional aerofoil, behaving completely independently of conditions at any other radius" [B.9]. The blade element theory relies on two key assumptions:

- There are no aerodynamic interactions between different blade elements.
- The forces on the blade elements are solely determined by the lift and drag coefficients.

G.4.2 Momentum Theory

"Momentum theory analyses the momentum balance on a rotating annular stream tube passing through a turbine" [B.3].

In other words it is a mathematical model to describe an ideal actuator disc, cf. a wind turbine.

For more information about actuator discs, etc. see section 3.2.3 and [B.2], [A.87].

G.4.3 The Concept of Fan Similarity

The concept of fan similarity relies on three pillars:

1) *Geometric similarity* in which two units have length dimensions in a constant ratio throughout and equivalent angles are equal.
2) *Kinematic similarity* in which the dimension of time is added to length and all peripheral flow velocities at any point within a machine are in a constant ratio to the velocities at corresponding points of the similar unit.
3) *Dynamic similarity* in which acceleration is introduced and the forces at corresponding points in the two machines also bear a constant relationship.

The following table G.2 has been abstracted from [S.14].

It shows the "recommendations for maximum divergences of these critical dimensions from strict geometrical similarity without invalidating the "Fan Laws" used in performance prediction, within the stated uncertainties of the method" [B.8]. More codes are [S.13] and [S.9], [S.10], [S.11].

Table G.2: Geometrical Similarity of an Axial Fan [B.8]

Critical Dimensions	**Pitch Design**	
	%	%
Impeller	Fixed	Variable
Blade Tip Diameter	± 0.25	+ 0.125 ÷ - 0.25
Hub Diameter	± 0.375	± 0.125
Blade Chord Length	± 0.1	± 0.1
Blade Profile	± 0.1	± 0.1
Blade Angle of Twist	+ 2.0 °	± 1.5 °
Blade Angular Setting	± 0.1 °	± 0.5 °
Blade Tip Clearance when *Running**	± 20.0	± 20.0
Casing		
Impeller Casing	± 0.2	± 0.2
Inlet Box, Inlet Bell and Discharge Casing	± 0.4	± 0.4
Angular Setting Guide Vanes	± 2.0 °	± 2.0 °
Axial Setting of Guide Vanes	± 0.2	± 0.2
Accessories	± 0.4	± 0.4

* Expressed as a percentage of actual clearances.

G.5 Turbine Layout

The turbine layout orients towards the application and general working parameters. For a SCPP a concept with one stator and one rotor row is favoured. Two designs will be presented within this section.

G.5.1 Inlet Guide Vane (IGV) Layout

The layout of the IGVs are gathered for two publications in table G.3.

Table G.3: Inlet Guide Vane Geometry

Author	**Blades**	**Profiles**	**Profile Type**	**Pitch/Chord**	**Aspect Ratio**
Gannon [T.9]	18	1	mod. NACA 4-digit	0.35	1.42
Fluri [T.8]	31	4	NACA 4-digit	[1]/85 mm	2.82

[1] No data available.

A variable pitch can serve to control the SCPP output and to close off the turbine flow passage(s) in case of emergency or maintenance.

G.5.2 Rotor Layout

The rotor layout is given in table G.4 for both publications as it has been done for the IGVs before.

Table G.4: Rotor Geometry

	Blades	**Profiles**	**Profile Type**	**Pitch/Chord**	**Aspect Ratio**
Gannon [T.9]	12	7	mod. NACA 4-digit	1.03÷4.50	[1]
Fluri [T.8]	16	5	NACA 4-digit	[1]/30 mm	7.2

[1] No data available.

The design can be adapted for the current problem via analytical calculations or by the use of a digital database, e.g [U.1].

G.6 Inflow and Outflow Condition

The schematic representation of the flow in the separation area on the suction side of a blade is depicted in figure G.10.

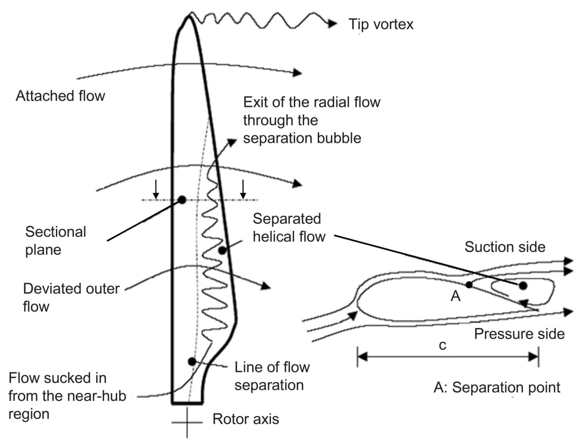

Figure G.10: Schematic Representation of the Flow in the Separation Area on the Suction Side of a Blade at Higher Wind Speed [B.16]

It shows the complexity and characteristics of the flow field of a blade. The experimental results for the velocity profiles, relative inlet and outlet rotor angles and the gas deflection angles are gathered in figure G.11.

Plotted against the fraction of diameter someone can see that all results vary with distance to the hub of the rotor. More experimental and numerical results can be found by [A.162], [A.44], [A.51] and [T.13].

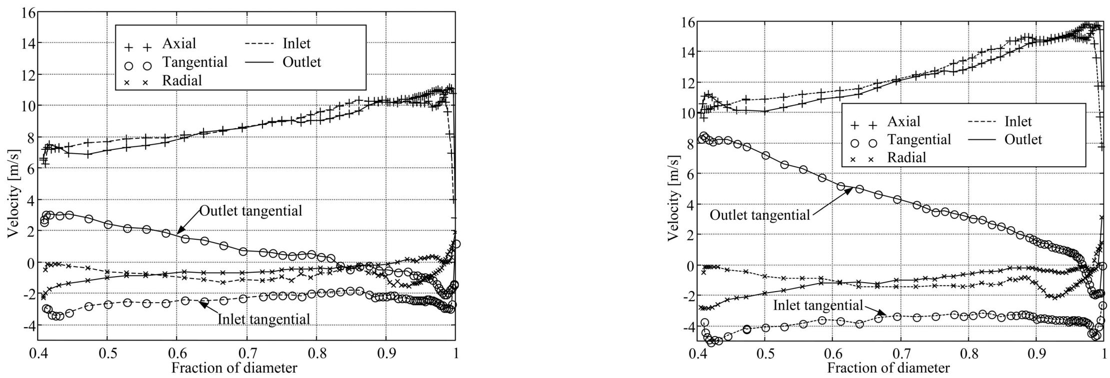

a) Velocity Profiles of Low (left) and High (right) Pressure Drop

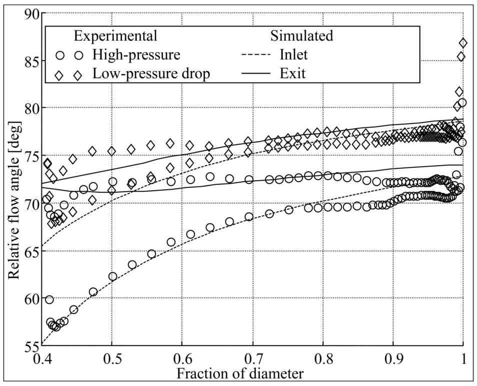

b) Relative Rotor Inlet and Outlet Angles

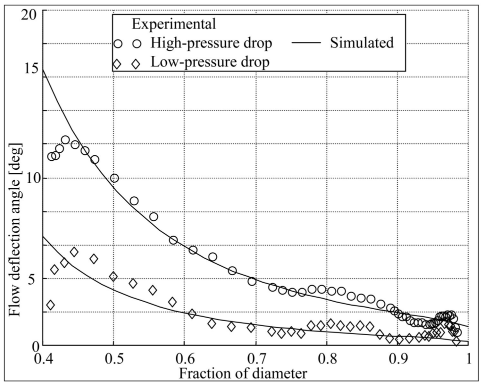

c) Gas Deflection Angles

Figure G.11: Experimental Results of Turbine Flow [T.9]

G.7 Conclusion

The presented model tests gain helpful information about the real flow situation within the transition section of a full scale SCPP. Although this model only allows a qualitative interpretation of the flow situation, it can be stated, that the influence of the turbines need to be taken into account when analysing this part of the SCPP. This is mainly due to the interaction and mixing of the flow streams leaving each turbine and the diversion into the vertical direction. This highly turbulent and transient part of the flow plays a decisive role when it comes to an efficiency analysis and therefore will be part of additional experimental and numerical tests. A wind tunnel model, which includes a simple approach of modelling the influence of the turbines, will be presented in part III.

The experimental and numerical modelling of the turbine influence on the flow field can be realized with two approaches. Firstly, the exact modelling of the turbine in strict accordance with fan similarity, cf. subsection G.4.3. Secondly, modelling of the outflow conditions to reproduce the impact of the turbines on the flow field. The second approach is generally used in CFD analysis. For more information please see chapter 3.

AppendixH

Design and Construction of a Solar Chimney Power Plant for Aswan, Egypt

H.1 Construction Site

The following work has been part of a joint research project (ID: 01DH14006A D0101232A) between Egypt and Germany, financed by the STDF and the BMBF, coordinated by the DLR. As one major part of my own work and certainly the reason why I decided to have a closer look at the SCPP technology, a short gathering of the main facts will be presented here. For a detailed overview of all information about our joint research project please read the final project report.

The prototype SCPP is located in Aswan, Egypt with the site coordinates given in table H.1.

Table H.1: Coordinates of Site

Corner	Coordinates		Height Above Sea Level
	North	East	m
1	23° 59' 22"	32° 50' 31"	186.5
2	23° 59' 22"	32° 50' 32"	186.5
3	23° 59' 21"	32° 50' 32"	187.0
4	23° 59' 21"	32° 50' 31"	187.0

Pictures of the construction site before the start of this joint research project and an elevation map are given in figure H.1.

With an average and always high temperature of about 40°C for more than half of the year and an average annual sunshine of about 4,000 hours, which is close to the theoretically maximum annual sunshine hours, Aswan is one of the hottest and sunniest cities in the world. This climatic condition makes the city an ideal place for implementing solar energy harvesting projects like SCPPs. Figure H.2 shows the mean annual air temperature and its range.

The average monthly sun hours and the relative humidity for each month are depicted in figure H.3.

As can be seen in the soil parameters of Africa, figure H.4 and the regional tectonic and historical earthquakes map of Egypt, figure H.5, Aswan is located in a seismically active region.

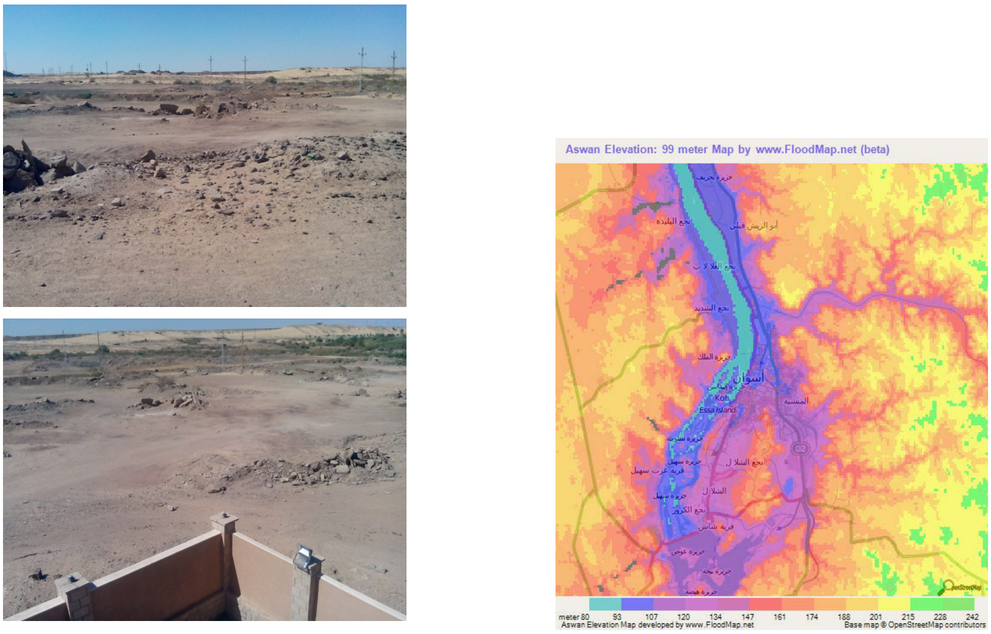

a) Construction Site b) Elevation Map [U.5]

Figure H.1: Construction Site

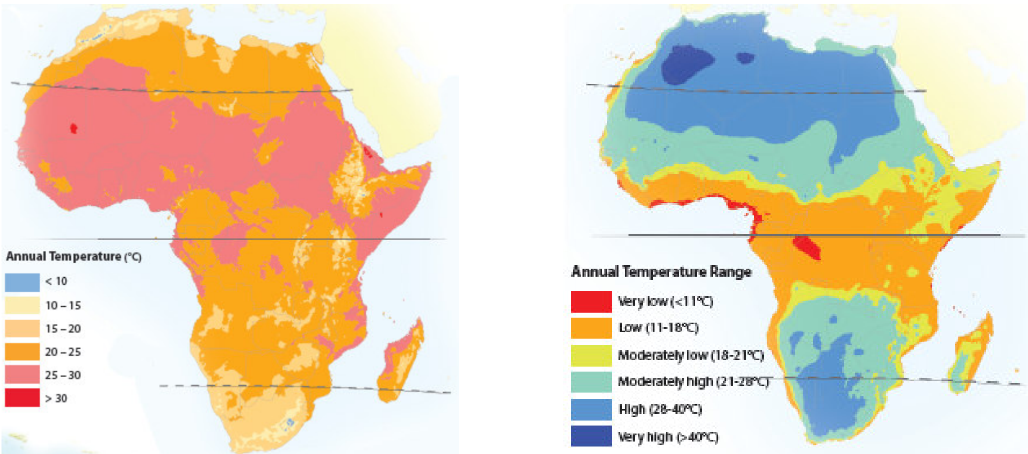

a) Mean Annual Air Temperature b) Annual Air Temperature Range

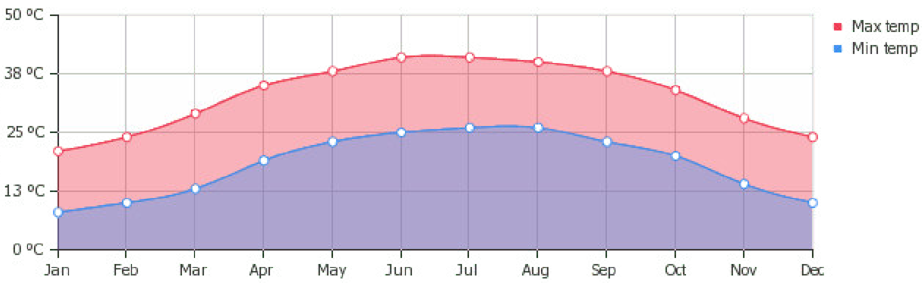

c) Average Min and Max Temperature in Aswan

Figure H.2: Mean Annual Air Temperature and Range [B.42], [U.10]

The soil regime is called hyperthermic, with a mean annual soil temperature of $\geq 22°C$ and a difference between mean summer and winter soil temperatures of $\geq 5°C$.

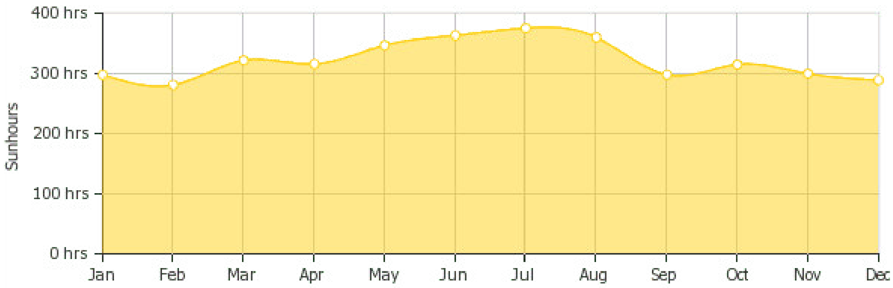

a) Average Monthly Sun Hours

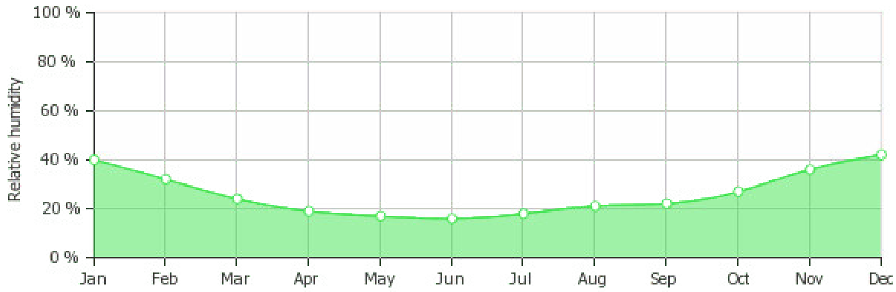

b) Relative Humidity

Figure H.3: Average Monthly Sun Hours and Relative Humidity in Egypt [U.10]

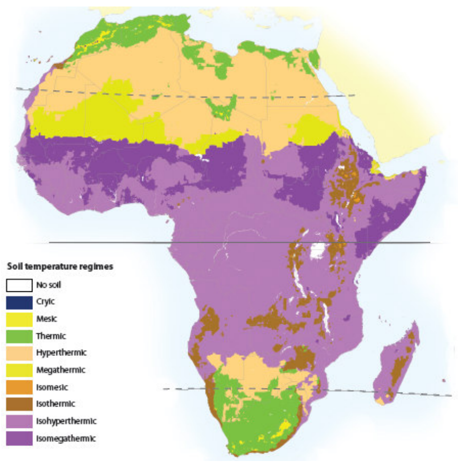

a) Soil Temperature Regimes

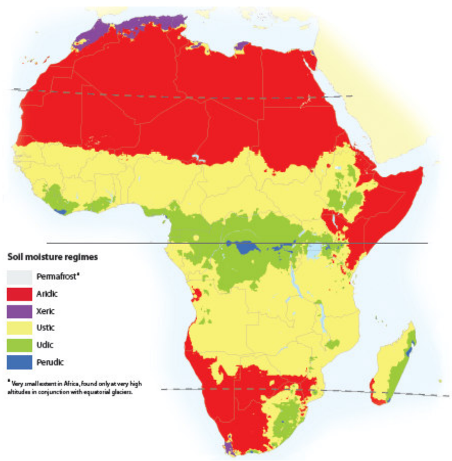

b) Soil Moisture Regimes

Figure H.4: Soil Parameters of Africa [B.42]

Figure H.6 shows the soil layers for the construction site of Aswan.

Whereas figure H.7 shows the wind distribution at the construction site with an average wind speed of 4 m/s.

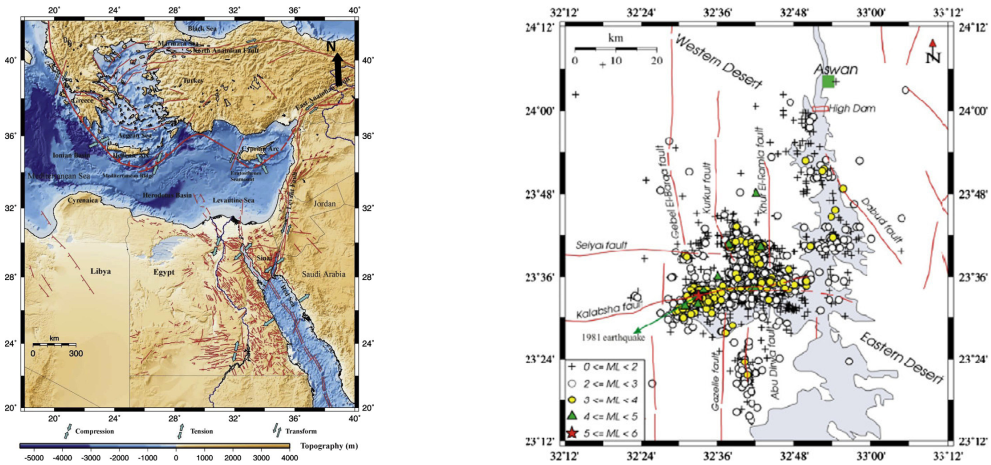

a) Regional Tectonic Setting b) Seismicity of Aswan Area

Figure H.5: Seismicity Map of Egypt [A.126]

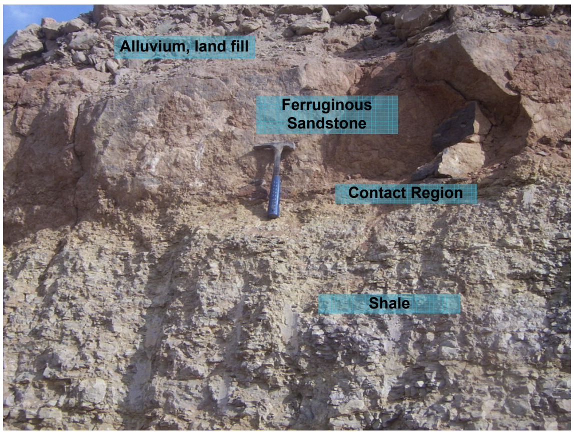

Figure H.6: Soil Layers

Table H.2: Soil Parameters

gm/cm^3-Sp.g	Element	Depth in m
1.70	Alluvium, land fill	0÷0.5
2.55	Ferruginous Sandstone	0.5÷1.0
1.80	Shale, green to red	1.0÷2.5
2.52	Fine grained Sandstone	2.5÷3.0

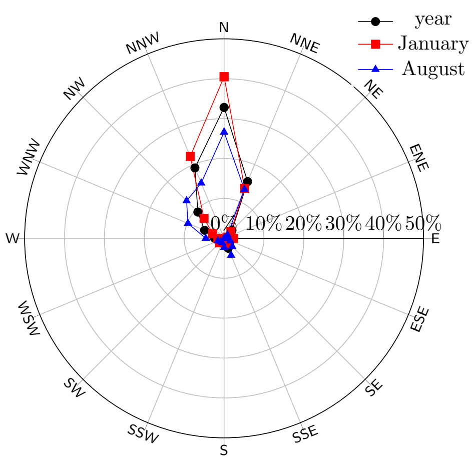

Figure H.7: Wind Data [U.12], [U.10]

H.2 Structural Model and Final Design

The designed solar chimney with a thickness of 6 mm, its supporting structure and the solar collector frame are made from S 235 steel while the foundation is made from C25/30 reinforced concrete. Glass panels are connected to the frame of the solar collector. All joints of the supporting structure have been welded while the tower has been built with two steel tubes connected via a flange. Figures H.8, H.9 and H.11 show the tower, the supporting frame structure of the tower and the solar collector with its glass panels, respectively.

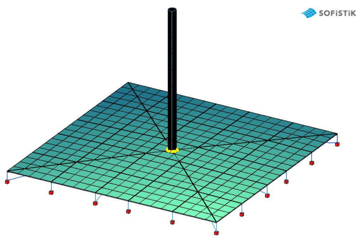

a) FE-Model

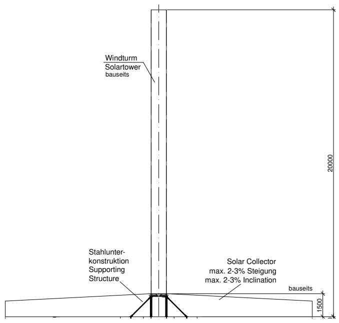

b) Technical Drawing

c) Aswan, Egypt

Figure H.8: Tower

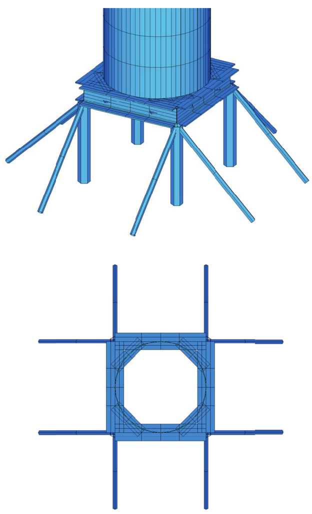

a) FE-Model

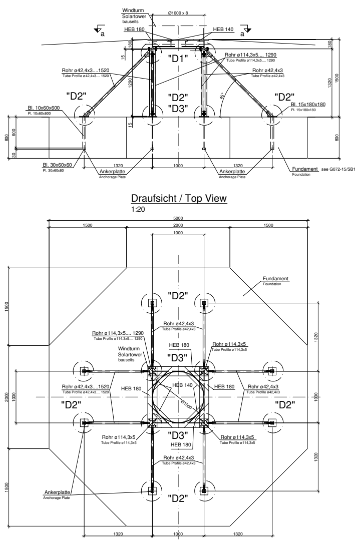

b) Technical Drawing

c) Aswan, Egypt

Figure H.9: Supporting Frame Structure

Inside the tower base a vertical axis turbine has been implemented with its general details given in table H.3 and figure H.12.

The turbine is connected to a generator which needs to withstand high temperatures due to the heating up of air underneath the SC. General parameters of the installed generator are listed

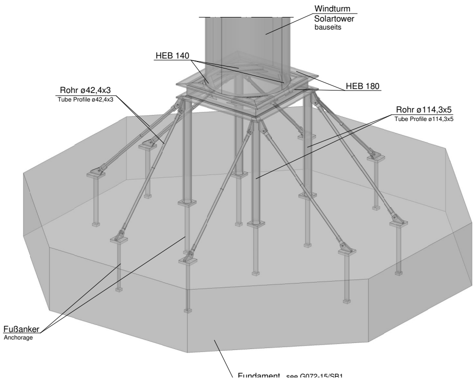

a) Technical Drawing

b) Aswan, Egypt

Figure H.10: Foundation

a) Glass Panels

b) Solar Collector

Figure H.11: Solar Collector with Glass Panels

Table H.3: Blade Parameter

Section	Section at radius from hub to tip	Chord section length	Blade twist angle at chord section
-	mm	mm	θ
1	85	125	8.2
2	138	119.4	6.5
3	190	111.6	5.0
4	231	104.16	4.3
5	290	96.1	3.5
6	340	88.04	2.4
7	400	83.08	1.6
8	465	77.5	1.0
9	500	74.4	0.3

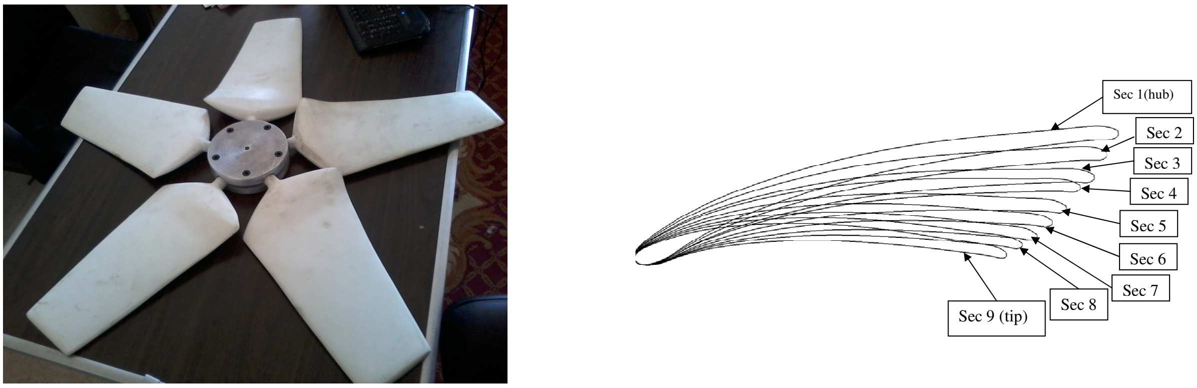

Figure H.12: Turbine with Blade Design

in table H.4.

Table H.4: Generator

Item	Range	Unit
Rated Power	1	kW
Rated Speed	500	RPM
Rated Voltage	AC 48	V
Insulation Class	F	-
Efficiency	93	%
Generator Type	3-Phase Permanent Magnet AC Synchronous	-
Service Life	over 20	years
Working Environment	-35 ÷ 60	°C
Speed Range	0-800	RPM

All data will be stored on site in a control room, depicted in figure H.13, situated close to the power plant. Via internet connection it is possible to gain access remotely and even get life data readings from the measuring sensors placed within the power plant.

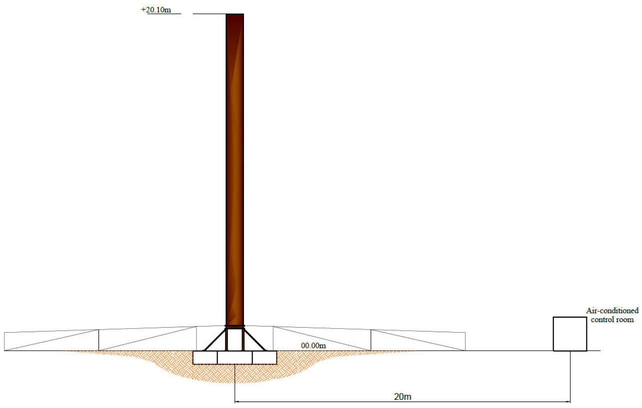

Figure H.13: Control Room at Construction Site

H.3 Monitoring and Measuring Devices

The SHM concept will be explained in detail in the final report and in [A.79]. Figure H.14 shows the monitoring sensor positions installed at the prototype at Aswan.

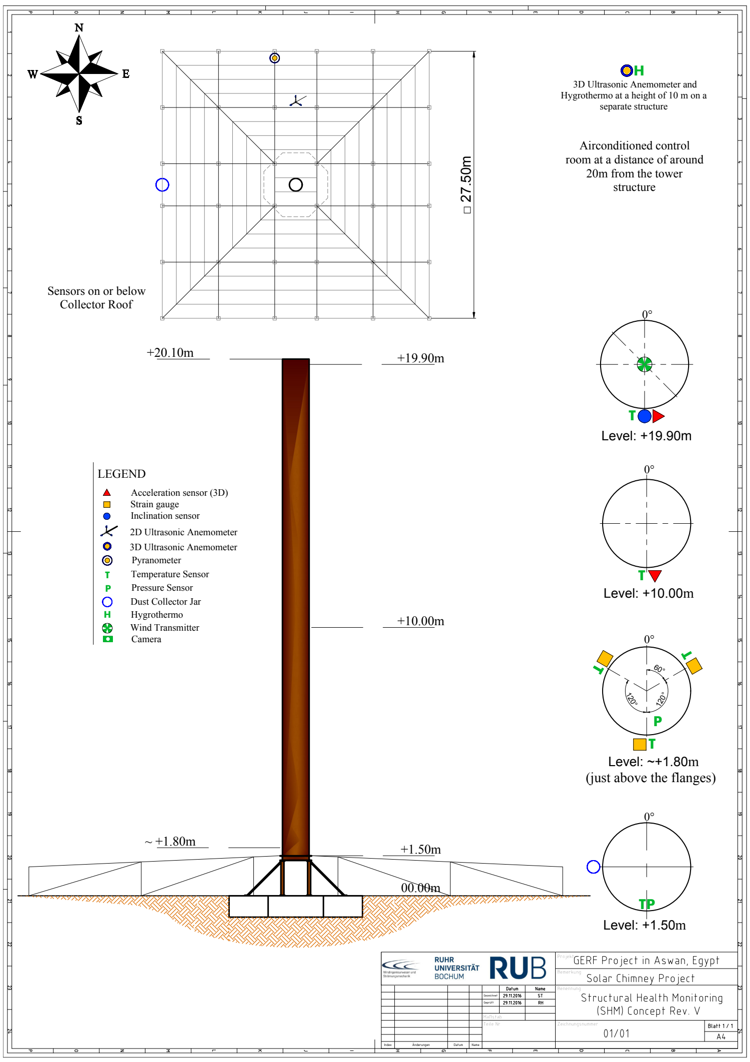

Figure H.14: Monitoring Sensor Positions